PRESSURE-TEMPERATURE-TIME CONSTRAINTS ON METAMORPHISM AND TECTONISM IN THE TAUERN WINDOW, EASTERN ALPS

by

JANE ELIZABETH SELVERSTONE

A.B. Princeton University
(1978)

M.S. University of Colorado, Boulder
(1981)

Submitted to the Department of
Earth, Atmospheric and Planetary Sciences
in Partial Fulfillment of the Requirements
for the Degree of

DOCTOR OF PHILOSOPHY

at the

MASSACHUSETTS INSTITUTE OF TECHNOLOGY

June 1985

Signature of Author_____
Department of Earth, Atmospheric and
Planetary Sciences, April 4, 1985

Certified by_____
Frank Spear
Thesis Supervisor

Accepted by_____
Theodore Madden
Chairman, Department Committee on Graduate Students

PRESSURE-TEMPERATURE-TIME CONSTRAINTS ON METAMORPHISM AND TECTONISM IN THE TAUERN WINDOW, EASTERN ALPS

by

JANE ELIZABETH SELVERSTONE

Submitted to the Department of
Earth, Atmospheric and Planetary Sciences
in Partial Fulfillment of the Requirements for the Degree of
Doctor of Philosophy in Geology
April, 1985

ABSTRACT

Pressure-temperature paths of metamorphism and uplift have been constructed for two tectonic units in the southwest corner of the Tauern Window, Austria/Italy. The hornblende garbenschist horizon of the Lower Schieferhülle (LSH) series contains the assemblage hornblende-kyanite-staurolite-garnet-biotite-plagioclase-epidote-quartz-carbonate-ilmenite-rutile, plus either chlorite or paragonite. P-T data based on geothermometry/barometry, pseudomorphs after lawsonite, thermodynamic modeling of mineral zoning, and fluid inclusion analysis yield a burial path through the lawsonite field to ≥10 kb, followed by heating to ~550°C during decompression. Application of the same techniques to the Upper Schieferhülle (USH) series indicates burial of this unit to only 6-7.5 kb and heating to ~475°C. Correlation of P-T path reversals calculated from zoned garnets in the two units supports the hypothesis that tectonic juxtaposition of the LSH and USH occurred prior to metamorphism; despite simultaneous growth, however, garnets are post-tectonic in the LSH and syntectonic in the USH.

Geochronologic data from the literature have been combined with the P-T paths to arrive at temperature-time and depth-time diagrams for both units. The slopes of these curves imply increasing cooling rates (0 to ~25°C/Ma) and decreasing uplift rates (~1.5 to ~0.3 mm/yr) as the rocks approached the surface. Variations in these rates between the units point to a history of differential uplift in the early stages of decompression. This is confirmed by geobarometric data indicating a vertical separation of ~10 km between the LSH and USH at the time of maximum burial, whereas the rocks are now separated by only 2-3 km of section. Textural features combined with these data suggest that initial uplift of the LSH was accomplished in part by ductile thinning of the USH, and possibly the overlying Austroalpine nappes.

A previous model of the Tauern Window ascribed the metamorphism to burial beneath a 15 km thick overthrust sequence. An important conclusion of this thesis is that the P-T conditions of the LSH and USH cannot

be explained by burial beneath such a thin thrust sheet. Thermal modeling calculations, combined with the petrologic results, show that the metamorphism can be adequately accounted for by burial of the LSH and USH to net depths of 40 and 30 km, respectively, beneath a 25 km thick overthrust. These data are incorporated into a revised model for burial, imbrication, metamorphism, and uplift in response to continental collision in the Eastern Alps.

Thesis supervisor: Frank S. Spear
Title: Associate Professor of Petrology

ACKNOWLEDGMENTS

Many people have aided and abetted my research for this thesis. First and foremost among them has been my advisor, Frank Spear, who first arranged for me to go to the Tauern Window and who subsequently spent many hours discussing Alpine petrology with me. Also deserving of special credit are Gerhard Franz of the Technische Universität Berlin and Giulio Morteani of the Technische Universität München, West Germany, whose geological expertise, encouragement, arguments, and kindness made working in the Alps a hard act to follow. Phil England assisted me with the thermal modeling calculations discussed in the last chapter, and Clark Burchfiel, Wiki Royden, and Kip Hodges helped keep me on the right track tectonically.

The field work for this thesis was carried out over three field seasons in Austria and Italy, and was assisted at various times by Frank Spear, Gerhard Franz, Giulio Morteani, Sabine Thomas, Bernd Lammerer, and David Gutzler. Sepp Volgger and his family and friends at Pfitscher Joch Haus provided unlimited quantities of schnapps and cappucino, nursed me through incipient pneumonia, and put up with my butchering of the German language. To all of these people, I offer my thanks.

Many of the ideas presented in this thesis have grown out of discussions with people almost too numerous to name. In addition to those mentioned above, they include Don Hickmott, Günter Grundmann, Friedhelm von Blanckenberg, Dave Klepacki, Page Chamberlain, Tim Grove, Doug Walker, Peter Crowley, Liz Schermer, and Jack Cheney; written comments from T.J.B. Holland and G. Hoschek substantially improved an earlier version of Chapter 3.

Financial assistance for this work came from a variety of sources: an

NSF Graduate Fellowship, a Shell Dissertation Fellowship, the M.I.T.-T.U.B. exchange program, Sigma Xi, a GSA research award, the Department of Earth, Atmospheric and Planetary Sciences at M.I.T., and NSF grant EAR83-18506 to Frank Spear. All of these funds are gratefully acknowledged.

Several individuals deserve special mention for the moral support they provided through my not-always-easy years at M.I.T. In addition to my parents, they include Julie Morris, Dana Geary, Allen and Reneau Kennedy, Don Hickmott, Peter Molnar, Tanya Furman, Michael Baker, David Gerlach, and Carrie Hengeveld. Above all, thanks go to my husband, Dave Gutzler, whose patience, humor, and love have sustained me throughout this "year of the thesis" and will no doubt continue to sustain me forever more; I hope I can return the favor.

TABLE OF CONTENTS

LIST OF FIGURES

LIST OF TABLES

CHAPTER 1

INTRODUCTION

INTRODUCTION

In the last decade there has been a dramatic shift in focus in the field of metamorphic petrology from determination of "peak" metamorphic conditions towards an attempt to evaluate the processes that produce these conditions. This shift is the result of many factors, of which two are particularly deserving of note. The first of these is that we are now in possession of a fairly extensive collection of quantitative geothermometers and geobarometers such that calculation of pressures and temperatures of peak metamorphism in many cases is relatively routine. The second is that thermal modeling studies imply that the array of "peak" P-T conditions exhibited by rocks across an orogenic belt may bear little to no resemblance to the actual path through P-T space followed by any individual rock through time (e.g., England and Richardson, 1977; Thompson, 1983; Royden and Hodges, 1984; England and Thompson, 1984; Thompson and England, 1984). In light of these modeling results, it has become necessary to examine the influence of a variety of tectonic processes on the P-T evolution of individual rocks, and consequently to devise means for reconstructing these paths from rocks we find in the field.

Much of the initial work done on relating metamorphic conditions to tectonic processes was carried out in the Tauern Window, Eastern Alps (e.g. Oxburgh and Turcotte, 1974; Bickle et al., 1975; England, 1978), and this area has served as the classic example of the influence of overthrusting on the thermal evolution of lower-plate rocks. When the original modeling calculations were carried out, however, few detailed petrologic studies of the rocks in the Tauern Window were available and

the thermal budget of the thrust-related metamorphism could not be uniquely constrained. This thesis attempts to provide these constraints by presenting the results of a detailed petrologic reevaluation of the metamorphic histories of two litho-tectonic units in the SW corner of the Tauern Window. New data from geothermometry/ barometry, pseudomorph phase equilibria, thermodynamic modeling of zoned minerals (Spear and Selverstone, 1983), and fluid inclusion analysis permit construction of quantitative P-T trajectories followed by the Lower and Upper Schieferhülle Series in response to the Alpine orogeny. When combined with mineral ages presented in the literature, these data are sufficient to evaluate the uplift and cooling histories of the units after the thermal peak of metamorphism and provide the necessary constraints for detailed tectonic models of the orogeny.

The ultimate purpose of this thesis is twofold. The first goal is to use modern petrologic techniques to reconstruct the detailed metamorphic history of an area in the Eastern Alps that has long served as a type locality for the effects of thrusting on metamorphism. The second and perhaps more important purpose is to demonstrate to what extent petrologic techniques can be used in conjunction with structural and geophysical data to place quantitative constraints on the interrelationships between tectonic and metamorphic processes. For the case of the SW Tauern Window, the combined data provide an exceptionally detailed view of the dynamic processes associated with a continent-continent collision.

GENERAL REMARKS

This thesis contains both publication-format and 'thesis-format' chapters, and as a result there is a certain amount of repetition of material. The bulk of Chapter 3 on the petrology of the Lower Schieferhülle series was originally published in the Journal of Petrology under the title 'High-pressure metamorphism in the SW Tauern Window, Austria: P-T paths from hornblende-kyanite-staurolite schists' (J. Petrol. 25, 501-531, 1984), and was coauthored with F. Spear, G. Franz, and G. Morteani. The only changes that have been made in incorporating it into this thesis are deletion of the general geology section (all of the relevant material is covered in Chapter 2) and addition of a section correlating fabric development with different stages in the P-T history of the rocks. The original summary and conclusion sections have been retained, although they are superceded to some extent by the material in the final chapter. Chapter 4 on the Upper Schieferhülle series follows the same format as Chapter 3 in order to allow for easier comparison between the units. Chapter 5 is the 'grand overview' in which all of the data from Chapters 3 and 4 are synthesized with geochronologic and geophysical data to arrive at a self-consistent model for the tectonic and metamorphic evolution of this region of the Alps. Each of these chapters more or less stands alone.

The hornblende garbenschist horizon of the Lower Schieferhülle series, which is the subject of Chapter 3, is referred to repeatedly as <u>the</u> LSH (Lower Schieferhülle). In fact, the LSH comprises many other lithologies which are not included in this thesis. I have, however, sampled and examined rocks from a complete cross section of the LSH, and have no reason to believe that the garbenschist horizon is in any way

atypical of the remainder of the unit. Sample localities for all lithologies of the LSH are shown in Appendix I, and several of these rock suites, in particular the Furtschaglschiefer, will be discussed in future papers.

Appendix II contains a brief paper on the effects of partial diffusional homogenization of mineral zoning profiles on the P-T paths calculated from analysis of garnet zoning. Although this paper is principally concerned with upper amphibolite facies rocks, it is included here to show some of the factors that can influence the direction and magnitude of garnet P-T trajectories such as those presented in Chapters 3 and 4. The simplified diffusion model used in Appendix II predicts extensive modification of "true" P-T paths in high-grade rocks containing small garnets. A general conclusion that can be drawn from the model, however, is that for the temperatures (<600°C) and grain sizes (radius > 1 mm) of concern in this thesis, diffusional processes are unlikely to have any detectable effect on garnet P-T paths over time intervals commensurate with the duration of the Alpine orogeny (~65 Ma).

Finally, many of the ideas in this thesis have been influenced indirectly by a number of publications that are not explicitly cited in the text. To the best of my knowledge, however, I have included all of these secondary sources in the reference list at the end of the text. Many of these are concerned with the geology of the Alps, but others relate more generally to interactions between tectonic and metamorphic processes. I hope this list proves useful for others interested in similar topics.

CHAPTER 2

GEOLOGIC FRAMEWORK OF THE TAUERN WINDOW

GENERAL GEOLOGY

The Tauern Window of western Austria is the largest of three tectonic windows in the Eastern Alps (Tauern, Engadine, and Wechsel windows; see Figure 2-1), and is the only one that exposes a complete cross section of the Pennine basement terrane beneath the overthrust units of the Austroalpine nappe sequence. This area thus provides a unique opportunity for investigating the interplay between tectonism and metamorphism of the European continental margin prior to and synchronous with overthrusting of the Austroalpine units during the Alpine orogeny. The general geology of the Tauern Window has been discussed at length in the literature throughout the last century, and only a brief review of the more salient features is presented here.

The Pennine basement terrane exposed in the Tauern Mountains can be subdivided into three principle tectono-stratigraphic units (Figure 2-2): a gneissic core, an autochthonous to parautochthonous cover sequence, and an allocthonous schist unit. The structurally lowest of these units is the Zentralgneis (ZG), which is composed of granitic to tonalitic augen gneisses, migmatites and intrusives (Morteani, 1974) that outcrop in three prominent massifs aligned along the E-W axis of the window. These rocks yield Rb/Sr whole rock ages of 310-280 Ma (Cliff, 1981; Satir and Morteani, 1982), corresponding to the culmination of the Hercynian orogeny; mineral ages of 14-21 Ma indicate an extensive Alpine overprint (Satir and Morteani, 1984).

In parautochthonous contact with the ZG is the Lower Schieferhülle (LSH) series, which encompasses rocks of both Paleozoic and Mesozoic age. In places, the LSH includes remains of the amphibolitic and metasedimentary country rocks into which the ZG intruded; these rocks

Figure 2-1. Sketch map of the Alps showing the locations of the Tauern, Engadine, and Wechsel windows (TF, E, and W, respectively) beneath the overthrust Austroalpine nappe sequence (narrow vertical ruling). The Helvetic, Penninic, and Flysch units of the European plate are indicated by the horizontal dashed lines. PN = Periadriatic Lineament. Map taken from Bögel and Schmidt (1976).

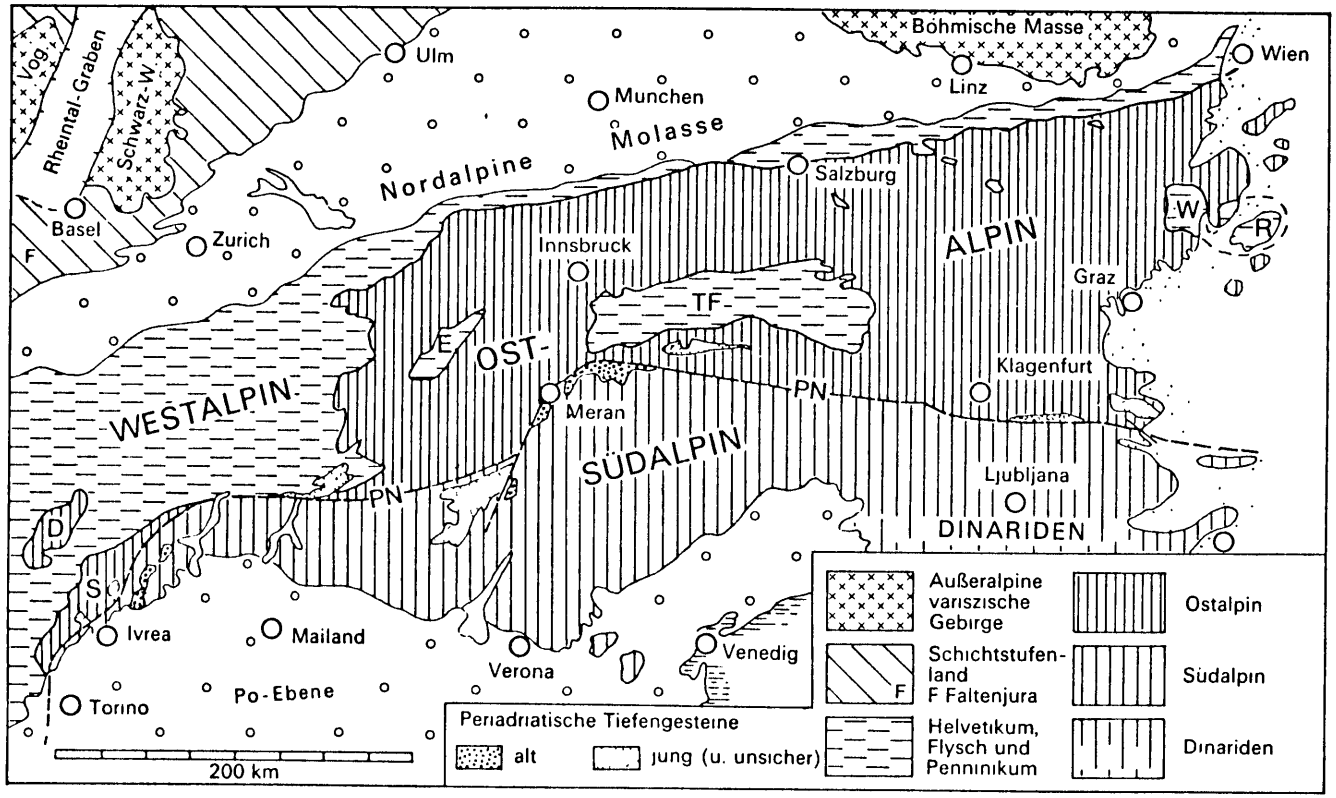
Vog.
Rheintal-Graben
Schwarz-W.
Ulm
Munchen
Molasse
Nordalpine
Böhmische Masse
Linz
Wien
Salzburg
Basel
Zurich
F
Innsbruck
ALPIN
W
R
Graz
TF
OST-
E
WESTALPIN
Meran
PN
Klagenfurt
SÜDALPIN
Ljubljana
DINARIDEN
D
S
Ivrea
Mailand
Verona
Venedig
Torino
Po-Ebene
200 km
Periadriatische Tiefengesteine
alt
jung (u. unsicher)
Außeralpine variszische Gebirge
Schichtstufenland
F Faltenjura
Helvetikum, Flysch und Penninikum
Ostalpin
Südalpin
Dinariden

Figure 2-2. Map showing the western and central portions of the Tauern Window. ZG = Zentralgneis, LSH = Lower Schieferhülle (Altkristallin and Permo-Mesozoic units), USH = Upper Schieferhülle, EZ = Eclogite Zone, and AA = Austroalpine nappes. Box indicates study area and location of Figure 2-5.

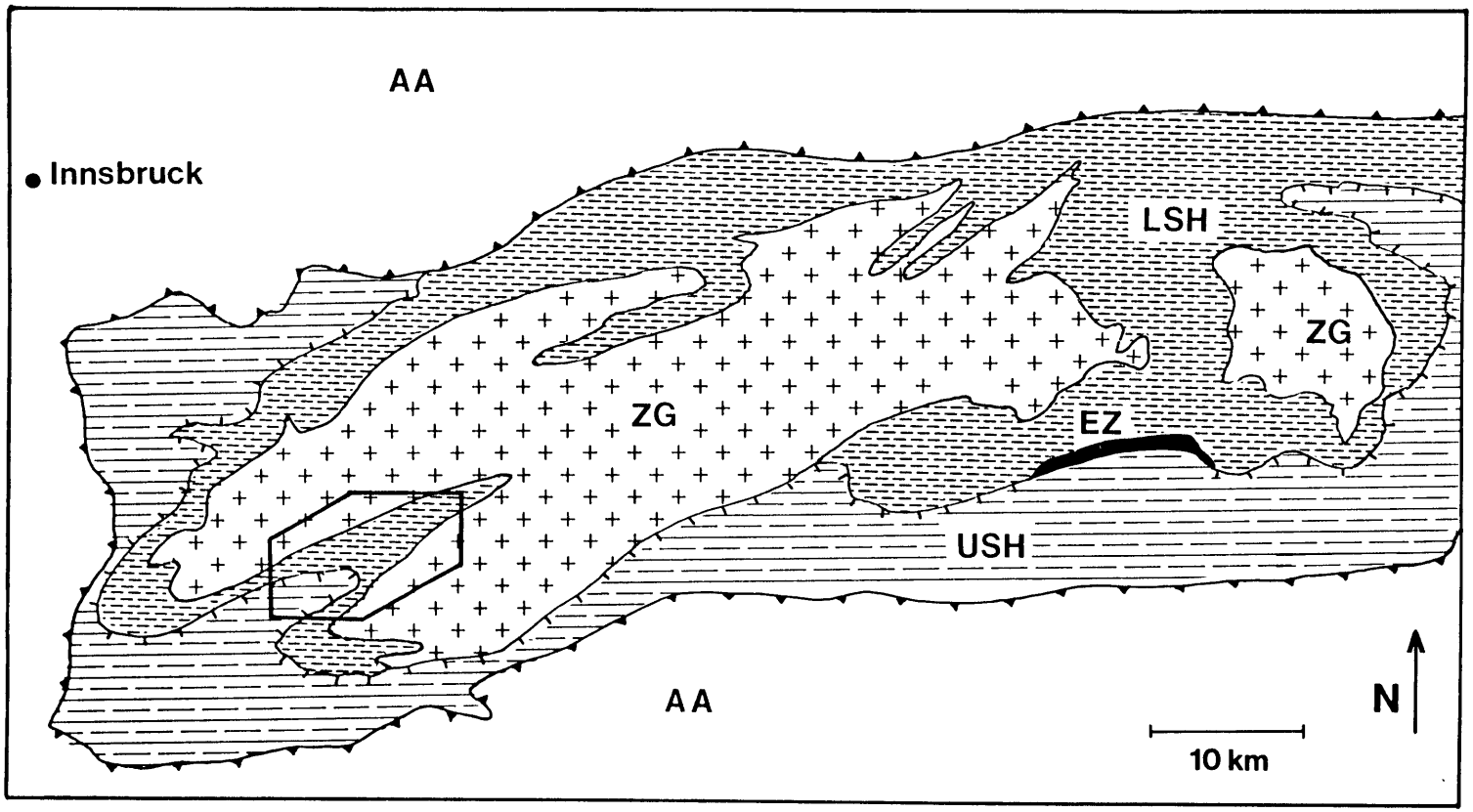
AA
Innsbruck
LSH
ZG
ZG
EZ
USH
AA
N
10 km

are referred to as the 'Altkristallin' and have been affected by both the Hercynian and Alpine orogenies. (Note that the crystalline basement of the overthrust Austroalpine units is also called the Altkristallin, but this unit occupies a very different tectonic position from the basement in the Tauern Window; to avoid confusion, the overthrust basement will be referred to specifically as the Austroalpine Altkristallin). Unconformably overlying the Altkristallin is a sequence of Permian to Cretaceous conglomerates, quartzites, marbles, pelites, and calcareous schists that is involved in several large Alpine nappe structures (Frisch, 1977; Lammerer, 1984).

The structurally highest unit within the Tauern Window is an allochthonous sequence of Permo-Mesozoic calcareous schists, marbles, and amphibolites belonging to the Upper Schieferhülle (USH) series (Morteani, 1974; Raith et al., 1977). Some serpentinite fragments are also present, and the unit as a whole represents material of predominantly oceanic provenance (Raith et al., 1977; Lammerer, 1984). The USH occurs as a prominant thrust nappe, which is referred to as the Glockner Decke throughout much of the Tauern Window.

In the central portion of the window, a thin unit of eclogites and blueschists (Miller, 1977; Holland, 1979) occurs in a carbonate matrix that also indicates metamorphism at pressures of ≈20 kb (Franz and Spear, 1983). This Eclogite Zone (EZ) presumably represents a separate allochthonous thrust slice sandwiched between the LSH and USH, although Miller (1974, 1977) considers it to be the basal portion of the USH.

The margins of the Tauern Window are defined by tectonic contacts with the overriding Austroalpine (AA) thrust sheets. These nappes represent continental crust derived from the Adriatic plate that was

thrust from south to north over the European plate during the Alpine orogeny (e.g. Dewey et al., 1973). The Austroalpine domain can be divided into Lower, Middle, and Upper units which are separated from one another by thrust surfaces. The dominant rock mass that overrode the Tauern Window consists of the pre-Alpine metamorphic basement rocks (Austroalpine Altkristallin) of the Middle AA and the essentially un-metamorphosed Grauwacken Zone and Northern Calcareous Alps of the Upper AA (Frey et al., 1974). The total thickness of these units is estimated to be between 15 and 20 km (Oxburgh, 1968; Oxburgh and Turcotte, 1974), based on measured sections and on sediment volumes in the peri-Alpine basins. Lammerer (1984) proposes a total thickness of ~30 km for the overthrust Austroalpine sequence by including the Lower AA units of the Ötztal massif as part of the overriding sequence; further documentation of this hypothesis is still necessary, however.

METAMORPHIC FRAMEWORK

The traditional view of the metamorphism in the Tauern Window is that three discrete 'events' of different ages affected the area, resulting in a complex polymetamorphic history for many of the rocks. In chronological order, these events can be summarized as follows (see also Pennine realm of Figure 2-3):

(1) Hercynian (~315-280 Ma; Hawkesworth, 1976; Cliff, 1981; Satir and Morteani, 1982). This event corresponds to the emplacement of the ZG intrusives and to the amphibolite (?) facies metamorphism of the Altkristallin. Pseudomorphs after andalusite in the northern part of the window (Grundmann and Morteani, 1982) represent contact metamorphic

Figure 2-3. Temperature-time diagrams representing traditional view of Eoalpine and Alpine phases of metamorphism as discrete thermal "events" that affected different units within the Tauern Window (Z=ZG, L=LSH, U=USH). Early Hercynian metamorphism not shown. Top diagram compiled by Morteani, bottom diagram by Kreuzer and Raith; note thermal pulse at ~20 Ma in latter case. Figure taken from Kreuzer et al., 1980.

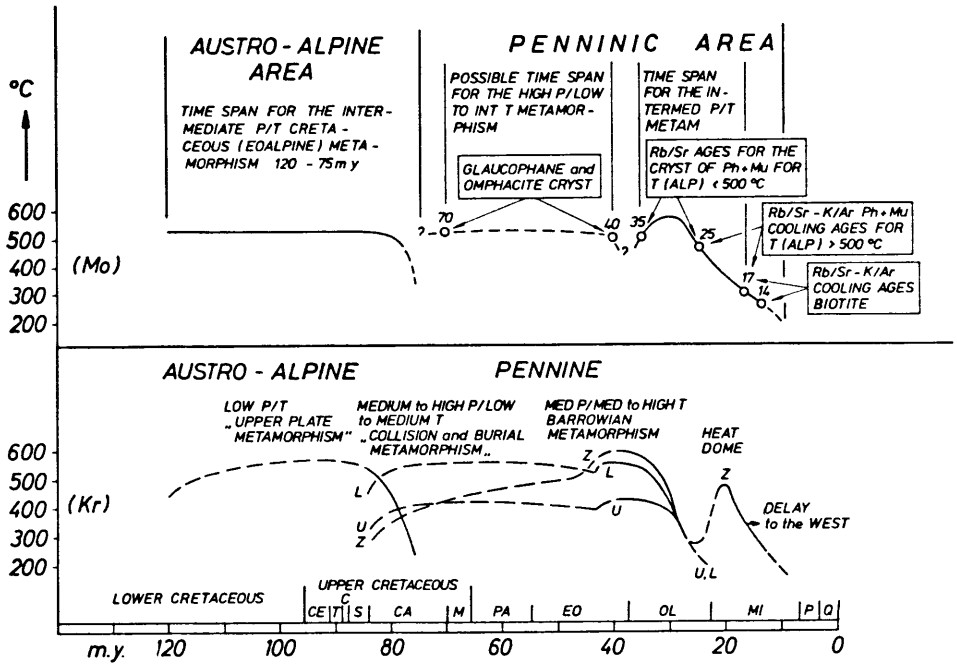
°C
600
500
400
300
200
(Mo)
AUSTRO - ALPINE AREA
TIME SPAN FOR THE INTER-MEDIATE P/T CRETA-CEOUS (EOALPINE) META-MORPHISM 120 - 75 m y
PENNINIC AREA
POSSIBLE TIME SPAN FOR THE HIGH P/LOW TO INT T METAMOR-PHISM
GLAUCOPHANE and OMPHACITE CRYST
TIME SPAN FOR THE IN-TERMED P/T METAM
Rb/Sr AGES FOR THE CRYST OF Ph+Mu FOR T (ALP) < 500 °C
Rb/Sr - K/Ar Ph+Mu COOLING AGES FOR T (ALP) > 500 °C
Rb/Sr - K/Ar COOLING AGES BIOTITE
70
40
35
25
17
14
AUSTRO - ALPINE
PENNINE
LOW P/T „UPPER PLATE METAMORPHISM"
MEDIUM to HIGH P/LOW to MEDIUM T „COLLISION and BURIAL METAMORPHISM„
MED P/MED to HIGH T BARROWIAN METAMORPHISM
HEAT DOME
DELAY to the WEST
(Kr)
L
U
Z
U,L
LOWER CRETACEOUS
UPPER CRETACEOUS
CE
T
C
S
CA
M
PA
EO
OL
MI
P
Q
m.y.
120
100
80
60
40
20
0

Figure 2-4. Sketch map showing isotherms of maximum temperatures (in ^{o}C) attained by rocks throughout the western and central Tauern Window in response to the Alpine orogeny. Outline of the ZG massif is shown for reference. Figure taken from Bögel and Schmidt (1976), based on the data of Morteani (1974) and Hoernes and Friedrichsen (1974).

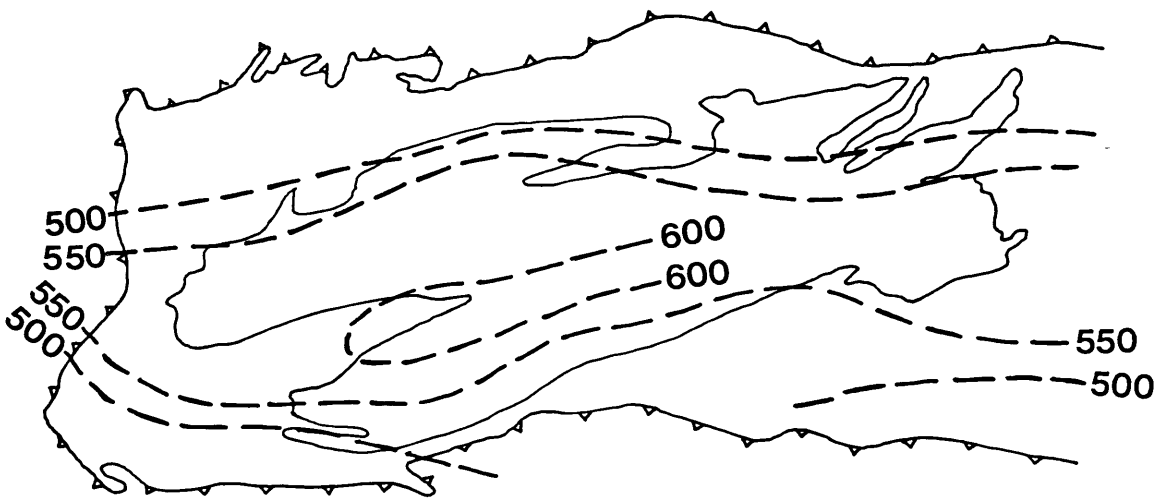
500
550
550
500
600
600
550
500

effects related to intrusion of the ZG at relatively shallow crustal levels. Relict eclogites thought to be of Hercynian age in the eastern part of the Tauern Window (Droop, 1983), however, suggest a phase of high-pressure metamorphism during Hercynian times. In sum, the ZG and Altkristallin are likely to have experienced a complex history prior to the Alpine orogeny, and must be evaluated with reference to probable polymetamorphism. The Mesozoic units of the LSH and all of the USH are too young to have been involved in this event, however.

(2) Eoalpine (>70 Ma; Raith et al., 1978; Kreuzer et al., 1980). This is generally thought to be a subduction-related, high-pressure event correlative with the blueschist facies metamorphism of the Western Alps (e.g. Ernst, 1973). Its traces are found predominantly in the Eclogite Zone, where estimated P-T conditions of 'peak' metamorphism are ~600°C, 18-25 kb according to Holland (1979) and Franz and Spear (1983), or ~600°C, 8-11 kb according to Miller (1974). Fry (1973), Miller (1974) and Raith et al. (1977) report the occurrence of pseudomorphs after lawsonite in some USH rocks that may indicate a high-P event in this unit, too; with the exception of these studies and the work of Selverstone et al. (1984; see also Chapter 3), however, no other evidence of high-pressure metamorphism in the LSH or USH has previously been discussed, and this 'event' has not been considered to have been widespread in the Tauern Window.

(3) Alpine (~50-25 Ma; Raith et al., 1978). This event, called the 'Tauernkristallisation' by Sander (1911), produced the dominant metamorphic signature in the Tauern Window in response to culmination of the Alpine orogeny. Isotherms constructed by Morteani (1974) and Hoernes and Friedrichsen (1974) for this metamorphic overprint form a concentric

array that increases continuously from greenschist to amphibolite facies conditions towards the center of the window (Figure 2-4), suggesting that tectonic juxtaposition of all of the units within the window occurred prior to this phase of metamorphism. "Peak" pressures for this event have been estimated by several authors to be in the range 5 to 7 kb (e.g. Morteani, 1974; Frey et al., 1974; Hoschek, 1980,1981, 1982; DeVecchi and Baggio, 1982), although Selverstone et al. (1984 and Chapter 3) report pressures of ~10 kb for the LSH.

Each of these so-called metamorphic "events" has been regarded as a discrete thermal pulse, in some cases of only local significance, followed by a hiatus (Kreuzer et al., 1982; see Figure 2-3). Although it is clear that such a time-temperature gap separated the Alpine orogeny from the Hercynian orogeny, the evidence presented in this thesis indicates a continuous pressure-temperature evolution of the rocks in the study area from ~80 Ma to ~5-10 Ma; the term "Alpine" is used loosely throughout this thesis to denote this entire time period.

THERMAL AND TECTONIC MODELS

The general features of the Alpine orogeny can be explained by subduction of the European plate beneath a southern continental landmass (the Adriatic plate), culminating in a continent-continent collision and overthrusting of the Austroalpine units onto the European basement in Eocene times (e.g. Dewey et al., 1973; Ernst, 1973; Oxburgh and Turcotte, 1974; Hawkesworth et al., 1975; Roeder and Bögel, 1978; Frisch, 1978, 1979). Within this general framework, several thermal models have been proposed to account for the observed Alpine metamor-

phism in the Tauern Window; because several of these models are referred to repeatedly throughout this thesis, a brief review is given here.

The first quantitative model relating metamorphism to tectonic processes in the Tauern Window was presented by Oxburgh and Turcotte (1974). These authors attempted to explain the pervasive greenschist to amphibolite facies metamorphism within the window as a direct result of emplacement of the overlying Austroalpine thrust sheets. The model assumes an initial post-thrusting "sawtooth" temperature distribution through the basement and nappe sequence that decays with time towards a steady state geotherm. The rocks of the ZG, LSH, and USH would thus experience an immediate increase in pressure due to the increased overburden thickness, followed by a gradual increase in temperature towards the new steady state value. For an assumed thickness of 15-20 km for the Austroalpine units (Oxburgh and Turcotte, 1974), maximum pressures of 4 to 5 kb would be expected for "Alpine" metamorphism in the USH.

For an overthrust thickness of 15 km and reasonable values for heat production in the ZG and LSH, Oxburgh and Turcotte (1974) demonstrated that it would have been possible to generate temperatures of ~500°C in the USH within 30 Ma of the overthrusting event; they point out, however, that this result only holds for values of Q_m (the deep-seated or "mantle" heat flux) equal to approximately 75 mW m^{-2}. This represents an anomalously high deep-seated contribution to the thermal budget relative to typical continental values of Q_m of <40 mW m^{-2} (e.g. Vitorello and Pollack, 1980). As there is no evidence for magmatism of Alpine age in the Tauern Window, however, even a transient value of Q_m=75 mW m^{-2} must be questioned. Thus, although Oxburgh and Turcotte (1974) were able to reproduce the general P-T conditions of the USH, the details of their

model appear to be unrealistic in explaining the overall metamorphism in the Tauern Window.

More generalized thermal models relating the Alpine metamorphism to overthrusting of the Austroalpine sheets have been proposed by Bickle et al. (1975) and England (1978). The gross features of these models are similar to that of Oxburgh and Turcotte (1974), but rather than considering fixed values of the input parameters, Bickle et al. (1975) and England (1978) specifically evaluated the effects of varying the thickness of the overthrust sheet, the erosion rate, the value of Q_m, and the temperature dependence of the thermal conductivities of the rocks. In both cases, the heat flow equation was solved for a range in values of these parameters; acceptable combinations of these values were those that exposed the rocks at the surface 65 Ma after thrusting and were capable of reproducing both the maximum metamorphic temperatures recorded in the Tauern Window and the measured values of present-day surface heat flow in the area (~67-84 mW m^{-2}; Clark, 1961). The only solutions that satisfy all of these conditions are those involving burial of the rocks to depths of ≥25 km and sustained values of $Q_m \leq 40$ mW m^{-2} (England, 1978). Thin thrust sheet calculations all require higher values of Q_m to produce the observed metamorphic conditions, which, if sustained through time, would result in excessive present-day surface heat flow values (≥110 mW m^{-2}). Bickle et al. (1975), England (1978), and subsequently Oxburgh and England (1980) all emphasize that the thermal models are most consistent with burial to greater depths than was assumed by Oxburgh and Turcotte (1974), but that the possibility of metamorphism beneath a 15 km thrust accompanied by a <u>transient</u> high Q_m cannot be ruled out based on the modeling results.

The results of the calculations summarized above indicate a dilemma with regard to Alpine metamorphism in the Tauern Window. If metamorphism occurred solely in response to emplacement of the Austroalpine sheets, which have an estimated thickness of 15-20 km, an anomalously high mantle contribution to surface heat flow would be required; to date, there is no evidence to suggest a high heat-flow regime ever existed in the area. In contrast, metamorphism of crust with a more "normal" thermal regime requires burial of the rocks to depths of 25-35 km, or nearly double most estimates of the Austroalpine nappe thickness (note, however, that Lammerer, 1984, has recently argued for such revised AA thicknesses). Detailed petrologic techniques are used in this thesis to quantify the pressure-temperature-time (PTt) histories of rocks from beneath the Austroalpine nappes in order to distinguish between the different scenarios outlined above.

STUDY AREA

The area of this study is in the SW corner of the Tauern Window, where a complete transect from the ZG through the lower half of the USH is particularly well-exposed (Figures 2-5 and 2-6). The overall structure of this region is that of a synform that has preserved a narrow belt of LSH and USH between two lobes of the ZG. The LSH here consists of amphibolitic and graphitic schist members of the Altkristallin (garbenschist and Furtschaglschiefer, respectively), and a relatively complete sequence of the Permian and Mesozoic units. The USH is represented primarily by calcareous schists and greenstones, and is missing the higher flysch members described by Frisch (1980).

Hercynian phases of folding can be recognized in the Paleozoic rocks of the area, but the dominant structure is related to at least two Alpine deformational events. The first of these (D_1) produced a series of large nappes and tight folds in both the ZG and LSH (e.g. the Wolfendorn nappe of Frisch, 1977) and resulted in extensive shearing of the limbs. Within the area of this study, these folds have been refolded by more open F_2 folds into a predominantly vertical orientation. These F_2 structures involve the USH in addition to the ZG and LSH (Lammerer, 1984; see Figure 2-6). Tight, isoclinal folds that predate F_2 are evident in the USH, but it is not clear whether or not these can be correlated with the previously described F_1 folding event.

The strong shearing associated with F_1 folding appears to have destroyed any remnants of Hercynian metamorphism in the Altkristallin of the study area, and growth of metamorphic porphyroblasts clearly post-dates this deformational event in the LSH. In contrast, growth of garnet and plagioclase in the USH commenced during the early folding event, and syntectonic porphyroblasts are ubiquitous in this unit. F_2 folds appear to post-date the development of the dominant metamorphic fabric in both units, although the evidence for this is somewhat ambiguous.

Previous petrologic investigations in this region have been principally concerned with the mineralogy and phase relations of different lithologies in the LSH (e.g. Ackermand and Morteani, 1973; Raith, 1976; Hoschek, 1980, 1981; DeVecchi and Baggio, 1982) and in the USH (Hoschek, 1980, 1984). Pressure-temperature conditions associated with "peak" metamorphism have been determined by these authors to be ~500-550°C, 5-7 kb throughout the area of this study, but no information is currently available concerning the earlier metamorphic histories of the units.

Figure 2-5. Generalized geologic map of study area in SW corner of the Tauern Window (see Fig. 2-2). The shaded patterns indicate the ZG and the location of a major shear zone, as shown on the legend. pLSH = Paleozoic LSH (Greinershiefer Series), including hornblende garbenschists, amphibolites, and serpentinites; Furt = graphitic schists of the Furtschaglschiefer. The Greinerschiefer Series and the Furtschaglschiefer together make up the Altkristallin. mLSH = conglomerates, quartzites, aluminous schists, and marbles of the Permo-Mesozoic LSH. cUSH = calcmica schists (Bündnerschiefer) of the USH; vUSH = greenstones and serpentinites of the USH. Axes of major Alpine folds are shown. A-A' indicates line of cross section shown in Figure 2-6; sample localities are given in Appendix I. R = Rotbachlspitze; PJ = Pfitscher Joch Haus; HF = Hochfeiler; GG = Großer Greiner. Map is based on field observations and on unpublished maps of G. Morteani, H. von Maravic, and B. Lammerer.

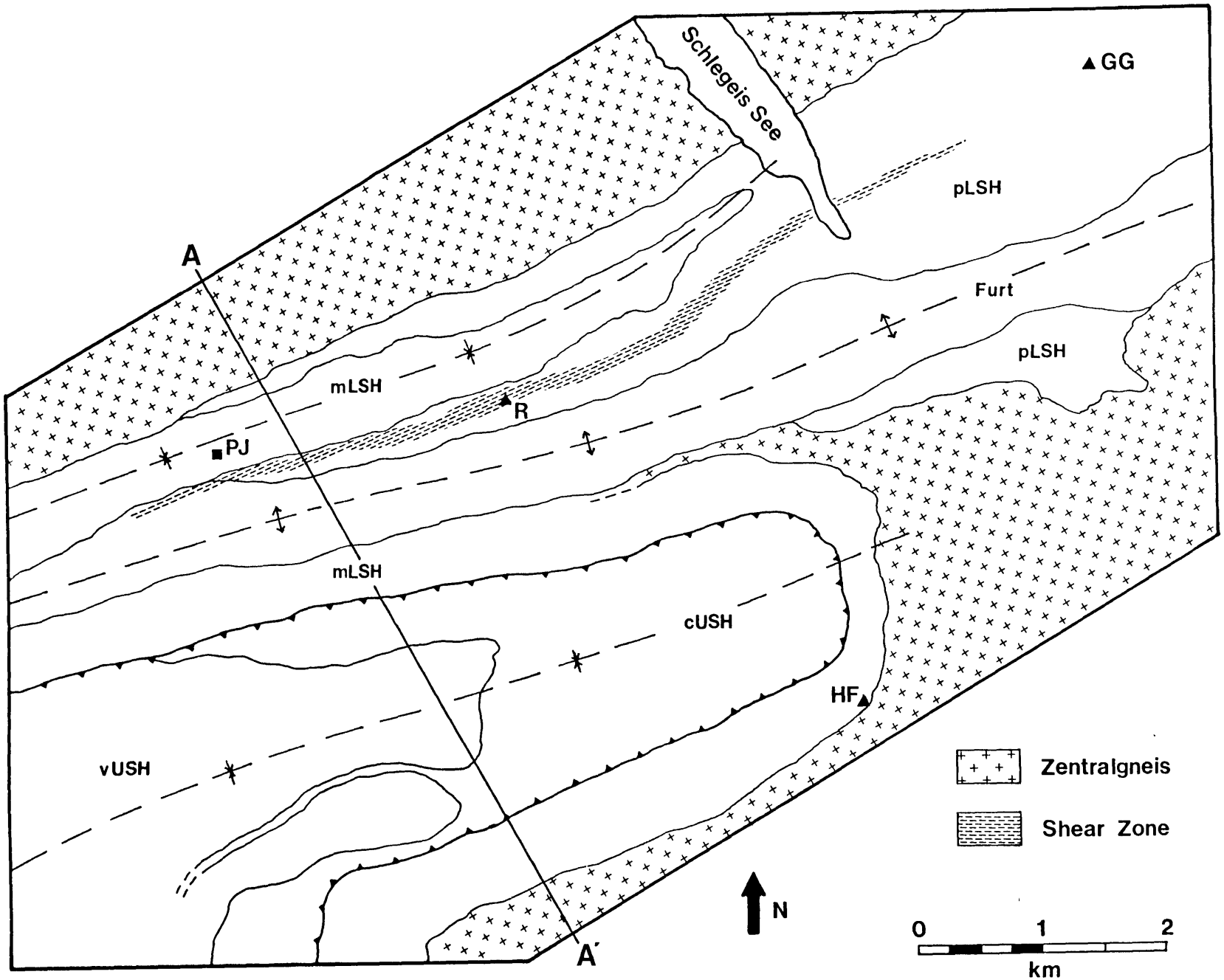
Schlegeis See
GG
pLSH
A
Furt
pLSH
mLSH
R
PJ
mLSH
cUSH
HF
vUSH
A'
N
0
1
2
km
Zentralgneis
Shear Zone

Figure 2-6. Schematic cross section along line A-A' of Figure 2-5, showing Hercynian folds in Altkristallin (pLSH) and large synform of Permo-Mesozoic LSH (mLSH) that can be correlated with the Wolfendorn nappe of Frisch (1977). Note involvement of ZG in Alpine folds related to (?) drag between the USH and LSH, and subsequent folding of USH thrust plane. Localities of samples collected on or near the line of section are also indicated (see Appendix I). 1 = ZG; pLSH: 2 = amphibolites and garbenschists, 3 = Furtschaglschiefer; mLSH: 4 = conglomerate, 5 = quartzite, 6 = biotite-epidote schist, 7= Hochstegen marble, 8 = aluminous and graphitic schists; USH: 9 = calcmica schists and greenstones. Structure modified after Lammerer (personal communication), in accord with field observations.

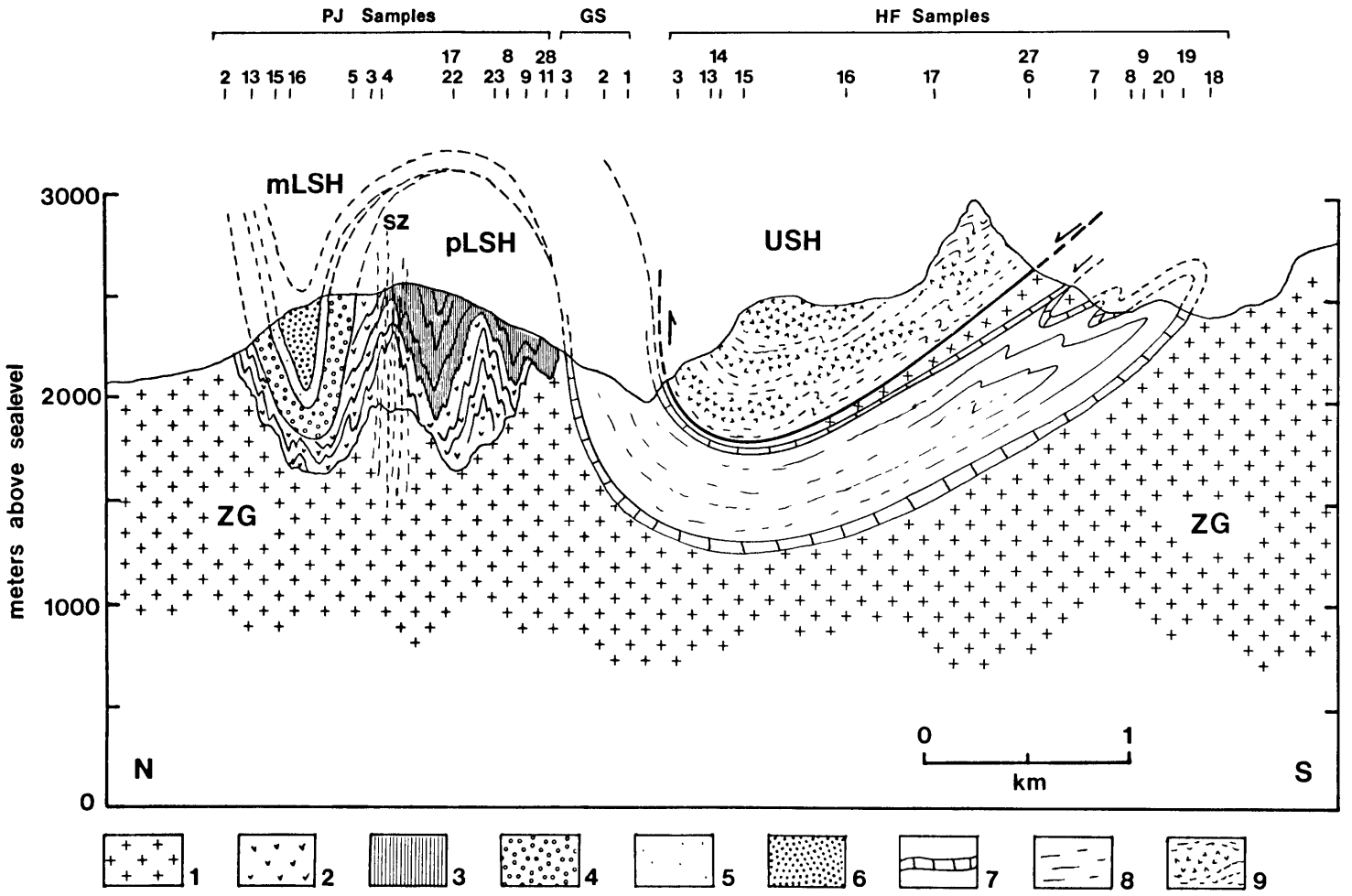
PJ Samples
GS
HF Samples
2 13 15 16 5 3 4 17 22 23 8 9 11 28 3 2 1
3 13 15 16 17 14 6 27 7 8 20 9 19 18
mLSH
sz
pLSH
USH
ZG
ZG
3000
2000
1000
0
meters above sealevel
N
S
0
1
km
1
2
3
4
5
6
7
8
9

This thesis presents the results of detailed petrologic studies aimed at documenting the complete P-T and tectonic histories of the LSH and USH in the SW Tauern Window. A similar study of the ZG in this region is being carried out by Sabine Thomas at the Technische Universität Berlin, but the results are not yet available for comparison.

CHAPTER 3

PETROLOGY AND P-T HISTORY OF THE HORNBLENDE GARBENSCHIST MEMBER OF THE LOWER SCHIEFERHÜLLE SERIES

ABSTRACT

The hornblende garbenschist horizon of the Lower Schieferhülle series (LSH) in the SW Tauern Window, Austria, contains the assemblage hornblende + kyanite + staurolite + garnet + biotite + epidote + plagioclase + ankerite + quartz + rutile + ilmenite, with either chlorite or paragonite present in all samples. These assemblages are divariant in the system SiO_2-Al_2O_3-TiO_2-Fe_2O_3-MgO-FeO-MnO-CaO-Na_2O-K_2O-H_2O-CO_2. Garnet-biotite geothermometry yields temperatures of final equilibration of ~550°C, and garnet-plagioclase-kyanite-quartz geobarometry indicates pressures of 6-8 kb for the matrix assemblage and 9-10 kb for plagioclase inclusions in garnet. Quantitative modeling of zoned garnet, hornblende and plagioclase indicates growth and equilibration along a decompression path from ~530°C, 10 kb to ~550°C, 7 kb. Fluid inclusion data constrain the uplift path to have passed through a point at ~375°C, 1.5 kb.

These data permit the construction of a relatively complete P-T loop for metamorphism associated with the Alpine orogenic cycle in the LSH of the SW Tauern Window. The maximum pressure conditions (~10 kb at 530°C) recorded along this loop are considerably higher than previous estimates of 5-7 kb for the region. Simple overthrust models developed for the Tauern Window cannot account for pressures of this magnitude; a more likely scenario involves partial subduction of the rocks to a depth of ~35 km, followed by prolonged heating in response to decay of the subduction isotherms. Initial uplift appears to have been rapid and occurred along a nearly isothermal path. Significant cooling did not occur until the rocks were within ~5 km of the surface. Detailed tectonic models for the evolution of the Tauern Window must be able to account for the quantitative features of the P-T loop.

INTRODUCTION

The Tauern Window of western Austria is a tectonic window in which the nappes of the Penninic basement terrane are exposed beneath the Austroalpine thrust sheets. This area provides a unique opportunity for investigating the interplay between tectonism and metamorphism in the eastern Alps prior to and synchronous with overthrusting. The general features of Alpine metamorphism in the Tauern Window have been discussed at length in the literature (e.g. Ernst, 1973; Frey et al., 1974; Morteani, 1974; Miller, 1977; Raith et al., 1978; Ackermand et al., 1978; Hoschek, 1980 a,b; Droop, 1981), and this metamorphic framework has served as a basis for the classic models of Oxburgh & Turcotte (1974), Bickle et al. (1975), and England (1978) concerning the influence of thrusting and rapid uplift upon the development and preservation of metamorphic facies. However, there is still considerable debate concerning the detailed pressure-temperature evolution of the Tauern Window, and reevaluation of this history based on additional petrologic data has great potential for constraining the complex relationships between tectonic and metamorphic processes. This paper presents a quantitative P-T path followed by rocks of the hornblende garbenschist horizon of the Lower Schieferhülle series in the SW Tauern Window, and discusses the tectonic implications of this metamorphic trajectory.

STUDY AREA

The area of this study is an inlier of LSH rocks, referred to as the Greinerschiefer Series, between two blocks of ZG in the southwest corner of the Tauern Window (see Appendix). Two sampling transects (FH-1 and Z3) were carried out across the strike of the hornblende garbenschist horizon of the Greinerschiefer series; no differences in assemblage were observed between the two areas, and they are therefore considered together in the following discussion. Detailed petrologic analysis of these samples has been carried out with an eye towards unraveling the metamorphic, and hence also tectonic, history of this region. Ernst (1973) has noted the surprising absence of high-pressure metamorphic rocks in the LSH and USH relative to the rocks of the Pennine nappes in the Western Alps, and has suggested that high-pressure metamorphism may in fact have affected the entire Tauern terrane, but later overprinting in the amphibolite facies totally obliterated its traces. The particular focus of this study is to reconstruct the early history of the LSH rocks with reference to possible high-pressure metamorphism such as that observed in the Pennine zone of the Western Alps.

ANALYTICAL TECHNIQUES

Mineral analyses were carried out using the automated Materials Analysis Corporation microprobe at M.I.T. Well-characterized glasses and natural minerals were used as standards. Most analyses represent averages of 3 spot analyses in close proximity to one another. Cores and rims of grains were analyzed to check for homogeneity, and step scan analyses were carried out on grains showing significant chemical zonation.

Fluid inclusions were analyzed using a Linkham TH 600 heating and freezing stage at M.I.T. Heating rates were 0.1°C/min at T<200°C and 1.0°C/min for T>200°C. Reproducibility was ±0.3°C for freezing temperatues, ±0.2°C for homogenization of CO_2 inclusions, and ±1°C for aqueous homogenization. All temperature determinations were repeated three times to ensure accuracy.

SAMPLE DESCRIPTION AND MINERAL CHEMISTRY

The hornblende garbenschist horizon of the LSH comprises a sequence of mafic to felsic metavolcanics and volcanogenic metasediments. The unit takes its name from the spectacular sheaves ("garben") of amphibole crystals up to 20 cm in length that are developed in the plane of the foliation (Fig. 3-1). The mineral parageneses are no less spectacular than the outcrop appearance of these rocks, and the dominant assemblage over a wide range of bulk compositions is hornblende + kyanite + staurolite + garnet + biotite + plagioclase + epidote + ankerite + quartz + ilmenite + rutile, with either paragonite or chlorite present in all cases (Table 3-1; see also Ackermand and Morteani, 1973). Margarite is common as a late-stage phase, but does not appear to be part of the stable assemblage; all other phases appear to be in textural equilibrium.

Most samples exhibit an early folded foliation defined by epidote, ilmenite, rutile, and rarely biotite or paragonite. This foliation has been overprinted by randomly oriented amphibole crystals and by euhedral garnets set in a foliated matrix of paragonite or chlorite; the matrix foliation is generally undeformed or only slightly warped. Hornblende grains typically exhibit tensional cracks that are filled with the same

Figure 3-1. A. Typical "garben" of hornblende, from which the Garbenschist takes its name. B. Large hornblende and garnet crystals in paragonite-rich matrix. Note tensional cracks in hornblende.

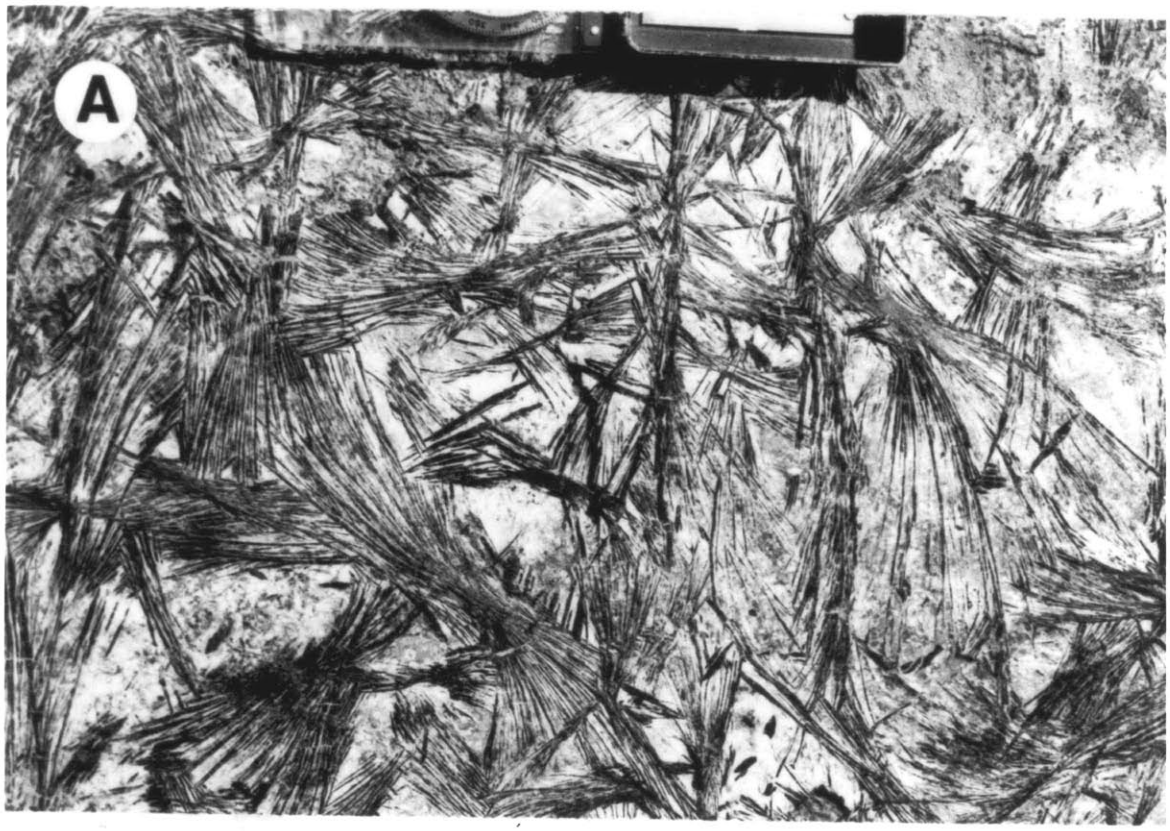
A

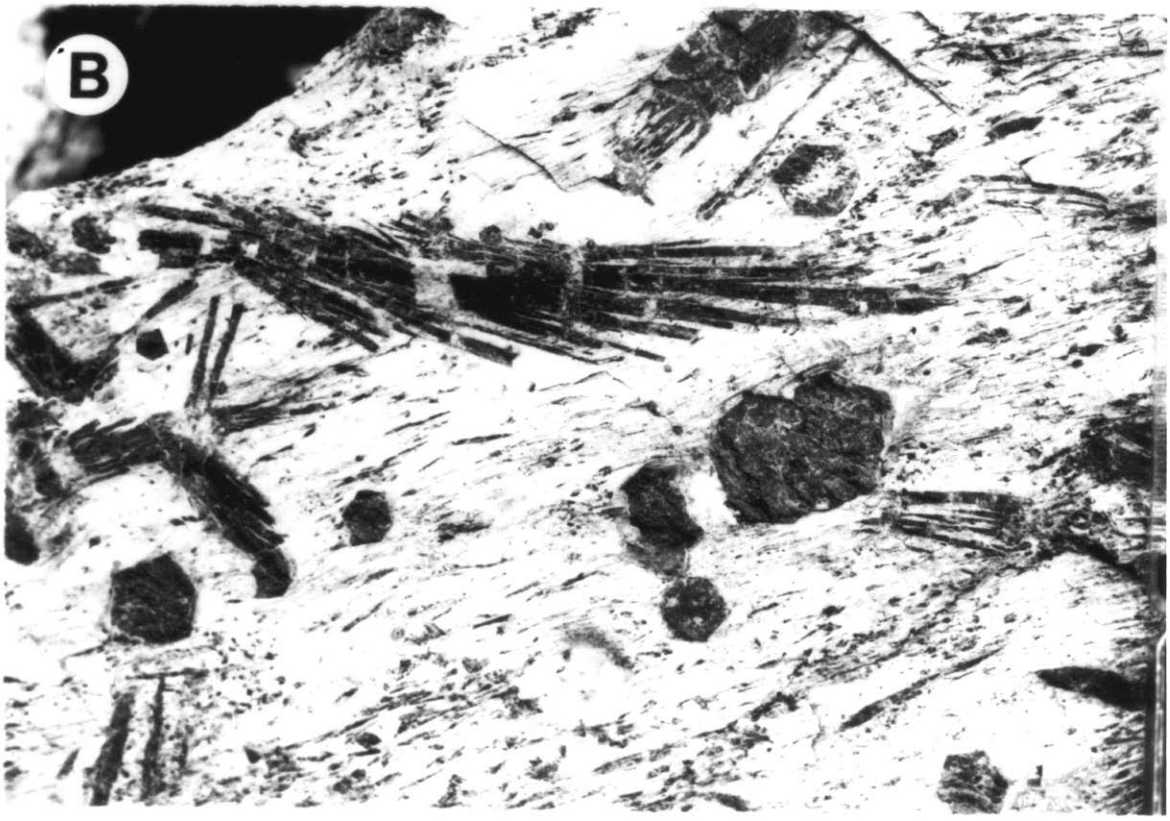
B

TABLE 3-1

Mineral Assemblages From Hornblende Garbenschist Horizon of the Greinerschiefer Series

Sample	Hbl	Kya	Staur	Gar	Bio	Chl	Parag	Plag	Epid	Ank	Qtz	Ru	Ilm	Marg
Z3-B	X	X	X		X		X	X	X		X	X	X	X
Z3-D	X			X	X	X		X	X	X	X		X	
Z3-H	X			X	X	X		X	X	X	X		X	
Z3-I	X				X		X	X	X	X	X	X	X	
Z3-K	X	X	X		X		X	X	X	X	X	X	X	X
Z3-M	X	X	X			X		X	X	X	X	X	X	X
Z3-N	X	X	X	X	X		X	X	X	X	X	X	X	X
Z3-O	X	X	X		X	X		X	X	X	X		X	X
Z3-Z	X			X	X	X		X		X	X		X	
Z3-BB	X	X	X		X	X		X	X	X	X		X	X
FH-1JA	X	X			X	X		X	X	X	X			X
FH-1L*	X	X	X	X	X	X	X	X	X		X		X	
FH-1M	X	X	X	X	X	X		X	X	X	X	X	X	X
FH-1N	X	X	X	X	X	X		X	X	X	X		X	X
FH-1O	X	X	X	X	X	X		X	X	X	X		X	X
FH-1P	X	X	X	X	X	X		X	X	X	X	X	X	X
FH-1Q*	X	X	X	X	X	X	X	X		X	X	X	X	X
FH-1R	X			X		X	X	X	X		X	X	X	X
FH-1S	X				X	X	X	X	X		X	X	X	X
FH-1U	X				X	X		X	X		X	X	X	

*FH-1L and FH-1Q are composed of alternating chlorite-and paragonite-rich layers. Chlorite and paragonite do not coexist within the layers.

assemblage as is found in the matrix. With the exception of mats of margarite formed around plagioclase and some replacement of hornblende by biotite + chlorite, evidence of retrogression is rare.

Hornblende (Hbl) occurs as large, elongate porphyroblasts containing abundant incusions of epidote, quartz, ankerite, plagioclase, ilmenite, and rutile; in rare instances, kyanite and staurolite also occur as inclusions near the outer margins of hornblende grains. The amphiboles show slight zonation in Fe/Fe+Mg ratio, Na(M4),and Na(A), but little variation in Al content. The overall composition of the amphiboles is pargasitic with up to 18 wt% Al_2O_3. Representative analyses of hornblende are presented in Table 3-2, with Fe^{3+} calculated according to the method of Spear & Kimball (1984).

Kyanite (Kya) is pure Al_2SiO_5 within the detection limits of the electron microprobe and occurs both as large poikilitic garben and as smaller nonpoikilitic matrix grains. Kyanite in many samples is clearly in textural equilibrium with both hornblende (Fig. 3-2) and ankerite; these unusual parageneses are discussed in a subsequent section.

Staurolite (Staur) is present as large euhedral crystals in chlorite-bearing samples (Fig. 3-2) and as small, anhedral grains peripheral to hornblende in paragonite-bearing rocks. In both cases, staurolite ranges from Fe/Fe+Mg = 0.69 to 0.79 and contains less than 1.0 wt% ZnO (Table 3-2). No compositional zoning has been observed.

Garnet (Gar) is typically subhedral to euhedral and contains abundant inclusions of quartz, plagioclase, epidote, ankerite, and ilmenite; no rotational fabrics have been observed. Compositional zoning is well-developed (Table 3-3), with cores enriched in grossular (17-24%) and spessartine components relative to the rims. In all cases, the Fe/Fe+Mg

Figure 3-2. Photomicrograph of hornblende (H) + kyanite (K) + staurolite (S) + epidote (E) in a chlorite (C) matrix, sample Z3-M. Scale bar is 1 mm long.

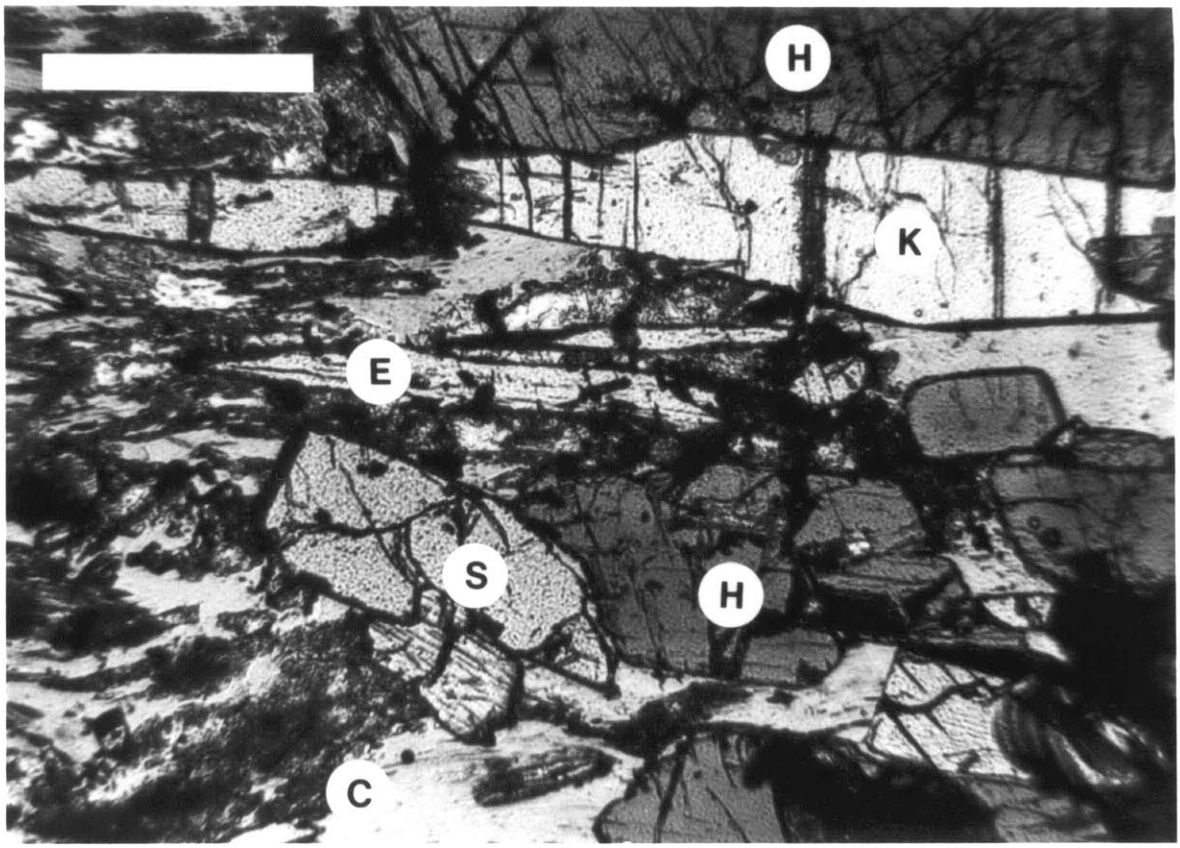
H
K
E
S
H
C

Table 2 - Representative Hornblende Analyses

	Z3-B core	Z3-B edge	Z3-M core	Z3-M edge	Z3-M+ pseudo	Z3-N core	Z3-N edge	FH-1M core	FH-1M edge	FH-1P core	FH-1P edge	FH-1Q core	FH-1Q edge	FH-1R core	FH-1R edge
SiO_2	43.50	43.89	42.87	41.71	46.98	42.56	43.20	42.09	42.13	41.48	41.81	41.77	42.98	43.19	43.36
Al_2O_3	15.20	14.64	17.07	17.88	11.34	15.88	15.36	16.07	17.68	16.49	18.48	16.58	16.56	16.40	17.03
TiO_2	.31	.33	.46	.17	.45	.43	.36	.20	.32	.36	.13	.28	.34	.34	.29
MgO	9.63	10.09	9.61	11.31	13.37	9.76	10.61	7.58	9.64	8.64	9.55	7.60	8.75	9.61	10.58
FeO	17.91	17.33	16.33	13.78	12.80	16.46	15.90	20.13	15.10	18.10	14.51	19.67	17.96	15.07	13.64
MnO	.12	.34	.36	.43	.00	.15	.18	.33	.13	.17	.39	.28	.15	.24	.18
CaO	9.74	9.91	10.43	10.79	11.60	10.49	10.62	9.23	10.21	9.58	10.51	10.22	9.75	10.80	10.85
Na_2O	1.67	1.80	1.81	1.81	1.39	1.89	1.98	1.82	1.90	1.99	1.66	1.64	1.65	1.94	1.84
K_2O	.33	.34	.36	.43	.11	.35	.35	.46	.25	.36	.24	.39	.29	.26	.12
TOTAL	98.41	98.67	99.30	98.31	98.04	97.97	98.56	97.91	97.36	97.17	97.28	98.43	98.43	97.85	97.89
						cations per 23 oxygens									
Si	6.319	6.350	6.159	5.987	6.738	6.217	6.257	6.221	6.136	6.129	6.084	6.148	6.246	6.293	6.251
Al^{IV}	1.681	1.650	1.851	2.013	1.262	1.783	1.743	1.779	1.864	1.871	1.916	1.852	1.754	1.707	1.749
Al^{VI}	.922	.847	1.051	1.013	.655	.952	.879	1.021	1.171	1.001	1.254	1.026	1.083	1.110	1.146
Ti	.034	.036	.050	.018	.049	.047	.039	.022	.035	.040	.014	.031	.037	.037	.031
*Fe^{3+}	.666	.697	.581	.745	.343	.544	.555	.695	.545	.714	.539	.638	.610	.354	.416
Mg	2.085	2.176	2.058	2.420	2.858	2.125	2.290	1.670	2.092	1.903	2.071	1.667	1.895	2.087	2.273
Fe^{2+}	1.509	1.400	1.381	.910	1.192	1.467	1.371	1.794	1.294	1.522	1.226	1.783	1.572	1.482	1.229
Mn	.015	.042	.044	.052	-	.019	.022	.041	.016	.021	.048	.035	.018	.030	.022
Ca	1.516	1.536	1.606	1.660	1.783	1.642	1.648	1.462	1.593	1.517	1.639	1.612	1.518	1.686	1.676
Na(M4)	.253	.267	.230	.182	.120	.204	.195	.295	.253	.281	.209	.208	.266	.214	.206
Na(A)	.217	.238	.274	.321	.266	.331	.361	.227	.284	.289	.259	.260	.199	.334	.308
K	.061	.063	.066	.079	.020	.065	.065	.087	.046	.068	.045	.073	.054	.048	.022
$Fe^{2+}/Fe^{2+}+Mg$	.420	.392	.402	.273	.294	.408	.374	.518	.382	.444	.372	.517	.453	.415	.351

* Fe^{3+} calculated according to the method of Spear and Kimball (1983).
\+ Hornblende adjacent to pseudomorph after lawsonite.

Table 3 - Representative staurolite, garnet, and chlorite analyses

	Staurolite					Garnet										Chlorite		
	Z3-B	Z3-M	FH-1M	FH-1M	FH-1Q	Z3-D edge	Z3-N core	Z3-N edge	FH-1M core	FH-1M edge	FH-1P core	FH-1P edge	FH-1Q edge	FH-1R core	FH-1R edge	Z3-M	FH-1M	FH-1M retro
SiO_2	28.31	28.84	28.32	28.42	28.45	36.30	36.95	38.17	38.21	38.14	37.60	37.53	37.88	37.32	37.70	27.25	26.42	24.88
Al_2O_3	53.20	54.27	54.69	54.41	54.06	20.61	21.70	21.95	20.96	21.64	21.24	21.57	21.30	21.64	21.85	23.83	22.96	22.00
TiO_2	.27	.32	.43	.41	.66	–	–	–	–	–	–	–	–	–	–	.04	.03	.03
MgO	2.55	2.90	1.77	2.01	1.97	4.08	2.35	4.22	1.97	4.56	2.87	4.01	3.86	2.20	2.99	24.97	22.70	16.67
FeO	12.89	11.55	12.30	12.16	13.40	30.26	27.80	26.07	28.94	30.99	32.47	30.37	31.24	25.15	27.38	14.17	15.68	23.62
MnO	.24	.37	.25	.12	.18	2.34	3.86	6.94	5.54	2.69	2.37	2.38	2.71	5.62	3.40	.10	.13	.21
CaO	–	–	–	–	–	5.23	8.36	5.00	5.97	3.92	4.93	4.36	4.06	8.72	7.75	–	–	–
ZnO	.35	.49	.93	.25	.12	–	–	–	–	–	–	–	–	–	–	–	–	–
TOTAL	97.81	98.75	98.69	97.79	98.84	98.82	101.05	102.36	101.60	101.94	101.49	100.22	101.05	100.64	101.08	90.36	87.93	87.41
	cations per 23 oxygens					cations per 12 oxygens										48 oxygens		
Si	3.919	3.931	3.881	3.912	3.899	2.943	2.931	2.965	3.022	2.977	2.979	2.978	2.992	2.960	2.965	5.232	5.264	5.219
Al	8.681	8.716	8.835	8.825	8.731	1.970	2.029	2.010	1.954	1.991	1.983	2.017	1.983	2.023	2.026	5.392	5.391	5.439
Ti	.028	.033	.044	.043	.068	–	–	–	–	–	–	–	–	–	–	.005	.005	.005
Mg	.526	.589	.361	.413	.402	.493	.278	.489	.232	.531	.339	.474	.454	.260	.351	7.145	6.743	5.211
Fe	1.493	1.316	1.410	1.399	1.536	2.052	1.845	1.693	1.914	2.023	2.151	2.015	2.064	1.668	1.801	2.275	2.613	4.144
Mn	.028	.043	.029	.014	.021	.160	.259	.457	.371	.178	.159	.160	.181	.377	.227	.017	.021	.037
Ca	–	–	–	–	–	.455	.713	.416	.506	.328	.419	.370	.344	.741	.653	–	–	–
Zn	.035	.050	.094	.026	.012	–	–	–	–	–	–	–	–	–	–	–	–	–
Σ	14.709	14.678	14.656	14.631	14.668	8.072	8.055	8.030	8.000	8.027	8.030	8.014	8.017	8.029	8.022	20.067	20.034	20.051
Fe/Fe+Mg	.739	.691	.795	.772	.792	.806	.869	.776	.891	.792	.863	.809	.819	.865	.837	.241	.279	.443
alm	–	–	–	–	–	.649	.596	.554	.633	.661	.701	.667	.678	.547	.594	–	–	–
pyr	–	–	–	–	–	.156	.089	.159	.076	.173	.110	.156	.149	.085	.115	–	–	–
gross	–	–	–	–	–	.143	.230	.136	.167	.107	.136	.122	.113	.243	.215	–	–	–
spess	–	–	–	–	–	.050	.083	.149	.122	.058	.051	.053	.059	.123	.074	–	–	–

ratio decreases from core to rim. Zoning profiles are smooth and continuous with no evidence for polymetamorphism or growth in response to changing assemblages.

Biotite (Bio) is the dominant potassic phase contained in these rocks, and its presence or absence seems related only to the original bulk compositions of the rocks. Where present, it inevitably occurs in two different parageneses within the same sample. First-generation biotite is aligned in the foliation, whereas second-generation biotite forms large, randomly oriented flakes pseudomorphous after hornblende garben; the replacement of hornblende by biotite (±chlorite) in these samples is not a ubiquitous feature, and many amphibole grains appear totally unaffected. Rocks that lack early biotite show no alteration of hornblende. First-generation biotites have consistently higher Ti and Al^{VI} contents than do the later biotites (Table 3-4).

Chlorite (Chl) is present in dense, well-foliated mats dominating the matrix assemblage of samples that do not contain paragonite. Rare unfoliated samples in which kyanite and staurolite are absent (e.g. sample FH-1S) contain minor amounts of chlorite interleaved with radiating sprays of coarse paragonite, but these rocks are clearly a different and subordinate bulk composition to the true garbenschists. In both occurrences, however, chlorite is magnesian ripidolite (Fe/Fe+Mg = 0.20-0.35). Minor secondary chlorite after hornblende is present in some samples; these chlorites have Al contents identical to those of primary chlorite, but are more Fe-rich (Fe/Fe+Mg = 0.45).

Paragonite (Parag) occurs in two distinct parageneses. Within the true garbenschist samples it is the dominant matrix mineral in chlorite-absent rocks and forms dense, fine-grained mats in the plane of the foliation In

Table 4 - Representative biotite, paragonite, and margarite analyses

	biotite					paragonite					marg
	Z3-B bio I	Z3-B bio II	Z3-D	FH-1M bio I	FH-1M bio II	Z3-B	Z3-N	FH-1Q	FH-1Q	FH-1R	FH-1M
SiO_2	37.34	38.66	37.41	38.66	37.05	46.13	43.91	47.55	47.84	46.35	38.47
Al_2O_3	18.39	17.40	18.11	18.71	17.31	38.98	41.37	39.74	39.43	39.87	43.18
TiO_2	1.40	.99	1.33	1.68	.97	.10	.09	.09	.06	.08	.03
MgO	13.69	14.17	13.61	15.01	12.78	.71	.38	.06	.07	.07	.31
FeO	15.24	15.78	16.95	13.79	19.32	1.24	.71	.47	.58	.40	.68
MnO	.04	.07	.11	.04	.09	-	-	-	-	-	-
CaO	.03	.02	.06	.04	.03	.79	2.67	.59	.26	.24	9.77
Na_2O	.29	.28	.18	.28	.09	6.17	5.49	6.76	6.90	7.05	3.03
K_2O	8.94	8.79	8.95	8.09	7.70	1.19	.93	.94	.83	.61	.13
TOTAL	95.37	96.15	96.71	96.31	95.34	95.30	95.56	96.19	95.97	94.66	95.61
	cations per 11 oxygens										
Si	2.766	2.838	2.755	2.791	2.745	2.968	2.824	3.011	3.032	2.978	2.521
Al	1.605	1.505	1.572	1.592	1.554	2.955	3.136	2.965	2.946	3.019	3.335
Ti	.078	.054	.074	.091	.055	.005	.004	.004	.003	.004	.002
Mg	1.511	1.551	1.495	1.616	1.451	.068	.036	.005	.007	.007	.030
Fe	.944	.969	1.044	.833	1.230	.067	.038	.025	.031	.021	.037
Mn	.003	.005	.007	.002	.006	-	-	-	-	-	-
Ca	.003	.001	.005	.003	.003	.054	.184	.040	.017	.016	.686
Na	.042	.039	.025	.039	.013	.769	.685	.830	.848	.878	.385
K	.845	.823	.840	.745	.748	.098	.077	.076	.067	.050	.011
Σ	7.797	7.786	7.817	7.713	7.803	6.983	6.984	6.955	6.950	6.973	7.008
Fe/Fe+Mg	.384	.384	.411	.340	.458	.496	.515	.823	.820	.764	.550
parag	-	-	-	-	-	.835	.724	.877	.910	.930	.360
musc	-	-	-	-	-	.106	.081	.080	.072	.053	.630
marg	-	-	-	-	-	.059	.194	.042	.018	.017	.010

Table 5 - Representative analyses of plagioclase, epidote, and ankerite

	Plagioclase											Epidote				Ankerite	
	Z3-M edge	Z3-M pseudo*	Z3-N edge	Z3-N in H^+	FH-1M edge	FH-1M in G^+	FH-1M core	FH-1M edge	FH-1P core	FH-1P edge	FH-1P in G^+	Z3-M	Z3-M in H^+	Z3-M pseudo	FH-1M	FH-1M in G^+	FH-1M
SiO_2	59.62	60.48	62.28	63.88	60.82	62.73	64.18	59.25	63.91	59.35	63.51	38.44	38.66	38.68	38.84	-	-
Al_2O_3	25.64	25.34	24.30	23.06	25.04	22.92	22.53	25.10	22.77	25.57	22.46	25.85	27.37	25.91	25.36	-	-
Fe_2O_3	-	-	-	-	-	-	-	-	-	-	-	10.43	8.76	10.23	11.08	-	-
MgO	-	-	-	-	-	-	-	-	-	-	-	.11	.12	.18	.05	12.95	16.63
FeO	.01	.23	.24	.14	.43	.05	.18	.15	.10	.28	.32	-	-	-	-	13.51	8.68
MnO	-	-	-	-	-	-	-	-	-	-	-	-	.02	.03	.17	1.26	.28
CaO	6.92	6.94	6.28	4.04	6.88	3.84	2.15	7.15	3.87	7.00	3.86	23.46	22.91	23.06	22.91	27.37	26.87
Na_2O	7.96	7.93	8.48	9.40	7.84	9.46	9.08	7.29	9.74	7.99	9.79	-	-	-	-	-	-
K_2O	.06	.06	.08	.07	.05	.06	.09	.07	.08	.09	.08	-	-	-	-	-	-
TOTAL	100.22	100.97	101.66	100.59	101.05	99.06	98.20	99.01	100.48	100.28	100.03	98.30	97.83	98.09	98.40	55.09	52.46
	cations per 8 oxygens											cations per 25 oxygens				6 cations	
Si	2.653	2.672	2.727	2.806	2.684	2.798	2.860	2.666	2.812	2.646	2.812	6.018	6.029	6.054	6.077	-	-
Al	1.345	1.319	1.254	1.194	1.302	1.205	1.184	1.331	1.181	1.343	1.172	4.771	5.029	4.780	4.676	-	-
Fe^{3+}	-	-	-	-	-	-	-	-	-	-	-	1.230	1.028	1.205	1.305	-	-
Mg	-	-	-	-	-	-	-	-	-	-	-	.027	.027	.042	.012	1.899	2.435
Fe^{2+}	.001	.009	.009	.005	.016	.002	.007	.006	.004	.011	.012	-	-	-	-	1.112	.713
Mn	-	-	-	-	-	-	-	-	-	-	-	-	.002	.004	.022	.105	.023
Ca	.330	.328	.295	.190	.325	.184	.103	.345	.182	.334	.183	3.936	3.828	3.868	3.841	2.885	2.829
Na	.687	.679	.719	.800	.671	.818	.784	.636	.831	.690	.841	-	-	-	-	-	-
K	.004	.004	.004	.004	.003	.003	.005	.004	.004	.005	.005	-	-	-	-	-	-
Σ	5.019	5.010	-	4.999	5.002	5.010	4.942	4.988	5.015	5.030	5.025	15.982	15.943	15.953	15.933	6.000	6.000
X_{An}	.324	.324	-	.192	.326	.18	.114	.349	.180	.324	.178	-	-	-	-	-	-
Fe/Fe+Mg	-	-	-	-	-	-	-	-	-	-	-	-	-	-	-	.369	.226

* in pseudomorph after lawsonite
\+ inclusion in hornblende (H) or garnet (G)

these samples, there is considerable solid solution towards margarite and/or muscovite. Paragonite also occurs with chlorite in coarse, randomly oriented sprays in unfoliated amphibolites. In this latter case paragonite is closer to endmember compositions, typically $Pa_{93}Ma_2Mu_5$.

Plagioclase (Plag) forms a granoblastic network of elongate matrix grains and is also present as inclusions in all poikilitic phases. Strong optical and chemical zonation is evident, with rim compositions of An_{30-35} and cores as sodic as An_{11}; plagioclase inclusions in the cores of garnet and hornblende are typically An_{18} in composition, whereas inclusions nearer the margins of the poikiloblasts are more calcic. In several samples, plagioclase grains are enveloped in mats of very fine-grained margarite but there is no apparent correlation between plagioclase composition and the development of this margarite.

Epidote (Epid) is ubiquitous as inclusions in all porphyroblast phases and as a stable matrix phase. Grains are generally homogeneous and contain approximately 20% of the pistacite endmember; there is little compositional variability either within or between samples.

Ankerite (Ank) is abundant as inclusions in hornblende and garnet, and also forms large porphyroblasts in several samples. Ankerite inclusions are generally more Fe-rich than matrix grains within the same sample (Fe/Fe+Mg = 0.35 and 0.20, respectively). Mn contents do not exceed 1.75 wt% MnO, and are typically in the range 0.50-1.00%.

Ilmenite (Ilm) and rutile (Ru) are abundant accessory phases and occur in both matrix and inclusion assemblages. Ilmenite shows no evidence of alteration or exsolution in these samples, although exsolution features are common in higher variance assemblages from the same area. No other Fe-Ti oxides or titanite have been observed in any of the samples.

Margarite (Marg) is present in several samples and occurs in fine-grained mats rimming plagioclase. In no case does it appear to be a primary phase. Compositions are variable and contain up to 45% of the paragonite endmember.

PHASE EQUILIBRIA

The garbenschist assemblages can be described in terms of the chemical system SiO_2-Al_2O_3-Fe_2O_3-TiO_2-FeO-MgO-MnO-CaO-K_2O-Na_2O-H_2O-CO_2. The two complete assemblages, Hbl + Parag + Kya + Staur + Gar + Bio + Plag + Epid + Ank + Qtz + Ru + Ilm and Hbl + Chl + Kya + Staur + Gar + Bio + Plag + Epid + Ank + Qtz + Ru + Ilm, are each divariant within this system; chemical variability of the phases in these assemblages is small, in accord with the relatively low variance of the rocks. Observed subassemblages of the complete 12-phase suites are characterized by the absence of (1) ankerite, (2) kyanite + staurolite, (3) garnet, or (4) biotite. A few samples contain the assemblage Hbl + Gar + Chl + Parag + Plag + Epid + Qtz; these are the only rocks in which chlorite and paragonite coexist.

Owing to the great number of components and phases in these rocks, graphical analysis of the assemblages is difficult, but several useful diagrams can be constructed to elucidate some of the more salient features of the phase equilibria. The first of these diagrams is a projection from quartz + H_2O + CO_2 into the tetrahedron Al-Na-Ca-(Fe+Mg), shown in Figure 3-3. This diagram illustrates the plotting positions of all of the principal garbenschist phases except biotite, which contains K_2O and therefore lies outside of this model system. The ranges in chemical variability of each phase are indicated by the heavy lines; note that

although epidote should not strictly be plotted in this system, it has been included to show the range in Al content resulting from substitution by Fe^{3+}. Tielines are drawn to illustrate the chemical limits of the phase volume occupied by the garbenschists, although several lines have been omitted for clarity in reading. As drawn, this is not a thermodynamically rigorous phase diagram, so the rather bewildering array of tielines should not be construed as implying reaction relationships. The purpose of this figure is primarily to demonstrate that, despite the unusual hornblende + staurolite + kyanite assemblages, the phase volume also encloses the realm of typical mafic volcanic bulk compositions and shows considerable overlap with the phase volumes of typical amphibolite facies assemblages (see, for example, Fig. 5 of Laird, 1980, and Fig. 11 of Spear, 1982), as will be discussed later.

Projection from biotite + epidote + ankerite + quartz + H_2O into the tetrahedron Al'-Na'-Ca'-(Fe+Mg)' is shown in Fig. 3-4. This diagram is a valid phase diagram in which up to five phases can coexist at equilibrium. If garnet can be considered to be stabilized by MnO as an extra component, the equilibrium assemblage can contain garnet as a sixth phase, although garnet has been omitted here. The two complete garbenschist assemblages on this diagram are Hbl + Gar + Kya + Staur + Plag + Chl and Hbl + Gar + Kya + Staur + Plag + Parag; paragonite plots slightly outside the tetrahedron in this projection due to the presence of minor muscovite component. From this figure, it is evident that the presence of paragonite (solid solution with muscovite/margarite) versus chlorite in the assemblage is simply a function of bulk composition, principally the Na_2O/CaO ratio of the rock. Pure paragonite is not excluded from coexistence with chlorite in the assemblage Hbl + Plag + Chl + Parag ± Gar; a subassemblage of this (Hbl + Plag + Chl + Parag + Gar) has been found.

Figure 3-3. Al-Ca-Na-(Fe+Mg) diagram projected from quartz + H_2O + CO_2, showing plotting positions and ranges of compositional variability of the garbenschist minerals.

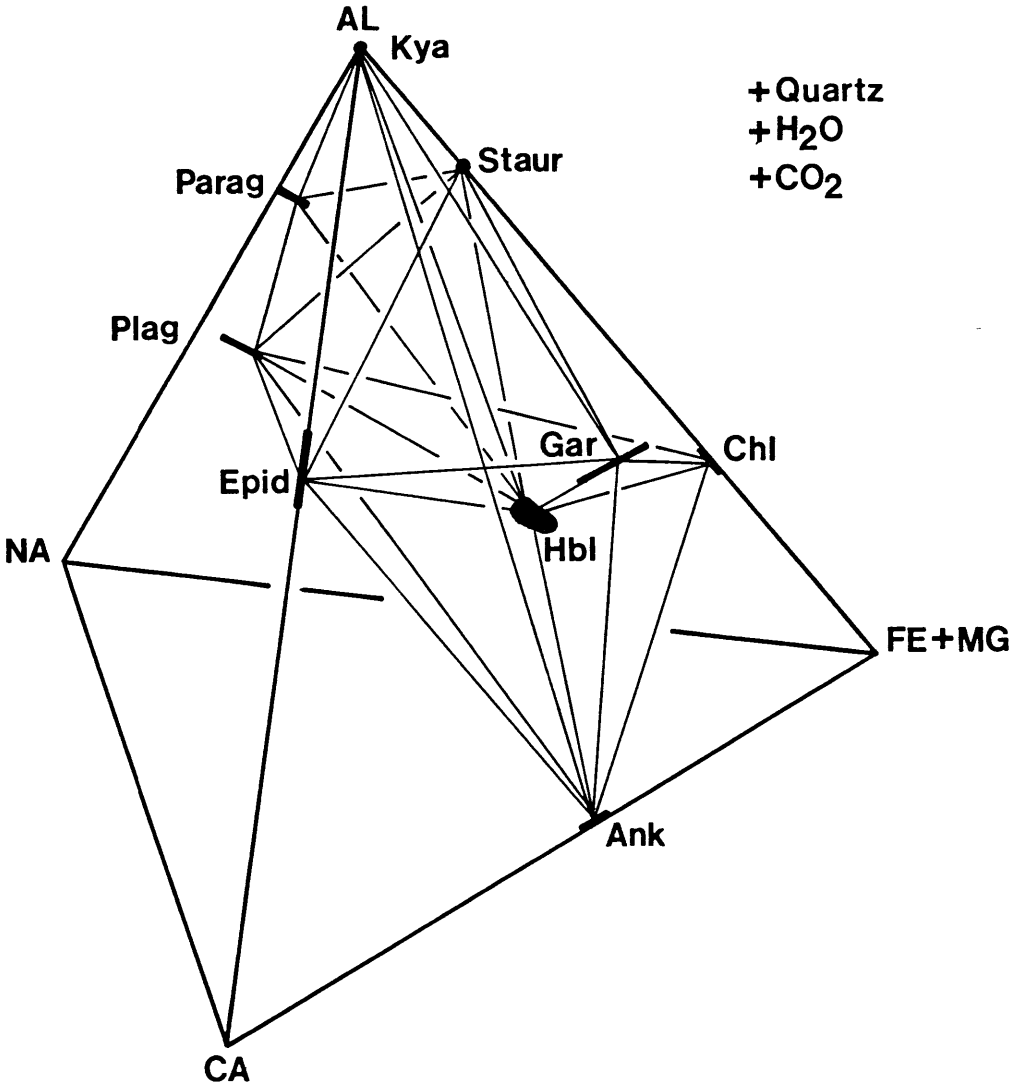
AL
Kya
+Quartz
+H_2O
+CO_2
Staur
Parag
Plag
Gar
Chl
Epid
Hbl
NA
FE+MG
Ank
CA

Figure 3-4. Projection from biotite + epidote + ankerite + quartz + H_2O into the tetrahedron Al'-Ca'-Na'-(Fe+Mg)'. Note that paragonite plots on the negative side of the Na-Al-(Fe+Mg) plane and thus paragonite and chlorite do not coexist except in Ca-poor bulk compositions. The three insets show typical assemblages found in the garbenschists.

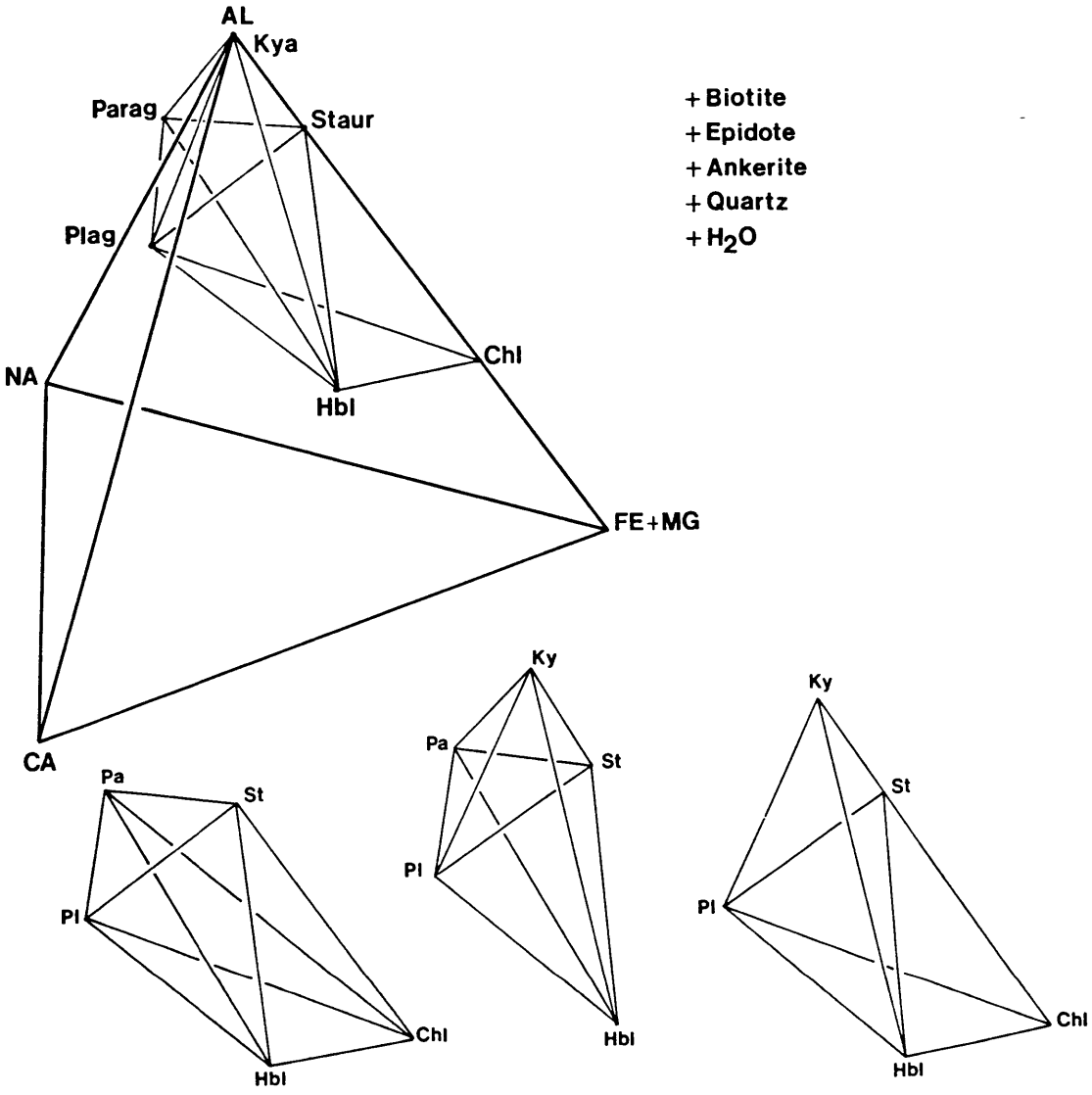
AL
Kya
Parag
Staur
Plag
NA
Chl
Hbl
FE+MG
CA
+ Biotite
+ Epidote
+ Ankerite
+ Quartz
+ H_2O
Pa
St
Pl
Chl
Hbl
Ky
Pa
St
Pl
Hbl
Ky
St
Pl
Chl
Hbl

Figure 3-5. Ca-Na-Fe-Mg diagram projected from biotite + epidote + kyanite + quartz + H_2O + CO_2 indicating the Fe-Mg partitioning among phases. Compositional variability (core-rim) of each mineral is indicated by the heavy lines; tielines connect edge compositions of the phases. Paragonite has been omitted for clarity in reading.

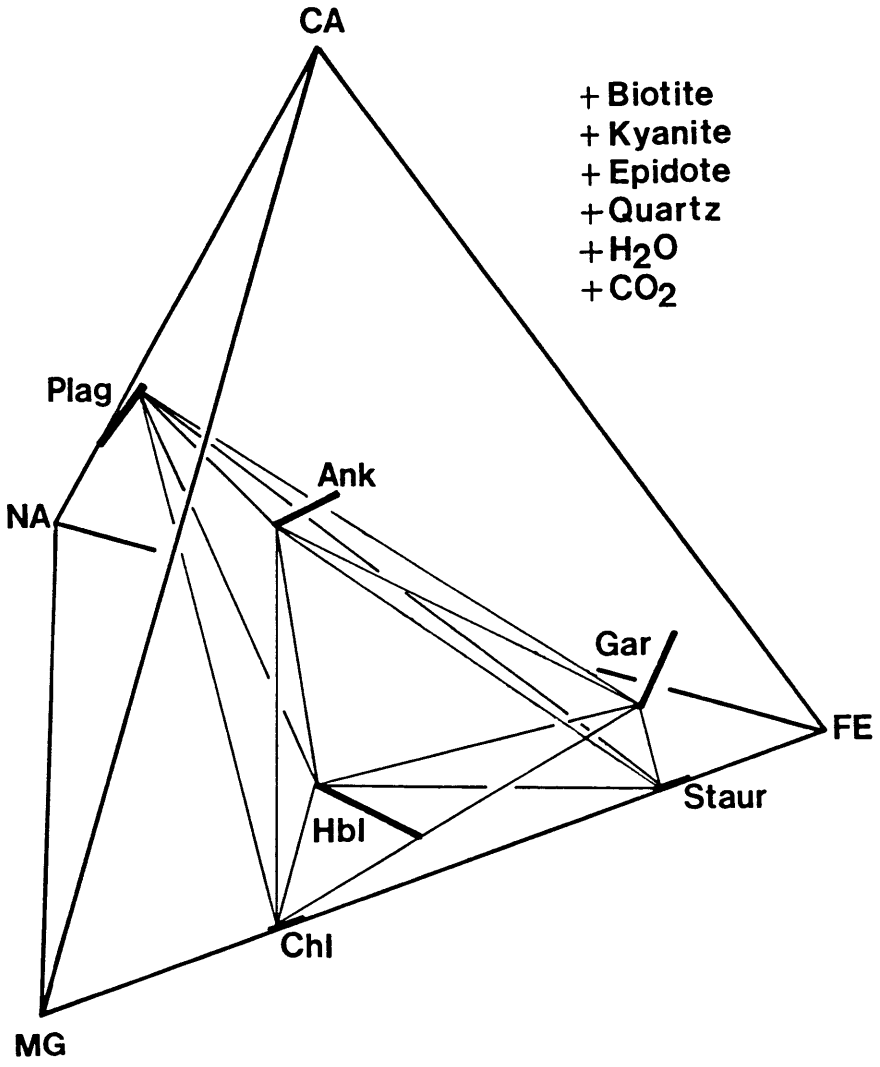
CA
+ Biotite
+ Kyanite
+ Epidote
+ Quartz
+ H_2O
+ CO_2
Plag
Ank
NA
Gar
FE
Staur
Hbl
Chl
MG

Figure 3-6. Schematic Al-Ca-Na-(Fe+Mg) diagram indicating the breaking of the plagioclase + chlorite ± garnet + epidote plane, thereby allowing hornblende to coexist with staurolite, kyanite, and/or paragonite.

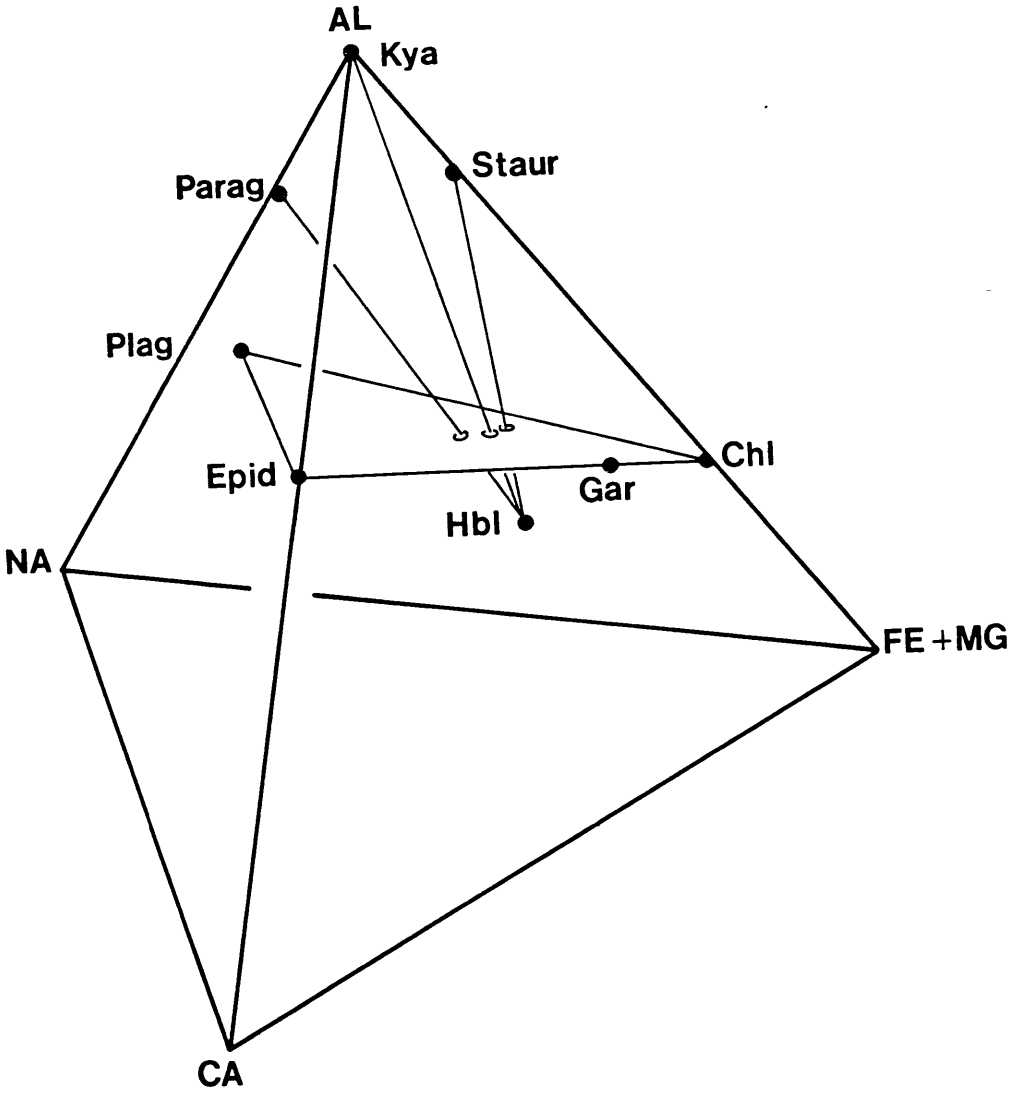
AL
Kya
Staur
Parag
Plag
Chl
Epid
Gar
Hbl
NA
FE+MG
CA

In order to examine the relative effects of Fe and Mg on the phase relations of the garbenschist assemblage, it is necessary to project from another phase to remove one of the components plotted in Figures 3-3 and 3-4. Kyanite was selected for a projection from biotite + kyanite + epidote + quartz + H_2O + CO_2 into the tetrahedron Ca'-Na'-Fe'-Mg' (Figure 3-5). CO_2 rather than ankerite was used as a projection point to allow observation of the Fe/Mg variability in ankerite. On this diagram, ankerite and garnet are stabilized by extra components (CO_2 and MnO) so a complete equilibrium assemblage is represented by four phases in addition to these two, e.g. Hbl + Staur + Plag + Chl. Another possible assemblage is Hbl + Staur + Plag + Parag, not shown on the diagram. The ranges in chemical composition from core to rim of individual grains are shown by the heavy lines, and tielines connect the edge compositions.

As can be seen from both Figures 3-4 and 3-5, the garbenschist assemblages can be represented in projected composition space with no invalid crossing tieline relationships. This supports the conclusion reached on textural grounds that the unusual mineral associations such as hornblende+kyanite+ staurolite and kyanite+ankerite cannot be explained as disequilibrium features. Laird (1980) has discussed the phase relations of the "common" mafic schist assemblage, Hbl + Plag + Chl + Epid ± Gar, found in typical amphibolite facies metavolcanic rocks. Algebraic analysis in the complete 11-component system indicates that the garbenschist assemblage is separated from the "common" assemblage by reactions such as Plag + Chl + Epid = Hbl + Staur ± Kya ± Parag, as is shown schematically in Figure 3-6. It is clear from this analysis and from Figure 3-6 that, as long as the Plag + Chl + Epid ± Gar plane is stable, hornblende cannot coexist with

kyanite, staurolite, or paragonite in rocks of any bulk composition. Abundant natural occurrences of amphibolites containing the "common" assemblage suggest that this plane is stable over a wide range of P-T conditions, and the relative scarcity of garbenschist assemblages implies that the conditions necessary to break it are not commonly attained during regional metamorphism.

Although it is difficult to sort out bulk compositional effects from P-T effects, several generalizations can be made concerning the stability of the garbenschist assemblage. The absence of hornblende + kyanite and hornblende + paragonite assemblages in amphibolites metamorphosed at pressures up to 6 kb (e.g. Spear, 1982) suggests that these associations represent high-pressure parageneses, at least in truly basaltic bulk compositions, at temperatures higher than those of more commonly reported blueschist facies assemblages. Spear (1982) does report the occurrence of hornblende + staurolite at 6 kb, but only in relatively aluminous samples. This implies that the Plag + Chl + Epid ± Gar plane has already been broken at these pressures, but that the aluminous phases are still inaccessible to typical mafic bulk compositions. Gibson (1979) and Cooper (1980) have described kyanite amphibolites from New Zealand that have been metamorphosed at 550-700°C and 9-10 kb. The rocks described by Gibson (1979) are part of a layered mafic intrusive complex and are apparently basaltic in composition; this implies that at pressures of this magnitude hornblende + kyanite may be a stable assemblage even in low-aluminum samples. Hornblende + kyanite, hornblende + staurolite, and hornblende + paragonite assemblages have also been found in rocks metamorphosed at 600-650°C and 10 kb near Prince Rupert, British Columbia (M. L. Crawford, personal communication). High-pressure metamorphic conditions are also indicated for the Tauern Window garbenschists, as is discussed below.

TEMPERATURE DETERMINATIONS

Temperatures of final equilibration between coexisting garnet and biotite were calculated according to the Ferry & Spear (1978) geothermometer (using modifications by Hodges & Spear, 1982), and the results are plotted as lines of constant K_D in Figure 3-7. From this diagram, it can be seen that temperatures range from 500° -600°C depending upon the pressure; at 6 kb, the average temperature is 550°C. For temperatures of this magnitude, retrograde exchange of Fe and Mg is unlikely to be an important effect (Hodges & Spear, 1981) and these values can therefore be considered to be estimates of the maximum temperatures experienced by the rocks. These temperatures are in good agreement with those estimated from oxygen isotope fractionation (Hoernes & Friedrichsen, 1978) in the same region of the Tauern Window.

No inclusions of biotite in garnet have been observed, so it is not possible to calculate the temperatures at which garnet cores crystallized based on garnet-biotite geothermometry.

PRESSURE DETERMINATIONS

Garnet-Plagioclase-Kyanite-Quartz Geobarometry

The distribution of Ca between coexisting garnet and plagioclase is a relatively sensitive indicator of pressures of metamorphism in aluminum-saturated rocks, as has been discussed in detail by Ghent et al. (1979). Due to the high activation energy of the coupled substitution $CaAlNa_{-1}Si_{-1}$ in plagioclase, diffusional reequilibration by simple exchange of Ca getween garnet and plagioclase should be negligible during uplift and

cooling from peak temperatures of 500-600°C. For this reason, the compositions of adjacent grains of garnet and plagioclase should record pressures of initial equilibration between these phases with little to no retrograde overprint.

Pressures have been calculated for seven garbenschist samples using the calibration of Ghent et al. (1979), with modified activity models for garnet and plagioclase as discussed by Hodges & Spear (1982). The results of these calculations are presented as lines of constant K_D in Figure 3-8. The calculations were carried out on two different populations of grains. The solid lines represent garnet edges in contact with matrix plagioclase of composition An_{29-35}. At 550°C, the pressures of equilibration of the mineral pairs range from 6.5 to 8.2 kb. As discussed previously, many of the garnets in these rocks contain inclusions of sodic ($\sim An_{18}$) plagioclase in their grossular-enriched cores. The dashed lines in Figure 8 show the pressures calculated from these inclusions and their host garnet compositions; no inclusions of kyanite have been observed in garnet, but the presence of kyanite inside hornblende grains suggests that kyanite was indeed an early phase and that the assumption of aluminum saturation in the inclusion assemblage is valid. As is clear from the figure, these plagioclase inclusions were entrapped at higher pressure and/or lower temperature conditions than those recorded by the matrix assemblage. At a constant temperature of 550°C, the pressures of equilibration of the inclusions range from 9.2 to 10.4 kb.

With no temperature control on the garnet cores, it is not possible to ascertain whether the separation of the rim and core K_D lines in Figure 8 indicates crystallization of garnet cores at higher pressures or lower temperatures, or both, than the rims. Other evidence, reported below, implies higher pressures at nearly constant temperature for growth of the garnet cores. This indicates garnet growth during decompression of ~3 kb.

Figure 3-7. Diagram showing lines of constant K_D for six samples determined from the garnet-biotite geothermometer of Ferry & Spear (1978). Average temperature of equilibration at 6-7 kb is 550°C. Al_2SiO_5 triple point of Holdaway (1971) is shown for reference. Dashed lines represent lines of constant K_D for the amphibole-kyanite equilibrium discussed in the text.

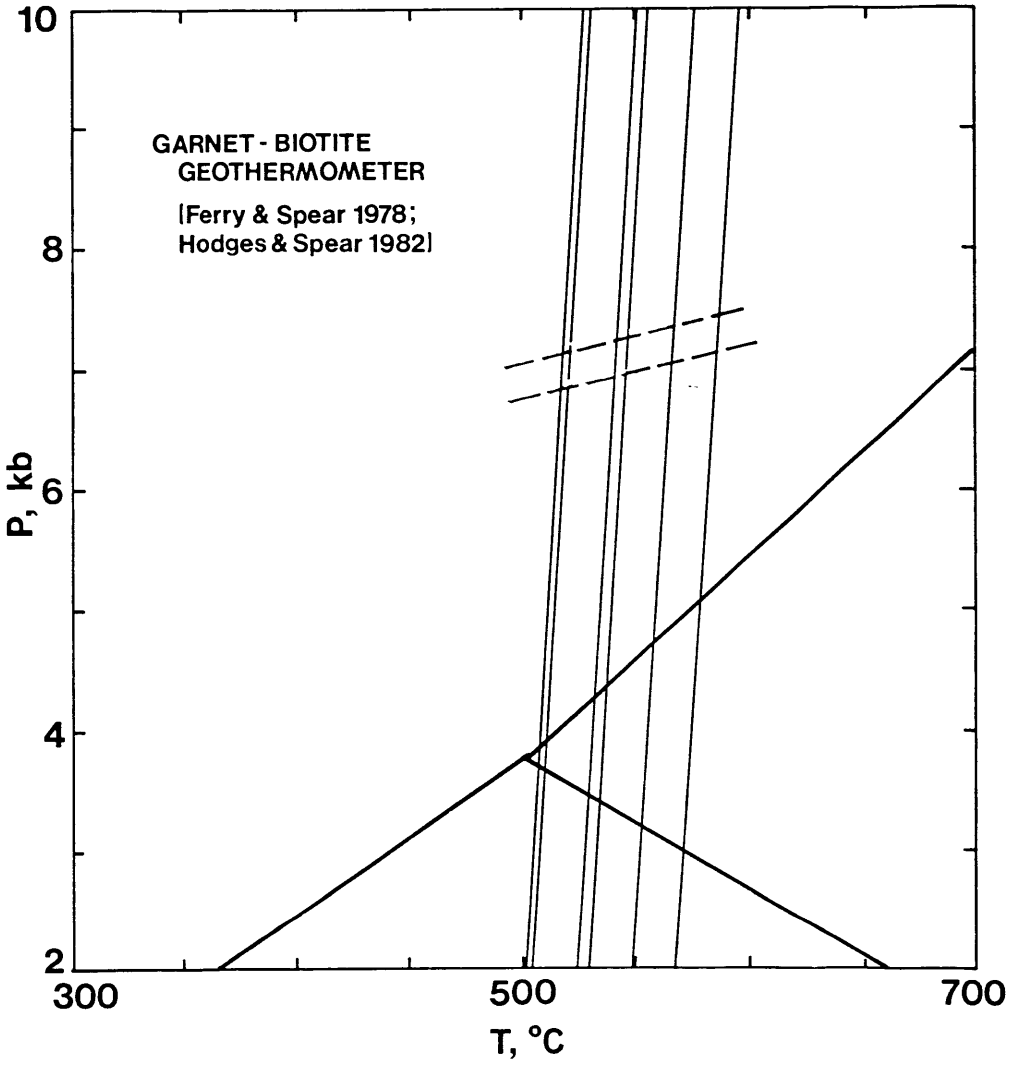
GARNET - BIOTITE
GEOTHERMOMETER
[Ferry & Spear 1978;
Hodges & Spear 1982]
10
8
6
4
2
P, kb
300
500
700
T, °C

Figure 3-8. Lines of constant Ca partitioning between garnet and plagioclase, as determined from the garnet-plag-kyanite-quartz geobarometer of Ghent et al. (1979) with modifications by Hodges & Spear (1982). Solid lines represent edge compositions of adjacent garnet and matrix plagioclase grains. Dot-dashed lines are determined from compositions of plagioclase inclusions in garnet cores.

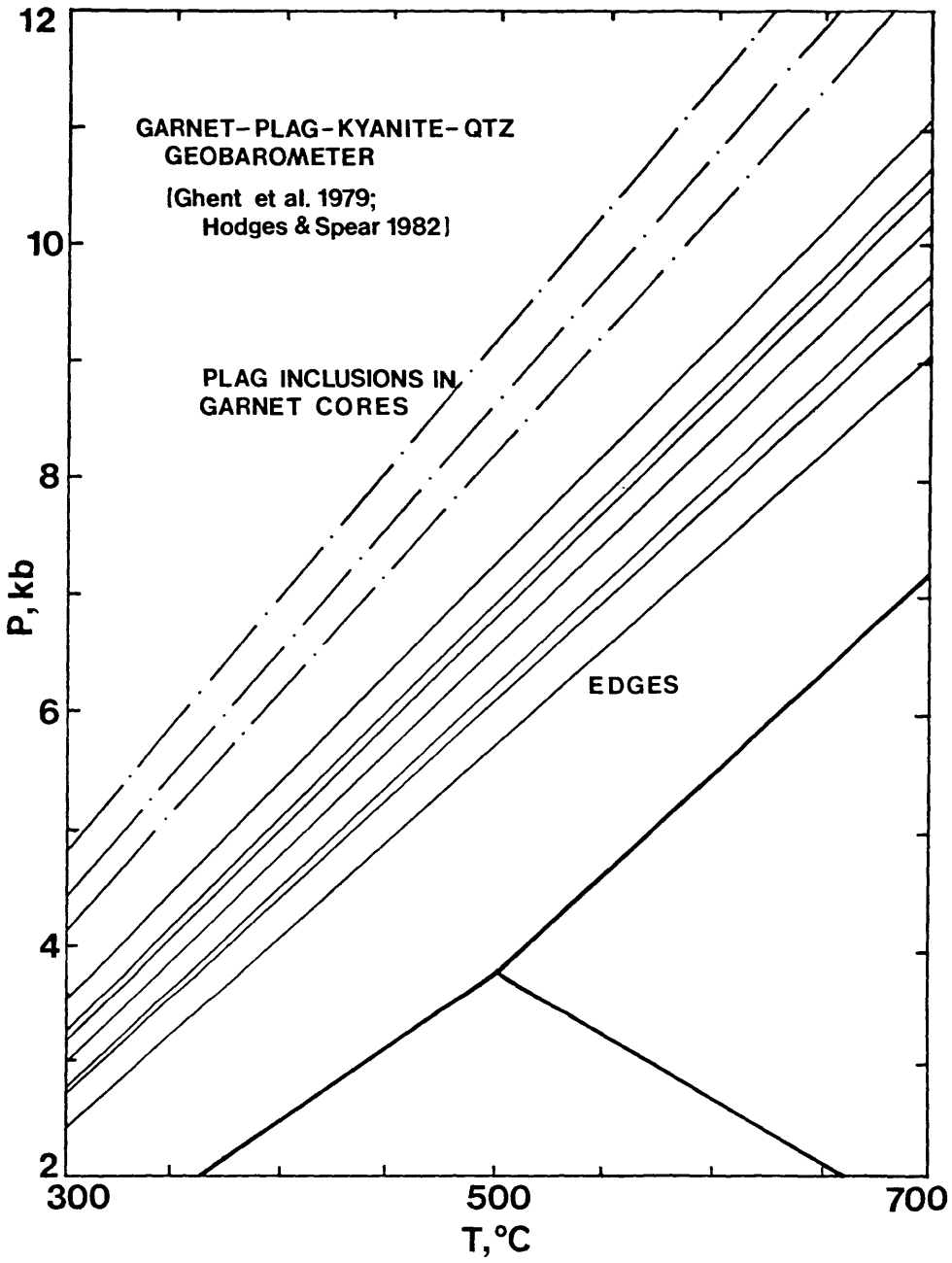
12
10
8
6
4
2
P, kb
300
500
700
T, °C
GARNET-PLAG-KYANITE-QTZ
GEOBAROMETER
(Ghent et al. 1979;
Hodges & Spear 1982)
PLAG INCLUSIONS IN
GARNET CORES
EDGES

Hornblende-Kyanite Equilibrium

Using entropy and volume data from Table 3-7, the Clapeyron slope for the vapor-absent equilibrium

$$4Mg_3Al_2Si_3O_{12} + 6CaAl_2Si_2O_8 + 3NaAl_3Si_3O_{10}(OH)_2 =$$

pyrope anorthite paragonite

$$3NaCa_2Mg_4AlAl_2Si_6O_{22}(OH)_2 + 10Al_2SiO_5 + 5SiO_2 \qquad (3\text{-}1)$$

pargasite kyanite qtz

was calculated to be 4.7 bar/deg. This relatively flat dP/dT slope combined with the small coefficients of the phases suggests that this reaction might be a suitable geobarometer for the paragonite-bearing garbenschist assemblages. The equilibrium condition for this reaction (assuming $\Delta C_p=0$) is given by the expression

$$\frac{14239}{RT} - \frac{9.08}{R} + \frac{1.914(P-1)}{RT} = \ln K \qquad (3\text{-}2)$$

where the coefficients were determined from the data of Helgeson et al. (1989) combined with Loomis and Nimick's (1982) value for $\Delta H^o_{f,pyrope}$, and K is the equilibrium constant,

$$K = \frac{(a^{hbl}_{parg})^3}{(a^{gar}_{pyr})^4 (a^{plag}_{an})^6 (a^{mica}_{parag})^3}. \qquad (3\text{-}3)$$

Activity terms for the phases involved can be quite complex, but several simplifying assumptions can be made; a list of the activity-composition relations used in the calculations is given in Table 3-6. All interactions in the quaternary garnet system have been treated as ideal, with the

Table 3-6

Activity-composition relations for amphibole-kyanite geobarometer

Hornblende	$a^{hbl}_{parg} = 4(X^{A}_{Na})(X^{M4}_{Ca})^2(X^{M13}_{Mg})^3(X^{M2}_{Al})(X^{M2}_{Mg})$ *
Paragonite	$a^{mica}_{parag} = X_{Na} = Na/Na+K+Ca$
Plagioclase	$a^{plag}_{An} = (X_{An}\gamma_{An})$ where $\gamma_{An} = 1.8$ †
Garnet	$a^{gar}_{pyr} = (X_{Mg}\gamma_{pyr})^3$
	$RT\ell n\gamma_{pyr} = W_{CaMg}[(X_{gros})^2+(X_{alm}X_{gros})+(X_{spes}X_{gros})]$ ‡
	$W_{CaMg} = 3300-1.5\ T\ (°K)$ +

* Site occupancies calculated assuming that Mg/Fe+Mg(M13) = Mg/Fe+Mg(M2); the factor of 4 in this expression is necessary to make the activity of pure pargasite equal to 1.0.

† Hodges and Spear (1982)

‡ Ganguly and Kennedy (1974)

+ Newton and Haselton (1981)

exception of mixing between pyrope and grossular components. Non-ideality along this join is accounted for by a Margules formulation, where W_{CaMg} = 3300 -1.5T(°K) (Newton & Haselton, 1981). Despite great uncertainties in determining activity coefficients for plagioclase, calculations were carried out for a value of γ_{An} = 1.8 (Hodges & Spear, 1982). Both pargasite and paragonite were treated as ideal solutions, which is clearly a drastic oversimplification. However, as these phases appear on opposite sides of reaction (1) and have identical stoichiometric coefficients, it is perhaps not unreasonable to assume that their nonideality corrections will cancel one another out, e.g.:

$$\frac{(\gamma^{hbl}_{parg})^3}{(\gamma^{mica}_{parag})^3} \approx 1 \qquad (3\text{-}4)$$

Although some data are available concerning nonideal interactions in paragonite solid solutions (e.g. Chatterjee & Froese, 1975), the assumption of equation (3-4) was thought preferable to use of these data so as not to increase the errors due to the necessary simplification of treating pargasite as an ideal solution.

As pointed out by Newton & Haselton (1981), the pyrope-grossular join in the garnet system displays a significant excess partial molar volume in the range 0-30 mol% grossular. The Hodges & Spear (1982) modification of the Ghent et al. (1979) geobarometer takes this volume correction into account, and hence all pressures determined from the garnet-plagioclase-kyanite-quartz parageneses include the nonideality effects. In order to be consistent with pressures calculated in the previous section, it is thus necessary to rewrite equation 3-2 as:

$$\frac{14239}{RT} - \frac{9.08}{R} - \frac{(P-1)\Delta\bar{V}}{RT} = \ell nK \qquad (5)$$

where $\Delta\bar{V}$ takes into account the excess volume of mixing of garnet, which is determined using the formulation of Newton & Haselton (1981).

Calculation of pressures of metamorphism of the garbenschist samples using this revised equation yields values of 7.0 and 7.3 kb at 550°C (Figure 3-7). These pressures are in good agreement with pressures of final equilibration determined from the garnet-plagioclase-kyanite-quartz geobarometer.

QUANTITATIVE P-T MODELING OF ZONED MINERALS

The pressures and temperatures calculated from standard geothermometric/barometric techniques indicate the P-T conditions of final equilibration of the garbenschists and also suggest that the rocks experienced higher pressures earlier in their history. From these techniques alone, however, it is impossible to determine either the specific P-T conditions of the high pressure "event" or the shape of the trajectory followed by the rocks from these conditions to those at which growth and equilibration of the phases ceased.

As an alternative approach, however, the analytical formulation of the phase equilibria of the system (Spear et al., 1982) provides a means of calculating both the shape and the position in P-T space of this trajectory. This technique thus enables one to see through the final

metamorphic overprint to the earlier history experienced by individual samples. The specific methodology has been described in detail elsewhere (Spear & Selverstone, 1983), but in brief it involves the calculation of ΔT and ΔP as functions of n compositional zoning parameters in a completely characterized mineral assemblage of variance n. The necessary input parameters are the compositions of all phases, $\overline{S}$, $\overline{V}$ and an expression for the curvature of the Gibbs function for each phase, and a starting pressure and temperature; all of these values are readily attainable or can be estimated reasonably for the garbenschist samples. Although it is obviously a simplification, ideal mixing models were used for all of the phases; because the technique utilizes the differential rather than the integrated forms of the thermodynamic equations, the effects of this simplification are minimized in most cases to errors of only a few degrees and a few tens of bars (Spear & Selverstone, 1983).

Minerals that are typically zoned in the garbenschist assemblage are garnet, plagioclase, and hornblende. Geothermometry and geobarometry yield P-T conditions of 550±25°C, 6-8 kb for the edge compositions of these phases, and values of ΔX_i for each of the phase components from rim to core can be determined with the electron microprobe. These data can be combined with the thermodynamic parameters mentioned above to yield values of ΔT and ΔP over which these zoned phases grew, assuming they maintained equilibrium with one another. Because the complete garbenschist assemblage is divariant, only two compositional parameters need be specified out of the six independently variable phase components among garnet, plagioclase, and hornblende. A list of the phase components monitored for all phases in the garbenschist assemblage, along with relevant thermodynamic data for these components, is given in Table 3-7; for all of the Fe-Mg silicates, X_{Mg} was

chosen to be the dependent variable. Due to the extremely slow rates of volume diffusion in garnet at temperatures less than ~650°C (e.g. Yardley, 1977), zoning profiles in garnet are thought to be most representative of compositional changes owing only to growth processes in the garbenschists (i.e. there is no diffusional reequilibration). For this reason, various combinations of two out of the three independent garnet components were selected as the two monitor parameters of the assemblage.

Sample FH-1M was chosen for these calculations for several reasons: (1) well-developed zoning profiles are preserved in garnet, plagioclase, and hornblende; (2) inclusions of sodic plagioclase occur in garnet cores, so an independent estimate of early P conditions can be obtained; (3) biotite and plagioclase are present in the matrix assemblage, so both P and T of garnet rim equilibration can be determined; and (4) all available evidence (i.e. from inclusion suites and zoning profiles) suggests that garnet growth occurred in a constant assemblage. The assemblage considered was garnet + hornblende + staurolite + kyanite + biotite + chlorite + plagioclase + quartz + fluid, which is divariant in the subsystem CNKFMnMASH; several phases of the complete assemblage were not considered because their presence appears related to the addition of extra components (e.g. Fe^{3+} in epidote; CO_2 in ankerite; Ti in rutile and/or ilmenite). These phases show little chemical variability in the garbenschist samples and their presence or absence does not change the variance of the assemblage; they were therefore ignored in these calculations.

The garnet zoning profile utilized in this method is shown in Fig. 3-9, and starting compositions of all phases are given in Table 3-7. For each half of the garnet, the profile was divided into 5 increments across the outer region where Ca shows significant zonation, and one further increment

Table 3-7 Thermodynamic data[1] and mineral compositions used in quantitative modeling of assemblages

Phase component	Formula	S^{o}[2]	V^{o}[3]	X_j,rim	X_j,core[4]	X_j,calc[5]
Quartz	SiO_2	9.88	.542	1.000	-	-
Water	H_2O	45.10	*	1.000	-	-
Kyanite	Al_2SiO_5	20.00	1.054	1.000	-	-
Anorthite	$CaAl_2Si_2O_8$	49.10	2.409	.320	.180	.160
Albite	$NaAlSi_3O_8$	49.51	2.396	.680	.820	.840
Almandine	$Fe_3Al_2Si_3O_{12}$	75.60	2.755	.661	.633	.633
Pyrope	$Mg_3Al_2Si_3O_{12}$	61.16	2.704	.174	.076	.082
Grossular	$Ca_3Al_2Si_3O_{12}$	60.87	2.995	.107	.167	.167
Spessartine	$Mn_3Al_2Si_3O_{12}$	74.50	2.818	.058	.122	.118
Phlogopite	$KMg_3AlSi_3O_{10}(OH)_2$	76.11	3.577	.675	-	.621
Annite	$KFe_3AlSi_3O_{10}(OH)_2$	95.20	3.688	.320	-	368
Mn-biotite	$KMn_3AlSi_3O_{10}(OH)_2$	100.50	3.805	.005	-	.011
Paragonite	$NaAl_3Si_3O_{10}(OH)_2$	66.4	3.167	-	-	-
Clinochlore	$Mg_{10}Al_4Si_6O_{20}(OH)_{16}$	222.4	9.901	.715	-	.659
Daphnite	$Fe_{10}Al_4Si_6O_{20}(OH)_{16}$	285.0	10.202	.275	-	.319
Mn-chlorite	$Mn_{10}Al_4Si_6O_{20}(OH)_{16}$	303.0	10.592	.010	-	.022
Mg-staurolite	$Mg_2Al_9Si_{3.75}O_{22}(OH)_2$	96.2	5.294	.210	-	.166
Fe-staurolite	$Fe_2Al_9Si_{3.75}O_{22}(OH)_2$	109.0	5.364	.770	-	.796
Mn-staurolite	$Mn_2Al_9Si_{3.75}O_{22}(OH)_2$	112.6	5.441	.020	-	.038
Tremolite+	$Ca_2Mg_5Si_8O_{22}(OH)_2$	131.19	6.523	-.363	-.432	-.514
Fe-tremolite	$Ca_2Fe_5Si_8O_{22}(OH)_2$	163.5	6.759	.468	.590	.573
Pargasite	$NaCa_2Mg_4Al_3Si_6O_{22}(OH)_2$	160.0	6.537	.895	.841	.941

1 Data from Helgeson et al. (1978) or estimated from $MgFe_{-1}$ and $MnFe_{-1}$ exchange potentials, as described by Spear and Selverstone (1983); $S°_{Fe\text{-}staur}$ is from Pigage and Greenwood (1982).
2 S^{o} in cal/deg.
3 V^{o} in cal/bar
4 Core compositions reported only for zoned phases.
5 Predicted compositions of phases in equilibrium with the garnet core, calculated by the method of Spear and Selverstone (1983), using X_{alm} and X_{gross} as monitor components; these values should be compared with the measured core compositions of the phases. See text for discussion.
* Calculated at P and T using a modified Redlich-Kwong equation of state (Holloway, 1977; Flowers, 1979).
+ Amphiboles modeled as a ternary reciprocal solution, hence negative X_{trem} value.

across the constant-Ca portion of the garnet into the core. Each of these increments was broken into 5 steps and a finite difference technique was employed to calculate ΔT and ΔP for each increment. As a consequence of the algebraic formulation of the phase equilibria, the compositions of all other dependent phase components in the rock can also be calculated from the changes in the independent parameters (Spear & Selverstone, 1983). These values can be compared with the actual core compositions of the other zoned phases in sample FH-1M to evaluate the assumption of equilibrium growth of all phases along the P-T path.

The results obtained from the calculations for the two halves of the garnet from sample FH-1M are presented in Figure 3-10, and several important features deserve note. First and foremost are the calculated values of ΔT and ΔP for the entire garnet zoning profile, which indicate that garnet growth commenced at ~530°C and 9-10 kb; these values correspond closely with the constant K_D lines obtained from garnet-plagioclase geobarometry and indeed confirm an early high-pressure phase of metamorphism for these rocks. Another striking result is the excellent agreement between the curves shown in Figure 3-10. Due to uncertainties in the thermodynamic data for the Mn endmembers of the phases coexisting with garnet, ΔX_{spes} was not thought to be as reliable a monitor component as ΔX_{alm} and ΔX_{gros}; nonetheless, the shape of the P-T trajectory determined from ΔX_{spess} corresponds to that of the other two curves, despite a difference of a kilobar in the pressures calculated for the core.

The curvature of the net trajectory is of interest in two regards. First is that it indicates that garnet growth occurred during a period of significant overall decompression (ΔP = -3 kb) accompanied by minor heating (ΔT = +20°C) and is consistent with the model of England and Richardson

Figure 3-9. Zoning profile across garnet from sample FH-1M used in quantitative modeling described in the text. Numbers represent mole percentages of the four endmember components. Roman numerals (I and II) indicate the two halves of the profile used in the calculations.

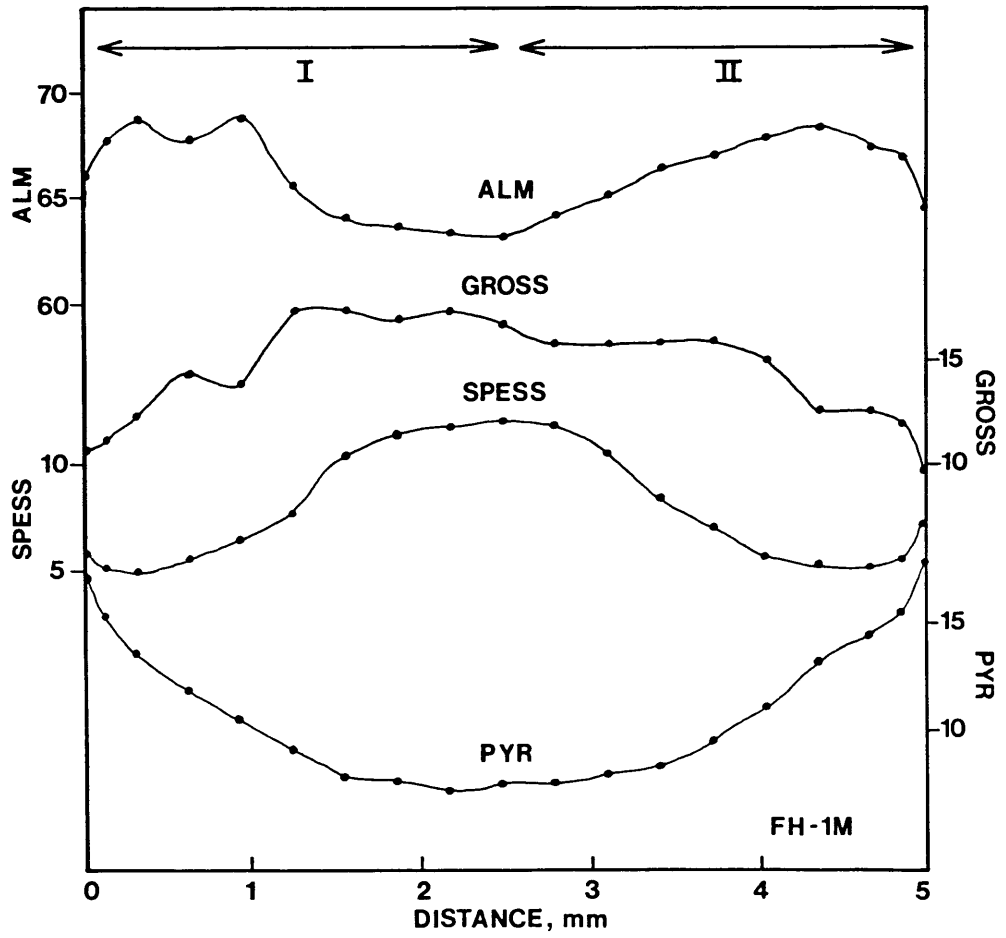
I
II
70
65
60
10
5
ALM
SPESS
ALM
GROSS
SPESS
PYR
15
10
15
10
GROSS
PYR
FH-1M
0
1
2
3
4
5
DISTANCE, mm

Figure 3-10. Pressure-temperature diagram showing the P-T trajectories calculated from quantitative modeling of zoned garnet in sample FH-1M. The three curves are for profiles I and II of Figure 3-9 and different pairs of monitor components. The large symbols represent P-T conditions calculated for the 6 increments discussed in the text, whereas the small dots are from the finite difference calculations within each increment. See text for further discussion.

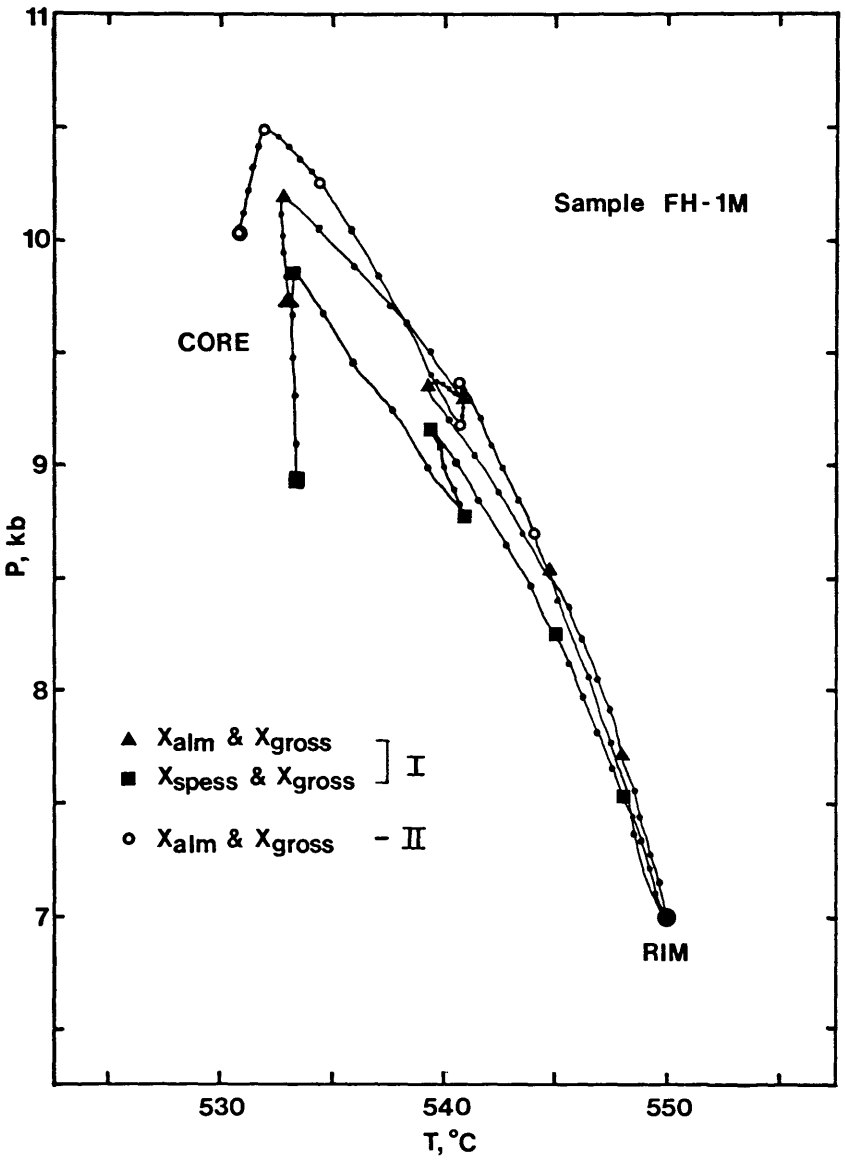
Sample FH-1M
CORE
RIM
▲ Xalm & Xgross
■ Xspess & Xgross
I
o Xalm & Xgross - II
P, kb
T, °C
11
10
9
8
7
530
540
550

(1977) whereby uplift and erosion controls mineral recrystallization. Second is that there are two small reversals superimposed upon the dominant P-T path that, if real, imply episodes of increased burial during the overall uplift history of the rocks. This is not an unreasonable supposition in a terrane characterized by large-scale nappe structures, although an alternative explanation is that these changes in slope of the trajectory simply represent the level of resolution of this technique.

Although a detailed error analysis of this technique is beyond the scope of this paper, a brief discussion of the uncertainties involved seems appropriate. The two principal sources of error stem from the use of simplified mixing models for the relevant phases and from uncertainties in the entropy and volume data used for the phase components. As mentioned above, we have run trials using a variety of different mixing models for garnet and amphibole and found the resultant values of ΔT and ΔP to be relatively insensitive to these models, at least for the case of sample FH-1M. Similarly, trial calculations indicate that small errors in $\overline{S}$ and $\overline{V}$ data affect the calculated ΔT and ΔP to only a few degrees and few tens of bars.

An additional and potentially more significant source of error results from the possibility that the assemblage did not remain constant throughout the period of garnet growth. Careful textural analysis of the samples is important in this regard. As a further check on this assumption, the core compositions of all zoned phases calculated to be in equilibrium with the garnet core can be compared with the actual measured core compositions of these minerals; these values are given in Table 3-7 for sample FH-1M. If equilibrium was maintained among the phases now present over the entire interval of garnet growth, the direction of zoning from rim to core in each

phase should be the same for both the measured and calculated profiles, although the magnitude of the zonation may vary (depending upon whether or not the phase in question was stable prior to the first appearance of garnet and on the ability of diffusional processes to relax the profiles in different phases). In sample FH-1M, this condition is met for all independent phase components (except pargasite component in hornblende), implying that the assumption of equilibrium garnet growth in a constant assemblage is reasonable.

The reproducibility of the curves in Figure 3-10 and similar results for other samples imply that the error limits on the calculated P-T trajectory are relatively small and that the reversals shown in Figure 3-10 are real. A decompression and heating path based on amphibole zoning studies was also determined in rocks from the Eclogite Zone by Holland and Richardson (1979); although the magnitudes of ΔT and ΔP are quite different, in accord with the different tectonic positions of the EZ and LSH, we feel that the overall trend is of great significance in understanding the tectonic evolution of the Tauern region.

MINERAL INCLUSIONS

Mineral phases preserved as inclusions in poikiloblastic host grains have the potential of providing information on assemblages that were stable prior to the "peak" assemblage, and can thereby place constraints on the early portion of the P-T path followed by an individual rock. In most cases, the inclusion suite enclosed within garnet and hornblende in the garbenschist samples consists of epidote, carbonate, plagioclase, quartz, rutile, and ilmenite, all of which are also present in the stable matrix assemblage.

Figure 3-11. Sketch from a photograph of pseudomorph after lawsonite enclosed in hornblende. Stippled pattern = epidote; ruled = chlorite. Hornblende (1) is original hornblende with 17 % Al_2O_3; hornblende (2) is reaction product with 11% Al_2O_3. Note trains of fluid inclusions extending outward from pseudomorph. (See Selverstone et al., 1984, for photograph). Sample Z3-M.

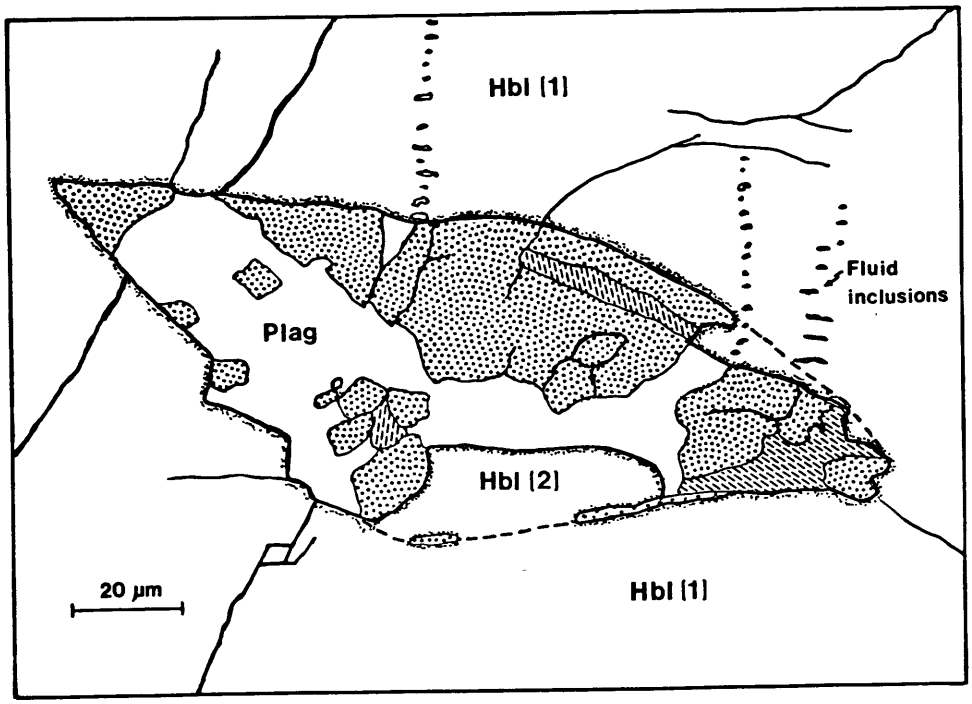
Hbl [1]
Fluid
inclusions
Plag
Hbl [2]
20 µm
Hbl [1]

These phases therefore provide little P-T information except insofar as their compositional changes can be related to growth trajectories in P-T space.

There are two samples (Z3-M and FH-1U), however, that display rather unusual and abundant multiphase inclusions within hornblende porphyroblasts. These inclusions consist of complex intergrowths of epidote + plagioclase ± chlorite and characteristically exhibit subhedral to euhedral prismatic or diamond-shaped outlines (Fig. 3-11), all of which suggests that they are pseudomorphs after some earlier phase. Epidote and plagioclase are similar in composition to their counterparts in the matrix (20% pistacite and An_{32-34}), in contrast to monophase inclusions of these minerals in the same hornblende grains (15% pistacite and An_{18}). Adjacent to the apparent pseudomorphs the host hornblende is zoned over a few microns from ~17 wt% Al_2O_3 to 11 wt% Al_2O_3, with an accompanying change in the Fe/Fe+Mg ratio from 0.40 to 0.29 and a decrease in the total Na content (Table 3-2). Taken together, these features imply a reaction relationship between hornblende and some original inclusion phase to produce a more actinolitic hornblende + epidote + plagioclase ± minor chlorite. Mass balance considerations are consistent with an identity of lawsonite for the original inclusion phase via a reaction such as

Pargasite + Lawsonite =

Actinolite + Epidote + Plagioclase ± Chlorite + H_2O (3-6)

Using real compositions of the phases (Tables 3-1 through 4, analyses for Z3-M) and a hypothetical pure lawsonite, the balanced reaction is:

Hbl I + 0.41 Laws ± O_2 = 0.52 Hbl II + 0.50 An_{33} + 0.24 Epid (3-7)

+ 0.16 Chl + 0.27 H_2O

which is consistent with the observed modal abundances of minerals in these polyphase inclusions. Small radiating fractures observed around many of the inclusions could have provided channelways for the escape of H_2O released by such a reaction.

If these inclusions do indeed represent pseudomorphs after lawsonite, it limits the possible P-T path followed by the rocks during the early stages of metamorphism. The restriction of lawsonite to relatively low-temperature, moderate- to high-pressure parageneses suggests a path that passed through blueschist facies conditions. In fact, reaction (6) could as easily be balanced with glaucophane instead of pargasite to be consistent with such an origin, although no glaucophanitic cores have been observed in any of the amphiboles.

FLUID INCLUSIONS

Late-stage fluid inclusions are abundant in the garbenschists and their densities can be utilized to constrain the uplift path followed by these rocks. No obviously primary inclusions have been observed, although there is considerable evidence for decrepitation of what were probably early inclusions. Among the secondary inclusions, four different generations were recognized for which crosscutting relationships of healed fractures permitted the establishment of a relative chronology of entrapment. The three oldest of these inclusion suites are composed of aqueous fluids, whereas the fourth and youngest generation consists of CO_2. Complex CO_2-CH_4-H_2O-NaCl inclusions were also observed in some samples (see also Luckscheiter and Morteani, 1980), but as it was not possible to determine

an unambigous trapping sequence for these inclusions relative to the other generations, they are excluded from this discussion.

For each of the four generations, measurements were made on 6-12 inclusions per healed crack in each of two different samples. Spot checks of additional fractures in other samples ensured representativity of the inclusions. The microthermometric data for these four generations are summarized in Table 8. The three earliest generations of inclusions become sequentially less dense and slightly more salt-rich; there is no evidence for a CO_2 or CH_4 component in these fluids. The youngest generation consists of carbonic fluid inclusions that melt instantaneously at $-56.6\pm0.2°C$, corresponding to pure CO_2 within analytical uncertainty.

Isochores for the different fluid densities can be determined from the data of Potter & Brown (1975) and Swanenberg (1974), and are shown in Figure 3-12. As can be seen in this figure, the CO_2 isochore (generation 4) has a considerably flatter dP/dT slope than the three aqueous ones, and it is this fact that allows relatively tight constraints to be placed on the uplift path followed by the garbenschist samples. In order to account for the observed age relations among the different generations of inclusions, all of the aqueous inclusions (isochores 1-3) must have been entrapped to the high P-T side of the intersection between the isochores for generations 3 and 4, which occurs at ~375°C, 1.5 kb. The CO_2 inclusions could have been entrapped anywhere along isochore 4, but in order to avoid decrepitation of the relatively large aqueous inclusions by exceeding the yield strengths of their host grains, the value of ΔP between entrapment of the aqueous and carbonic fluids must have been small (Hollister et al. 1979; Leroy, 1979). This implies that the CO_2 inclusions were not entrapped at temperatures significantly above that of the intersection with isochore 3, e.g. 375°C;

TABLE 3-8 - Data for secondary fluid inclusions

Generation	T_m, °C	T_H, °C	ave ρ, g/cm^3	composition
1	-1.7±0.2	148-160	0.94	H_2O + 3% NaCl
2	-3.0±0.2	190-208	0.90	H_2O + 5% NaCl
3	-3.0±0.2	240-256	0.85	H_2O + 5% NaCl
4	-56.6±0.2	23.5±0.4	0.72	CO_2

T_m = temperature of final melting

T_H = homogenization temperature

Figure 3-12. Isochores for intersecting planes of late-stage H_2O-rich and CO_2-rich fluid inclusions. Intersection of the CO_2 isochore with the aqueous ones constrains the uplift path of the garbenschists to a trajectory such as the one shown here by the heavy arrow. See text for further discussion.

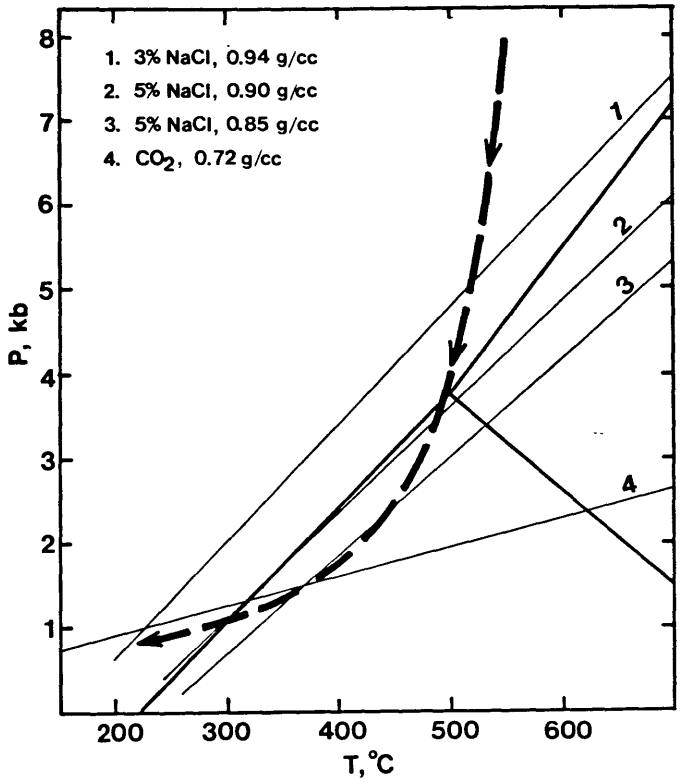
1. 3% NaCl, 0.94 g/cc
2. 5% NaCl, 0.90 g/cc
3. 5% NaCl, 0.85 g/cc
4. CO_2, 0.72 g/cc
P, kb
T, °C
1
2
3
4
8
7
6
5
4
3
2
1
200
300
400
500
600

indeed, fluid entrapment could as easily have ocurred at considerably lower temperatures along the CO_2 isochore. A possible uplift path starting at the conditions of final matrix equilibration (~550°C, 7 kb) and consistent with all of the fluid inclusion data is indicated by the arrow in Fig. 3-12. This path implies that the majority of the decompression experienced by the garbenschists occurred at relatively high temperatures; significant cooling apparently did not commence until the rocks were within ~5 km of the surface. Although this path passes through the andalusite field, no andalusite has been observed as a late-stage mineral in any of the samples.

SUMMARY OF P-T DATA

All of the pressure-temperature data and constraints discussed above are combined into a single diagram in Figure 3-13, and a relatively complete P-T loop for the garbenschists results. Although the earliest and latest portions of the metamorphic trajectory cannot be retrieved, information on a considerable portion of the metamorphic history of these rocks is available. The reconstructed path indicates that the rocks initially reached high pressures via the blueschist facies; subsequent heating at high P resulted in development and equilibration of the garbenschist assemblage at conditions of ~520±25°C, 9-10 kb. Porphyroblast growth continued along a decompression path to ~550±25°C, ~7 kb, the final recorded stage of metamorphic reequilibration and recrystallization. A further 5.5 kb of decompression was accompanied by a temperature change of less than 175°C, and final cooling towards a more normal geotherm did not occur until the rocks were quite close to the surface. There are no data to indicate any

breaks in slope along this loop that might represent distinct metamorphic "events"; rather, the shape implies a single metamorphic continuum from initial burial through final uplift of the terrane, although the rates of progress along different portions of the trajectory could be quite variable.

Previous estimates of "peak" metamorphic pressures in this region of the Tauern Window have been in the 5-7 kb range (Morteani, 1974; Hoschek, 1980, 1981, 1982; DeVecchi & Baggio, 1982). Geobarometry on the garbenschist samples indicates that the dominant amphibolite facies overprint occurred in the 6-8 kb range, in agreement with these earlier estimates. The early 10 kb pressures determined from quantitative modeling of the growth trajectories of the zoned phases and from plagioclase inclusions in garnet, however, are significantly higher than the previous estimates of maximum pressures for this area. These early high pressure conditions have significant implications for understanding the tectonic evolution of the Tauern Window.

Figure 3-13. Summary P-T diagram combining the data of Figures 3-7, 3-8, 3-10, and 3-12. Heavy arrow indicates metamorphic trajectory followed by garbenschists consistent with these data. Solid portion of the curve is the path calculated from quantitative modeling of garnet zoning. The boxes represent P-T conditions determined from standard geothermobarometry. Dashed portions of curve are inferred from pseudomorphs after lawsonite and from fluid inclusion data; two possible paths from the blueschist facies are shown as there are no data to constrain the curvature in this region. Lawsonite stability curves are from Chatterjee (1976); Zo = zoisite, Wair = wairikite. See text for further discussion.

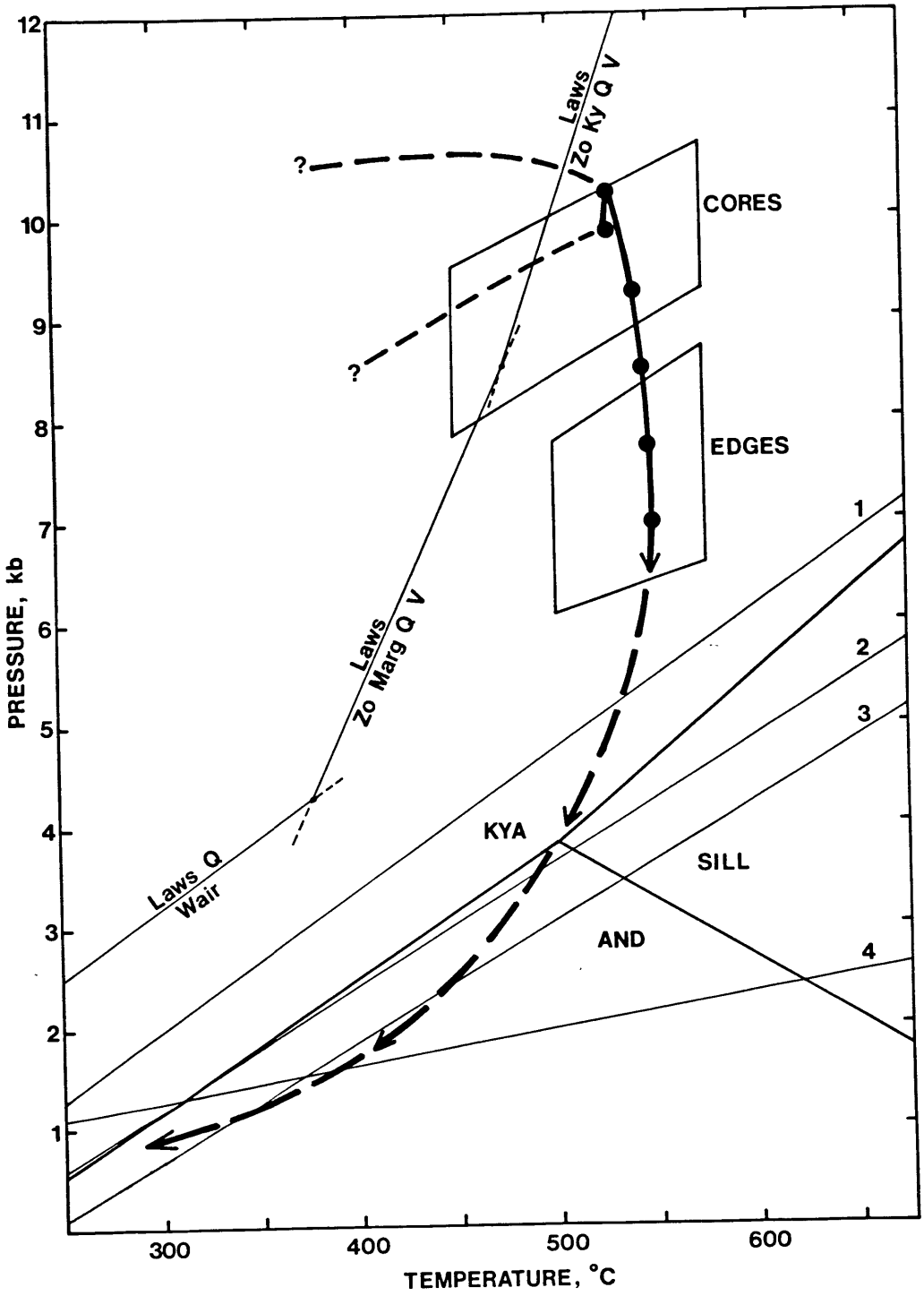
PRESSURE, kb
TEMPERATURE, °C
300
400
500
600
1
2
3
4
5
6
7
8
9
10
11
12
?
?
CORES
EDGES
Laws
Zo Ky Q V
Laws
Zo Marg Q V
Laws Q
Wair
KYA
SILL
AND
1
2
3
4

P-T HISTORY OF FABRIC DEVELOPMENT

Several textural features of the Garbenschist samples can be added to the P-T loop of Figure 3-13 to arrive at a relationship between fabric development and the pressure-temperature history of this unit. In particular, these are:

(1) Hornblende garben randomly overprint a well-developed early foliation and lineation defined by mica ± chlorite ± epidote; in many cases, quartz and plagioclase in the foliated matrix appear to have undergone dynamic recrystallization such as would be expected from ductile deformation.

(2) Lawsonite pseudomorphs are always enclosed within hornblende and are oriented parallel to the matrix foliation.

(3) Garnets are subhedral to euhedral, and show little to no evidence of rotation.

(4) Hornblende garben are cracked perpendicular to their length, and these cracks are filled with unzoned plag (An_{33}) + quartz ± kyanite ± biotite.

Observations (1) and (2) imply that the rocks developed a prominent foliation in response to ductile deformation prior to the growth of hornblende garben. In addition, lawsonite must have been a stable phase in the assemblage at this time, placing this part of the rocks' history within the P-T regime of the blueschist facies. Onset of amphibole growth must also have occurred within the lawsonite stability field in order to account for the inclusions of lawsonite within hornblende. Although the association hornblende + lawsonite is not a common one, it has been reported from other localities (e.g. see Turner, 1981). The random orientation of the hornblende garben indicates growth in the absence of a directional stress field.

Breakdown of lawsonite, involving amphibole as an additional reactant (equations 3-6 and 3-7), must have occurred to the low-T side of the reaction marking the ultimate stability limit of lawsonite.

Due to the lack of quantitative constraints of the shape and position of earlier portions of the garbenschist P-T path, it is not possible to determine precisely the positions at which each of the above-mentioned textural features were developed. However, their relative chronology within the blueschist facies is clear, and is shown schematically by positions I through III on the P-T loop of Figure 3-14. Position IV indicates the onset of garnet growth, as determined from geobarometric calculations using plagioclase inclusions in garnet cores and from the thermodynamic modeling of garnet zoning. The absence of rotational features in any of the garnets combined with the random orientation of the amphiboles implies that little internal deformation occurred within this portion of the Lower Schieferhulle as it was transported along the part of the P-T path defined by the garnet zoning modeling (V).

The lack of zoning in plagioclase filling cracks in stretched amphibole crystals suggests that plagioclase growth occurred over a limited range of P-T conditions. The composition of plagioclase in hornblende cracks is identical to that of the edges of matrix plagioclase grains (An_{33}), and when used in conjunction with garnet edge compositions adjacent to some of these filled cracks, the garnet-plagioclase-kyanite-quartz geobarometer yields pressures of 6-8 kb at 550°C. These are the same P-T conditions as those of the final equilibration of the garbenschist assemblage, implying that cracking of the hornblende occurred synchronously with the last equilibration (VI). This also agrees with data on the zoning in hornblende: both cracked and uncracked grains show identical zonation from cores to

3-14. P-T diagram correlating fabric development of the garbenschist samples with the relative position of the rocks along their P-T trajectory. (I) Development of foliation. (II) Growth of amphibole. (III) Breakdown of lawsonite by reaction with amphibole. (IV) Onset of garnet growth. (V) Cracking of hornblende porphyroblasts. (VI) Final mineral equilibration. Positions I, II, and III are only schematic due to lack of quantitative P-T data on the early history of the rocks. See text for further discussion.

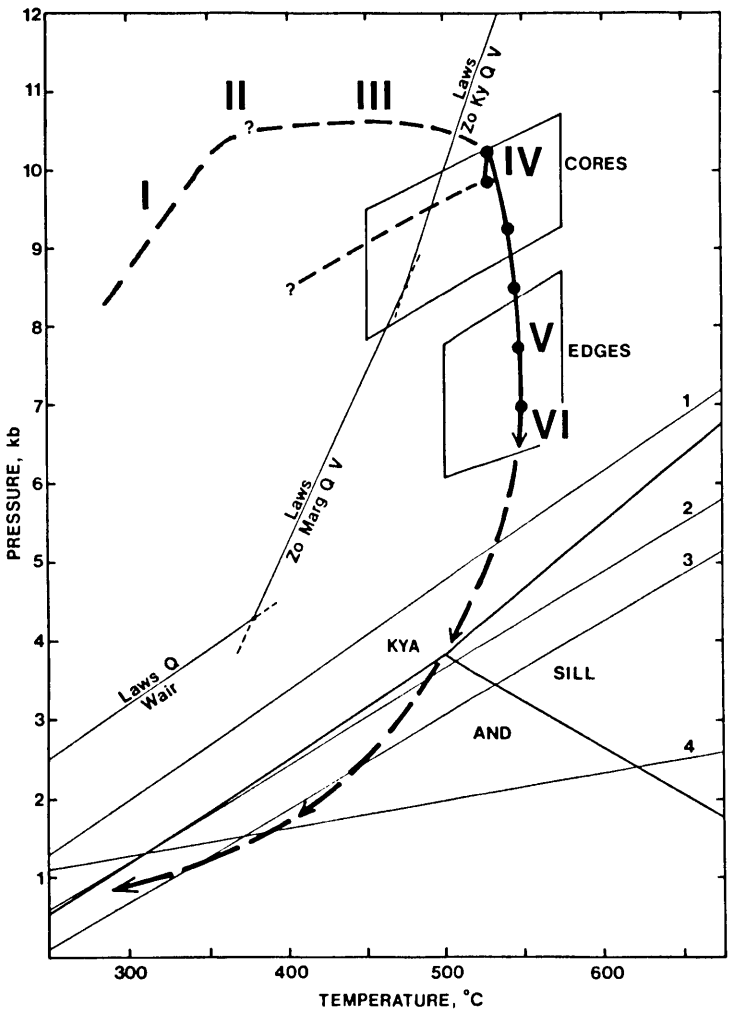

I. Shearing and development of foliation

II. Onset of amphibole growth:

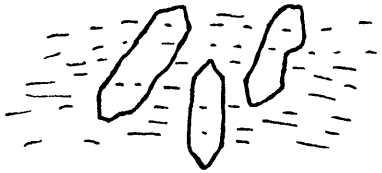

III. Breakdown of amphibole + lawsonite:

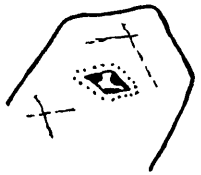

IV. Onset of garnet growth

V. Cracking of amphibole porphyroblasts

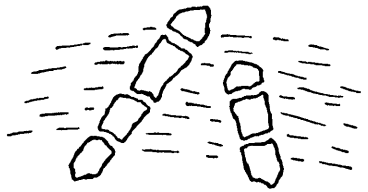

VI. Final mineral equilibration

matrix edges, but there is no detectable zonation developed from the cracks into the hornblende. These data indicate that the rocks experienced a period of extension at the same time as or slightly postdating the cessation of porphyroblast growth and equilibration.

The picture that emerges from combining these textural observations with the reconstructed P-T path is one of compression and/or shearing during burial of the rocks at relatively low temperatures. At the maximum depth of burial and during the early stages of uplift, there is little evidence of penetrative deformation, and randomly oriented euhedral porphyroblasts grew across the earlier foliation with no signs of rotation or physical realignment. Later in the uplift history the rocks experienced an extensional event that resulted in cracking of earlier porphyroblasts, particularly hornblende. The significance of each of these stages will be returned to in the discussion of tectonics in Chapter 5.

DISCUSSION

The classic model of Oxburgh & Turcotte (1974) concerning the influence of overthrusting on thermal gradients in regional metamorphism was initially developed to account for the metamorphic features of the Tauern Window. The model assumes the relatively rapid emplacement of a thick thrust sheet with hot rocks at its base over a sequence of unmetamorphosed rocks, and examines the evolution of P-T conditions above and below the thrust with time. Immediately post-thrusting, the thermal profile through the thickened crust will have a sawtooth form (Figure 2 of Oxburgh & Turcotte, 1974) that will decay with time towards the steady-state geotherm for the thickened package

of rocks. Thus, rocks of the lower plate will experience an immediate increase in pressure, owing to the increased overburden, and a subsequent episode of heating. In practice, the rocks will never attain the conditions of the steady-state geotherm before uplift and erosion affect the thermal profile, but a significant temperature increase should nonetheless occur in the lower plate.

Oxburgh & Turcotte (1974) used this model to explain the metamorphism of the Lower and Upper Schieferhülle series as a direct consequence of the emplacement of the Austroalpine thrust sheets, although they had to call upon an increased heat flow from the mantle to generate the amphibolite facies temperatures. An average thickness of 15 km for the Austroalpine sheets (Oxburgh & Turcotte, 1974) would generate pressures of ~5 kb on the ~4 km thick Schieferhülle series. This corresponds well with the pressures that had been estimated for the LSH and USH at the time of Oxburgh & Turcotte's (1974) study, and the timing constraints on overthrusting and heating also appeared to fit the model.

In light of calculated pressures of ~10 kb for early metamorphism in the LSH, however, it is clear that a simple overthrust model cannot account for the P-T conditions preserved in the lower plate. Pressures of this magnitude require an overburden with a minimum thickness of 35 km, or twice the known thickness of the Austroalpine sequence. Blueschist facies rocks preserved in the Western Alps apparently resulted from partial subduction of the European continent beneath the Austroalpine continent (Ernst 1973), and such a process also seems relevant in the Tauern Window (e.g., Frisch, 1978, 1979; Klemm et al., 1978). Transport of sedimentary and volcanic material down a subduction zone would generate the high pressures observed in the garbenschists, although at lower temperatures. A lag time between cessation

of subduction and ensuing uplift and erosion or tectonic emplacement into shallower crustal levels would result in approximately isobaric migration of isotherms towards higher temperatures (e.g. Richardson & England, 1979), which could account for the ~530°C. 10 kb conditions discussed in this paper. Subsequent P-T conditions shown in Figure 3-13 are most strongly characterized by decompression accompanied first by heating and later by cooling; this portion of the P-T loop is consistent with the model of England & Richardson (1977) whereby uplift and erosion exert the dominant control on mineral equilibria. Transport of the rocks towards the surface, either by thrusting or isostatic readjustment, must have been sufficiently rapid to have avoided significant heat exchange with the surroundings.

CONCLUSIONS

The unusual hornblende + kyanite + staurolite ± paragonite assemblages present in the garbenschist horizon of the LSH appear to represent a high-pressure paragenesis of the amphibolite facies for volcanogenic lithologies, rather than "normal" metamorphism of anomalous bulk compositions. Although the garbenschist assemblage is not a common one, it is known from several other localities (e.g. Vermont, U.S.A.: Hepburn, 1972; Central Alps: Frey, 1974; New Zealand: Cooper, 1980; Gibson, 1978, 1979; Japan: cited in Gibson, 1978; British Columbia: M.L. Crawford, personal communication) and its occurrence may be an important indicator of high-pressure metamorphism in these terranes.

Construction of the P-T loop shown in Figure 3-13 from geothermometry/ barometry, pseudomorphing relations quantitative modeling of garnet zoning, and fluid inclusion data provides the basis for correlating the metamorphic

history of the garbenschists with the tectonic processes responsible for this metamorphism. The shape of the metamorphic trajectory and the quantitative P-T conditions it records imply partial subduction of the Lower Schieferhülle to a depth of ~35 km beneath the Austroalpine continent. Although high-pressure conditions indicative of subduction have been reported from the USH and EZ of the Venediger area (e.g. Raith et al., 1978; Holland, 1979), such high-pressure metamorphism has not previously been documented in the Lower Schieferhülle.

Comprehensive studies of the Zentralgneis and Upper Schieferhülle, in addition to other units of the Lower Schieferhülle, are in progress to compare the P-T histories experienced by these tectonic units with that of the garbenschist horizon. In this way, it should be possible to relate timing and style of metamorphism to the tectonic juxtaposition of the various allochthonous units in the SW Tauern Window. Ultimately, it is hoped that reliable age dates will become available for different portions of the P-T trajectories of these rocks, particularly the high-pressure portion. It is only by combining data on P-T paths of metamorphism with absolute ages and heat flow modeling (e.g. England, 1978) that a complete understanding of the tectonic evolution of the Tauern Window will be gained.

CHAPTER 4

PETROLOGY AND P-T EVOLUTION OF THE UPPER SCHIEFERHULLE SERIES

INTRODUCTION

The Mesozoic Upper Schieferhülle (USH) series, also referred to locally as the Glockner Decke, is composed of greenstones, calcareous schists, marbles, and calcic pelitic schists that are separated from the underlying ZG and LSH by a well-defined thrust zone. The upper contact of the USH is the prominent basal thrust of the Austroalpine nappe complex. The rocks of the Glockner Decke are thought to represent the remains of the South Penninic ocean basin (e.g. Frisch, 1980), and have been correlated with the famous Bündnerschiefer lithologies of the Western Alps, in which blueschist and eclogite assemblages are locally abundant (e.g. Ernst, 1973; Frisch, 1980). The Eclogite Zone of the central Tauern Window is ascribed by some authors to the USH, based on lithologic similarities between the units (Miller, 1974; Raith, 1976), whereas others argue that it is a separate tectonic slice sandwiched between the LSH and USH (Franz and Spear, 1983). In the area of this study, no prominent eclogite horizon is evident in the field, and although there is a prevailing sentiment that the USH experienced high-pressure metamorphism (e.g. Morteani, personal communication; Raith et al., 1977), this has not been well-documented. The goal of this chapter is to use detailed petrologic techniques to reconstruct the pressure-temperature history of the USH in the contact zone with the LSH, and thus to constrain the conditions of imbrication of the two units.

Within the area of this study, the USH occurs in the core of a large syncline between two lobes of the ZG, as was shown in the map of Figure 2-5 and the cross section of Figure 2-6. The thrust contact with the LSH is slightly discordant to the layering of the lower plate rocks, and is

marked by a narrow (0.1-1.0 m) zone of quartz and carbonate veining. Isoclinal folding of both units is prominent near the contact and is probably related to drag along the thrust.

Just above the contact zone, the dominant lithology is calcareous schist with thin (<10 cm) interlayers of pelitic material and lenses of fine-grained greenstone. The percentage of amphibolitic material within the calcmica schist increases up-section, and the highest levels of the USH that are exposed are composed predominantly of greenstones with pods of serpentinite. Pelitic horizons occur throughout, but never attain any significant thickness within the study area. Because of the wealth of petrologic information that can be extracted from the pelitic schists, however, they represent the dominant focus of this chapter. A brief discussion of the greenstones is also included. A recent study of the calcareous schists is presented by Hoschek (1984).

PELITIC HORIZONS

Sample description and mineral chemistry.

Within the syncline of USH preserved in the area of this study, pelitic layers are thin and discontinuous and do not account for a significant percentage of the USH sequence. Elsewhere in the Tauern Window, however, pelitic schists are the predominant lithology in the highest part of the USH (Frisch, 1980). The pelitic samples discussed here are from layers less than 1 m in thickness that occur within the lower half of the USH sequence. The structurally lowest of these (localities HF-6 and HF-27) were collected within 1 m of the contact with the underlying LSH; localities HF-2, HF-3, and HF-29 are from higher in

the section. The structurally highest samples (HF-17) were collected from a pelitic horizon in the contact zone between sections of the USH composed predominantly of calcareous schist and of greenstone (see Figure 2-6 and Appendix I).

All of the pelitic horizons are extremely graphitic and most contain abundant garnets 1-5 mm in diameter. The larger garnets are clearly synkinematic, with rotational growth patterns that are evident in outcrop; smaller garnets are typically euhedral in outline, although rotated cores are visible in many thin sections. Quartz and carbonate veins are common in the pelitic layers, and the schists typically grade into graphitic, impure marbles or into thin lenses of calcareous hornblende garbenschist. Within the pelitic layers themselves, the assemblage is garnet - biotite - chlorite - phengite - plagioclase - quartz - ilmenite - graphite - rutile ± epidote ± carbonate ± margarite ± hornblende (Table 4-1), indicating that the overall bulk composition of these rocks is unusually calcareous for pelites. Representative analyses of all minerals in the pelitic assemblages are given in Table 4-6 at the end of this chapter.

Garnets are highly variable in morphology and range from euhedral to subhedral to grains that are flattened and strung out in the foliation (Figure 4-1). With the exception of graphite, which generally defines the rotational fabric of the garnets, inclusions of other phases are rare. Compositional zoning is pronounced in some samples. In HF-3A, which lacks plagioclase, garnet zones from $Alm_{40}Py_{1}Gr_{19}Sp_{40}$ in the core to $Alm_{69}Py_{9}Gr_{21}Sp_{1}$ at the rim; in other samples, such as hornblende-bearing HF-17A, total zonation of garnet does not exceed 6 mol percent of any phase component. These two samples represent the extremes; in all

Table 4-1

Mineral assemblages in pelitic schist members of the USH

Sample	Gar	Bio	Chl	Pheng	Marg	Plag	Epid	Carb	Hbl
HF-2C	x	x	x	x	x		x		
HF-2D	x	x	x	x	x	tr	x	x	
HF-2E	x	x	tr	tr		x			
HF-3A	x	x	x	x			x		
HF-3C	x	x	x	x					
HF-6A	x	x	x		x	x	x		
HF-6B	x	x		x	x	x		x	
HF-11	x	x	x	x		x			
HF-17A	x	x	x	x		x	x		x
HF-17D	x	x	x	x		x			
HF-17E	x	x	x	x	tr	x		x	
HF-17F	tr	x	x	x		x	x		tr
HF-17G	x	x	x	x		x		x	
HF-27A	x	x	x	x		x	x	tr	
HF-27B	x	x	x			x	x		
HF-27D	x	x		x		x	x	x	
HF-27E	x	x	x			x	x	x	
HF-29	x	x				x	x	x	

All samples contain quartz, graphite, ilmenite, and trace amounts of rutile in addition to the phases listed above. tr - trace.

samples containing the "typical" pelitic assemblage, garnets show many complex reversals in their zoning profiles. This is discussed further in the section on modeling of garnet zonation.

Biotite occurs in two habits, although compositions of the two types are indistinguishable. The oldest biotite grains are ragged and anhedral and display cleavage traces oriented perpendicular to the dominant foliation, despite physical elongation of the grains parallel to this foliation. More commonly, biotite is both physically and optically aligned with the foliation defined by mats of phengite. Fe/Fe+Mg ratios range from 0.40 to 0.55, with biotites adjacent to garnet typically 3-4 mol % more enriched in Fe than isolated biotites in any one sample. Early biotites show some slight alteration to chlorite, but elsewhere there is little evidence of retrogression.

Chlorite is part of the stable assemblage in all of the studied USH pelites. It occurs as euhedral to subhedral grains aligned with the foliation, and typically has Fe/Fe+Mg ratios of 0.36-0.45. This pelitic suite is the only set of rocks from the LSH or USH in the study area in which chlorite and white mica coexist stably as part of the dominant assemblage.

Phengite is the principal white mica phase in these samples. Paragonite contents are less than 10 mol % in all cases, whereas celadonite contents range from 13-37% (Figure 4-2), with the samples from the contact zone with the LSH showing the lowest values. Note that all of the phengite analyses plot slightly to the right of the ideal $(Mg,Fe)SiAl_{-1}^{vi}Al_{-1}^{iv}$ line in Figure 4-2; this is probably due either to the presence of minor amounts of Fe^{3+} that have been recast from the microprobe analyses as Fe^{2+} or to a small amount of dioctahedral-trioctahedral substitution.

Figure 4-1. Sketches from photographs of typical garnet porphyroblasts in graphitic schists of the USH. HF-2D: anhedral, syntectonic garnets strung out in the foliation. HF-6A: subhedral garnet with rotational fabric defined by graphite inclusions. HF-27B: subhedral syn- to post-tectonic garnet with inclusions of graphite and quartz. These textures contrast with garnets of the LSH garbenschists which are euhedral and post-tectonic. Heavy lines indicate approximate locations of microprobe traverses across garnets in samples HF-6A and HF-27B.

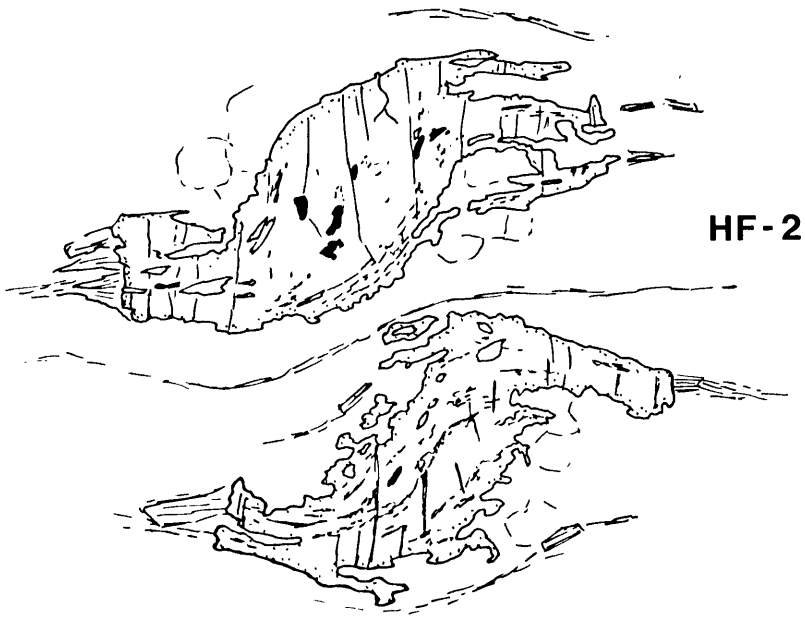

HF-2D

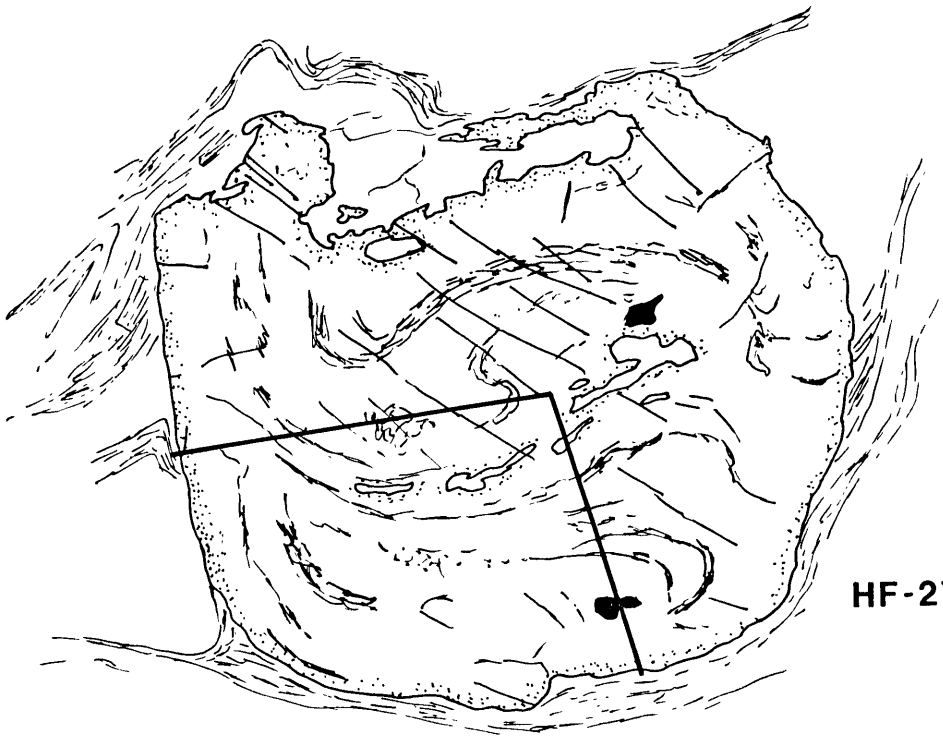

HF-27B

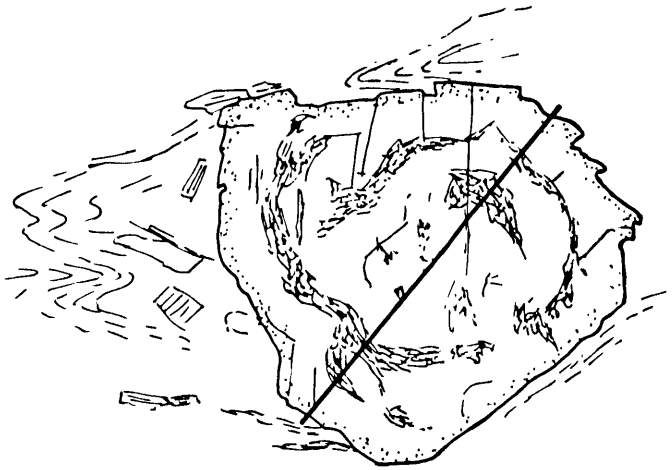

HF-6A

2 mm

Figure 4-2. Plot of Al content versus Mg+Fe+Mn+Si for USH phengites. The solid line represents the degree of Tschermak's substitution ($MgSiAl^{vi}_{-1}Al^{iv}_{-1}$) and is contoured in percent celadonite content; pure muscovite would plot in the lower right hand corner. The slight shift of the analyses off of the Tschermak's line may be due to the presence of minor amounts of Fe^{3+}, or to an additional substitution mechanism such as $2Al^{3+}=3Mg^{2+}$ (dioctahedral-trioctahedral exchange). Note large degree of variability in celadonite content of phengites even in a single sample (e.g. HF-17A). This appears to be due to heterogeneity in layering of samples rather than to disequilibrium or presence of multiple generations of phengite.

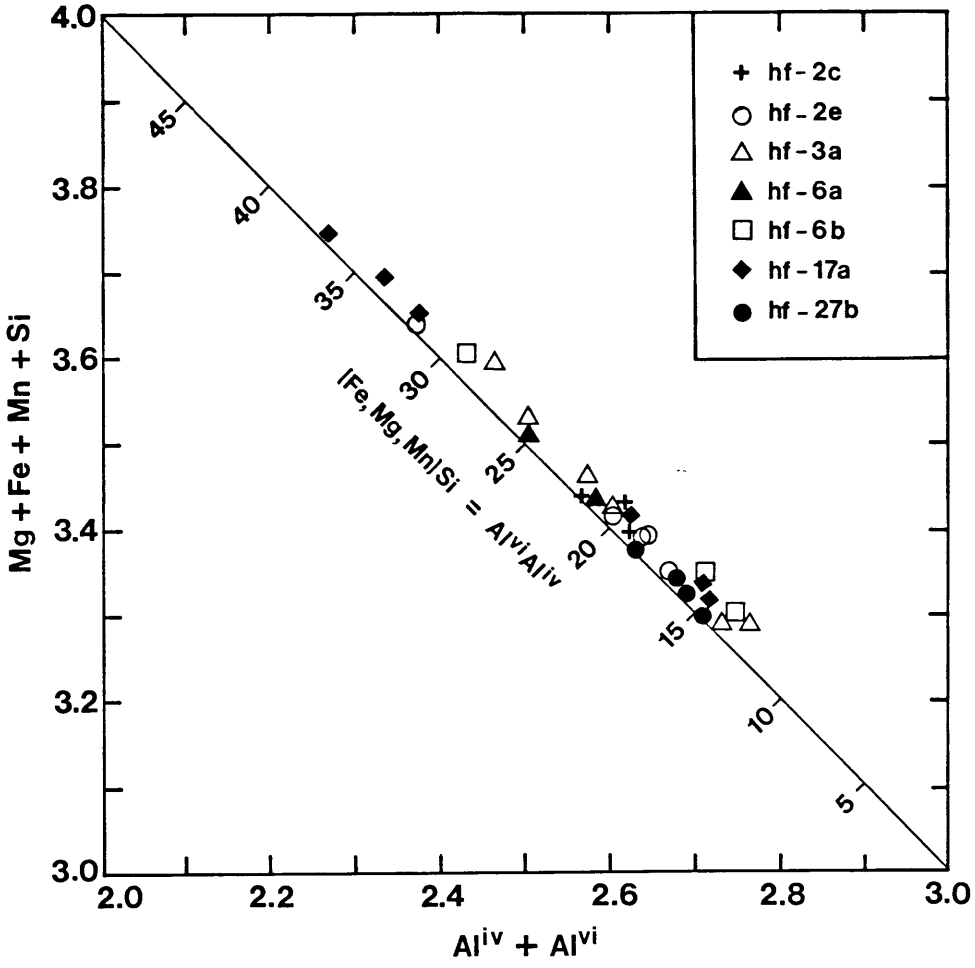
4.0
3.8
3.6
3.4
3.2
3.0
2.0
2.2
2.4
2.6
2.8
3.0
Mg + Fe + Mn + Si
Al^iv + Al^vi
45
40
35
30
25
20
15
10
5
[Fe, Mg, Mn]Si = Al^viAl^iv
hf - 2c
hf - 2e
hf - 3a
hf - 6a
hf - 6b
hf - 17a
hf - 27b

Figure 4-3. K-Na-Ca diagram showing compositions of white micas in the USH. The regular array of tielines between muscovite (phengite) and margarite suggests that margarite is part of the primary mineral assemblage, in agreement with the textural evidence. Analyses of micas from the LSH garbenschists and Furtschaglschiefer are shown for comparison.

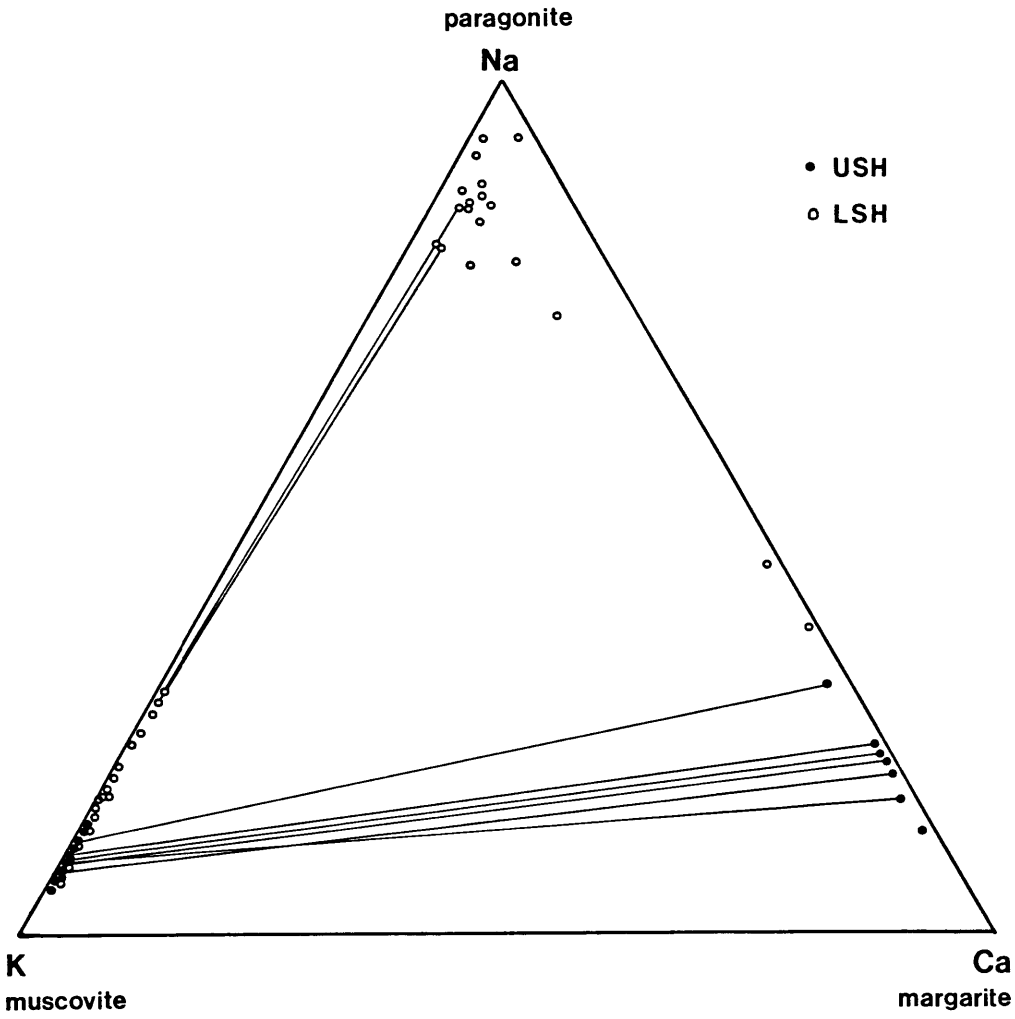
paragonite
Na
• USH
o LSH
K
muscovite
Ca
margarite

Margarite is present in minor abundances in some samples where it occurs in fine-grained mats intergrown with phengite. In contrast to the LSH samples, margarite here appears to be a part of the stable mineral assemblage. This conclusion is supported by the general lack of crossing tieline relationships on the Na-Ca-K plot of coexisting phengite and margarite shown in Figure 4-3. Typical compositions range from $Ma_{81}Pa_{18}Mu_1$ to $Ma_{69}Pa_{29}Mu_2$.

Plagioclase is an abundant constituent of all of the pelitic samples except HF-2D and HF-3A. It occurs both as large syntectonic poikiloblasts with strong optical zonation and as small granoblastic matrix grains. In both cases, compositions are highly variable, even in a single area of a thin section. In general, plagioclase edges adjacent to garnet are in the range An_{43-50} and are more calcic than edges adjacent to any other phase, which are typically An_{29-40}. Core compositions vary from An_{27} to An_{54}. Inclusions of plagioclase in garnet have edge compositions of An_{20-25} and cores as sodic as An_{17}. Reversals in zoning are common; this is discussed further in a subsequent section. Evidence of retrogression is rare.

Epidote is present as small accessory grains in most of the samples. Edge compositions span the range 31-64 % $FeAl_2Ep$ (where $FeAl_2Ep$ is equal to 100(3-Al) on the basis of 12.5 oxygens per formula unit; see Raith, 1976), and there is no evidence for a miscibility gap in the system at the conditions of final equilibration of these samples. In general, the grain size is too small to resolve any chemical zonation.

Calcite occurs as a minor constituent of several of the pelitic schists, and in samples HF-6B and HF-29, both calcite and dolomite coexist in the matrix and as inclusions in garnet.

Hornblende has been obseved in only a single garnetiferous pelitic schist (HF-17A). It occurs as euhedral to subhedral porphyroblasts, generally surrounded by (but not altered to) chlorite, and contains 20 wt % Al_2O_3. No compositional zoning was detected.

Graphite, rutile, and ilmenite are ubiquitous accessory phases in the matrix and as inclusions in garnet. Ilmenite shows no sign of oxidation or alteration. Sphene was not observed in any of the samples.

Phase equilibria.

The chemical variability of the calcareous USH pelites can be described within the model system SiO_2-Al_2O_3-TiO_2-FeO-MgO-MnO-CaO-K_2O-Na_2O-C-O-H. The dominant assemblage Gar-Bio-Chl-Pheng-Plag-Epid-Qtz-Graph-Ilm-Ru-Fluid is trivariant within this system, and the carbonate and/or margarite-bearing samples represent still lower variance assemblages. There is no obvious textural evidence for reaction relationships among the phases, and the general lack of mineral inclusions or pseudomorph aggregates makes it difficult to identify assemblages stable prior to the equilibration of the presently observed assemblage.

When plotted on a Thompson (1957) AFM diagram, abundant crossing tielines are evident for the subassemblage Gar-Bio-Chl (Figure 4-4). Several possibilities exist to explain the crossed tieline relationships: (1) chlorite is a retrograde phase and hence out of equilibrium with garnet and biotite; (2) different compositions of phengite in each of the samples make projection from pure muscovite onto the AFM plane invalid; (3) the chemical potential of water, μ_{H2O}, is variable within or between samples; (4) additional components such as Ca and/or

Figure 4-4. AFM projection from quartz, muscovite, and water showing three-phase triangles for the assemblage Gar-Chl-Bio in graphitic schists of the USH. Crossing tielines are evident even for 3-phase assemblages within different areas of a single thin section (e.g. HF-17A and HF-27B). See text.

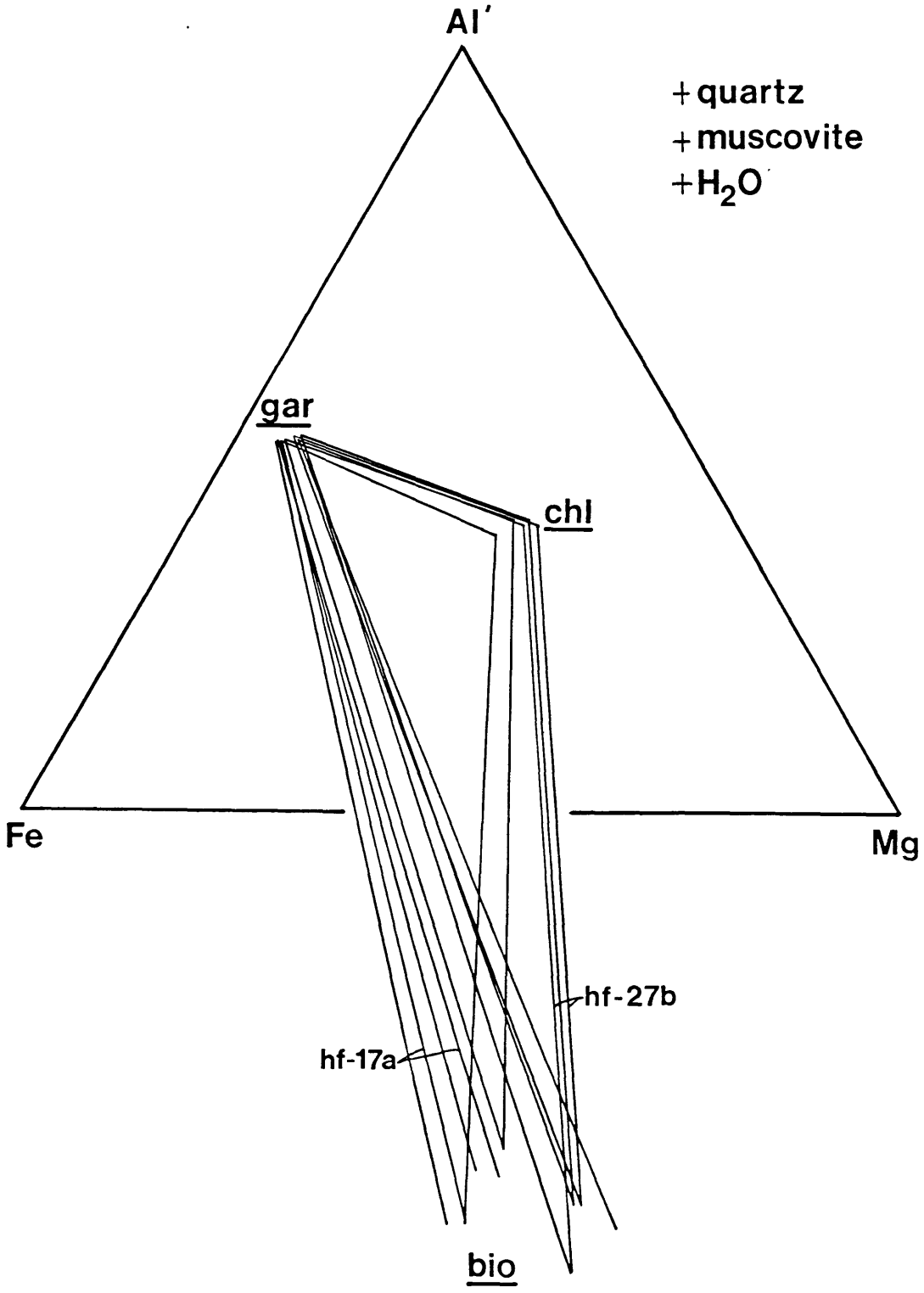
Al'
+quartz
+muscovite
+H_2O
gar
chl
Fe
Mg
hf-27b
hf-17a
bio

Mn are stabilizing garnet; (5) final equilibration did not occur at the same P-T conditions for all samples. Because determination of the pressure-temperature history of these rocks rests upon the assumption of attainment of equilibrium among all phases, each of these possibilities is briefly addressed here.

(1) It is not always possible to distinguish between "prograde" and "retrograde" phases based on textural criteria, but the mode of occurrence of chlorite in these samples strongly indicates that it is part of the primary mineral assemblage. Chlorite is evenly distributed throughout most of the samples, and is subparallel to the foliation. There is little development of chlorite along cleavage traces in biotite, and ilmenite and rutile inclusions, which are common in chlorite that has replaced titaniferous biotite, are completely absent; cracks in garnet are also devoid of chlorite. All of these features are consistent with a "prograde" origin for chlorite.

(2) Although the celadonite content of the phengites is highly variable in these rocks, the Fe/Fe+Mg ratios, which exert the dominant control on the plotting positions of the other phases in AFM space, are relatively restricted. Projecting each Gar-Bio-Chl assemblage from the unique composition of each coexisting phengite does not remove the crossing tielines evident in Figure 4-4, and hence pure muscovite is retained as a projection point in this diagram.

(3) The abundance of graphite in these samples implies the presence of a mixed C-O-H fluid phase dominantly controlled by equilibria such as:

$$2C + 2H_2O = CO_2 + CH_4 \qquad (4\text{-}1)$$

(e.g. Holloway, 1984). In light of this, it is evident that the assumption of fixed μ_{H2O} may be particularly suspect in considering the phase equilibria of graphitic samples. To test the validity of this assumption in the USH pelites, H_2O was removed as a projection point, and the assemblage Gar-Bio-Chl was projected from Plag (An_{45})-Pheng-Epid-Qtz into the phase volume Al'-Fe'-Mg'-H_2O (Figure 4-5). If the crossing tielines on the original AFM diagram were due to local variations in μ_{H2O}, they would be removed in this diagram (e.g. Rumble, 1976). It is evident from Figure 4-5, however, that the crossing tielines remain, and variability in the fluid phase cannot be the sole factor involved in producing the apparent disequilibrium relationships on the AFM diagram. The USH pelites consist of thin horizons of graphitic material embedded within huge thicknesses of greenstone or calcareous schist; it is likely that reactions within these surrounding lithologies exerted the dominant control over the fluid phase in the pelites, and that local variations in fluid phase equilibria were of only minor significance.

(4) In contrast to "normal" pelitic schists, the USH samples are highly calcareous, as is evident by the abundance of calcic plagioclase, epidote, and margarite in these samples. Garnet typically contains 18-23% of the grossular endmember at the rim, and zones to higher values in the core. In order to examine the influence of Ca as an extra component on the phase equilibria of these samples, a projection from An_{45}-Pheng-Qtz-H_2O into the phase volume Al'-Fe'-Mg'-Ca' is shown in Figure 4-6. When projected into this space, all crossing tieline relationships in the assemblage Gar-Bio-Chl are removed, and we see a fan of three-phase planes that vary primarily in Ca content. In those samples with the highest Ca contents (e.g. HF-2C, -6A, -6B, and 27B), margarite is also

Figure 4-5. Projection from An_{45} + phengite + epidote + quartz into the phase volume Al-Fe-Mg-H_2O to evaluate the influence of variable μ_{H2O} on the assemblage Gar-Bio-Chl. The persistence of crossing tie-lines and intersecting planes on this diagram indicates that variations in μ_{H2O} at constant P and T cannot be solely responsible for the phase equilibria of these samples.

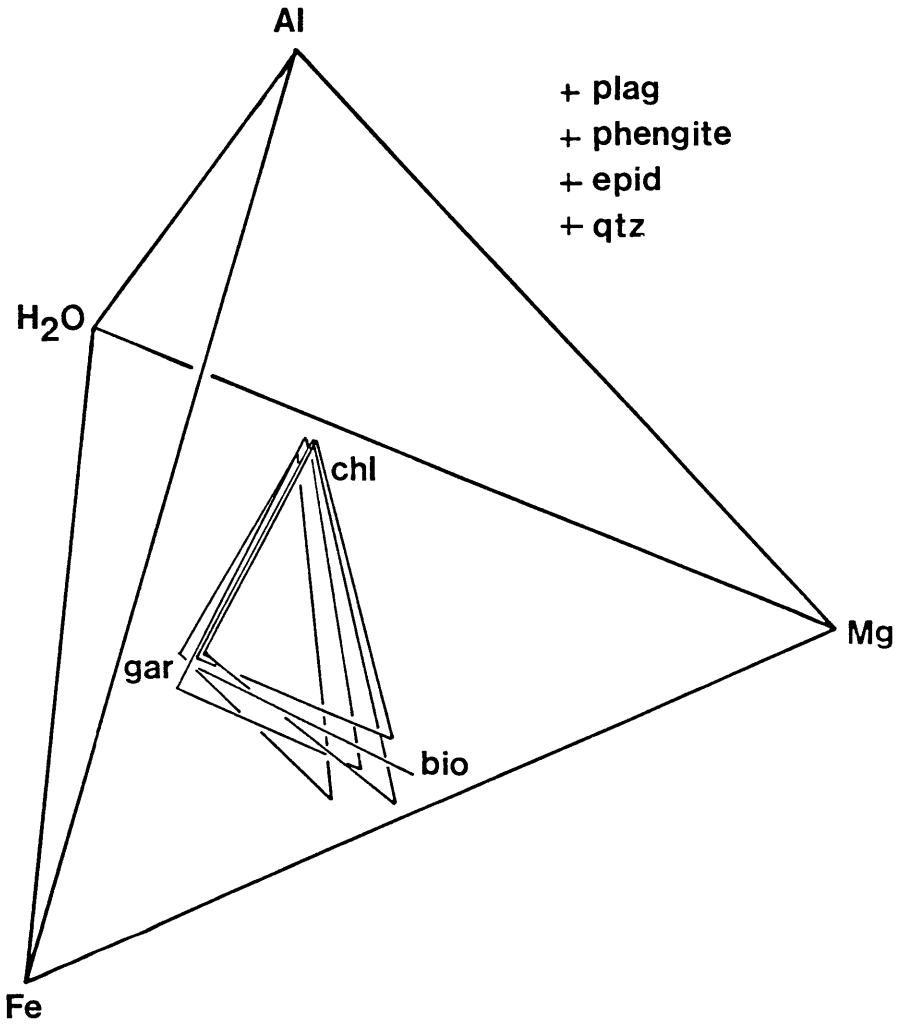
Al
+ plag
+ phengite
+ epid
+ qtz
H_2O
chl
gar
bio
Mg
Fe

Figure 4-6. Projection from An_{45} + phengite + quartz + H_2O into the tetrahedron Ca-Al-Fe-Mg. Consideration of Ca in this system results in removal of the crossing tielines for the assemblage Gar-Bio-Chl illustrated in Figures 4-4 and 4-5. Samples with the highest Ca contents contain margarite as an additional phase.

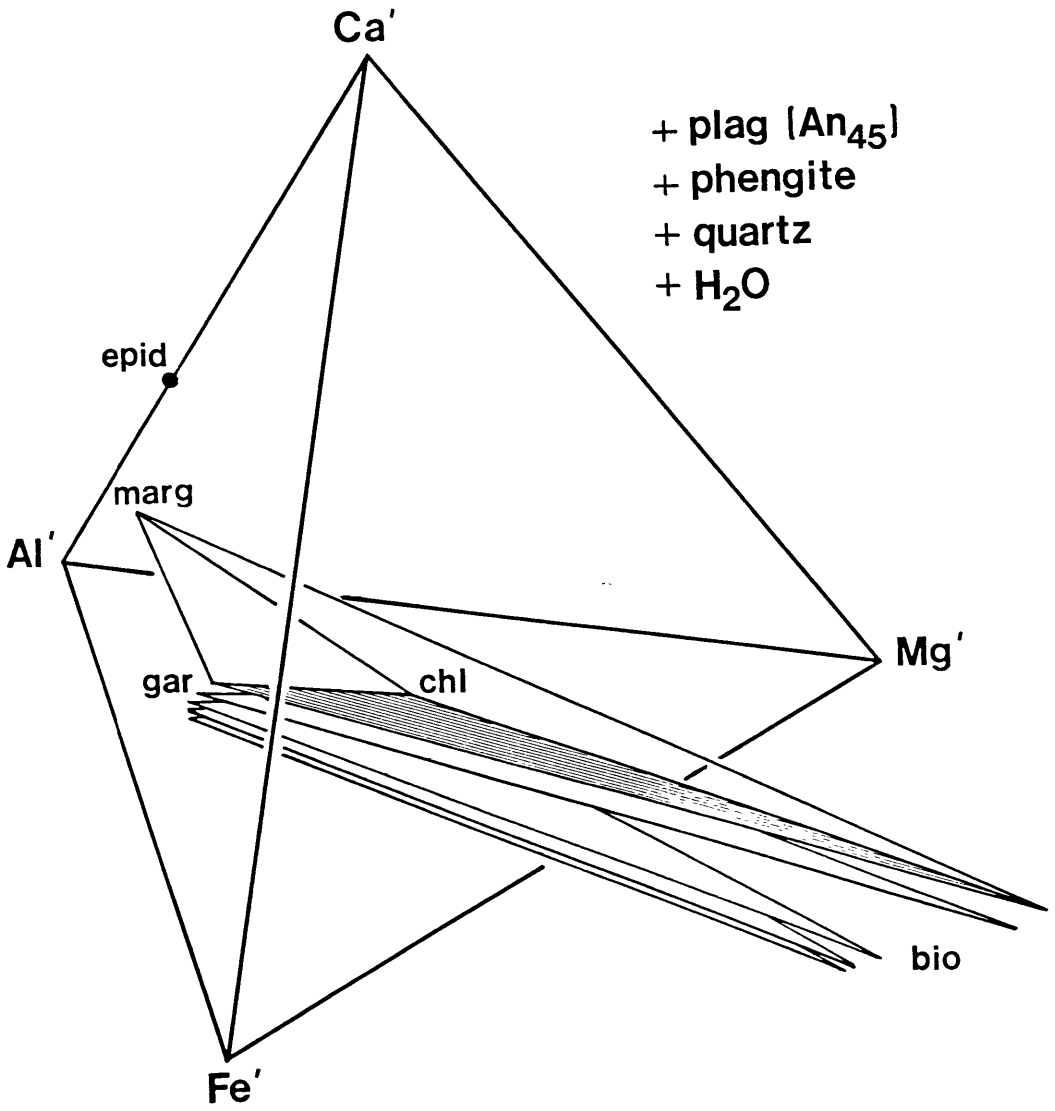
Ca'
+ plag [An45]
+ phengite
+ quartz
+ H2O
epid
marg
Al'
Mg'
gar
chl
bio
Fe'

present and defines the four-phase volume Marg-Gar-Bio-Chl. Epidote is also present in most samples, and is presumably stabilized by Fe^{3+} as an extra component. The absence of crossing tielines in this projection implies that Ca as an extra component has a major effect on the phase equilibria of these samples, and that the phase compositions are consistent with final equilibration of all samples at approximately the same P-T conditions.

(5) All of the samples under consideration were collected from within 1 km of one another along strike and 0.5 km across strike. There is little evidence for extensive post-metamorphic deformation of the USH, and these distances are unlikely to have been significantly greater at the time of final equilibration of the rock samples. It is thus also unlikely that the "peak" P-T conditions experienced by any one of these rocks were significantly different from those at any other locality within such a restricted area in a coherent tectonic unit. It <u>is</u> possible, however, that minerals in some samples maintained equilibrium longer than in other samples and resulted in the apparent disequilibrium relationships of Figure 4-4.

In summary, the consistency in calculated maximum temperatures (see below), the fact that diffusional reequilibration of Fe and Mg between garnet and biotite is notoriously slow at T<550-600°C (e.g. Hodges and Spear, 1981), and the removal of crossing tielines by consideration of Ca as an extra component all suggest that final equilibration occurred at approximately the same conditions in all samples examined in this study.

Temperature determinations.

Temperatures of final equilibration of the USH pelites were calculated using the garnet-biotite geothermometer of Ferry and Spear (1978), as modified by Hodges and Spear (1982). The results of these calculations for all samples are plotted as lines of constant K_D(Fe-Mg) in Figure 4-7; in the pressure interval from 4 to 8 kb, the calculated temperatures of final equilibration range from 450 to 500°C. At a model pressure of 6 kb, the mean temperature determined from 20 garnet-biotite pairs is 474°C, with a 1 σ uncertainty of ±15°C; maximum temperatures attained by the USH samples are conservatively quoted here as 475±25°C. No inclusions of biotite in garnet were observed, so it was not possible to obtain directly any information on the temperature conditions prevailing at the onset of garnet growth.

Pressure determinations.

Pressures of final equilibration have been calculated using the garnet-plagioclase-biotite-muscovite geobarometer of Ghent and Stout (1981), as modified by Hodges and Crowley (1985). This geobarometer is based on the partitioning of Ca between garnet and plagioclase as controlled by the reaction:

$$\underset{\text{grossular}}{Ca_3Al_2Si_3O_{12}} + \underset{\text{almandine-pyrope}}{(Mg,Fe)_3Al_2Si_3O_{12}} + \underset{\text{muscovite}}{KAl_3Si_3O_{10}(OH)_2} =$$

$$\underset{\text{anorthite}}{3CaAl_2Si_2O_8} + \underset{\text{biotite}}{K(Mg,Fe)_3AlSi_3O_{10}(OH)_2} \qquad (4\text{-}2)$$

The Hodges and Crowley (1985) calibration of this reaction takes into

Figure 4-7. Diagram showing lines of constant K_D for graphitic schists of the USH, determined from the garnet-biotite geothermometer of Ferry and Spear (1978), as modified by Hodges and Crowley (in press). Average temperature of equilibration at 5-6 kb is 475°C. Al_2SiO_5 triple point of Holdaway (1971) is shown for reference.

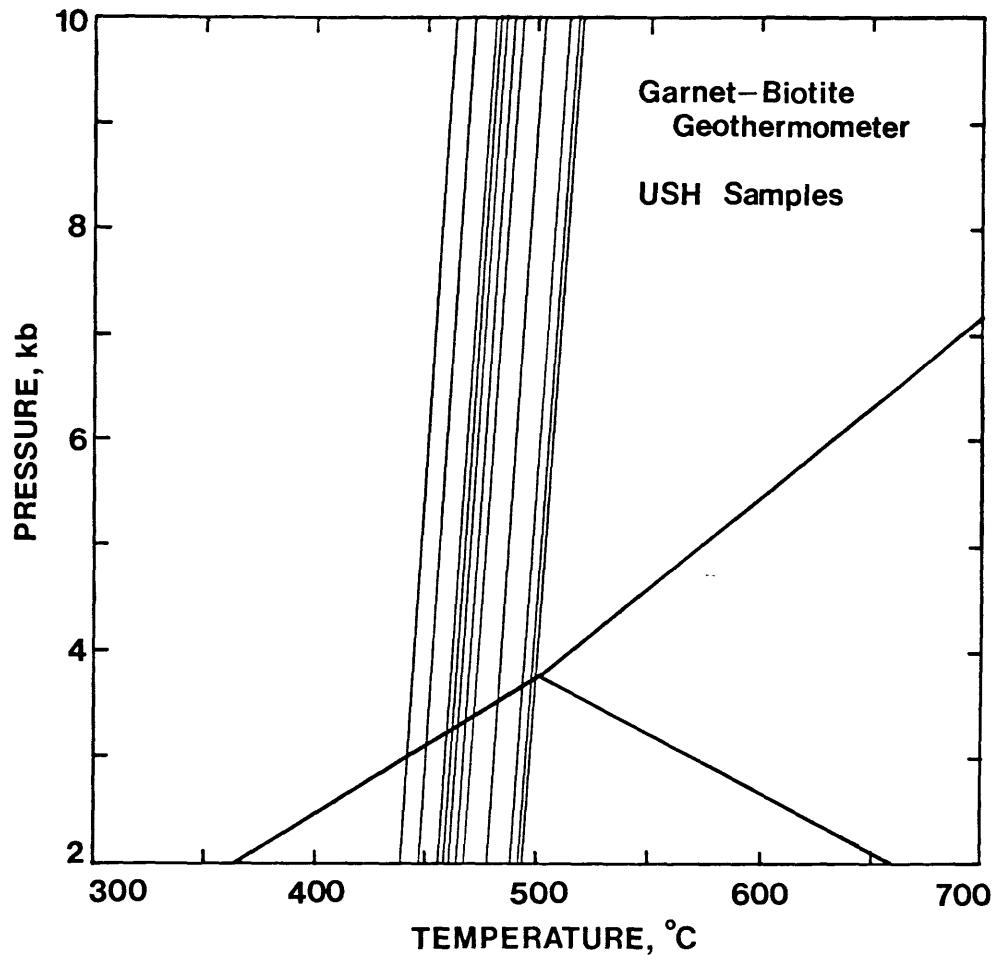
Garnet–Biotite
Geothermometer
USH Samples
PRESSURE, kb
10
8
6
4
2
300
400
500
600
700
TEMPERATURE, °C

Figure 4-8. Diagram showing lines of constant Ca partitioning between garnet and plagioclase, as determined from the garnet-plagioclase-biotite-muscovite geobarometer of Hodges and Crowley (in press). The solid lines represent edge compositions of adjacent garnet and matrix plagioclase grains. Dashed lines are determined from adjacent edges in sample HF-17A. Dot-dashed lines are from inclusions of plagioclase and white mica in garnet in sample HF-17A.

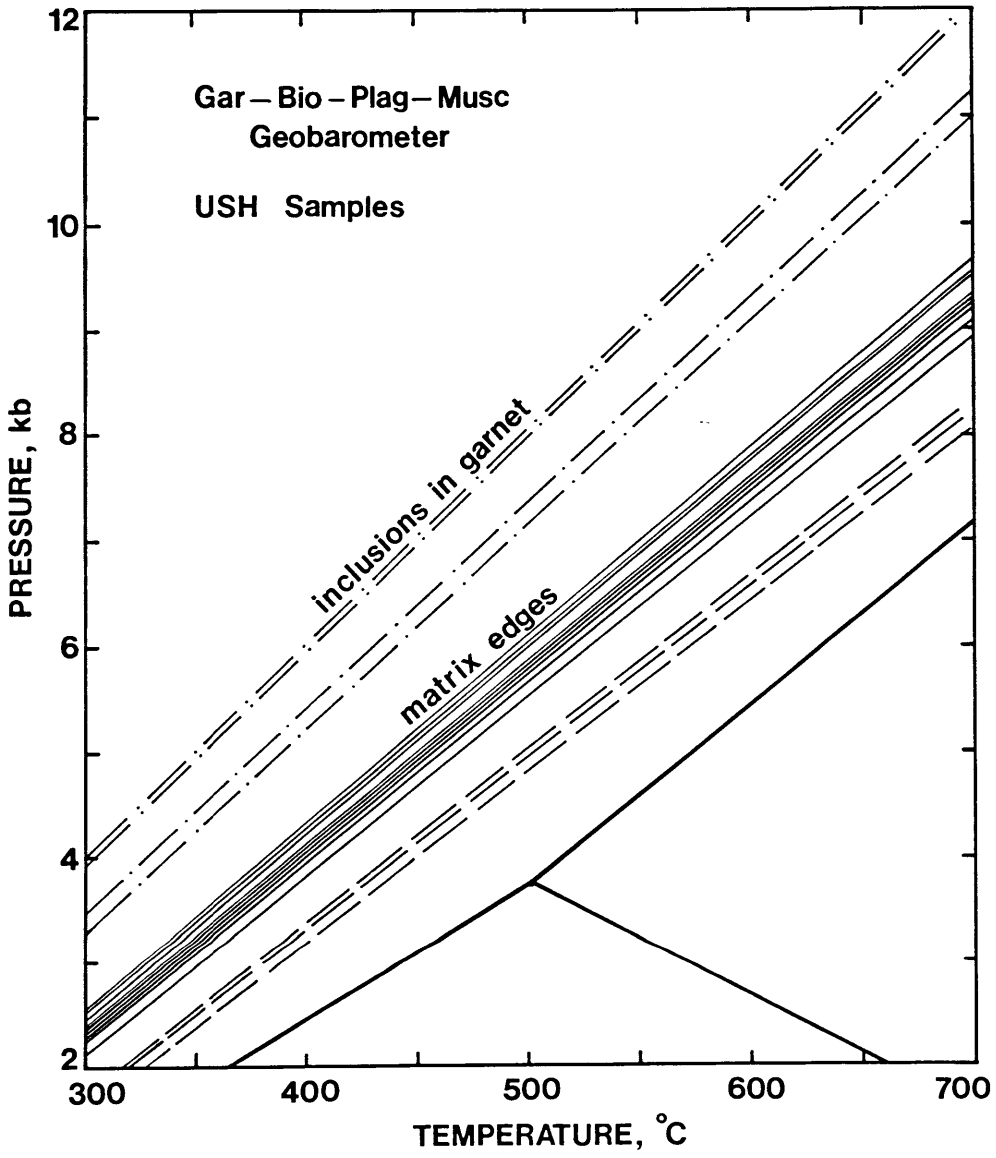
Gar – Bio – Plag – Musc
Geobarometer
USH Samples
inclusions in garnet
matrix edges
PRESSURE, kb
TEMPERATURE, °C
12
10
8
6
4
2
300
400
500
600
700

account the excess volume of mixing of grossular component in garnet and incorporates non-ideal mixing models for both garnet and plagioclase; all other activity-composition relations are as given in Hodges and Royden (1984). The same arguments concerning diffusional reequilibration of Ca between garnet and plagioclase that were discussed in Chapter 3 for the garnet-plagioclase-kyanite-quartz geobarometer also apply here.

Lines of constant K_D(Ca) were computed for 18 coexisting Gar-Plag(An_{43-50})-Bio-Pheng assemblages in 5 samples for which complete compositional data were obtained, and the total range is shown by the 9 solid lines in Figure 4-8. At 475°C, these K_D lines fall between 5.0 and 6.0 kb. The three dashed lines in the figure represent all of the edge compositional data for sample HF-17A and indicate pressures of 4.0-4.5 kb at 460-475°C (temperatures of final equilibration calculated from this sample also fall at the low end of the range illustrated in Figure 4-7). Although this pressure difference is not statistically significant in light of an uncertainty of approximately ±2.0 kb (Hodges and Crowley, 1985), the fact that it is consistent and reproducible requires some discussion. HF-17A is the structurally highest sample collected in this suite, so the lower pressures of equilibration could be real, although a pressure difference of 1.0 kb between HF-17A and the remaining samples would imply a vertical separation of 3-4 km, in contrast to the ~0.5 km presently separating the rocks in the field. An alternative explanation that could account for the unifomly lower pressures calculated from this sample is simply that garnet growth and equilibration with the remaining phases continued over a greater portion of the uplift history than in the other samples of this suite; in this case, the calculated pressures

need not necessarily represent a significant difference in depth of burial among the samples. It is not possible to distinguish absolutely between these two hypotheses, but in light of the different assemblage preserved in sample HF-17A, it is likely that reaction mechanisms differed from those in the other pelites and hence that the second hypothesis is the more probable.

The dot-dashed lines plotted in Figure 4-8 represent lines of constant K_D determined from plagioclase (An_{17-24}) and muscovite inclusions located approximately halfway between the cores and rims of garnets in sample HF-17A. No biotite inclusions were present in these garnets, so matrix biotites were used instead in determining pressures for the inclusion suite; because the geobarometer is quite insensitive to changes in Fe/Fe+Mg ratios in biotite or garnet, this introduces little additional uncertainty into the calculations. It is apparent from these K_D lines that entrapment of the inclusion suite by the growing garnet occurred at higher P (up to 7.5 kb) and/or lower T than equilibration of the matrix assemblage. This conclusion is reinforced by the results of the garnet zoning analysis presented below.

Quantitative modeling of zoned minerals.

Quantitative P-T paths of garnet growth have been determined by utilizing the technique of Spear and Selverstone (1983; see also discussion in Chapter 3) for three of the USH pelites. Samples HF-6A and HF-27B both contain the assemblage Gar-Bio-Chl-Pheng-Plag-Epid-Qtz, which, in the presence of a fluid phase, is trivariant in the model system CNKFMnMASH; sample HF-17A contains hornblende as an additional

Figure 4-9. Representative zoning profiles of garnets in graphitic schists of the USH. Top: sample HF-6A; bottom: sample HF-27B. Locations of the line traverses are shown in Figure 4-1. The dotted lines divide the garnets into growth zones (denoted by capitol letters) that can be correlated between garnets from different samples. See text for further discussion.

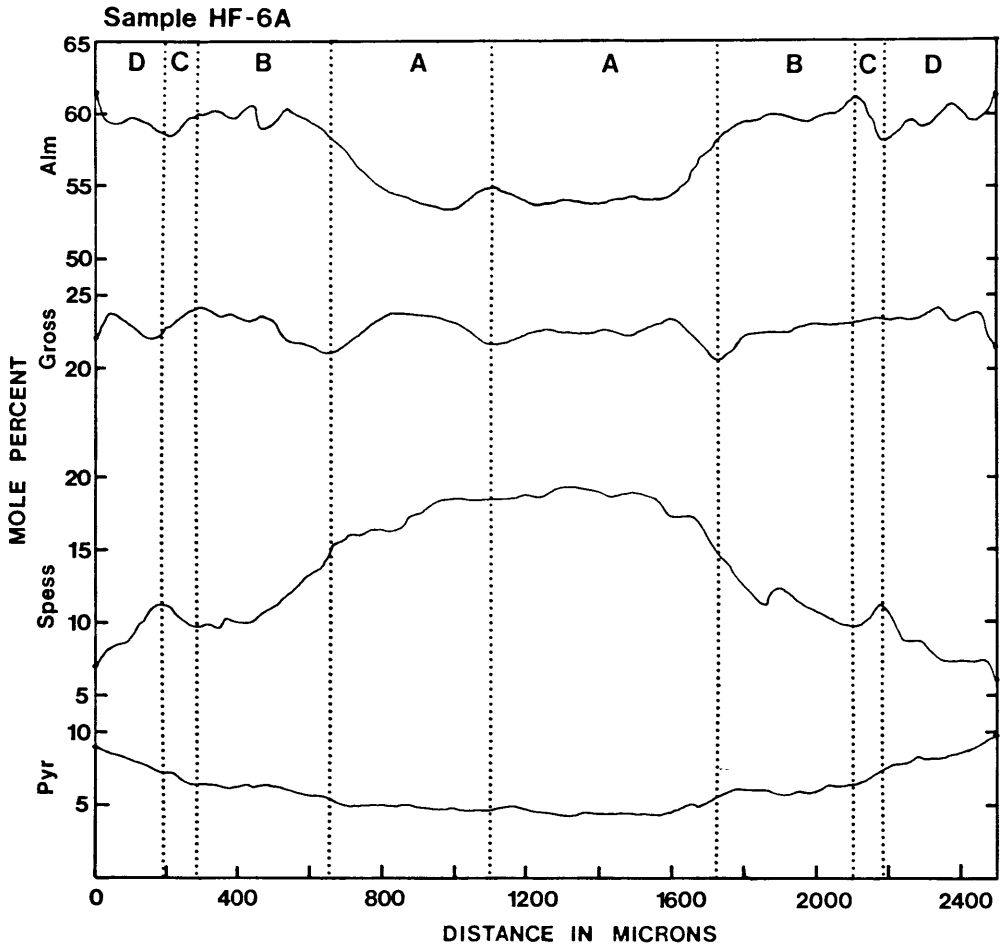
Sample HF-6A
D
C
B
A
A
B
C
D
Alm
Gross
Spess
Pyr
MOLE PERCENT
65
60
55
50
25
20
20
15
10
5
10
5
0
400
800
1200
1600
2000
2400
DISTANCE IN MICRONS

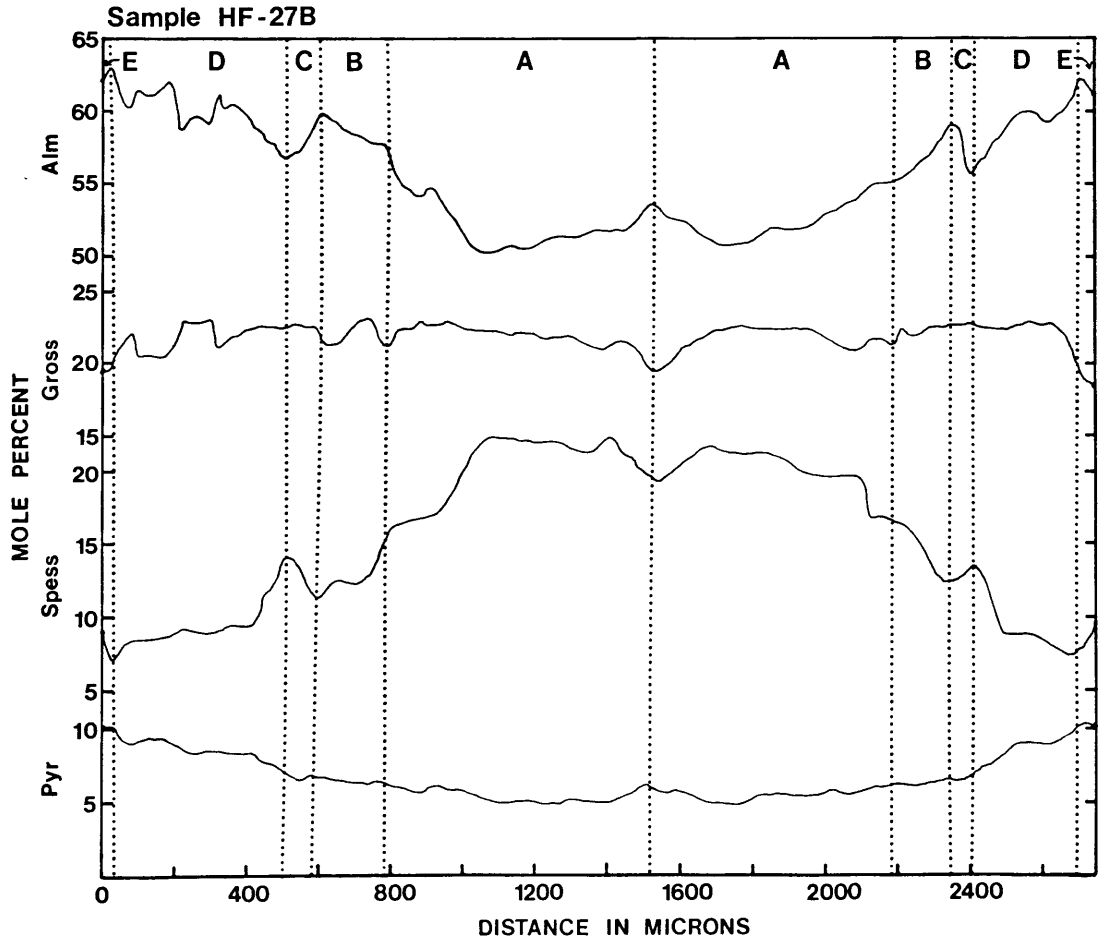
Sample HF-27B
E
D
C
B
A
A
B
C
D
E
Alm
Gross
Spess
Pyr
MOLE PERCENT
65
60
55
50
25
20
15
20
15
10
5
10
5
0
400
800
1200
1600
2000
2400
DISTANCE IN MICRONS

phase within this system and is hence divariant. (Note that margarite is also present in both HF-6A and HF-27B, but rarely occurs in garnet-bearing layers, and hence has not been considered in the calculations that follow). Algebraic modeling of the 9-component system suggests that garnet growth and zonation was controlled by the continuous reaction:

$$\text{Chlorite} + \text{Phengite} + \text{Epidote} + \text{Quartz} \rightarrow$$
$$\text{Garnet} + \text{Biotite} + \text{Plagioclase} + H_2O + O_2 \qquad (4\text{-}3)$$

Phengite, epidote, and quartz inclusions are common in garnet, and there is no evidence in any of these samples for an assemblage change at any time during the growth history of garnet. There is also no evidence for partial resorption of garnet due to back reaction during the period of net garnet growth.

Zoning profiles of two of the garnets utilized in the modeling calculations are shown in Figure 4-9 and are based on microprobe analyses taken at 4-8 μm intervals. Despite the overall complexity of the zonation, there is a remarkable similarity between the garnet profiles for samples HF-6A and HF-27B, which contain the same assemblage. The vertical dotted lines in Figure 4-9 divide these garnets into growth zones that can be correlated between the two samples: A extends from the core to a point of reversal in the Ca profile, B continues to a trough in Mn and corresponding high in Fe content, C to a trough in Fe and peak in Mn, and D continues out to the rim in sample HF-6A, which is marked by high Fe and low Ca and Mn contents; in sample HF-27B there is an additional thin rim, E, that is characterized by reversals in the Fe and Mn trends. For the sake of simplicity, only these

Table 4-2

Mineral compositions utilized in quantitative modeling of assemblages

Phase Component	HF-6A			HF-17A			HF-27B		
	$X_{i,rim}$	$X_{i,core}$[1]	$X_{i,calc}$[2]	$X_{i,rim}$	$X_{i,core}$	$X_{i,calc}$	$X_{i,rim}$	$X_{i,core}$	$X_{i,calc}$
Quartz	1.000	-	-	1.000	-	-	1.000	-	-
Water	1.000	-	-	1.000	-	-	1.000	-	-
Muscovite	1.000	-	-	1.000	-	-	1.000	-	-
Clinozoisite	1.000	-	-	1.000	-	-	1.000	-	-
Anorthite	0.440	0.375	0.368	0.490	0.175	0.142	0.460	0.375	0.412
Albite	0.560	0.625	0.632	0.510	0.825	0.858	0.540	0.625	0.588
Almandine	0.614	0.545	0.545*	0.658	0.628	0.628*	0.614	0.523	0.523*
Pyrope	0.093	0.047	0.047	0.075	0.061	0.061	0.098	0.055	0.055
Grossular	0.220	0.228	0.228*	0.165	0.205	0.205*	0.196	0.191	0.191*
Spessartine	0.073	0.180	0.180*	0.102	0.106	0.106	0.091	0.231	0.231*
Phlogopite	0.583	-	0.458	0.506	-	0.484	0.590	-	0.496
Annite	0.414	-	0.531	0.491	-	0.573	0.407	-	0.493
Mn Biotite	0.003	-	0.011	0.003	-	0.003	0.003	-	0.011
Clinochlore	0.620	-	0.494	0.548	-	0.523	0.618	-	0.522
Daphnite	0.374	-	0.484	0.448	-	0.474	0.376	-	0.456
Mn Chlorite	0.006	-	0.022	0.004	-	0.004	0.006	-	0.022
Mg Hornblende	-	-	-	0.359	0.360	0.348	-	-	-
Fe Hornblende	-	-	-	0.638	0.637	0.648	-	-	-
Mn Hornblende	-	-	-	0.003	0.003	0.003	-	-	-

[1] Core compositions reported only for zoned phases. [2] Predicted compositions of phases in equilibrium with the garnet core, calculated according to the method of Spear and Selverstone (1983); these values should be compared with the measured core compositions of the phases.
* Component used as monitor parameter in the modeling calculations. Thermodynamic data for the phase components are given in Table 3-7.

Figure 4-10. Pressure-temperature diagram showing P-T paths calculated from quantitative modeling of zoned garnets in the assemblages Gar-Bio-Chl-Pheng-Plag-Epid-Qtz-H_2O (samples HF-6A and HF-27B) and Gar-Bio-Chl-Pheng-Hbl-Plag-Epid-Qtz-H_2O (sample HF17A). See text for discussion of technique. Large symbols correspond to P-T conditions calculated from compositional increments specified in the model, small dots are from finite-difference calculations between increments. Letters A through E correlate with the compositional zones shown in Figure 4-9 for samples HF-6A and HF-27B; note excellent agreement between paths calculated for these two samples.

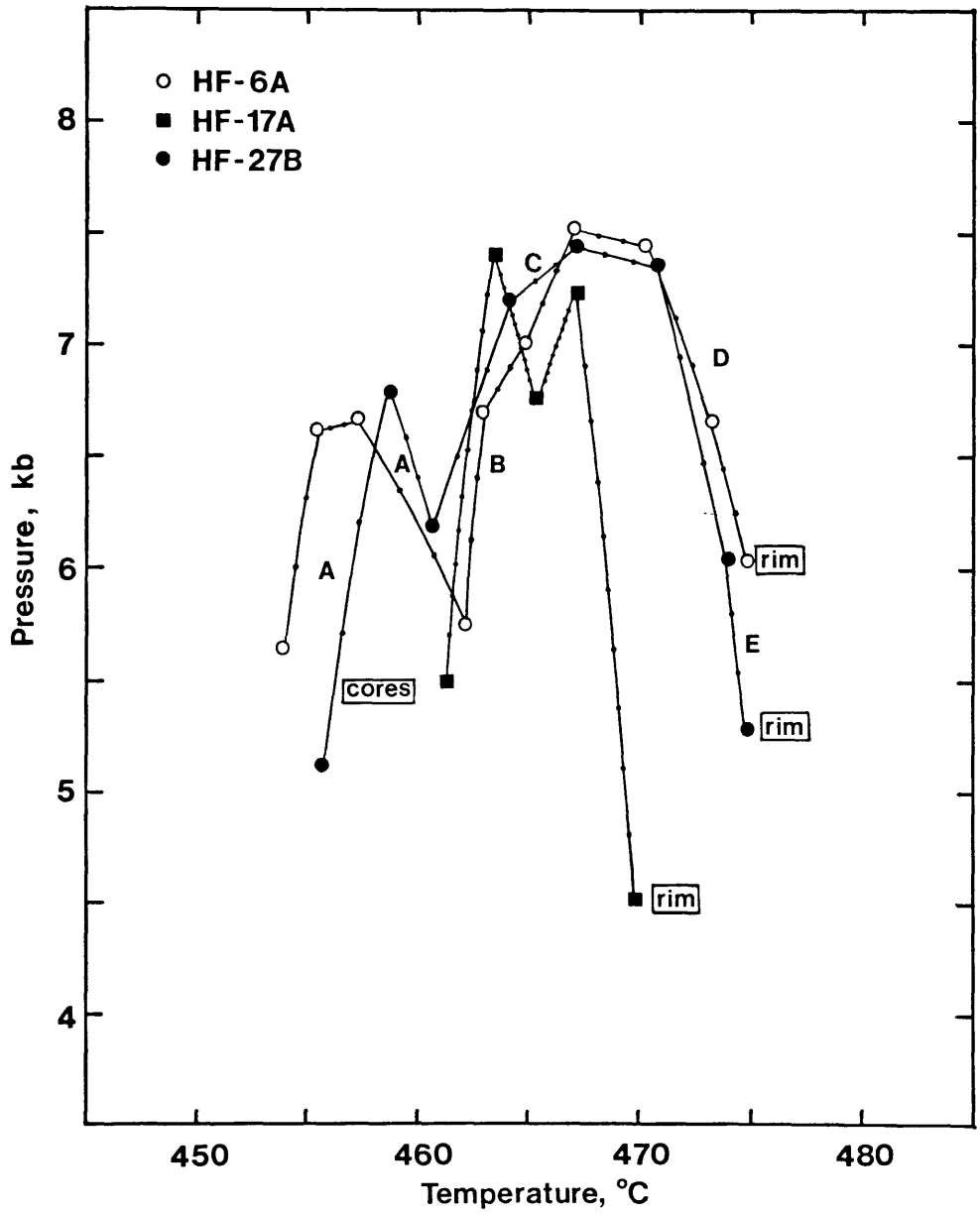
HF-6A
HF-17A
HF-27B
Pressure, kb
8
7
6
5
4
450
460
470
480
Temperature, °C
A
A
B
C
D
E
cores
rim
rim
rim

major reversals have been noted, but several other correlations between the profiles can be observed and were used as increments in the path calculations. No such correlations are obvious in the garnet profile of sample HF-17A, which contains a different mineral assemblage.

Starting conditions, e.g. conditions of final equilibration of the garnet rims, were assumed to be the average pressures and temperatures calculated previously for each of the samples. These values are: ~475°C, 6.0 kb (HF-6A), ~475°C, 5.25 kb (HF-27B), and ~470°C, 4.5 kb (HF-17A). Edge compositions of all other phases in the modeled assemblage are listed in Table 4-2. For the trivariant assemblages, three monitor parameters among the eight independently variable phase components (ΔX_{alm}, ΔX_{gross}, ΔX_{spes}, ΔX_{An}, ΔX_{FeBio}, ΔX_{MnBio}, ΔX_{FeChl}, and ΔX_{MnChl}) need to be specified, and the three garnet components were selected. This allows ΔX_{An} to be calculated as a dependent variable and the results compared with plagioclase zoning profiles in samples HF-6A and HF-27B. Only two monitor parameters must be specified in a divariant assemblage, and ΔX_{alm} and ΔX_{gross} were chosen in sample HF-17A. Zoned plagioclase and unzoned hornblende served as checks on the calculations in this sample.

The P-T paths calculated from the garnet zoning profiles in these three samples are shown in Figure 4-10, and a striking similarity among the trajectories is evident. In each case, four pressure-temperature regimes of garnet growth are apparent: (1) initial growth in response to an approximately isothermal pressure increase; (2) decompression accompanied by minor heating; (3) increased burial with concomitant heating; and (4) a final stage of decompression and heating that terminates at the presumed conditions of final equilibration. The maximum pressure

attained during the interval of garnet growth is ~7.5 kb, which is considerably lower than the 10 kb determined from garnet zoning in the LSH. Despite the differences in calculated P_{max} and overall length of the paths, however, similar stages of garnet growth can be recognized in both the LSH and USH, and it is tempting to correlate the paths in time. It was noted in Chapter 3 that reversals in trend of the calculated P-T paths could represent the response to emplacement of structurally higher nappes or thrust sheets, or they could simply reflect the level of resolution of the garnet zoning technique. The reproducibility of these reversals in rocks with different assemblages in both the LSH and USH strongly supports the argument that these are real features with tectonic significance, and also implies that the LSH and USH shared a common history throughout the time of garnet growth. This is discussed at length in the following chapter on the imbrication history of these units, but requires further assessment of the uncertainties in the calculated paths.

A rigorous error analysis of the garnet zoning technique is in progress, but is not yet sufficiently advanced to permit numeric evaluation of the uncertainties. Several geologic lines of evidence can be used to constrain the results, however. One of these is that the trajectories calculated above from different rocks with different mineral assemblages are remarkably similar to one another, yet are quite unlike paths calculated from rocks from other tectonic settings (see Spear and Selverstone, 1983, and Spear et al., 1984). Two other more quantitative checks on the method are discussed below.

(1) Agreement between the predicted and measured core compositions of phases thought to have maintained equilibrium with garnet throughout

its growth is a necessary, though not sufficient, test of the modeling technique. The calculated core compositions of plagioclase ± hornblende are compared with the measured values in Table 4-2; in each case, the trend of the plagioclase zonation is correct, although the magnitude of the predicted zonation in some instances exceeds the measured amount. This may reflect errors in the thermodynamic data or solution models used in the technique; alternatively, it could indicate only that the microprobe analyses were not obtained on center cuts of three-dimensional grains and hence underestimate the total amount of chemical zonation present. Modeling of the garnet zonation in samples HF-6A, 17A, and 27B results in reversals in the calculated plagioclase zoning, which are not indicated in Table 4-2; in each case, however, these reversals agree in trend with the complex reversals in anorthite content observed in these samples. As an example, the calculated plagioclase profile in HF-6A zones from An_{44} at the rim to an intermediate value of An_{28} and finally to An_{32} in the core. The observed zoning in matrix plagioclase in this sample is from An_{44} to a low of An_{29} and a core composition of An_{37} (see Table 4-6). No plagioclase inclusions in garnet were observed in this sample, so a more detailed comparison of the zoning is not possible. Hornblende in sample HF-17A is unzoned, whereas the model predicts an increase in the Fe/Fe+Mg ratio of 0.01 from rim to core; this represents an excellent agreement, particularly in light of the simplified thermodynamic mixing models used for calcic amphiboles in the calculations.

(2) An additional check on the modeling calculations comes from comparing the pressures obtained at various points along the path with those obtained from geobarometry on plagioclase inclusions within garnet

in HF-17A. Plagioclase inclusions in this sample are located approximately midway across the modeled garnet traverse, and the pressures obtained from standard geobarometry at temperatures of 450-475°C range from 6.25 to 7.5 kb (see Figure 4-8). The garnet zoning technique yields pressures of 6.8 to 7.5 kb at corresponding points along the traverse, in addition to reproducing the plagioclase compositions.

The good agreement between the model results and the data presented above suggest that the garnet zoning technique can be applied reliably to these samples. One source of uncertainty that has not yet been addressed, however, is the effect of reduced activities of H_2O on the magnitude of the calculated P-T paths. The zoning calculations, as currently formulated, do not take into account the possibility of changing composition of a multicomponent fluid phase, although this could have an important effect on phase equilibria in graphitic schists. One approach to this problem has been proposed by Spear (personal communication) and involves removing the Gibbs-Duhem equation for H_2O (see Spear and Selverstone, 1983) from the modeling calculations. This removes consideration of H_2O as a phase and permits monitoring of changes in $\mu(H_2O)$ in a multicomponent (i.e. C-O-H) fluid phase, but also has the effect of increasing the apparent thermodynamic variance of the system by 1. This requires the use of 3 monitor parameters to model sample HF-17A; the resultant path shows the same reversals as the path calculated previously, but with P_{max}=6.8 kb instead of 7.5 kb and ΔT=65° instead of 10°C. Four monitor parameters (e.g. ΔX_{An} in addition to the 3 garnet parameters) are needed to model samples HF-6A and HF-27B with this approach, and it is thus only possible to calculate rim to core P-T paths. These paths have approximately the same slope as rim-core paths

calculated assuming water is present as a phase, but are considerably longer. In fact, they indicate onset of garnet growth at conditions of 300-350°C and 3 to 3.5 kb. These conditions are below those of typical garnet isograd reactions (e.g. Turner, 1981), and imply the unlikely scenario of garnet growth in a constant assemblage over a temperature interval of ~175°C. In addition, these P-T paths do not enter the lawsonite stability field, whereas there is abundant evidence in the interlayered greenstones for the early presence of lawsonite (see section on greenstone lithologies).

In light of these results, the model system with H_2O as a phase has been retained; this is equivalent to assuming that $X(H_2O)$ (but not necessarily $\mu(H_2O)$) in the fluid phase remained approximately constant throughout the period of garnet growth. The calculations discussed above for sample HF-17A suggest that the reversals in trend of the P-T paths are real and cannot be ascribed to inaccurate assumptions regarding the fluid phase during metamorphism, although uncertainties in the net values of ΔT and ΔP may result from these assumptions. Addition of a Redlich-Kwong model for mixing in multicomponent fluids to the garnet zoning technique of Spear and Selverstone (1983) remains a goal of future research. At the present time, however, the consistency of predicted and measured mineral compositions noted above and the excellent agreement between the pressures determined from garnet zoning and those obtained from geobarometry on plagioclase inclusions in garnet suggest that the magnitudes of the P-T trajectories calculated for the USH are meaningful.

Fluid inclusions.

Fluid inclusions are abundant in quartz-rich layers in several of the USH pelites and belong to several texturally distinct parageneses (see Figure 4-11) for which a relative chronology of entrapment can be established. The oldest inclusions (Type I) occur in isolated clusters in the cores of grains and are obliterated near grain boundaries; texturally, they appear to predate the final recrystallization of quartz in these samples. The grain boundaries themselves are lined with what appear to be decrepitated fluid inclusions; Type II inclusions occur in clusters or along healed fractures that terminate adjacent to these grain boundaries and may represent reentrapment of fluids originally present in the decrepitated grain boundary inclusions. Type II inclusion clusters overprint Type I inclusions where present in the same grain. The texturally youngest inclusions (Type III) occur along healed fractures that generally crosscut grain boundaries and both other inclusion types.

Compositions and densities of over 75 Type I and Type III inclusions in sample HF-3C were measured using microthermometric techniques. This sample was selected for analysis because it contains all inclusion types observed in the complete USH suite and because the coarse-grained quartz in HF-3C minimized the sample preparation problems encountered with finer-grained specimens. The microthermometric data for these inclusions are summarized in Table 4-3. No Type II inclusions are discussed because their complex phase relations in the system H_2O-CO_2-CH_4-NaCl precluded accurate determination of compositions and densities. Type I inclusions are composed of a dense H_2O-CO_2 mixture with no evidence for CH_4 or NaCl components. Several generations of Type III inclusions are present and are composed dominantly of H_2O-CO_2-NaCl mixtures, with some younger fractures containing CO_2-CH_4 fluids. One set of

Figure 4-11. Sketches illustrating the different types (I through III) and generations (1 to 4b) of fluid inclusions observed in sample HF-3C. I = isolated inclusions in core of quartz grain; black = decrepitated inclusions. II = inclusions adjacent to decrepitated grain boundary inclusions, and inclusions along healed crack that terminates at grain boundary. III = late-stage inclusions along fractures that cross grain boundaries. Note varying ratios of CO_2 to H_2O in 3-phase inclusions of generations 4a and 4b along the same fracture. Long dimension of each sketch is ~100 μm.

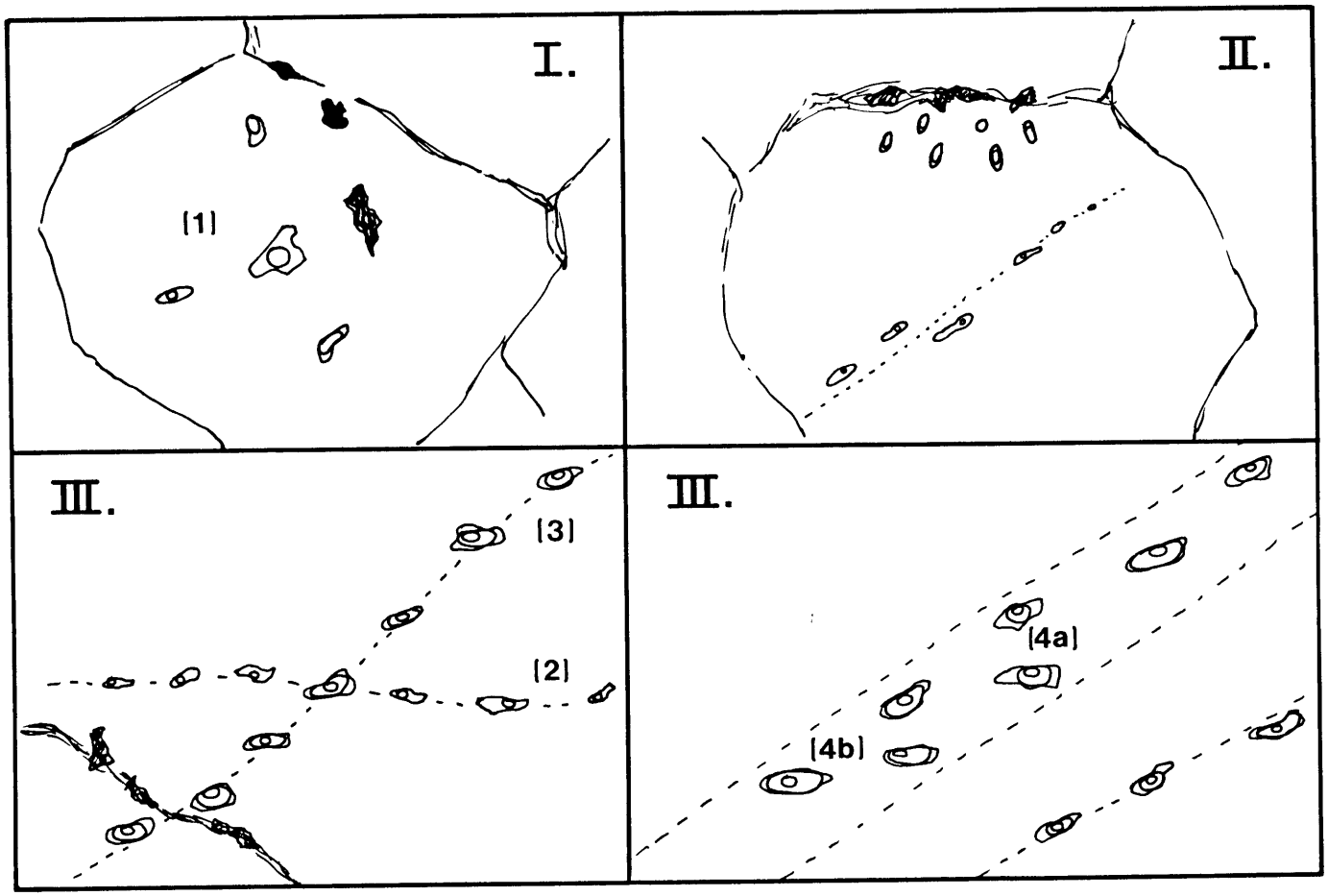
I.
[1]
II.
III.
[3]
[2]
III.
[4a]
[4b]

parallel fractures contains inclusions with two different H_2O:CO_2 ratios, although the calculated CO_2 density (0.73 g cm^{-3}) and salt content (~6.5 wt % NaCl) are the same regardless of the amount of CO_2 present; this is evidence for the simultaneous entrapment of immiscible fluids in the system H_2O-CO_2-NaCl. For 6 wt % NaCl, the solvus crest in this system is at ~400°C (Gehrig, 1980, as cited in Bowers and Helgeson, 1983), implying entrapment of these inclusions in the two-phase field at T<400°C.

Isochores for the different generations of fluid inclusions were constructed from the data of Potter and Brown (1977) and Swanenberg (1979), and from a modified Redlich-Kwong equation of state as incorporated in the program ISOCHORE (Holloway, 1981); the results are shown in Figure 4-12. The slopes of isochores for immiscible H_2O-CO_2-NaCl inclusions have been calculated assuming X_{NaCl}=0; this simplification is thought to be justified since the addition of up to a few weight percent NaCl does not significantly affect bulk molar volumes in the multicomponent system (Bowers and Helgeson, 1983), and thus should have little effect on isochore slopes.

The isochore for the oldest inclusions present (Generation 1) passes just to the high-pressure (6.0-6.5 kb) side of the box for final equilibration conditions determined by geothermometry/barometry, confirming the textural evidence that these are early inclusions that predate the final stages of recrystallization of quartz grain boundaries. For comparison with these inclusions, the composition of the fluid phase expected to be in equilibrium with graphite at 475°C, 6.2 kb was calculated according to the method of Ohmoto and Kerrick (1977), using fugacity coefficients from the following sources: H_2O, Burnham et al. (1969);

Table 4-3

Summary of fluid inclusion data

Type	Gen	n	T_m CO_2	T_m ice	T_m clath	T_H	V_B	Composition†
I	1	13	-56.8±0.2	-0.1±0.1	+9.5±0.5	+5.8 to 7.0 (L)	25	H_2O(75)-CO_2(25)
III	2	9		-4.2±0.2		+222 to 225 (L)	0.89*	H_2O + 6.7% NaCl
III	3	8	-56.7±0.2	≃ -2	+7.2	+23.3±0.2 (L)	35	H_2O(60)-CO_2(40) + 5% NaCl
III	4a	9	-56.9±0.2	≃ -4	+6.7±0.2	+23.2±0.2 (L)	37	H_2O(80)-CO_2(20) + 6.5% NaCl
III	4b	7	-56.9±0.2	?	+6 to 7	+24.0±0. (L)	45	H_2O(40)-CO_2(60) + 6.5% NaCl
III	5	13	-57.0±0.2			+21.8±0.4 (crit)	38	CO_2(90)-CH_4(10)

Gen = generation; n = number of inclusions analyzed; T_m = melting temperature of CO_2, ice, and clathrate (CO_2•5.75 H_2O) phases in multicomponent inclusions, °C; T_H = homogenization temperature in °C of CO_2 or H_2O-rich fluid (no total H_2O+CO_2 homogenization temperatures were obtaind due to decrepitation of the inclusions; V_B = average bulk molar volume, cm^3 mol^{-1}; * indicates density in g cm^{-3}.

†Weight percent NaCl determined from freezing point depression of aqueous phase, where observable, and from clathrate melting temperatures. Composition and density of CO_2-CH_4 inclusions determined according to the method of Burruss (1981).

Figure 4-12. Isochores for one generation of early fluid inclusions (#1) and five sets of late-stage fluid inclusions (2 to 5); sequential isochore numbers correspond to decreasing age of entrapment of the inclusions. Generations 4a and 4b represent simultaneous entrapment of immiscible H_2O-CO_2-NaCl fluids, and hence must have been entrapped at the point of intersection of their isochores. The rectangular box indicates the approximate uncertainty in location of this intersection. The box marked "peak" represents the P-T conditions of final equilibration of the mineral assemblage. A possible uplift path consistent with the petrologic and fluid inclusion data is indicated by the dashed curve.

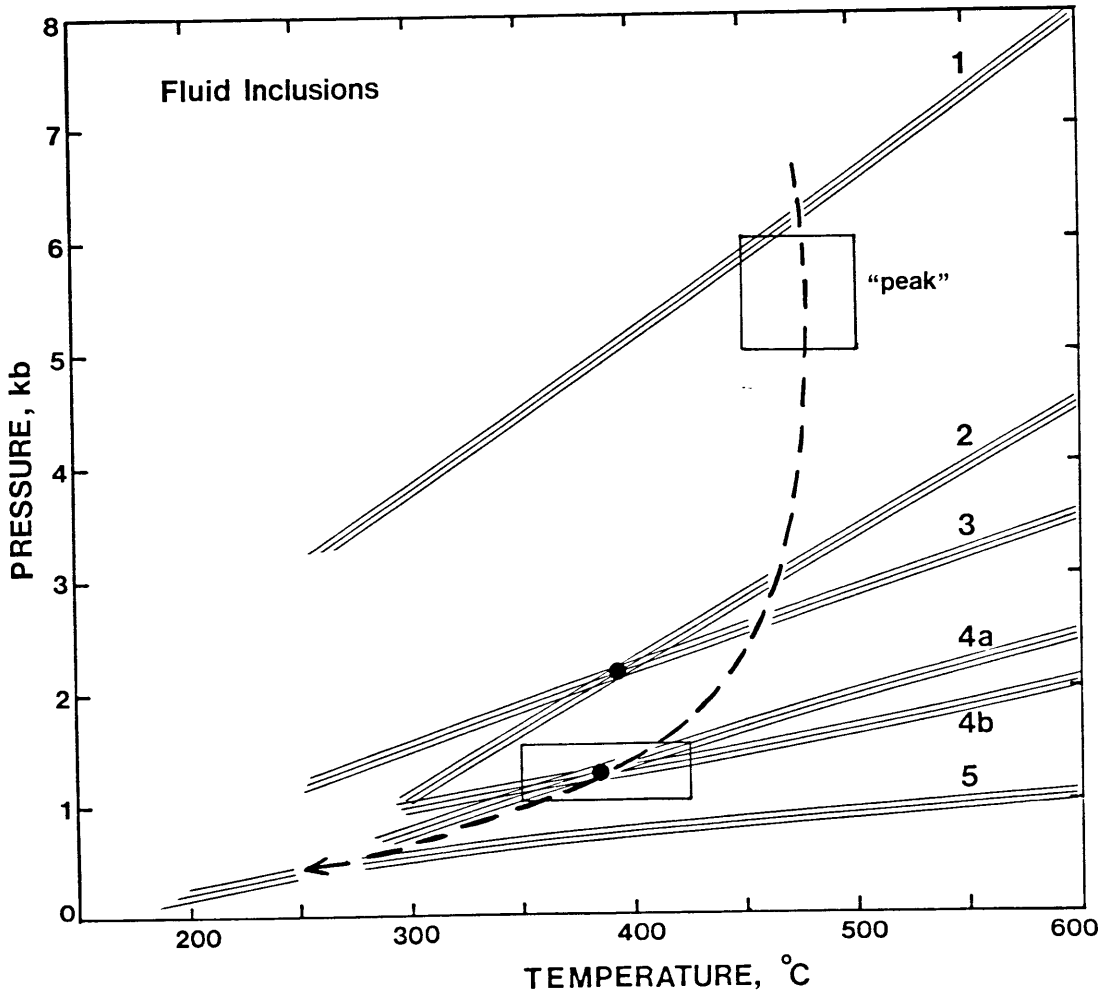
Fluid Inclusions
1
"peak"
2
3
4a
4b
5
PRESSURE, kb
TEMPERATURE, °C
0
1
2
3
4
5
6
7
8
200
300
400
500
600

CO_2, Shmulovich and Shmonov (1975); CH_4, CO, H_2, and O_2, Ryzhenko and Volkov (1971). The fugacity of oxygen was assumed to be controlled by the presence of graphite and the stability of calcite + rutile + quartz (see Ohmoto and Kerrick, 1977); at the P and T of interest, these equilibria constrain f_{O2} to the range 10^{-25} to 10^{-24} bars. Using these data and the equilibrium constant terms given by Ohmoto and Kerrick (1977), the total pressure equation (assuming $P_{total} = P_{fluid}$):

$$P_{total} = \frac{f_{H_2O}}{\gamma_{H_2O}} + \frac{f_{CO_2}}{\gamma_{CO_2}} + \frac{f_{CH_4}}{\gamma_{CH_4}} + \frac{f_{CO}}{\gamma_{CO}} + \frac{f_{H_2}}{\gamma_{H_2}} + \frac{f_{O_2}}{\gamma_{O_2}} \qquad (4\text{-}4)$$

was solved for the fugacities of the fluid components at P and T; the mole fractions of each of the components in the fluid phase were derived from the relationship:

$$X_i = \frac{(f_i)_{P,T}}{(\gamma_i)_{P,T} P_f} \qquad (4\text{-}5)$$

At 475°C, 6.2 kb, the composition of the fluid phase calculated to be in equilibrium with the graphitic schists is X_{H2O}=0.944, X_{CO2}=0.048, X_{CH4}=0.008, whereas the composition of the fluid preserved in fluid inclusions of Generation 1 is X_{H2O}=0.75, X_{CO2}=0.25. Even allowing for considerable errors in the fluid inclusion measurements and calculations, this is a large discrepancy that suggests that the fluid in the inclusions was not in equilibrium with the host pelites. This would indicate either that the inclusions represent entrapment of a fluid phase generated in the neighboring calcareous schists, or that the fluid was in equilibrium with the pelites, but was entrapped at earlier

P-T conditions elsewhere along the isochore. It is not possible to distinguish conclusively between these possibilities on the basis of the data currently available.

Inclusions of Generation 2 occur along healed fractures that terminate at grain boundaries, but are crosscut by trains of inclusions that extend across these boundaries (Generation 3). This clearly establishes Generation 3 as the younger of the two sets of inclusions, and indicates that the P-T path of the rocks must have crossed isochore 2 prior to isochore 3. Because the H_2O-rich fluids of Generation 2 and CO_2-rich fluids of Generation 3 would have been completely miscible at temperatures greater than ~375°C, they cannot have existed simultaneously as free fluid phases at the P-T conditions of intersection of their isochores. This suggests that the uplift path crossed these isochores well to the right of their point of intersection (Figure 4-12).

In contrast, the simultaneous entrapment of the immiscible H_2O-CO_2-NaCl inclusions of Generations 4a and 4b must have occurred at the P-T conditions corresponding to the point of intersection of their isochores, which is shown as 380±30°C, 1.3±0.2 kb in Figure 4-12. The data of Gehrig (1980, in Bowers and Helgeson, 1983) yield a temperature of ~360°C for the observed coexisting fluid compositions (40 mol % H_2O and 80 mol % H_2O for Generations 4a and 4b, respectively) in a system with 6 wt % NaCl at 1.5 kb. This is in good agreement with the temperature determined from intersection of the isochores, despite the assumption that $X_{NaCl}=0$ that was used in constructing the isochores. This point of intersection places tight constraints on the shape and position in P-T space of the uplift path followed by the host rocks.

The youngest generation of inclusions present (#5) defines an isochore that never exceeds a pressure of 1 kb over the entire temperature range of interest, implying entrapment at near-surface conditions. The fluid phase in this set of inclusions cannot have been locally derived, since mixed CO_2-CH_4 fluids cannot coexist in equilibrium with graphite over this P-T interval (Holloway, 1984). In any case, it is highly unlikely that dehydration reactions would have occurred in the host pelites at such low P-T conditions, and these fluids must certainly have been externally derived.

Overall, the sequence of isochores presented in Figure 4-12 constrains the uplift path of the rocks to have passed from 450-500°C, 6 kb through a point at ~380°C, 1.3 kb. A possible path consistent with all of the data presented above is shown in Figure 4-12. A significant feature of this path is that it implies that Generation 1 inclusions were able to withstand internal pressures of 3-4 kb without decrepitating. Laboratory experiments on the strength of quartz indicate that inclusions ≥12-15 μm in diameter generally decrepitate at ~1 kb internal pressure (Leroy, 1979), but smaller inclusions seem capable of withstanding internal pressures of >1 kb up to as much as ~6 kb (Leroy, 1979; Swanenberg, 1980, cited in Roedder, 1984; Selverstone, 1982). Traces of decrepitated inclusions are found in association with Generation 1 inclusions (Fig. 4-11), suggesting that the internal pressure was sufficient to rupture large inclusions, but smaller inclusions (≤12 μm) were preserved. This supports the steep decompression path shown in Figure 4-12. In agreement with the data obtained for the LSH, Figure 4-12 indicates that significant cooling of the USH did not occur until the rocks were within ~5 km of the surface.

GREENSTONES

Sample description and mineral chemistry.

The greenstone lithologies of the USH are highly variable in texture and modal mineralogy, but in all samples examined in this study the dominant assemblage is amphibole + plagioclase + epidote + quartz + rutile ± chlorite ± carbonate (Table 4-4). Most samples are fine-grained and massive, though foliated amphibolites and coarse, epidote-rich lithologies were also observed. One of the most striking features of the greenstone sequence is the common occurrence of 0.3-1.2 cm wide rectangular, diamond-shaped, and triangular clots of intergrown Plag + Epid + Chl set in the amphibolitic matrix (see Figure 4-13). The euhedral outline of these clots and the complex intergrowths of the phases within them imply that these are pseudomorphs after an earlier mineral phase, as is discussed in detail below. Representative analyses of minerals in the matrix and pseudomorph assemblages are given in Table 4-7 at the end of this chapter.

Most of the greenstones within the USH occur as discontinuous lenses or pods, and even where amphibolites are the dominant rock type, it is difficult to trace a single layer over any great distance. Although pillows are well-preserved within the amphibolite sequence of the Eclogite Zone (Miller, 1977), no such features were observed in the area of this study.

Matrix mineralogy.

Amphibole occurs as fine-grained, euhedral to subhedral crystals that dominate the matrix assemblage in most of the samples studied. The rims of these grains are composed of dark-green hornblende with 10-12 wt

Figure 4-13. Comparison between form of polyphase pseudomorphs (heavy lines) in sample HF-12 and crystal habit of lawsonite. Note good agreement between (A) and 101 face of lawsonite and between (C) and 010 face. Pseudomorphs traced from photographs; long dimension of each box is 5 mm. Sketch of lawsonite taken from Tröger (1971).

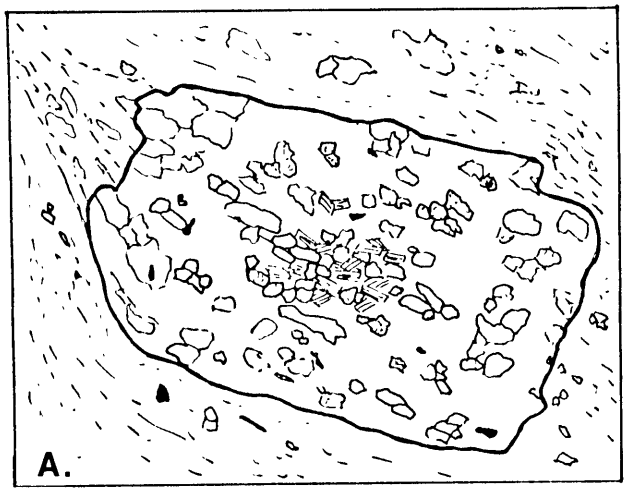

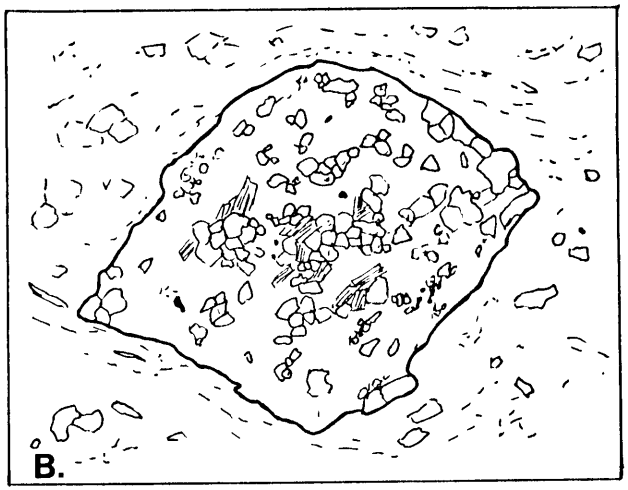

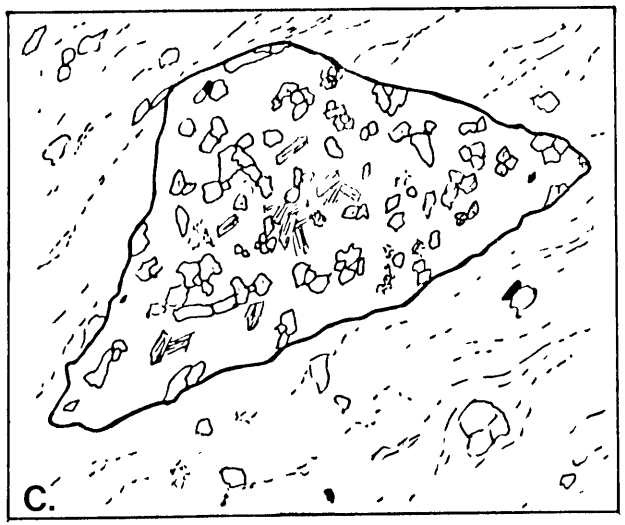

lawsonite:

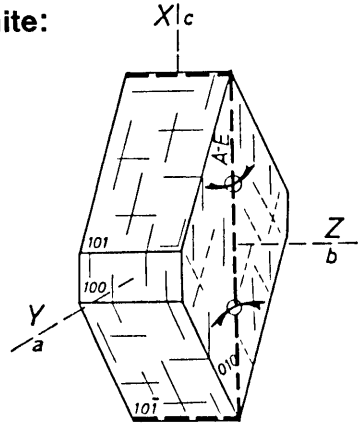

Table 4-4

Mineral assemblages in USH greenstones

Sample	Amph	Chl	Plag	Epid	Carb	Ilm	Ru
HF-1C	x	x	x	x	x		x
HF-2A*	x	x	x	x			x
HF-2B	x	x	x				
HF-12*	x	x	x	x			x
Hf-13	x	x	x	x	x		x
HF-14A	x	x	x	x	x	x	x
HF-14B*	x	x	x	x		x	x
Hf-14C	x		x	x	x	x	x
HF-15	x	x	x	x	x	x	x
HF-16	x	x	x	x		x	x

An asterisk (*) denotes samples that contain pseudomorphs visible in thin section.

wt % Al_2O_3, but the cores are typically colorless to pale green actinolite with 1-2 wt % Al_2O_3. In general, the boundary between the two types of amphibole is sharply defined. Large (2-4 mm), ragged amphibole porphyroblasts that predate development of the matrix hornblende are also present in most samples. These too show a well-defined rim of hornblende, identical in composition to the edges of the smaller matrix grains, but the core regions are composed of patchy intergrowths of actinolite and hornblende. In some cases (e.g. sample HF-2A), the intergrowths appear to be distinctly lamellar rather than patchy; microprobe analyses of these areas yield mixed analyses that are intermediate between hornblende and actinolite (Figure 4-14), with no trend towards any other phase such as chlorite. Preliminary examination with the transmission electron microscope (with the assistance of T.L. Grove) confirms that the lamellae represent fine-scale intergrowths of two amphiboles with similar cell dimensions, such as hornblende and actinolite. The potential existence of a solvus between these two amphiboles has been a subject of considerable interest in recent years (see discussion in Robinson et al., 1981, for a review); the USH samples may be the first samples to yield definitive proof of this solvus in the form of exsolution lamellae. Research aimed at providing further documentation of this phenomenon is currently in progress.

Plagioclase makes up a granoblastic network between amphibole grains in the matrix. Grains are untwinned and show only slight chemical zonation, from ~An_{19} in the cores to An_{23-24} at the rim.

Epidote is a ubiquitous matrix phase and occurs both individually and in clots of subhedral to euhedral grains. Compositions are highly variable, with edges falling in the range 34-68 % $FeAl_2Ep$ (Figure 4-15).

Figure 4-14. Projection from quartz + H_2O into the tetrahedron Al-Na-Ca-(Fe+Mg), showing the phase volume defined by edge compositions of hornblende, chlorite, epidote, and plagioclase in the USH greenstones. Also shown is the degree of zonation from rim to core of each of these phases. Of particular note is the array of analyses spanning the presumed miscibility gap between hornblende and actinolite: these are mixed analyses from porphyoblasts with distinctly lamellar appearance, and may indicate coexistence of discrete lamellae of hornblende and actinolite on a submicroscopic scale.

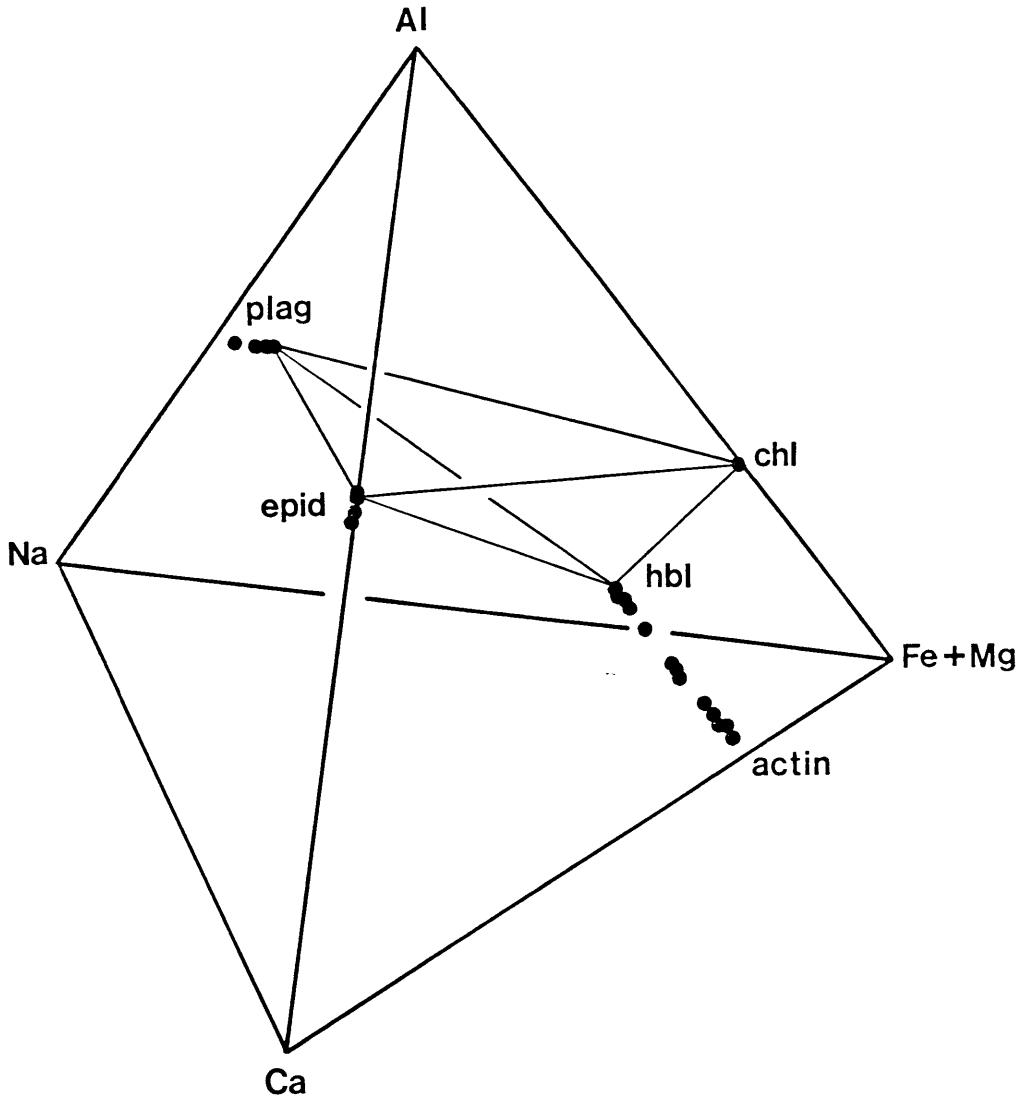
Al
plag
chl
epid
Na
hbl
Fe+Mg
actin
Ca

In general, cores are richer in the $FeAl_2Ep$ endmember than are the rims.

Chlorite appears to be part of the stable matrix assemblage rather than a retrograde phase, and Fe/Fe+Mg ratios are consistently 0.27 in all samples.

Carbonate is a minor constituent in the matrix of roughly half of the greenstones studied, but was not analyzed with the microprobe.

Rutile occurs as an abundant accessory phase in all of the greenstones. Ilmenite was observed in half of the samples, and shows no signs of exsolution or alteration.

Pseudomorph mineralogy.

Two compositionally distinct types of epidote coexist in subequal amounts in the pseudomorphs, making epidote the most abundant mineral in the assemblage. Edge compositions fall in the ranges 30-37% $FeAl_2Ep$ and 57-64% $FeAl_2Ep$. Analyses of epidote cores are also confined to these two compositional ranges, but in most cases grains with Fe-rich rims have Fe-poor cores and vice versa; a sharp optical and chemical boundary separates the core and rim regions. The compositions of pseudomorph epidotes are compared with matrix epidotes and epidotes from the graphitic schists in Figure 4-15; the coexisting epidote compositions in the pseudomorphs indicate a miscibility gap that is not in evidence in the epidotes from other parageneses. Raith (1976) has also described coexisting epidotes in USH and Eclogite Zone rocks near the center of the Tauern Window, although the compositions he reports are more enriched in the $FeAl_2Ep$ endmember than those presented here, and they occur as part of the matrix assemblage rather than in pseudomorphs. No evidence for the persistence of a miscibility gap at the conditions of final equi-

libration of the matrix assemblage has been found in the area of this study.

Two coexisting plagioclases, albite and oligoclase, also occur within the pseudomorphs and define the peristerite gap. Albite grains are abruptly zoned from edge compositions of An_{4-5} to cores as calcic as An_{19}. In contrast, oligoclase grains are more homogeneous, with rims of An_{24-26} and cores of An_{18-20}. The two types of plagioclase occur in contact with one another, and both appear to be stable minerals in the assemblage, although oligoclase is roughly four times as abundant as albite. Neither variety of plagioclase shows any signs of alteration.

Chlorite occurs in all of the pseudomorphs, and is most abundant near the centers of these features. In all cases, it is identical in composition to its counterpart in the matrix.

Quartz is a minor constituent of the pseudomorph assemblage, and rutile is present as an accessory phase.

Pseudomorph reaction.

The overall mineralogical similarity between the Epid-Plag-Chl intergrowths in the greenstones and the pseudomorphs after lawsonite described from the garbenschist samples (Chapter 3) suggests that the pseudomorph precursor phase was also lawsonite in the USH. The well-preserved triangular and prismatic outlines of the mineral aggregates are consistent with the crystal habit of lawsonite (Figure 4-13); Fry (1973) has proposed that similar features in the central part of the Tauern Window also represent pseudomorphs after lawsonite. A model identity of lawsonite is hence proposed for the pseudomorph precursor in the greenstones, but several distinctions between the USH and LSH

Figure 4-15. Diagram comparing epidote compositions from different parageneses in the USH. Solid symbols = cores, open symbols = rims. Within the greenstones, epidotes in the pseudomorph assemblage clearly define a compositional gap between 38 and 54% $FeAl_2Ep$, whereas epidotes in the matrix assemblage completely span this gap. No gap is evident in the graphitic schist samples. The implication of these data is that the pseudomorphs developed under P-T-f_{O2} conditions at which a miscibility gap in the epidote system exists, but that these conditions were exceeded by the time of final equlibration of the matrix assemblage.

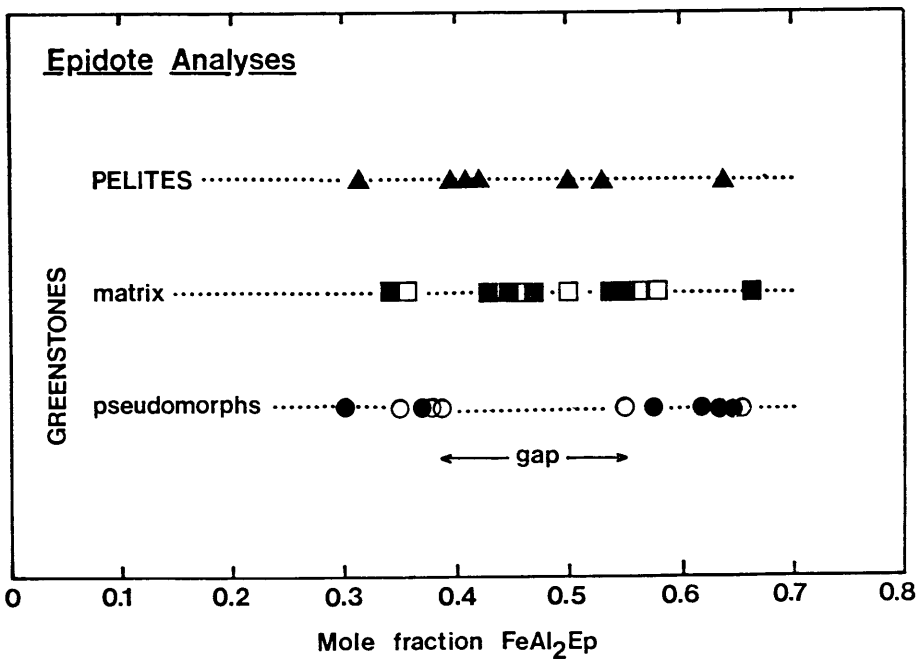
Epidote Analyses
PELITES
matrix
pseudomorphs
gap
GREENSTONES
0
0.1
0.2
0.3
0.4
0.5
0.6
0.7
0.8
Mole fraction $FeAl_2Ep$

pseudomorphs must be noted before mass balance calculations can be carried out:

(1) The modal abundances of product phases are quite different in the two populations of pseudomorphs (Epid>>Chl>Plag>Qtz in the USH as compared to Amph>Plag≈Epid>Chl in the LSH).

(2) Amphibole grains adjacent to the pseudomorphs in the USH are identical to those elsewhere in the matrix, and there is no textural or compositional evidence that amphibole is a product of the pseudomorph reaction. There is also no textural evidence to suggest whether the pseudomorph reaction took place before or after the development of hornblende rims around pre-existing actinolite, and it is thus not obvious which amphibole, if either, participated as a reactant in this reaction.

(3) The pseudomorph reaction in the USH samples occurred under P-T(-f_{O2}) conditions at which miscibility gaps exist in both the feldspar (peristerite) and epidote systems, resulting in two plagioclase and two epidote compositions as part of the stable product assemblage. In contrast, only a single plagioclase and single epidote are present within the LSH pseudomorphs.

Taken together, these features indicate that the specific reaction between lawsonite and pargasite proposed for the LSH pseudomorphs cannot be applied to the USH samples, and also that the P-T-f_{O2} conditions at which the pseudomorph assemblages were produced must have differed between the two rock suites. In order to ascertain the net reaction responsible for producing the polyphase aggregates, mass balance calculations were performed utilizing a hypothetical endmember lawsonite, pure quartz, and measured compositions of hornblende, actinolite, two

plagioclases, two epidotes, and chlorite. Because the petrographic evidence concerning amphibole involvement in the reaction is ambiguous, the calculations were carried out for all possible combinations of hornblende and/or actinolite with the remaining phases. The results of these calculations were recast into volume percent and compared with the modal abundances of reaction products determined by point counting 100 points in each of five pseudomorphs. It was not possible to distinguish between the two plagioclases and two epidotes under the microscope, hence only total plagioclase and total epidote could be counted. Based on microprobe analyses, however, oligoclase appears to be ~4 times as abundant as albite, whereas the modes of the two epidote compositions are approximately the same. The measured compositions of these phases were multiplied by these abundances to arrive at average compositions for use in the calculations, thereby allowing comparison of calculated and observed modes.

Two net transfer reactions capable of producing the observed pseudomorph assemblage were determined from the mass balance calculations, and the results are compared with the measured modes in Table 4-5. Each of the reactions as written is univariant in the model system SiO_2-Al_2O_3-FeO-MgO-CaO-Na_2O-H_2O-O_2 and involves only a single amphibole of fixed composition:

$$\text{Laws} + \text{Actin} \pm O_2 \rightarrow An_5 + An_{24} + \text{FeEp} + \text{AlEp} + \text{Chl} + \text{Qtz} + H_2O \qquad (4\text{-}6)$$

$$\text{Laws} + \text{Hbl} \pm O_2 \rightarrow An_5 + An_{24} + \text{FeEp} + \text{AlEp} + \text{Chl} + \text{Qtz} + H_2O \qquad (4\text{-}7)$$

Obviosly, these two reactions could be combined to yield a continuous reaction that results in changing compositions of amphibole, such as the

Table 4-5

Comparison of predicted and observed modal abundances of product phases in lawsonite pseudomorphs

	Coefficient (4-6)	Coefficient (4-7)	Molar vol.	Volume, cm^3 (4-6)	Volume, cm^3 (4-7)	Volume percent (4-6)	Volume percent (4-7)	Volume percent obs.
Lawsonite	-100	-100	-	-	-	-	-	-
Actinolite	-20	0	-	-	-	-	-	-
Hornblende	0	-37	-	-	-	-	-	-
Epidote	69	81	138	95.1	111.8	63	56	58
Plagioclase	2	21	99	2.5	20.8	2	10	15
Chlorite	7	12	417	27.9	50.0	19	24	18
Quartz	105	79	28	23.6	22.1	16	9	8
H_2O	132	103	-	-	-	-	-	-

Amphibole compositions are average actinolite and hornblende compositions from sample HF-12. Epidote = 50% $FeAl_2Ep$. Plagioclase = An_{20}. Chlorite is from sample HF-12. (4-6) and (4-7) refer to reactions listed in the text.

Laws + Amph reaction described in Chapter 3. As written, however, reaction 4-7 provides a remarkable fit with the modal abundances actually observed in the pseudomorphs, suggesting that 4-7 behaved as an essentially discontinuous reaction in these rocks. If this is the case, reaction 4-7 probably occurred as a direct result of the transition from actinolite to hornblende as the dominant amphibole in the assemblage. The ability of reaction 4-7 to account for the phase equilibria of the pseudomorphs also provides strong circumstantial evidence that lawsonite was indeed the precursor to the pseudomorph assemblage, and that the P-T path followed by the rocks passed through the blueschist facies prior to the conditions of final equilibration.

Progressive metamorphism.

Due to the lack of suitable geothermometer and geobarometer assemblages in the greenstones, it is difficult to place quantitative limits on the P-T path followed by the rocks through the blueschist facies, or on the nature of the transition from blueschist to greenschist conditions. Several petrologic observations allow inferences to be made regarding the overall shape and general position of the rock path in P-T space, however. With respect to development of the pseudomorphs, there is good evidence that (1) the reaction involved lawsonite and amphibole as reactants; (2) the amphibole was probably hornblende rather than actinolite; (3) the appearance of hornblende in the rocks postdates that of actinolite; and (4) the reaction took place below the consolute temperatures of both the epidote and peristerite miscibility

Figure 4-16. Plots of 100 Na/Ca+Na versus 100 Al/Si+Al and Na(M4) versus Na(A) + K for hornblende rims (open circles) and actinolite cores (closed circles) in USH greenstones. Also shown are boundaries of high, medium, and low-pressure amphibole fields defined by Laird and Albee (1981: Fig. 12). USH analyses lie dominantly within the medium-pressure field and show no trend towards the high-pressure field. Medium-P field of Laird and Albee (1981) is constructed from rocks metamorphosed between ~5 and 7 kb.

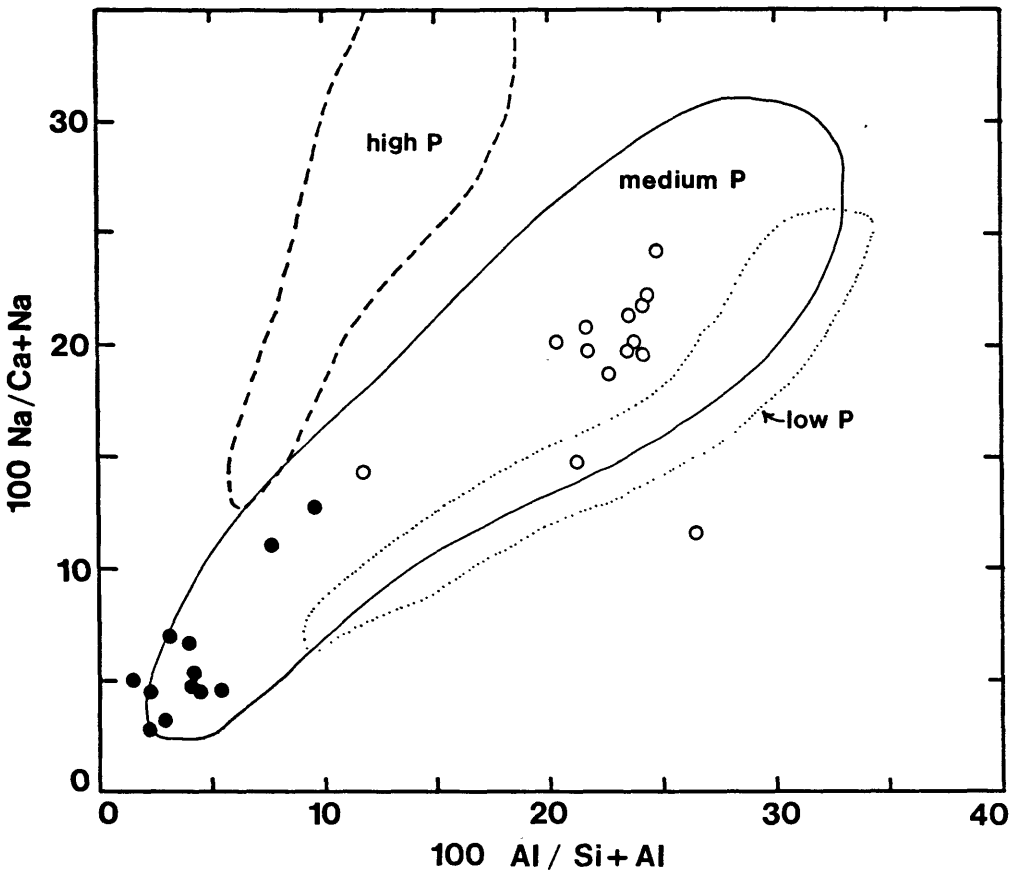
high P
medium P
low P
100 Na/Ca+Na
100 Al / Si+Al
0
10
20
30
40

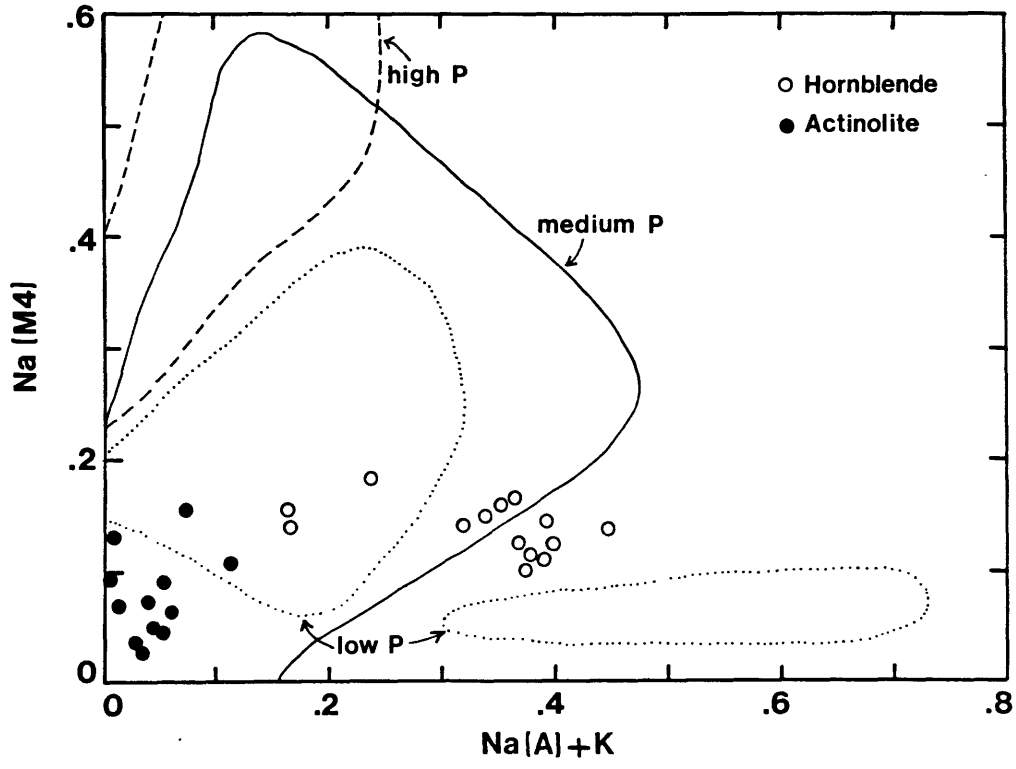
high P
medium P
low P
Hornblende
Actinolite
Na [M4]
Na[A]+K
0
.2
.4
.6
.8

gaps. There is no evidence to suggest that glaucophane was ever a constituent of the mineral assemblage, implying that the Plag-Chl-CaAmph plane in Al-(Fe,Mg)-Ca-Na space was stable throughout. This is consistent with metamorphism in the lawsonite-albite-chlorite subfacies of the blueschist facies, as described by Turner (1980), or the equivalent medium-pressure facies series of metabasic rocks discussed by Laird (1980). Figure 4-16 shows aluminum and alkali contents of the USH amphiboles relative to the low-, medium-, and high-pressure amphibole fields defined by Laird and Albee (1981); both actinolite and hornblende analyses fall within the medium-P field, and there is no trend indicative of metamorphism in a high-pressure environment.

The generalized progression of assemblages that can be documented petrographically can be described by the following schematic reactions, in approximate chronological order:

$$\text{Actinolite} \rightarrow \text{Hornblende} \qquad (4\text{-}8)$$

$$\text{Laws} + \text{Hbl} \rightarrow \text{Ep}_1 + \text{Ep}_2 + \text{Pl}_1 + \text{Pl}_2 + \text{Chl} \qquad (4\text{-}9)$$

$$\text{FeEp} + \text{AlEp} \rightarrow \text{Epidote} \qquad (4\text{-}10)$$

It is not possible to reconstruct unambiguously the reaction responsible for the actinolite → hornblende transition, but it may have been combined with crossing of the peristerite gap in the feldspar system via a reaction such as:

$$\text{Actin} + \text{Albite} + \text{Epid} + \text{Chl} \rightarrow \text{Hbl} + \text{Oligoclase} \qquad (4\text{-}11)$$

(Spear, 1981). In any case, the compositions of amphiboles and plagioclases present in the greenstones are consistent with crossing rather than closing of the miscibility gaps in these systems, implying that the transitions occurred below the critical curves for Hbl + Actin and peristerite.

Regardless of the effects of amphibole solid solution on the equilibrium constant for reaction 4-9, the reaction boundary must lie to the low-temperature side of the maximum stability limit of lawsonite. Hence, the curve for the breakdown of lawsonite to clinozoisite + margarite + quartz (Chatterjee, 1976; see Figure 4-17) represents the locus of maximum temperatures at which the pseudomorph aggregates could have been produced for any P or f_{O2} conditions. It is not been possible to locate the position of reaction 4-9 any more explicitly than this due to insufficient data on thermodynamic mixing models for coexisting epidotes and coexisting plagioclases, and because the reaction boundary will be sensitive to changes in f_{O2} which cannot be determined.

The existence of a miscibility gap in the epidote system (reaction 4-10) has been a subject of some debate, with Strens (1965), Holdaway (1972), Hietanen (1974) and Raith (1976) presenting data in favor of such a gap, and Liou et al. (1984) arguing against it. The data presented in this study show a clear compositional gap between coexisting epidotes in the pseudomorphs, and no such gap in the matrix epidotes. This suggests that a miscibility gap does exist, but that its consolute temperature lies below middle greenschist facies temperatures for the P and f_{O2} conditions of the USH samples. Reaction 4-9, which produced polyphase aggregates of AlEp + FeEp + Plag + Chl in the greenstones, must lie to the left of the epidote critical curve, whereas final equilibration of the matrix took place at supersolvus conditions.

The qualitative data on reactions 4-8, 4-9, and 4-10 discussed above suggests that the blueschist-greenschist transition occurred at temperatures near the upper stability limit of lawsonite. Unfortunately, it is not possible to calculate directly the pressures associated with

Figure 4-17. Summary P-T diagram showing probable path followed by USH samples during progressive metamorphism and uplift. Early dashed portion of curve is based on pseudomorphs after lawsonite in greenstones and on amphibole data indicating metamorphism at medium P. Solid portion of curve is from garnet zoning paths shown in Fig. 4-10, terminating at "peak" P-T conditions determined from geothermometry/barometry (box). Dashed uplift path is constrained by fluid inclusion data (isochores 1 to 5 and box indicating conditions of entrapment of immiscible fluids). Lawsonite stability field is from Chatterjee (1976).

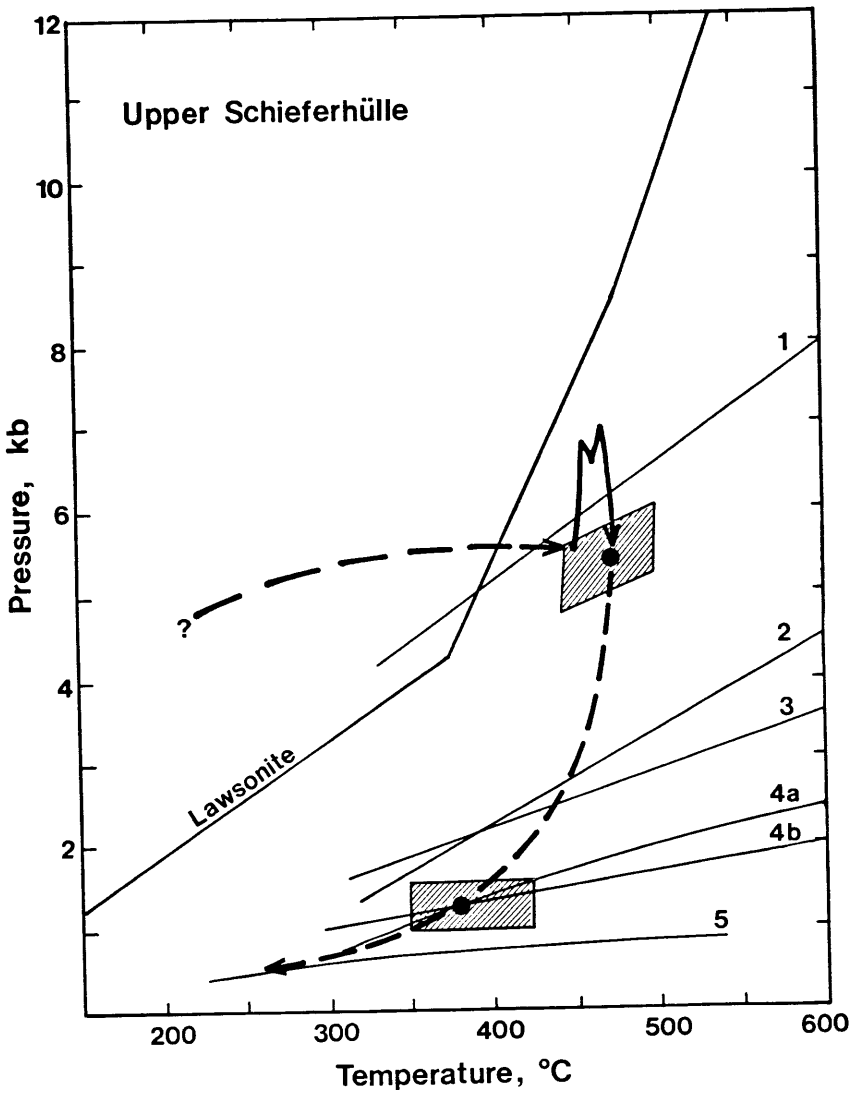
Upper Schieferhülle
Pressure, kb
Temperature, °C
12
10
8
6
4
2
200
300
400
500
600
1
2
3
4a
4b
5
Lawsonite
?

this transition, although the lack of direct evidence for glaucophane in the blueschist assemblage and the medium-P trend shown in Figure 4-16 argue against a trajectory originating at high pressure. An approximately isobaric P-T path is illustrated in Figure 4-17; this path is consistent with the phase equilibria, but can only be considered as a model trajectory in the absence of data that quantitatively constrain the early pressure history of these rocks.

SUMMARY OF P-T DATA

All of the pressure-temperature data calculated from the pelitic schists and inferred from the greenstones are combined into a single P-T diagram in Figure 4-17. The progressive development of assemblages in the greenstones, and in particular the pseudomorphs after lawsonite, indicate an early phase of metamorphism at low T and moderate P in the Laws+Ab+Chl subfacies of the blueschist facies. Subsequent heating resulted in development of the dominant greenschist facies assemblages. Garnet growth occurred initially in response to an increase in pressure at nearly constant temperature, then continued during uplift until the maximum temperature of 475±25°C was attained at P≈5.5 kb. The maximum pressures recorded during the period of garnet growth were ~7.5 kb, corresponding to a depth of burial of approximately 26-28 km. Decompression from ~7 kb to ~2.5 kb occurred along a nearly isothermal path, and the rocks remained at temperatures of 350-400°C until they were within ~5 km of the surface.

The two phases of pressure increase recorded during the growth of zoned garnet porphyroblasts imply discrete tectonic events that resulted

in an increased depth of burial of the USH samples. Such reversals in the P-T paths followed by individual rocks are probably common features of metamorphism in actively deforming orogenic regions, but cannot be resolved by most petrologic techniques; the smooth uplift curve that has been constructed based on the fluid inclusion data should thus only be considered to be an approximate rock P-T path.

Several previous workers in the USH have argued for higher pressures of metamorphism for these rocks than for the LSH, in particular if the rocks of the USH are part of the same lithotectonic unit as the Eclogite Zone (e.g. Miller, 1977; Raith et al., 1977). No evidence of pressures greater than 7.5 kb has been documented in the USH in this study, however (in agreement with the results of Frisch, 1984); if the rocks did experience early metamorphism at greater depths of burial, the record of these higher pressures has been extensively overprinted within the area of this study. The tectonic significance of the USH P-T path, assuming that P_{max}=7.5 kb, is discussed in detail in the following chapter.

TABLE 4-6

Representative analyses of garnet, plagioclase, biotite, phengite, chlorite, epidote, and margarite in graphitic schists of the USH

Representative garnet analyses

	HF-2C 2-4 E-chl	HF-2C 2-12 core	HF-2C 2-20 E-qtz	HF-2D 1-2 E-bio	HF-2D 1-6 core	HF-2D 1-10 E-qtz	HF-2D 2-1 E-bio	HF-2E 1-1 E-bio	HF-2E 4-4 E-bio	HF-2E 4-8 core	HF-2E 4-9 E-qtz	HF-3A 1-1 core	HF-3A 1-7 E-bio	HF-3A 2-1 core	HF-3A 2-6 E-bio	HF-3A 3-1 core	HF-3A 3-2 E-bio	HF-6A 2-2 E-bio	HF-6A 2-7 E-qtz	HF-6A 2-18 core	HF-6A 2-22 E-bio
SiO_2	36.62	37.59	38.21	37.62	37.00	36.87	36.16	37.49	36.91	35.99	37.56	38.03	37.26	36.91	37.52	36.21	37.88	38.11	38.16	37.87	38.29
Al_2O_3	21.46	21.06	21.02	21.46	21.19	21.25	21.30	21.41	21.34	21.18	21.05	20.83	21.74	21.23	21.55	21.00	21.66	22.24	22.22	21.73	22.15
MgO	2.04	1.47	2.35	2.62	0.64	2.39	2.15	2.68	2.47	1.21	1.42	0.59	2.03	0.28	1.89	0.34	1.46	2.38	2.36	1.16	2.43
FeO	31.23	30.64	31.14	32.09	24.00	32.25	31.83	32.71	32.81	31.39	30.89	21.67	30.99	17.84	30.73	17.22	30.90	27.89	28.16	24.80	27.98
MnO	0.73	1.94	0.85	0.34	8.45	0.22	0.26	0.43	0.40	2.74	1.22	11.44	0.50	17.50	0.62	17.87	0.81	3.31	3.32	8.10	3.31
CaO	7.28	8.13	7.18	6.17	8.36	6.31	6.59	6.22	6.52	7.76	7.99	7.95	7.78	6.48	7.77	5.61	8.42	7.83	7.88	8.08	7.73
Total	99.35	100.83	100.74	100.30	99.64	99.29	98.29	100.95	100.46	100.28	100.13	100.51	100.30	100.25	100.09	98.25	101.12	101.76	102.08	101.74	101.89
Cations per 12 oxygens																					
Si	2.954	2.996	3.028	2.993	2.988	2.973	2.950	2.975	2.953	2.916	3.007	3.040	2.968	2.983	2.991	2.984	2.995	2.977	2.975	2.987	2.986
Al	2.041	1.979	1.964	2.013	2.017	0.020	2.049	2.003	2.013	2.023	1.987	1.963	2.041	2.023	2.025	2.040	2.019	2.048	2.042	2.020	2.037
Mg	0.245	0.174	0.277	0.311	0.077	0.287	0.262	0.317	0.295	0.146	0.169	0.070	0.241	0.034	0.225	0.042	0.172	0.277	0.274	0.136	0.282
Fe	2.107	2.042	2.064	2.135	1.621	2.175	2.172	2.171	2.195	2.127	2.068	1.449	2.064	1.206	2.049	1.187	2.043	1.822	1.836	1.636	1.825
Mn	0.050	0.131	0.057	0.023	0.578	0.015	0.018	0.029	0.027	0.188	0.083	0.775	0.034	1.198	0.042	1.247	0.054	0.219	0.219	0.541	0.219
Ca	0.629	0.694	0.610	0.526	0.723	0.545	0.576	0.529	0.559	0.674	0.685	0.681	0.664	0.561	0.664	0.495	0.713	0.655	0.658	0.683	0.646
Fe/ Fe+Mg	0.896	0.921	0.882	0.873	0.955	0.883	0.892	0.873	0.882	0.936	0.924	0.954	0.895	0.973	0.901	0.966	0.922	0.868	0.870	0.923	0.866
pyr	0.081	0.057	0.092	0.104	0.026	0.095	0.087	0.104	0.096	0.047	0.056	0.024	0.080	0.011	0.076	0.014	0.058	0.093	0.092	0.045	0.095
alm	0.695	0.671	0.686	0.713	0.541	0.720	0.717	0.713	0.714	0.678	0.688	0.487	0.687	0.402	0.688	0.400	0.685	0.613	0.615	0.546	0.614
spess	0.016	0.043	0.019	0.008	0.193	0.005	0.006	0.010	0.009	0.060	0.028	0.261	0.011	0.399	0.014	0.420	0.018	0.074	0.073	0.181	0.074
gross	0.208	0.228	0.203	0.176	0.241	0.180	0.190	0.174	0.182	0.215	0.228	0.229	0.221	0.187	0.223	0.167	0.239	0.220	0.220	0.228	0.217

Representative garnet analyses (cont'd.)

	HF-6B 1-2 E-bio	HF-6B 1-3 core	HF-6B 3-4 E-bio	HF-6B 3-7 core	HF-17A 1-1 E-bio	HF-17A 1-16 C-WM	HF-17A 4-1 E-WM	HF-17A 4-16 C-Plg	HF-27B 1-3 E-bio	HF-27B 1-19 core	HF-27B 2-2 E-bio
SiO_2	37.74	36.22	36.84	37.13	38.17	36.73	37.19	37.84	38.00	35.60	36.30
Al_2O_3	22.28	22.11	22.08	22.01	21.54	21.60	21.44	21.34	21.86	20.95	21.24
MgO	2.64	1.49	2.61	0.65	1.86	1.81	1.83	1.52	2.67	1.34	2.63
FeO	31.57	32.02	29.88	24.48	28.39	28.33	29.52	28.52	28.47	23.37	28.04
MnO	3.12	5.31	2.92	12.49	4.57	3.98	4.54	4.78	3.50	10.23	3.88
CaO	5.09	3.88	6.25	4.53	6.43	6.93	5.80	7.25	6.89	6.69	6.94
Total	102.44	101.03	100.58	101.29	100.96	99.39	100.32	101.25	101.41	98.18	99.04
					cations per 12 oxygens						
Si	2.954	2.913	2.932	2.969	3.019	2.961	2.980	3.000	2.984	2.934	2.938
Al	2.056	2.097	2.072	2.075	2.009	2.053	2.025	1.995	2.024	2.035	2.027
Mg	0.308	0.179	0.309	0.077	0.219	0.217	0.219	0.180	0.313	0.164	0.317
Fe	2.067	2.154	1.989	1.637	1.878	1.910	1.978	1.891	1.870	1.611	1.898
Mn	0.207	0.362	0.197	0.846	1.306	0.272	0.308	0.321	0.233	0.714	0.266
Ca	0.427	0.334	0.533	0.388	0.545	0.599	0.498	0.616	0.580	0.591	0.602
Fe/ Fe+Mg	0.870	0.923	0.866	0.955	0.896	0.898	0.900	0.913	0.857	0.908	0.857
pyr	0.102	0.059	0.102	0.026	0.074	0.072	0.073	0.060	0.104	0.053	0.103
alm	0.687	0.711	0.657	0.555	0.637	0.637	0.659	0.629	0.624	0.523	0.616
spess	0.069	0.120	0.065	0.287	0.104	0.091	0.103	0.107	0.078	0.232	0.086
gross	0.142	0.110	0.176	0.132	0.185	0.200	0.166	0.205	0.194	0.192	0.195

Representative plagioclase analyses

	Hf-2D 3-6 core	HF-2D 3-7 edge	HF-2E 2-1 edge	HF-2E 2-2 core	HF-2E 2-3 core	HF-2E 2-4 edge	HF-6A 1-1 edge	HF-6A 1-2 core	HF-6A 2-18 mid	HF-6A 2-19 E-gar	HF-6A 2-20 core	HF-17A 1-11 core	HF-17A 1-13 E-gar	HF-17A 4-19 in gt C	HF-17A 4-20 in gt E	HF-17A 3-4 E-qtz	HF-27B 1-8 E-gar	HF-27B 1-10 core	HF-27B 1-11 core	Hf-27B 1-14 E-bio
SiO_2	62.22	62.10	53.19	55.06	53.91	57.61	58.63	62.03	61.70	57.33	58.62	58.66	56.14	64.20	61.82	55.53	56.10	58.81	58.20	55.51
Al_2O_3	23.15	22.23	29.66	28.31	28.31	26.42	26.78	24.35	24.73	28.04	26.28	27.35	28.30	23.30	23.91	28.51	27.71	26.34	25.88	28.06
FeO	0.05	0.05	0.37	0.21	0.16	0.08	0.00	0.05	0.16	0.16	0.11	0.14	0.38	0.19	0.62	0.27	0.42	0.11	0.24	0.32
CaO	3.93	3.59	12.38	10.84	11.44	8.29	7.89	5.63	6.09	9.63	7.81	8.12	10.79	3.93	5.26	10.09	9.05	7.75	7.93	10.38
Na_2O	9.69	9.78	4.80	5.39	5.03	6.86	7.21	8.16	8.17	6.04	7.09	6.93	6.04	10.19	9.26	5.81	5.92	7.06	7.15	5.69
K_2O	0.12	0.07	0.17	0.09	0.07	0.10	0.11	0.11	0.11	0.14	0.14	0.73	0.07	0.07	0.05	0.14	0.28	0.11	0.14	0.14
Total	99.16	97.82	100.57	99.90	98.91	98.91	100.61	100.34	100.95	101.34	100.06	101.93	101.72	101.88	100.92	100.35	99.49	100.17	99.53	100.11
										cations per 8 oxygens										
Si	2.779	2.808	2.402	2.485	2.462	2.588	2.600	2.744	2.715	2.539	2.626	2.583	2.492	2.793	2.731	2.485	2.533	2.621	2.617	2.500
Al	1.219	1.185	1.579	1.506	1.524	1.410	1.400	1.270	1.283	1.464	1.388	1.420	1.481	1.195	1.245	1.504	1.475	1.384	1.372	1.490
Fe	0.002	0.002	0.014	0.008	0.006	0.003	0.000	0.002	0.006	0.006	0.004	0.005	0.014	0.007	0.023	0.010	0.016	0.004	0.009	0.012
Ca	0.188	0.174	0.599	0.524	0.560	0.402	0.375	0.267	0.287	0.457	0.375	0.383	0.513	0.183	0.249	0.484	0.438	0.370	0.382	0.501
Na	0.839	0.857	0.420	0.472	0.445	0.604	0.620	0.700	0.697	0.519	0.616	0.592	0.520	0.860	0.793	0.504	0.518	0.610	0.623	0.497
K	0.007	0.004	0.010	0.005	0.004	0.006	0.006	0.006	0.006	0.008	0.008	0.041	0.004	0.004	0.003	0.008	0.016	0.006	0.008	0.008
An	0.182	0.168	0.582	0.523	0.555	0.398	0.375	0.274	0.290	0.464	0.375	0.377	0.495	0.175	0.238	0.486	0.451	0.375	0.377	0.498
Ab	0.811	0.828	0.408	0.472	0.441	0.596	0.619	0.719	0.704	0.527	0.617	0.583	0.501	0.821	0.759	0.506	0.533	0.619	0.615	0.494
Or	0.007	0.004	0.010	0.005	0.004	0.006	0.006	0.006	0.006	0.008	0.008	0.040	0.004	0.004	0.003	0.008	0.016	0.006	0.008	0.008

Representative phengite analyses

	HF-2D 2-3 matrix	HF-2E 1-6 matrix	HF-2E 3-4 matrix	HF-2E 4-1 by gt	HF-2E 4-2 matrix	HF-3A 1-9 matrix	HF-3A 1-10 by gt	HF-3A 2-7 by gt	HF-3A 2-9 matrix	HF-3A 3-5 by gt	HF-6A 1-6 matrix	HF-6A 1-11 matrix	HF-6A 2-6 by gt	HF-68 1-9 matrix	HF-6B 1-10 matrix	HF-6B 3-11 by gt
SiO_2	46.75	48.09	47.53	49.54	48.14	46.17	45.92	49.61	47.39	48.10	47.78	48.49	48.68	46.57	47.37	49.88
Al_2O_3	34.17	34.03	33.62	30.03	33.27	34.44	35.04	31.92	34.50	32.87	33.73	33.26	31.79	35.20	34.97	31.44
TiO_2	0.27	0.28	0.28	0.18	0.24	0.37	0.35	0.20	0.34	0.24	0.32	0.36	0.22	0.32	0.16	0.20
MgO	1.09	1.15	1.16	2.17	1.22	1.07	1.17	2.32	1.32	1.71	1.36	1.57	1.65	1.49	1.29	2.44
FeO	1.25	1.90	2.03	1.80	1.82	1.33	1.73	2.14	1.56	1.78	1.28	1.54	1.49	1.25	1.74	1.66
MnO	0.00	0.04	0.00	0.00	0.04	0.00	0.04	0.04	0.00	0.00	0.00	0.00	0.02	0.05	0.00	0.00
CaO	0.03	0.07	0.06	0.03	0.01	0.03	0.08	0.06	0.03	0.06	0.00	0.03	0.06	0.03	0.01	0.07
Na_2O	0.74	0.88	1.12	0.44	0.80	1.02	0.80	0.70	1.03	0.79	0.58	0.93	0.52	0.63	0.67	0.51
K_2O	9.30	9.02	9.03	9.99	9.46	9.36	9.35	9.37	9.53	9.60	10.05	9.63	9.95	10.08	9.76	9.80
Total	93.59	95.46	94.83	94.18	95.00	93.79	94.49	96.35	95.69	95.15	95.10	95.82	94.36	95.62	95.99	96.00
							cations per 11 oxygens									
Si	3.142	3.172	3.163	3.322	3.196	3.106	3.073	3.249	3.127	3.194	3.171	3.193	3.253	3.081	3.118	3.275
Al^{iv}	0.858	0.828	0.837	0.678	0.804	0.894	0.927	0.751	0.873	0.806	0.829	0.807	0.747	0.919	0.882	0.725
Al^{vi}	1.849	1.818	1.801	1.696	1.800	1.837	1.837	1.714	1.811	1.767	1.810	1.775	1.757	1.827	1.832	1.709
Ti	0.014	0.014	0.014	0.009	0.012	0.019	0.018	0.010	0.017	0.012	0.016	0.018	0.011	0.016	0.008	0.010
Mg	0.109	0.113	0.115	0.217	0.121	0.107	0.117	0.226	0.130	0.169	0.135	0.154	0.164	0.147	0.127	0.239
Fe	0.070	0.105	0.113	0.101	0.101	0.075	0.097	0.117	0.086	0.099	0.071	0.085	0.083	0.069	0.096	0.091
Mn	0.000	0.002	0.000	0.000	0.002	0.000	0.002	0.002	0.000	0.000	0.000	0.000	0.001	0.003	0.000	0.000
Σ oct	2.042	2.052	2.043	2.023	2.036	2.038	2.071	2.069	2.044	2.047	2.032	2.032	2.024	2.062	2.063	2.049
Ca	0.002	0.005	0.004	0.002	0.001	0.002	0.006	0.004	0.002	0.004	0.000	0.002	0.004	0.002	0.001	0.005
Na	0.096	0.112	0.145	0.057	0.103	0.133	0.104	0.089	0.102	0.102	0.074	0.119	0.068	0.081	0.086	0.065
K	0.797	0.759	0.767	0.855	0.801	0.803	0.798	0.783	0.813	0.813	0.851	0.809	0.848	0.851	0.820	0.821
Σ A	0.895	0.876	0.916	0.914	0.905	0.938	0.908	0.876	0.919	0.919	0.925	0.930	0.920	0.934	0.907	0.891
Fe/ Fe+Mg	0.391	0.482	0.496	0.318	0.455	0.412	0.453	0.341	0.398	0.369	0.345	0.356	0.336	0.319	0.430	0.276
marg	0.002	0.006	0.004	0.002	0.001	0.002	0.007	0.005	0.004	0.004	0.000	0.002	0.004	0.002	0.001	0.006
parag	0.107	0.128	0.158	0.062	0.114	0.142	0.115	0.102	0.111	0.111	0.080	0.128	0.074	0.087	0.095	0.073
musc	0.891	0.866	0.837	0.935	0.857	0.856	0.879	0.894	0.885	0.885	0.920	0.870	0.922	0.911	0.904	0.921

Representative phengite analyses (cont'd.)

	HF-17A 1-6 by gt	HF-17A 1-15 in gt	HF-17A 2-4 by gt	HF-17A 4-24 matrix	HF-17A 4-25 matrix	HF-17A 4-27 by gt	HF-27B 1-6 by gt	HF-27B 1-7 by gt	HF-27B 2-8 matrix
SiO_2	48.81	46.21	47.60	51.08	51.14	50.36	47.04	47.45	48.85
Al_2O_3	35.06	36.89	35.09	30.22	29.09	30.53	34.63	34.44	34.29
TiO_2	0.26	0.25	0.30	0.22	0.16	0.22	0.34	0.38	0.32
MgO	1.02	0.96	1.13	2.36	2.56	2.17	1.12	1.18	1.34
FeO	1.57	1.86	2.03	2.02	1.91	2.03	1.19	1.15	1.19
MnO	0.00	0.04	0.04	0.04	0.00	0.04	0.00	0.00	0.00
CaO	0.03	0.04	0.04	0.01	0.00	0.04	0.01	0.01	0.06
Na_2O	1.02	0.84	0.71	0.47	0.48	0.37	0.96	0.92	0.70
K_2O	9.28	9.01	9.71	9.48	9.87	9.76	9.83	9.39	10.00
Total	97.05	96.11	96.64	95.91	95.23	95.52	95.12	94.93	96.75
				cations per 11 oxygens					
Si	3.162	3.114	3.116	3.350	3.386	3.325	3.122	3.144	3.181
Al^{iv}	0.838	0.886	0.884	0.650	0.614	0.675	0.878	0.856	0.819
Al^{vi}	1.840	2.045	1.824	1.687	1.657	1.701	1.832	1.834	1.813
Ti	0.013	0.013	0.015	0.011	0.008	0.011	0.017	0.019	0.016
Mg	0.098	0.096	0.110	0.231	0.253	0.214	0.111	0.117	0.130
Fe	0.085	0.105	0.111	0.111	0.106	0.112	0.066	0.064	0.065
Mn	0.000	0.002	0.002	0.002	0.000	0.002	0.000	0.000	0.000
Σ oct	2.036	2.261	2.062	2.042	2.024	2.040	2.026	2.034	2.024
Ca	0.002	0.003	0.003	0.001	0.000	0.003	0.001	0.001	0.004
Na	0.128	0.110	0.090	0.060	0.062	0.048	0.124	0.118	0.088
K	0.767	0.775	0.811	0.793	0.834	0.822	0.832	0.794	0.831
Σ A	0.897	0.885	0.904	0.854	0.896	0.873	0.957	0.913	0.923
Fe/ Fe+Mg	0.464	0.522	0.502	0.325	0.295	0.344	0.373	0.354	0.333
marg	0.002	0.003	0.003	0.001	0.000	0.003	0.001	0.001	0.004
parag	0.143	0.124	0.100	0.070	0.069	0.055	0.130	0.129	0.095
musc	0.855	0.873	0.897	0.929	0.931	0.942	0.869	0.870	0.900

Representative biotite analyses

	HF-2D 1-1 by gt	HF-2D 2-2 by gt	HF-2E 1-3 by gt	HF-2E 2-5 matrix	HF-2E 3-2 x fol	HF-2E 4-3 by gt	HF-3A 1-5 by gt	HF-3A 2-5 by gt	HF-3A 3-4 by gt	HF-3A 3-7 matrix	HF-6A 1-13 matrix	HF-6A 2-1 by gt	HF-6A 2-21 by gt	HF-6B 1-1 by gt	HF-6B 2-1 matrix	HF-6B 3-1 by gt	HF-17A 1-4 by gt	HF-17A 2-2 by gt	HF-17A 4-26 by gt	HF-27B 1-20 by gt	HF-27B 2-1 by gt
SiO_2	35.47	38.40	35.36	36.18	36.73	36.27	36.73	36.15	36.73	37.49	37.77	37.27	37.67	36.66	37.55	35.38	37.25	36.54	36.55	38.07	37.38
Al_2O_3	19.01	22.30	18.83	18.72	18.44	18.25	19.59	18.94	19.77	19.20	19.59	19.62	18.73	19.79	19.79	19.71	18.56	19.53	19.96	19.29	18.69
TiO_2	1.13	1.03	1.22	1.08	1.37	0.97	0.72	0.98	0.76	1.13	1.23	0.61	1.20	1.40	1.40	1.07	1.51	1.52	1.96	2.26	1.20
MgO	10.55	7.27	10.64	12.01	11.34	11.27	11.03	11.79	12.21	12.52	12.84	12.97	12.28	11.90	11.90	12.52	10.57	10.34	10.58	11.84	13.42
FeO	19.23	16.51	19.54	17.90	17.40	19.17	18.83	18.11	17.50	17.05	14.68	15.92	15.56	16.87	16.87	16.96	18.21	18.30	17.24	15.18	14.61
MnO	0.14	0.05	0.05	0.05	0.06	0.00	0.09	0.11	0.08	0.08	0.02	0.08	0.11	0.13	0.13	0.17	0.17	0.06	0.08	0.11	0.11
CaO	0.00	0.00	0.01	0.00	0.00	0.04	0.06	0.07	0.06	0.00	0.00	0.03	0.01	0.00	0.00	0.00	0.02	0.02	0.00	0.06	0.00
Na_2O	0.26	0.06	0.16	0.18	0.06	0.07	0.21	0.17	0.21	0.26	0.10	0.08	0.01	0.10	0.10	0.15	0.09	0.14	0.17	0.09	0.14
K_2O	8.37	8.33	8.81	8.92	8.64	8.13	8.60	8.26	8.67	8.47	9.35	8.98	8.96	9.00	9.00	8.78	8.70	8.82	0.82	8.49	8.85
Total	94.15	93.94	94.61	95.05	94.04	94.16	95.87	94.58	96.01	96.18	95.57	95.56	94.53	95.86	95.94	94.74	95.09	95.28	95.36	95.39	94.40
											cations per 11 oxygens										
Si	2.717	2.857	2.703	2.728	2.782	2.763	2.745	2.731	2.725	2.763	2.778	2.757	2.811	2.720	2.767	2.666	2.798	2.744	2.727	2.798	2.784
Al^{iv}	1.283	1.143	1.297	1.272	1.218	1.237	1.255	1.269	1.275	1.237	1.222	1.243	1.189	1.280	1.233	1.334	1.202	1.256	1.273	1.202	1.216
Al^{vi}	0.434	0.813	0.400	0.392	0.429	0.402	0.471	0.418	0.454	0.431	0.477	0.468	0.459	0.451	0.480	0.417	0.442	0.473	0.483	0.469	0.425
Ti	0.066	0.058	0.071	0.062	0.079	0.056	0.041	0.056	0.043	0.063	0.069	0.034	0.068	0.079	0.028	0.061	0.086	0.087	0.111	0.126	0.068
Mg	1.204	0.806	1.212	1.350	1.280	1.279	1.228	1.328	1.350	1.375	1.407	1.430	1.366	1.316	1.400	1.406	1.183	1.157	1.176	1.297	1.489
Fe	1.232	1.027	1.249	1.129	1.102	1.221	1.177	1.144	1.086	1.051	0.903	0.985	0.971	1.047	1.003	1.069	1.144	1.149	1.076	0.933	0.910
Mn	0.009	0.003	0.003	0.003	0.004	0.000	0.006	0.007	0.005	0.005	0.001	0.005	0.007	0.008	0.005	0.011	0.011	0.004	0.005	0.007	0.007
Σ oct	2.945	2.707	2.935	2.936	2.894	2.958	2.923	2.953	2.938	2.925	2.857	2.932	2.871	2.901	2.916	2.964	2.866	2.870	2.851	2.832	2.899
Ca	0.000	0.000	0.001	0.000	0.000	0.003	0.005	0.006	0.005	0.000	0.000	0.002	0.001	0.000	0.004	0.000	0.002	0.002	0.000	0.005	0.000
Na	0.038	0.008	0.023	0.027	0.009	0.011	0.030	0.025	0.030	0.037	0.014	0.012	0.001	0.015	0.025	0.022	0.013	0.020	0.024	0.013	0.020
K	0.818	0.791	0.859	0.858	0.835	0.790	0.820	0.796	0.821	0.796	0.877	0.847	0.853	0.852	0.832	0.844	0.834	0.845	0.840	0.796	0.841
Σ A	0.856	0.799	0.883	0.885	0.844	0.804	0.855	0.827	0.856	0.833	0.891	0.861	0.855	0.867	0.861	0.866	0.849	0.867	0.864	0.814	0.861
Fe/ Fe+Mg	0.506	0.560	0.508	0.455	0.463	0.488	0.489	0.463	0.446	0.433	0.391	0.408	0.415	0.443	0.417	0.432	0.492	0.498	0.478	0.418	0.379

Representative chlorite analyses

	HF-2C 1-6 R-bio	HF-2C 1-7 R-bio	HF-2C 2-1	HF-2C 2-2	HF-3A 2-10	HF-3A 2-11	HF-6A 2-23	HF-17A 3-2	HF-17A 3-3	HF-27B 1-15	HF-27B 1-16
SiO_2	26.30	29.56	25.03	25.51	24.75	27.67	26.32	26.32	25.06	26.49	25.63
Al_2O_3	20.97	22.06	22.02	22.39	23.31	25.20	23.29	21.03	22.81	22.63	23.01
TiO_2	0.06	0.04	0.00	0.01	0.00	0.00	0.00	0.00	0.00	0.00	0.00
MgO	14.03	11.71	16.48	16.43	17.64	14.89	18.60	16.84	15.70	19.03	18.36
FeO	25.98	22.76	23.75	24.39	21.48	19.47	20.00	23.05	23.71	19.14	20.02
MnO	0.15	0.11	0.16	0.12	0.01	0.06	0.30	0.17	0.24	0.20	0.31
CaO	0.04	0.05	0.07	0.03	0.00	0.02	0.02	0.00	0.00	0.00	0.00
Total	87.52	86.31	87.51	88.88	87.18	87.31	88.52	87.41	87.52	87.49	87.33
	cations per 28 oxygens										
Si	5.555	6.137	5.245	5.265	5.134	5.596	5.319	5.485	5.240	5.392	5.264
Al	5.222	5.404	5.439	5.448	5.701	6.008	5.549	5.166	5.624	5.432	5.573
Ti	0.009	0.006	0.000	0.002	0.000	0.000	0.000	0.000	0.000	0.000	5.619
Mg	4.416	3.624	5.147	5.055	5.453	4.487	5.603	5.232	4.894	5.773	3.440
Fe	4.589	3.953	4.161	4.211	3.726	3.293	3.380	4.018	4.147	3.259	0.054
Mn	0.029	0.019	0.028	0.021	0.002	0.011	0.051	0.030	0.042	0.035	0.000
Ca	0.008	0.012	0.015	0.007	0.000	0.004	0.005	0.000	0.000	0.000	0.000
Fe/ Fe+Mg	0.510	0.522	0.447	0.454	0.406	0.423	0.376	0.434	0.459	0.361	0.380

Representative epidote analyses

	HF-2C 2-22 in gt	HF-2D 2-4	HF-E 3-1	HF-3A 1-8	HF-3A 3-14	HF-6A 1-9	HF-6A 1-10	HF-6A 2-5	HF-27B 1-17	HF-27B 1-18
SiO_2	38.54	38.38	37.19	36.55	37.63	37.81	39.17	38.57	38.63	40.37
Al_2O_3	28.20	28.27	27.23	26.96	28.04	28.31	30.14	28.47	30.31	29.87
TiO_2	0.06	0.00	0.00	0.04	0.00	0.00	0.00	0.00	0.00	0.00
MgO	0.12	0.08	0.00	0.36	0.11	0.10	0.07	0.13	0.13	0.20
FeO	7.28	6.66	7.48	10.71	6.28	6.03	4.84	6.30	5.24	4.49
MnO	0.24	0.22	0.36	0.19	0.11	0.00	0.00	0.08	0.27	0.15
CaO	21.98	23.46	22.64	21.04	22.80	22.68	23.54	22.48	21.86	21.73
TOTAL	97.21	97.07	95.93	97.05	95.68	95.60	98.31	96.75	97.02	97.53
	cations per 25 oxygens									
Si	6.018	6.008	5.930	5.797	5.974	5.994	6.006	6.036	6.015	6.210
Al	5.192	5.215	5.120	5.041	5.247	5.292	5.447	5.253	5.564	5.390
Ti	0.007	0.000	0.000	0.005	0.000	0.000	0.000	0.000	0.000	0.000
$*Fe^{3+}$	0.917	0.785	0.998	1.421	0.834	0.799	0.621	0.825	0.682	0.575
Mg	0.028	0.019	0.000	0.084	0.027	0.024	0.017	0.030	0.030	0.046
Mn	0.032	0.030	0.048	0.025	0.015	0.000	0.000	0.011	0.036	0.019
Ca	3.678	3.934	3.868	3.576	3.879	3.853	3.868	3.770	3.648	3.565
$FeAl_2Ep$	0.458	0.392	0.499	0.710	0.417	0.399	0.310	0.412	0.341	0.287

*All Fe recast as Fe^{3+}

Representative margarite analyses

	HF-2C 1-4	HF-2D 3-1	HF-2D 3-2	HF-2D 3-3	HF-6A 1-7	HF-6B 1-8	HF-27B 2-6	HF-27B 2-7
SiO_2	33.00	33.25	31.45	30.30	35.16	31.39	34.48	34.86
Al_2O_3	48.42	47.12	48.84	49.88	47.35	51.23	44.68	45.70
TiO_2	0.02	0.08	0.08	0.06	0.06	0.10	0.24	0.16
MgO	0.22	0.32	0.12	0.14	0.45	0.14	1.64	1.30
FeO	0.50	0.55	0.43	0.34	0.66	0.27	2.13	1.50
MnO	0.00	0.00	0.00	0.00	0.02	0.00	0.00	0.00
CaO	10.82	9.63	11.32	12.37	9.30	11.71	8.66	9.14
Na_2O	1.47	2.24	1.42	0.91	1.37	1.20	1.43	1.54
K_2O	0.64	0.28	0.13	0.15	1.71	0.19	2.08	1.52
Total	95.10	93.46	93.77	94.16	96.07	96.23	95.32	95.70
	cations per 11 oxygens							
Si	2.189	2.236	2.116	2.037	2.305	2.069	2.305	2.307
Al^{iv}	1.811	1.764	1.884	1.963	1.695	1.931	1.695	1.693
Al^{vi}	1.975	1.972	1.990	1.990	1.965	2.050	1.826	1.873
Ti	0.001	0.004	0.004	0.003	0.003	0.005	0.012	0.008
Mg	0.022	0.032	0.012	0.014	0.044	0.014	0.163	0.128
Fe	0.028	0.031	0.024	0.019	0.036	0.015	0.119	0.083
Mn	0.000	0.000	0.000	0.000	0.001	0.000	0.000	0.000
Σ oct	2.026	2.039	2.030	2.026	2.049	2.084	2.120	2.092
Ca	0.769	0.694	0.816	0.891	0.653	0.827	0.620	0.648
Na	0.189	0.294	0.185	0.119	0.174	0.153	0.185	0.197
K	0.054	0.024	0.011	0.013	0.143	0.016	0.177	0.128
Σ A	1.012	1.010	1.012	1.023	0.970	0.996	0.982	0.973
marg	0.560	0.687	0.806	0.871	0.673	0.830	0.631	0.666
parag	0.187	0.289	0.183	0.116	0.179	0.154	0.188	0.202
musc	0.053	0.024	0.011	0.013	0.147	0.016	0.180	0.132

TABLE 4-7

Representative analyses of amphibole, plagioclase, chlorite, and epidote in USH greenstones

Representative amphibole analyses

	HF-2A 1-1 actin C	HF-2A 1-3 hbl E	HF-2A 2-7 hbl matrix	HF-2A 3-1 actin C	HF-2A 3-3 actin mixed	HF-2A 3-5 hbl E	HF-2A 3-8 actin C	HF-2A 3-11 actin mixed	HF-2A 3-14 hbl E	HF-12 1-15 actin C	HF-12 1-16 hbl E	HF-12 2-1 actin C	HF-12 2-2 hbl E	HF-12 3-14 actin C	HF-12 3-15 hbl E	HF-12 3-18 hbl matrx
SiO_2	54.69	48.77	46.46	56.24	52.83	45.74	55.48	51.57	45.36	55.38	45.81	55.98	46.76	54.46	45.88	44.97
Al_2O_3	2.73	8.26	12.17	1.61	4.78	12.24	2.11	5.94	11.95	2.17	12.33	1.44	10.98	3.87	12.61	12.50
TiO_2	0.00	0.15	0.28	0.00	0.03	0.26	0.00	0.12	0.32	0.07	0.39	0.00	0.31	0.11	0.33	0.35
MgO	19.03	14.06	13.05	18.84	16.99	12.70	18.95	16.43	12.80	18.65	12.37	18.57	12.92	17.41	12.31	12.38
FeO	8.35	12.99	13.00	8.73	9.87	13.32	8.44	10.27	13.13	9.13	13.71	9.35	13.40	9.68	13.66	13.43
MnO	0.15	0.18	0.13	0.14	0.12	0.12	0.19	0.12	0.20	0.19	0.25	0.24	0.30	0.28	0.33	0.18
CaO	12.51	11.03	11.61	11.92	11.79	11.28	12.02	11.91	11.43	12.58	11.74	12.50	11.67	11.77	11.23	11.33
Na_2O	0.33	1.35	1.57	0.37	0.96	1.74	0.38	0.73	1.58	0.33	1.60	0.24	1.60	0.78	1.76	1.99
K_2O	0.06	0.23	0.30	0.06	0.14	0.29	0.05	0.09	0.27	0.02	0.14	0.05	0.28	0.10	0.19	0.12
Total	98.06	97.37	98.87	97.95	97.72	98.02	97.71	97.43	97.40	98.67	98.64	98.51	98.50	98.63	98.65	97.57
							cations per 23 oxygens									
Si	7.660	7.057	6.653	7.858	7.464	6.620	7.791	7.344	6.609	7.735	6.597	7.840	6.744	7.620	6.597	6.543
Al^{iv}	0.340	0.943	1.347	0.142	0.536	1.380	0.209	0.656	1.391	0.265	1.403	0.160	1.256	0.380	1.403	1.457
Al^{vi}	0.110	0.466	0.707	0.124	0.260	0.708	0.140	0.342	0.661	0.092	0.691	0.078	0.610	0.259	0.734	0.687
Ti	0.000	0.016	0.030	0.000	0.003	0.029	0.000	0.013	0.035	0.007	0.043	0.000	0.034	0.012	0.036	0.039
$*Fe^{3+}$	0.219	0.384	0.336	0.038	0.234	0.366	0.099	0.279	0.396	0.154	0.336	0.079	0.296	0.169	0.380	0.346
Mg	3.972	3.032	2.785	3.923	3.578	2.739	3.966	3.487	2.780	3.883	2.654	3.875	2.777	3.631	2.639	2.685
Fe^{2+}	0.759	1.188	1.221	0.982	0.932	1.246	0.892	0.944	1.204	0.913	1.315	1.016	1.320	0.964	1.263	1.288
Mn	0.018	0.022	0.016	0.017	0.014	0.015	0.023	0.014	0.025	0.022	0.030	0.028	0.037	0.033	0.040	0.022
Σ oct	5.078	5.108	5.095	5.084	5.021	5.103	5.120	5.074	5.101	5.071	5.069	5.076	5.074	5.068	5.090	5.067
Ca	1.878	1.710	1.781	1.784	1.785	1.750	1.808	1.817	1.785	1.883	1.811	1.876	1.804	1.765	1.730	1.767
Na(M4)	0.044	0.182	0.124	0.132	0.194	0.147	0.072	0.104	0.114	0.046	0.102	0.040	0.112	0.155	0.162	0.136
Na(A)	0.045	0.198	0.313	0.000	0.069	0.340	0.031	0.097	0.331	0.043	0.346	0.025	0.334	0.056	0.330	0.426
K	0.011	0.042	0.055	0.011	0.025	0.053	0.009	0.016	0.050	0.004	0.026	0.009	0.051	0.018	0.035	0.022
Σ A	0.056	0.240	0.368	0.011	0.094	0.393	0.040	0.113	0.381	0.047	0.372	0.034	0.385	0.074	0.365	0.448
Fe/Fe+Mg	0.160	0.282	0.305	0.200	0.207	0.313	0.184	0.213	0.302	0.190	0.331	0.208	0.322	0.210	0.324	0.324
Fe^{3+}/Fe_T	0.224	0.244	0.216	0.037	C.201	0.227	0.100	0.228	0.248	0.144	0.204	0.072	0.183	0.149	0.231	0.212

$*Fe^{3+}$ calculated according to the method of Spear and Kimball (1984).

Representative plagioclase analyses

	HF-2A 2-1 matrix C	HF-2A 2-2 matrix E	HF-2A 2-3 matrix C	HF-2A 2-9 matrix E	HF-12 1-1 pseudo E	HF-12 1-2 pseudo C	HF-12 1-10 pseudo E	HF-12 1-11 pseudo C	HF-12 3-9 matrix C	HF-12 3-10 matrix E	HF-12 3-11 matrix C	HF-12 3-12 matrix E	HF-12 4-11 pseudo C	HF-12 4-14 pseudo E
SiO_2	63.85	63.17	63.21	63.41	62.84	62.79	67.31	64.58	63.32	62.68	63.61	63.39	63.04	64.19
Al_2O_3	23.08	23.36	23.59	23.26	24.41	23.41	20.23	23.43	23.67	23.79	23.29	24.06	23.54	23.03
FeO	0.11	0.14	0.25	0.22	0.16	0.08	0.14	0.11	0.16	0.19	0.25	0.22	0.16	0.11
CaO	4.16	5.04	5.04	4.56	5.43	4.51	1.12	3.92	4.59	4.99	4.40	5.13	5.01	4.26
Na_2O	9.14	8.57	8.82	8.94	8.55	9.13	11.07	9.35	9.69	9.30	9.76	9.33	9.93	9.83
K_2O	0.09	0.09	0.07	0.09	0.07	0.14	0.07	0.09	0.11	0.11	0.13	0.07	0.09	0.09
Total	100.42	100.36	100.98	100.47	101.46	100.07	99.94	101.47	101.54	101.06	101.43	102.20	101.78	101.51
	cations per 8 oxygens													
Si	2.807	2.784	2.773	2.791	2.745	2.791	2.964	2.815	2.768	2.755	2.796	2.755	2.757	2.801
Al	1.196	1.214	1.220	1.207	1.257	1.227	1.050	1.204	1.220	1.233	1.188	1.233	1.214	1.185
Fe	0.004	0.005	0.009	0.008	0.006	0.003	0.005	0.004	0.006	0.007	0.009	0.008	0.006	0.004
Ca	0.196	0.238	0.237	0.215	0.254	0.215	0.053	0.183	0.215	0.235	0.204	0.239	0.235	0.199
Na	0.779	0.732	0.750	0.763	0.724	0.787	0.945	0.790	0.821	0.793	0.819	0.786	0.842	0.832
K	0.005	0.005	0.004	0.005	0.004	0.008	0.004	0.005	0.006	0.006	0.007	0.004	0.005	0.005
An	0.200	0.244	0.239	0.219	0.259	0.213	0.053	0.187	0.206	0.227	0.198	0.232	0.217	0.192
Ab	0.795	0.751	0.757	0.776	0.737	0.779	0.943	0.808	0.788	0.767	0.795	0.764	0.778	0.803
Or	0.005	0.005	0.004	0.005	0.004	0.008	0.004	0.005	0.006	0.006	0.007	0.004	0.005	0.005

Representative epidote analyses

	HF-2A 2-10 E	HF-2A 3-15 E	HF-12 2-5 C	HF-12 2-6 E	HF-12 3-4 E	HF-12 3-5 C	HF-12 3-6 E	HF-12 3-8 E	HF-12 1-5 E	HF-12 1-6 C	HF-12 1-7 E	HF-12 1-8 C	HF-12 4-4 E	HF-12 4-6 E	HF-12 4-10 E
	←matrix→								←pseudomorph→						
SiO_2	38.77	38.48	38.71	39.17	39.06	38.50	39.25	39.09	38.45	39.09	39.55	38.26	39.03	37.98	39.30
Al_2O_3	25.57	24.56	27.22	28.43	25.80	25.75	28.32	26.03	25.88	28.68	29.76	26.75	25.94	25.34	28.57
TiO_2	0.00	0.00	0.00	0.00	0.00	0.00	0.00	0.00	0.00	0.00	0.00	0.00	0.00	0.00	0.00
MgO	0.05	0.10	0.02	0.07	0.11	0.11	0.13	0.29	0.07	0.04	0.06	0.06	0.14	0.22	0.12
FeO	9.73	10.80	7.65	6.90	8.43	8.69	5.21	8.27	9.63	6.01	4.72	8.41	9.18	9.32	5.74
MnO	0.00	0.00	0.00	0.02	0.19	0.14	0.22	0.20	0.09	0.00	0.04	0.03	0.18	0.13	0.16
CaO	23.28	23.76	23.94	24.12	23.71	23.48	23.67	23.24	23.44	24.10	24.07	23.95	23.50	23.56	23.89
Total	98.48	98.88	98.39	99.47	98.23	97.63	97.38	98.12	98.64	98.59	98.72	98.40	98.98	97.59	98.41
	cations per 25 oxygens														
Si	6.059	6.028	6.017	5.999	6.097	6.058	6.100	6.101	6.006	6.021	6.046	5.973	6.039	6.000	6.054
Al	4.711	4.538	4.988	5.133	4.749	4.778	5.189	4.789	4.766	5.207	5.362	4.922	4.731	4.719	5.189
Ti	0.000	0.000	0.000	0.000	0.000	0.000	0.000	0.000	0.000	0.000	0.000	0.000	0.000	0.000	0.000
*Fe^{3+}	1.271	1.416	0.994	0.884	1.100	1.144	0.677	1.079	1.258	0.774	0.603	1.098	1.188	1.231	0.739
Mg	0.011	0.023	0.005	0.016	0.021	0.025	0.030	0.067	0.016	0.009	0.014	0.014	0.032	0.052	0.027
Mn	0.000	0.000	0.000	0.002	0.025	0.018	0.029	0.026	0.012	0.000	0.005	0.004	0.023	0.018	0.021
Ca	3.898	3.991	3.987	3.958	3.966	3.959	3.942	3.887	3.923	3.978	3.942	4.006	3.896	3.987	3.944
$FeAl_2Ep$	0.635	0.708	0.497	0.442	0.550	0.572	0.338	0.539	0.629	0.387	0.301	0.549	0.594	0.615	0.369

*All Fe recast as Fe^{3+}.

Representative chlorite analyses

	HF-2A 1-6	HF-2A 2-8	HF-12 1-4	HF-12 1-9	HF-12 1-17	HF-12 3-13	HF-12 4-1	HF-12 4-2
	---matrix---		------pseudo-------			matrx	---pseudo---	
SiO_2	27.53	27.53	27.62	27.57	27.56	26.60	27.11	26.95
Al_2O_3	21.78	22.07	21.81	21.74	22.01	21.65	21.86	21.31
TiO_2	0.00	0.01	0.02	0.00	0.01	0.00	0.00	0.00
MgO	22.50	22.77	22.46	22.59	22.36	22.84	22.96	22.71
FeO	15.37	14.99	15.35	15.39	15.26	15.47	15.71	15.55
MnO	0.11	0.14	0.10	0.16	0.13	0.18	0.23	0.18
CaO	0.06	0.01	0.05	0.08	0.09	0.13	0.06	0.25
TOTAL	87.34	87.52	87.40	87.53	87.41	86.87	87.94	86.95
	cations per 28 oxygens							
Si	5.501	5.478	5.512	5.501	5.498	5.368	5.402	5.435
Al	5.131	5.179	5.133	5.113	5.177	5.150	5.137	5.066
Ti	0.000	0.001	0.003	0.000	0.001	0.000	0.000	0.000
Mg	6.702	6.753	6.680	6.716	6.649	6.870	6.820	6.824
Fe	2.569	2.495	2.562	2.567	2.546	2.611	2.619	2.622
Mn	0.018	0.023	0.017	0.027	0.022	0.030	0.039	0.030
Ca	0.012	0.003	0.010	0.018	0.019	0.029	0.013	0.055
Fe/Fe+Mg	0.277	0.270	0.277	0.277	0.277	0.275	0.277	0.278

CHAPTER 5

PETROLOGIC CONSTRAINTS ON THE BURIAL, IMBRICATION, METAMORPHISM AND UPLIFT HISTORY OF THE SW TAUERN WINDOW

INTRODUCTION

The two preceding chapters have focused primarily on the use of petrologic data to reconstruct the P-T histories of two tectonically juxtaposed units, the Lower and Upper Schieferhülle series. The P-T conditions experienced by these two packages of rocks provide information on the tectonic and thermal history of the area and on the dynamics of continent-continent collision. The principal aim of this chapter is to use this petrologic data base to develop a self-consistent model of the burial, imbrication, metamorphism, and uplift histories of the rocks presently exposed in the southwest Tauern Window, and to relate this model to large-scale processes involved in the Alpine orogeny.

Relating P-T data to an absolute timescale is clearly a necessary step in evaluating the relationships between tectonism and metamorphism. No age determinations were made as a part of this thesis, but geochronological data for this area of the Tauern Window are available in the published literature and are compiled in this chapter. By combining age determinations with the petrologic data from the previous two chapters, it is possible to place numerical constraints on burial rates, the thermal parameters of metamorphism, timing of tectonic events, and variation of uplift and cooling rates with time. These data provide a detailed view of the Alpine orogeny in this region of the window.

COMPARISON OF THE LSH AND USH P-T PATHS

One of the problems in reconstructing the tectonic history of the Tauern Window is documenting the extent to which the continental rocks of the LSH and the oceanic rocks of the USH shared a common history. In

the central portion of the window the two units are separated by the Eclogite Zone, which is characterized by blueschists and eclogites that record pressures of ~20 kb (Holland, 1979; Franz and Spear, 1983). There are no reliable geochonological data on the rocks of the Eclogite Zone and it is not possible to document unambiguously the timing of the eclogite facies metamorphism relative to the dominant metamorphism of the surrounding LSH and USH. If the ages of metamorphism are the same in all three units, each unit must have been metamorphosed separately (since there is no evidence for 20 kb conditions in the LSH or USH) and tectonic juxtaposition must have occurred after this metamorphism. Alternatively, the eclogite facies metamorphism may be an earlier event that predated imbrication of the units; in this case, final metamorphism would have affected all three units 'en masse'.

No Eclogite Zone separates the USH from the LSH in the area of this study, but the implications of the scenarios described above remain the same; it is essential to any tectonic reconstruction to determine the relative timing of imbrication and metamorphism of the units. To this end, the P-T paths constructed for the LSH and USH are compared with one another in Figure 5-1. Several important differences exist between the paths, of which the most notable are the recorded values of P_{max} and T_{max}: $P_{max} \approx$ 10 kb in the LSH and 7 to 7.5 kb in the USH, and $T_{max} \approx$ 550°C in the LSH and 475°C in the USH. However, the overall form of the two paths is similar.

It is difficult to reconstruct the early history of either unit with any degree of certainty, although the lack of evidence for early glaucophane and the preservation of pseudomorphs after lawsonite in both the LSH and the USH suggests similar burial trajectories for the

Figure 5-1. Diagram comparing the P-T paths for the LSH and USH, compiled from Figs. 3-13 and 4-17. Note that the values of P_{max} and T_{max} differ by approximately 3 kb and 75° between the two units. Note also that the uplift curves for the two units, as constrained by the fluid inclusion data (Chapters 3 and 4), cross one another at ~425°C, 2.3 kb; the shaded area indicates a conservative estimate of the uncertainty in location of this crossover. Letters (a to c, a' to c') indicate points of reversal in P-T paths determined from modeling of zoned garnets; see text.

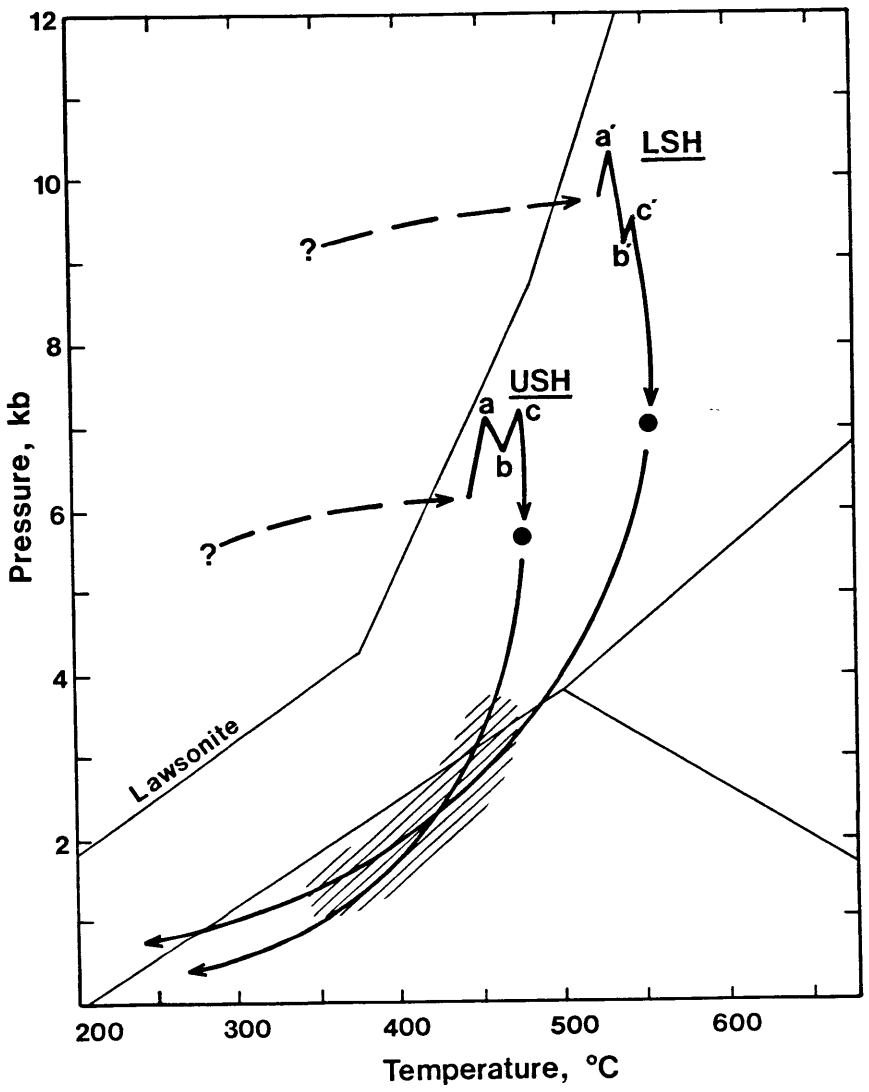
12
10
8
6
4
2
Pressure, kb
200
300
400
500
600
Temperature, °C
a'
LSH
c'
b'
?
USH
a
c
b
?
Lawsonite

two units. This does not prove that the units were imbricated during the burial phase of metamorphism, but does imply that similar tectonic processes affected both units at this time. The results of the thermal modeling discussed below are consistent with imbrication prior to attainment of T_{max}.

The most conclusive petrologic evidence for the timing of imbrication of the two packages of rocks comes from the thermodynamic modeling of garnet zonation (Spear and Selverstone, 1983). Reversals in trend of the P-T paths calculated from zoned garnets can be correlated between the LSH and USH, implying that the two units shared a common history throughout the time interval of garnet growth. For both the LSH and USH the paths determined from the garnet zoning show four stages alternating between positive and negative values of dP/dT (Fig. 5-1). Despite variation in the lengths of the P-T segments between the two units, the slopes are quite similar; this similarity is the more remarkable for resulting from modeling of several samples containing three different mineral assemblages. The good correlation between these paths argues strongly that the LSH and USH were imbricated prior to the onset of garnet growth, and thereafter behaved as a single tectonic unit.

A significant result of the correlation between the garnet zoning paths for the LSH and USH is that lines connecting the points of reversal in trend of the paths approximate constant time lines, assuming that the tectonic events responsible for the reversals acted on both units simultaneously. Thus, three iso-time lines can be constructed between the LSH and USH paths: one at the first transition from burial to uplift (a-a' in Fig. 5-1), a second marking the start of the next phase of burial (b-b'), and the third at the onset of the final phase of

uplift (c-c'). It is important to note that the starting and end points of the paths (the cores and rims of garnets, respectively) do not necessarily represent constant time lines. The onset of garnet growth in a particular rock occurs in response to intersection of the P-T path with the garnet-in reaction for a specific bulk composition, and may also depend on kinetic factors. There is no reason to expect that garnet growth should have begun simultaneously in the different lithologies of the LSH and USH. Similarly, the termination of garnet growth is probably controlled dominantly by attainment of T_{max} and associated devolatilization, which are unlikely to have occurred at the same time in different rocks. Thus, no tectonic significance should be attributed to the different P-T lengths of the initial and final segments of the garnet growth paths in the LSH versus the USH.

In contrast, the lengths of the middle two path segments in the two units (a to c and a' to c' in Fig. 5-1) may well be tectonically important. Ideally, if the LSH and USH behaved as a single unit subjected to identical tectonic events, the lengths of each of these line segments would be the same for the LSH as for the USH. The fact that they differ between the units can be interpreted in two ways: (1) due to uncertainties in the garnet zoning technique for calculating P-T paths, the difference in length of these segments between the units is not significant, or (2) the variations are real and reflect a history of ductile shearing and/or differential uplift between the LSH and USH such that constant distances were not maintained between specific points in the units during deformation. It is not yet possible to eliminate the first explanation, but the consequences of assuming the second case are discussed more fully in a subsequent section.

An additional feature of interest in Figure 5-1 is the intersection and crossover of the LSH and USH P-T paths at conditions of ~400-450°C, 2-3 kb. Based on the petrologic data, at the conditions of maximum burial of the LSH and USH the units were separated by ~3 kb, or approximately 10-11 km of vertical section; both units are now exposed at similar elevations and are separated across strike by only ~2 km of section. These observations point to a history of differential uplift of the units, which could cause their P-T paths to intersect and cross during uplift. However, other factors can also cause such a crossover in P-T paths, as is discussed in a later section.

AGE CONSTRAINTS

Isotopic and fission track mineral ages can be used to date either the time of growth of a specific mineral in an assemblage or the time at which the host rock cooled below the closure temperature (T_c) for that mineral-isotopic system. The distinction between growth and cooling ages depends upon the maximum temperature attained by a rock during and following growth of the specific mineral. Geochronologic data are available for a variety of different mineral phases in both the LSH and USH within the confines of the study area and a few adjacent localities. Although some of the data on amphibole grains can be interpreted as growth ages, most of the dates appear to be cooling ages. These ages represent the times at which the rocks were at specific temperatures during cooling, and thus place constraints on the cooling rates experienced by the units during unroofing of the mountain belt. Because the P-T paths are known, however, cooling ages also constrain the uplift

rates during exhumation.

Figure 5-2 shows the P-T trajectories of the LSH and USH along with ages determined from the following systems: (1) K/Ar in hornblende, $T_c \approx 530 \pm 30^\circ C$; (2) K/Ar in white mica, $T_c \approx 350 \pm 30^\circ C$; and (3) K/Ar and Rb/Sr in biotite, $T_c \approx 300 \pm 30^\circ C$ (closure temperatures quoted here are based on those cited by Harrison and McDougall, 1980). In each case, a dotted line has been extended up from the closure temperature on the T-axis to the point of intersection with the P-T path of the relevant rock unit. For example, K/Ar ages on white mica in the LSH indicate that the rocks cooled through a temperature of $350 \pm 30^\circ C$ at a time of 17-20 Ma, and the P-T path shows that the rocks were at a depth corresponding to a pressure of ~1.8 kb at this time. In this figure, the closure temperatures are shown as constants, although the real value of T_c in a specific example will depend on both cooling rate and grain size (Dodson, 1973); in subsequent figures, uncertainites are shown that take into account both the errors in location of the P-T path itself and the possible variation in value of T_c.

These age data and the corresponding temperature and depth conditions are compiled in Table 5-1, based on the assumption that 1 kb = 3.5 km of overburden (for an average rock density of 2.85 g cm^{-3}). Also listed in the table are age apatite fission track ages from a study by Grundmann and Morteani (in press). These data were obtained on samples of the ZG in the NE portion of the study area, and it is assumed here that the LSH samples in contact with the ZG should yield approximately the same ages. The depth at which the rocks passed through a temperature of 105-120°C (range in $\sim T_c$ for annealing of fission tracks in apatite;

Figure 5-2. Dated PTt paths for the LSH and USH obtained by combining the mineral ages from Table 5-1 with the P-T paths of Fig. 5-1. The dotted lines at 300, 350, and 530°C represent approximate closure temperatures for Rb/Sr in biotite and K/Ar in phengite and hornblende (Harrison and McDougall, 1980), and are extended up to points of intersection with the P-T curves. Ages are shown in bold face, in millions of years. Sources of data are given in Table 5-1; see text for further discussion.

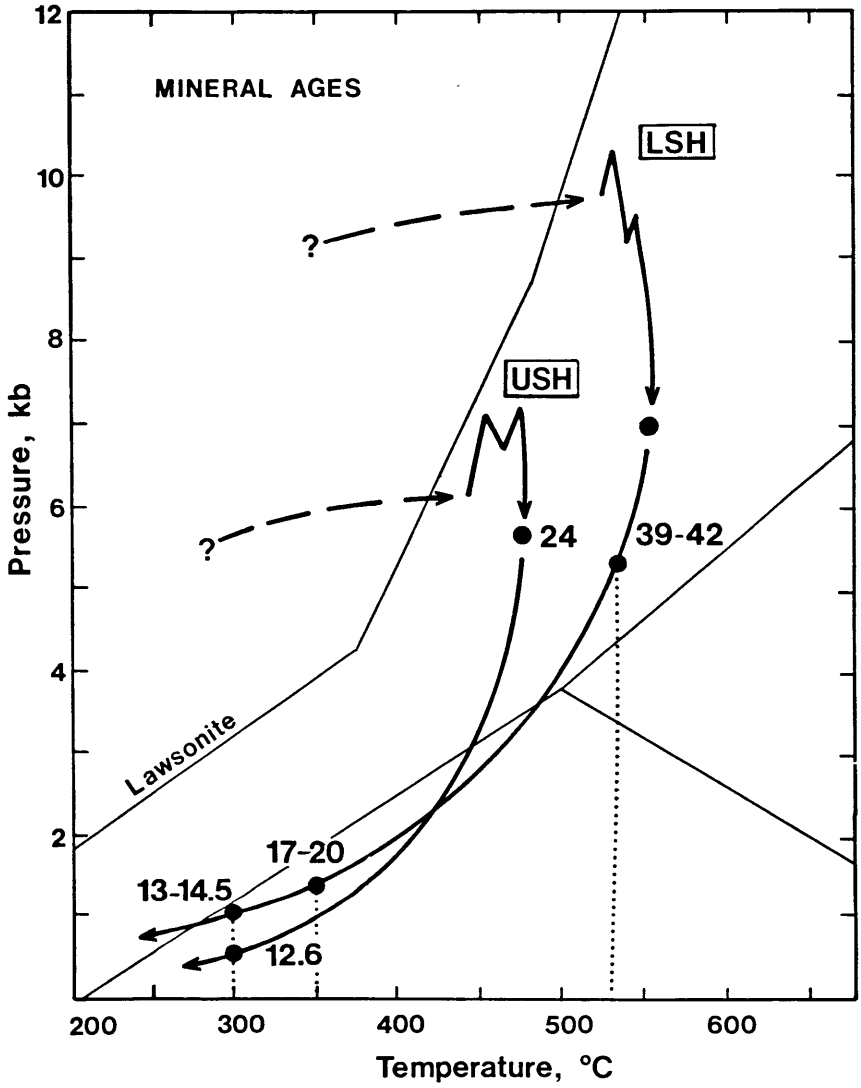
MINERAL AGES
LSH
USH
?
?
24
39-42
17-20
13-14.5
12.6
Lawsonite
Pressure, kb
Temperature, °C
12
10
8
6
4
2
200
300
400
500
600

Table 5-1 - Time-temperature-depth data for the LSH and USH determined by correlating mineral cooling ages with the P-T paths of Figure 5-1.

Unit	System	Mineral	~T_C, °C	Age, Ma	Depth, km	Ref
LSH	K/Ar	Hornblende	530±30	39-42	14-28	(1)
	K/Ar	Phengite	350±30	17-20	4.4-6.3	(1)
	K/Ar; Rb/Sr	Biotite	300±30	13-14.5	2.8-4.4	(1)
	Fission tracks	Apatite	105-120	5-6.5	1-3	(2)
USH	K/Ar	Actinolite core	*	60	>15?	(1)
	K/Ar	Hornblende rim	*	24	15-25	(1)
	Rb/Sr	Biotite	300±30	12-13	1-4	(3)

* Amphibole ages for the USH repreent growth rather than cooling ages; see text for discussion. Depths determined from Figure 5-2, assuming 1 kb = 3.5 km of overburden. References: (1) Raith et al., 1978; (2) Grundmann and Morteani, in press; (3) Borsi et al., 1978. Closure temperatures (T_C) are those cited by Harrison and McDougall (1980), Grundmann and Morteani (in press), and Parrish (1983).

Parrish, 1984; Grundmann and Morteani, in press) was estimated by extrapolating the P-T path to surface conditions, e.g. 0 kb at ~15°C.

One of the ages presented in Figure 5-2 and Table 5-1 requires additional explanation. Raith et al. (1978) report K/Ar ages of 24 Ma for hornblende rims surrounding actinolite from the USH ~10 km east of the study area. If the dated samples experienced a similar metamorphic history to the USH in the study area, the temperature never exceeded T_c for Ar diffusion in amphibole, and the 24 Ma age must be a growth age. It must also represent an <u>average</u> hornblende age unless only an infinitessimal portion of the rim was analyzed. Correlation of this age with a single point on the USH P-T curve is thus difficult. As an approximation, it is assumed here that hornblende maintained equilibrium with the surrounding phases in the matrix until T_{max} was attained, and that little reequilibration occurred during cooling (due to the relatively low temperatures of metamorphism in the USH). Thus, the 24 Ma age is tentatively correlated with T_{max} in the USH, although this assignment is clearly only approximate until further age dates are obtained on this unit. Coarse actinolite grains from the same locality yield ages of 60 Ma (Raith et al., 1978); due to the lack of quantitative information on actinolite stability in the USH, however, no attempt has been made to locate this age on the USH P-T path. The low initial K contents of actinolite in any case lead to large uncertainties in K/Ar ages determined from this mineral.

Information on the early history of both units comes from the ages of the youngest sediments incorporated in the USH series, which Frisch (1980) postulates are lower Upper Cretaceous in age based on correlations with similar fossiliferous units to the west; this assignment

corresponds to an age of ~80 to 90 Ma. A similar conclusion was reached by Oberhauser (1968, cited in Hawkesworth, 1976) regarding the age of the youngest rocks preserved in the eastern part of the Tauern Window. These ages imply that burial of the USH, and by inference the LSH, cannot have begun prior to 80 Ma.

Detailed studies by Hawkesworth (1976) and Borsi et al. (1978) indicate extensive resetting of ages in the Caledonian to Hercynian rocks of the Austroalpine Altkristallin adjacent to the contact with the underlying rocks of the Tauern Window. Rb/Sr whole rock ages in the AA Altkristallin fall in the range 380±30 Ma, but a zone of intensely retrogressed rocks at the base of the AA along the eastern margin of the Tauern Window yields mineral ages of 59-83 Ma, with the youngest ages closest to the contact (Hawkesworth, 1976). These ages were determined on minerals that are physically aligned in a foliation that can clearly be related to thrust movement of the AA units over the rocks of the Tauern Window, and the ages thus provide a minimum estimate for the timing of movement of the AA nappes. Near the southwestern border of the window, Borsi et al. (1978) report that Rb/Sr cooling ages of biotite have been reset to values of 16-30 Ma in the AA within 5 km of the contact with the USH, whereas elsewhere in the AA they cluster around 280±15 Ma. It is clear from these data that the tectonic juxtaposition of the Austroalpine nappes with the underlying rocks of the Tauern Window resulted in heating of the basal AA units to temperatures sufficient to grow biotite and/or reset the Rb/Sr mineral ages, while generally preserving the whole rock ages. According to Hawkesworth (1976), the isotopic data are most consistent with overthrusting of the AA Altkristallin by ~65 Ma; in his interpretation, the younger mineral

ages are cooling ages recorded by biotites that were heated above T_c during the thrusting event.

Taken together, these data indicate that burial of the LSH and USH beneath the Austroalpine units began sometime after 80 Ma and was complete by ~60 Ma. Following this overthrusting event, the rocks remained at depth and underwent heating in response to the thickening of the crust. This heating phase continued after the onset of uplift: the LSH reached T_{max} at ~40 Ma and the USH attained its maximum temperatures at ~24 Ma. Exposure of the rocks at the surface occurred within the last 5 Ma, based on the apatite fission track ages discussed by Grundmann and Morteani (in press).

Despite the magnitude of the uncertainties in many of the ages discussed above, and in the correlation of these ages with the LSH and USH P-T paths, the overall patterns that emerge shed light on many aspects of the Alpine orogeny in this area. It is hoped that in the future more detailed age determinations, including $^{40}Ar/^{39}Ar$ work (as applied by Frank and Stettler, 1979, in the Swiss Alps), will become available for the SW Tauern area. The following discussion is intended to provide a model to be tested by such future work. It is also meant to emphasize the importance of combining P-T data with geochronologic studies by illustrating the different time-temperature-depth histories experienced by adjacent packages of rocks with similar tectonic histories.

UPLIFT AND COOLING HISTORIES

Rate determinations

All of the pressure-temperature-time data discussed above and presented in Table 5-1 were used to construct the temperature-time (T-t) and depth-time (Z-t) diagrams shown in Figure 5-3. The boxes in these diagrams represent dated temperature and depth conditions for the LSH and USH from 40 Ma to the present, and inferred conditions for times prior to 40 Ma. Curves have been empirically constructed to pass through these data boxes; the early portions of these curves, for which the uncertainties are greatest, are indicated by dashed lines and should only be considered as approximations. Although many different curves could be envisaged that would pass through the data points, those shown here were constructed specifically to be consistent with the P-T paths for the two units. The curves show clearly the time interval separating the conditions of maximum burial from the attainment of maximum temperature in both the LSH and USH, and also the 15-20 Ma delay in reaching T_{max} experienced by the USH relative to the LSH. What is particularly striking, however, is the difference that exists between the Z-t curves for the two units; these curves indicate that for a significant length of time, the LSH was at shallower depths than the USH during uplift.

Cooling and uplift rates for the LSH and USH were obtained by noting that the instantaneous slope of a temperature-time curve is dT/dt, whereas for a depth-time plot it is dZ/dt. These differentials are numerically equal to instantaneous values of the heating or cooling and burial or uplift rates, respectively. Thus, if the PTt path of a rock is sufficiently well-known, it is theoretically possible to evaluate the variation with time of these rates throughout much of the

metamorphic history by differentiating the T-t and Z-t curves for the rock. In practice, such detailed petrologic and geochronologic data are often not available and it is only possible to estimate time-averaged rates between two or more dated points (e.g. Hodges, 1982). In the case of the LSH and USH paths, however, sufficient data exist on the PTt history of the rocks to permit a more detailed evaluation of the uplift and cooling rates.

Plots showing dT/dt versus time and dZ/dt versus time for both the LSH and USH are presented in Figure 5-4. The boxes in these diagrams were obtained by numerically evaluating the slope of the tangent to each of the dated points in Figure 5-3, and assigning reasonable uncertainties to these values. Curves were then fit empirically to these data points and in accord with the requirements that dT/dt = 0 at T_{max} and dZ/dt = 0 at P_{max} (Z_{max}) for each unit. Further constraints were imposed by the shapes of the T-t and Z-t curves over the remaining intervals. Again, as for Figure 5-3, there is considerable latitude in drawing of the curves, but the configuration shown in Figure 5-4 is consistent with the petrologic and age data presented above. Note that it is not possible, in either Figure 5-3 or Figure 5-4, to take into account the reversals in the P-T paths obtained from the analysis of garnet zoning, due to the absence of geochronologic data on the timing or duration of these reversals.

Figure 5-4 indicates not only how the uplift and cooling histories of the LSH and USH differ from one another, but also how these rates varied with time within each of these two units. Within the LSH, cooling commenced at ~40 Ma and reached a rate of 20-25^{o}C/Ma prior to exposure of the rocks at the surface. For the first 15 million years of this

Figure 5-3. Temperature-time and depth-time diagrams for the LSH (shaded boxes) and USH (open boxes), based on data in Fig. 5-2 and constraints on onset and culmination of continental collision in the Eastern Alps. Temperature and depth conditions at 80 Ma are hypothetical, based on the assumption that the rocks lay on a geotherm similar to the one shown in Fig. 5-6. Time of attainment of P_{max} is based on the data of Hawkesworth (1976). Dashed boxes illustrate the large uncertainties associated with the 24 Ma hornblende age in the USH. Curves were fit by eye to the data boxes; dashed where approximate. Note lag in attainment of T_{max} by USH relative to LSH, and dissimilar uplift histories of the two units between 40 and 15 Ma.

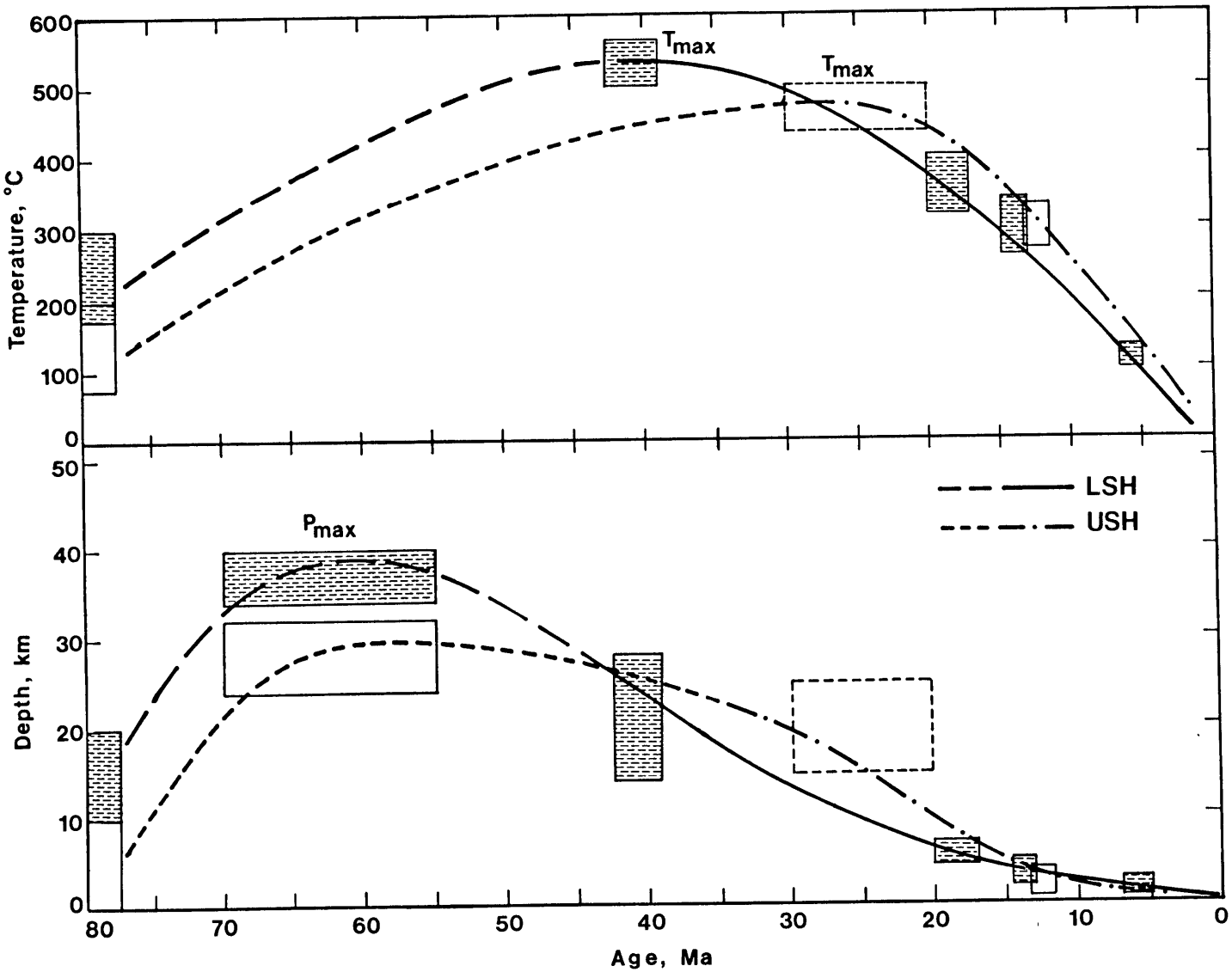
600
500
400
300
200
100
0
Temperature, °C
Tmax
Tmax
LSH
USH
50
40
30
20
10
0
Depth, km
Pmax
80
70
60
50
40
30
20
10
0
Age, Ma

Figure 5-4. Plots of dT/dt vs. time and dZ/dt vs. time for the LSH and USH, determined from slopes of T-t and Z-t curves in Fig. 5-3; symbols are the same as in that figure. Thin dashed lined represent transitions between heating and cooling (upper diagram) and burial and uplift (lower diagram); negative values of dT/dt and dZ/dt correspond to cooling and uplift rates, respectively. The uplift rate curves vary markedly for the two units between 55 and 15 Ma and indicate a history of differential uplift; this is consistent with petrologic and field data indicating thinning of the intervening units from ~10 km to ~2-3 km during uplift. Dotted line indicates the uplift rates used in thermal modeling calculations; see text.

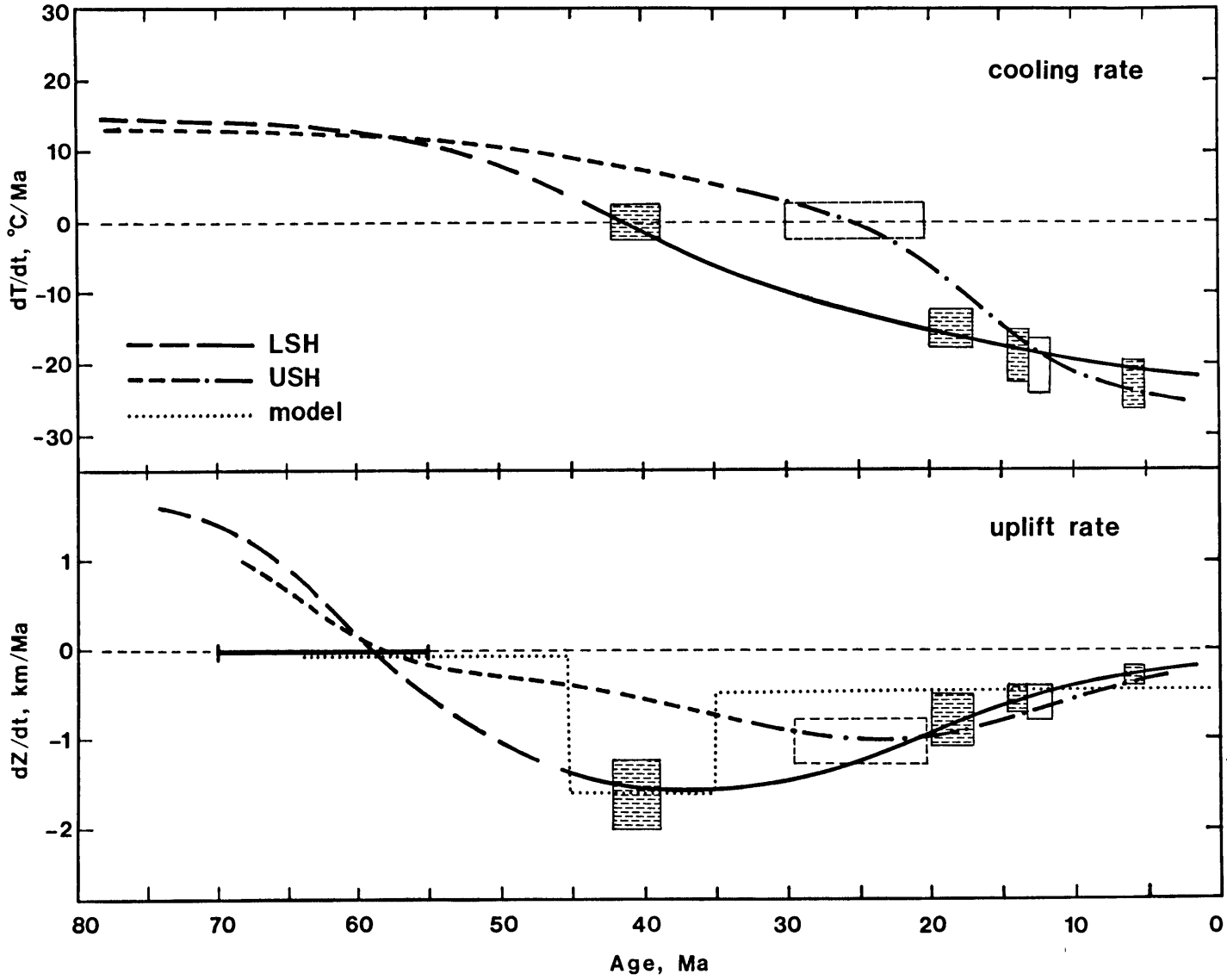
cooling rate
uplift rate
LSH
USH
model
dT/dt, °C/Ma
dZ/dt, km/Ma
Age, Ma
30
20
10
0
-10
-20
-30
1
0
-1
-2
80
70
60
50
40
30
20
10
0

interval, the USH was still undergoing heating, although by 10 Ma, the cooling rates of the two units are virtually indistinguishable. Uplift of both units began at approximately the same time, but within the LSH the initial rates were considerably faster than those in the USH at any given time (e.g. ~1.5 versus 0.4 km/Ma, respectively, at 40 Ma). From 25 Ma until exposure at the surface, however, the USH rates exceed those of the LSH. In both units, the maximum uplift rates occur at or shortly after the thermal peak of metamorphism. Estimated present-day uplift rates of ~0.2 to 0.4 km/Ma are in excellent agreement with those determined by Grundmann and Morteani (in press) based on fission track dating of samples separated by considerable vertical relief in the eastern part of the study area.

Uncertainties.

There are many sources of error in the uplift and cooling rates presented above. These uncertainties can be divided into four principal categories, each of which is briefly discussed here:

(1) Errors in the age determinations. Errors in this category stem from uncertainties in the estimated closure temperature (which is itself a weak function of cooling rate) for each mineral system, and from the determination of the absolute age at which the mineral passed through this temperature during cooling of the rock. Additional uncertainties are introduced by using age determinations for samples other than those from which the petrologic data were obtained. This is particularly the case with respect to the 24 Ma age for T_{max} in the USH; if this age is significantly in error (e.g. underestimates the age of T_{max} by >6-7 Ma), the Z-t paths for the USH and the LSH would be indistinguishable from

~40 Ma to the present. However, this would not change the conclusion that the initial uplift rates differed between the two units. Further work is necessary to date the USH P-T path accurately.

(2) Errors associated with the direct correlation of pressure with depth. The total pressure experienced by a rock is here considered to be due only to the thickness of the overburden. This does not take into account the possibility of periods of hydrostatic rather than lithostatic pressure conditions, nor does it consider the effects of tectonic overpressure. Both of these possibilities are thought to be of only minor significance for the LSH and USH in light of textural evidence for ductile behavior of the rocks throughout much of their history.

(3) Errors in the PTt paths. Accurate determination of the depth conditions corresponding to a dated temperature rests upon knowledge of both the curvature and position of a rock's path in P-T space. Evaluation of the relationships between dT/dt and time and dZ/dt and time is possible only if the curvatures of the T-t and Z-t plots are well-constrained, and these in turn are derived from the curvature of the PTt path. Because it is the slopes of these T-t and Z-t paths that are of interest, the curvature of the PTt path is ultimately more important in determining the time dependence of the uplift and cooling rates than is accurate positioning of the path. Thus, constraining the shape of the uplift path, e.g. from fluid inclusion data, is a critical factor in meaningful construction of diagrams such as Figure 5-4.

(4) Errors associated with the determination of empirical relationships between dT/dt and time and dZ/dt and time. In many orogenic terranes the uplift rate is likely to be a complex function of time due to ongoing overthrusting or folding of the rocks during the exhumation

process. These tectonic processes will almost certainly produce perturbations that cannot be resolved by petrologic techniques, and hence will not appear on the PTt path. Representation of the dT/dt-time and dZ/dt-time relationships by smooth curves will thus lead only to time-averaged values of the uplift and cooling rates over certain portions of the PTt loop.

Despite this lengthy list of potential uncertainties, the uplift and cooling data presented in Figure 5-4 for the LSH and USH provide important information on the histories of these units that is not readily acccessible by other techniques. It is not possible, for either the LSH or the USH, to construct an uplift path from T_{max} to the surface that is composed of a single straight line and is consistent with all of the fluid inclusion data (Chapters 3 and 4). This implies that the uplift and cooling rates for both units must have varied with time during the exhumation process. The data shown in Figure 5-4 are equally consistent with this variation having resulted from a continuous or discontinuous process. Because it is difficult to envision a physical process that would result in instantaneous variations in uplift and cooling rates, followed by extended periods of time throughout which these rates remained constant, a scenario of continuous variation in these rates is preferred here (e.g. as shown in Fig. 5-4).

Differential uplift history.

Calculated values of P_{max} indicating an initial vertical separation of 10-11 km between sample localities that are currently separated by only 2 km provide strong empirical evidence for a history of differential uplift between the units. The data shown in Figure 5-4 confirm

that such a history occurred, and illustrate some of its details. It was mentioned earlier that the difference in length of the reversals in the LSH and USH paths determined from modeling of garnet zoning (Figure 5-1) could result from faster uplift of the LSH relative to the USH at some time prior to attainment of T_{max}. Although the reversals in trend of the PTt paths were smoothed out in construction of the curves in Figure 5-5, it is clear from this figure that the <u>average</u> uplift rates for the LSH exceed those of the USH for all times from ~60 Ma to 30 Ma, and are thus in agreement with the path lengths calculated for the two units.

Textural evidence also favors a model of differential movement of the units. The reversals in PTt paths determined from modeling of garnet zonation provide empirical evidence for simultaneous growth of garnet in both units, yet in the LSH these garnets are postkinematic and in the USH they are synkinematic (see Chapters 3 and 4). These observations are consistent with relative motion between the LSH and USH throughout the time of garnet growth, with most of the strain taken up by ductile deformation of the USH. Cracking of hornblende porphyroblasts in the LSH (Chapter 3) also occurred during this time of maximum difference in uplift rates for the two units, and may indicate extensional strain in the LSH at a time when the USH was experiencing shearing strain. The tectonic implications of differential movements between the units are discussed in a later section.

THERMAL MODELING

Calculations.

The petrologic and uplift rate data presented above can be combined with the general tectonic framework for the Eastern Alps to place constraints on the thermal budget of metamorphism in this area. Previous models aimed at characterizing the thermal parameters of metamorphism in the Tauern Window (e.g. Oxburgh and Turcotte, 1974; Bickle et al., 1975; England, 1978) have been necessarily general due to the lack of detailed petrologic and geochronologic data. The revised calculations of this study (undertaken with the assistance of P.C. England) are intended to provide a more complete thermal model for the metamorphism and also, as a result, to reassess the details of the tectonic scenario responsible for this metamorphism.

Evaluation of the thermal budget of metamorphism requires solving the heat flow equation for a constant-conductivity medium moving in the Z direction:

$$\frac{1}{\kappa}\frac{\partial T}{\partial t} = \frac{\partial^2 T}{\partial Z^2} - \frac{u(Z,t)}{\kappa}\frac{\partial T}{\partial Z} + \frac{h(Z,t)}{K} \qquad (5\text{-}3)$$

(e.g. Carslaw and Jaeger, 1959), where T is temperature, Z is depth, t is time, κ is thermal diffusivity, K is thermal conductivity, u is velocity in the Z direction, and h is the rate of internal heat generation for the volume of rock under consideration; note that u and h are rigorously considered to be functions of both depth and time. Lateral transfer of heat is ignored.

The values of P_{max} determined from the petrologic data in Chapters 3 and 4 indicate burial of the USH and LSH to depths of approximately 30 and 40 km, respectively. Allowing for an initial thickness of the USH

of approximately 5 km (e.g. Frisch, 1980), this implies an overburden thickness (above the USH) of approximately 25 km. In keeping with these constraints, the model examines the thermal evolution of rocks located 5 and 15 km beneath the base of a 25 km thick overthrust unit; the overthrusting event is assumed to have occurred instantaneously at 65 Ma. Prior to thrusting, both the upper and lower plates are considered to be in equilibrium with a 'mantle' heat flux (Q_m) of 33 mW m^{-2} and a heat generation rate of 2 μW m^{-3} from the surface to a depth of 15 km; h=0 for depths greater than 15 km. The thermal diffusivity and the thermal conductivity are taken to be 10^{-6} m^2 s^{-1} and 2.5 W m^{-1} K^{-1} throughout. Model uplift and erosion begin at 45 Ma after a 20 Ma period of thermal relaxation (e.g. England, 1978; Oxburgh and England, 1980).

For the sake of simplicity, it was assumed that imbrication of the LSH and USH occurred prior to the overthrusting event and that the two units behaved as a single coherent block thereafter. In any case, imbrication of such thin units prior to or during the main overthrusting event is likely to result in only a minor perturbation to the thermal evolution of the rocks (see discussion in Chamberlain and England, in press). The overall uplift history is treated as a two-stage process: commencing at 45 Ma, initial uplift occurs at a rate of 1.6 km Ma^{-1} for 10 Ma, followed by 35 Ma of uplift at a rate of 0.48 km Ma^{-1}. Net uplift is therefore 33 km, resulting in exposure of the USH but not the LSH at the surface. Differential uplift between the units is not explicitly modeled, but the effects such a process would have on the results are considered qualitatively. The physical significance of the modeled uplift rates is represented graphically by the dotted lines in Figure

Figure 5-5. Results of thermal modeling calculations showing thermal evolution of rocks 5 and 15 km beneath a 25 km thick overthrust sheet (model "LSH" and "USH", respectively; dotted lines). Solid line shows temperature distribution immediately post-thrusting at 65 Ma; dashed lines are instantaneous geotherms 20, 40, and 60 million years after thrusting. Large dots indicate 5 Ma intervals. Model allows for 20 Ma with no uplift, 10 Ma at 1.6 mm yr^{-1}, and 35 Ma at 0.48 mm yr^{-1}; net uplift is 33 km. Note crossover of paths at ~18 km depth. Other parameter values are: K=2.5 W m^{-1} K^{-1}; $\kappa=1\times10^{-6}$ m^2 s^{-1}; Q_m=33 mW m^{-2}; h=2 μW m^{-3}. See also Table 5-2.

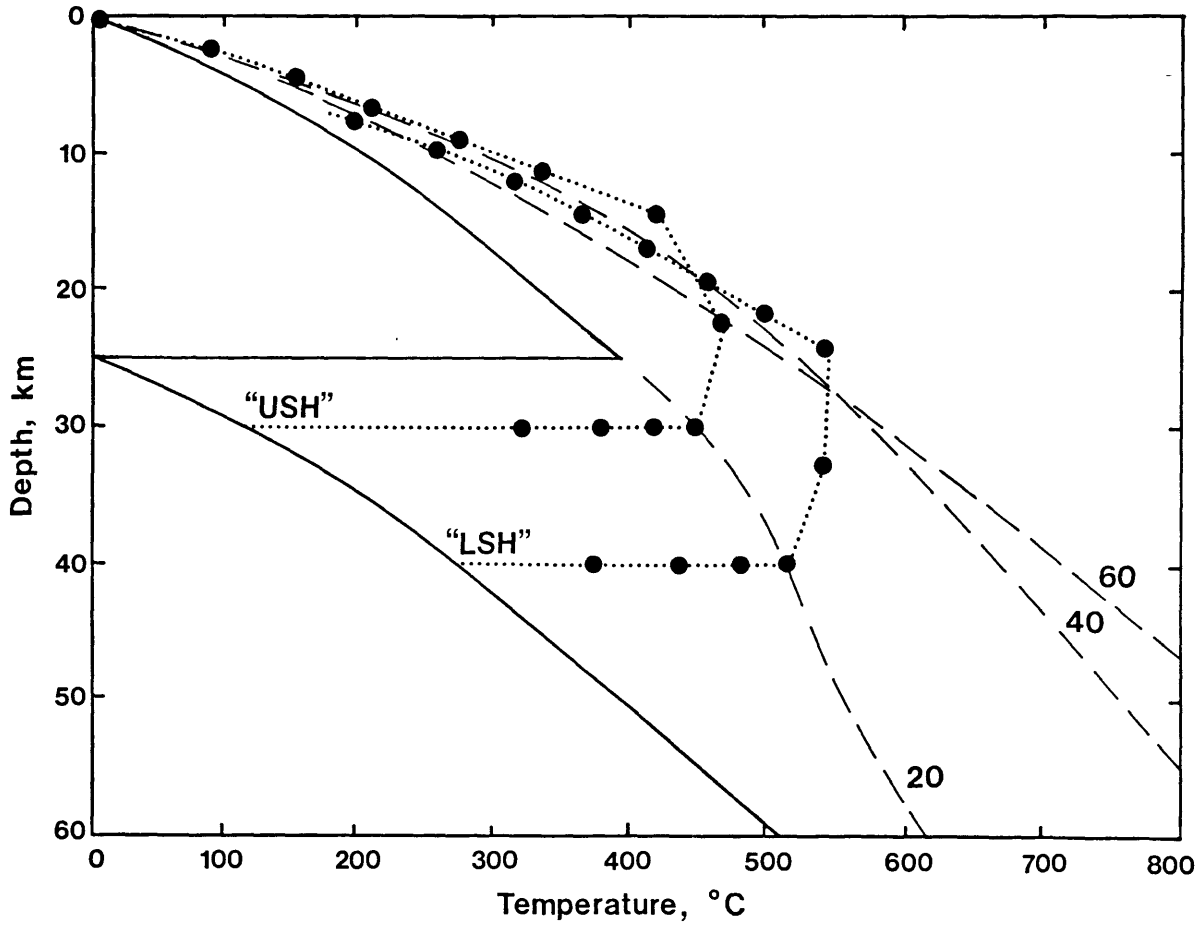
0
10
20
30
40
50
60
Depth, km
"USH"
"LSH"
60
40
20
0
100
200
300
400
500
600
700
800
Temperature, °C

Table 5-2 - Comparison between petrologic data and results of thermal modeling for the thermal peak of metamorphism in the LSH and USH.

Unit	Depth below thrust, km	T_{max}, °C		P (depth) at T_{max}, kb (km)		time at T_{max}, Ma	
		obs	calc	obs	calc	obs	calc
LSH	15	550±25	538	7.0±1 (21-28)	7.4 (26)	>39	35-40
USH	5	475±25	462	5.5±1 (16-23)	6.4 (22)	≈24	40

Observed values are based on petrologic and geochronologic data summarized in Figure 5-2. Calculated values are from thermal model with two-stage uplift process discussed in the text.

5-4. These rates were selected to provide linear approximations to the dZ/dt-time curve for the LSH without resulting in complete removal of the overlying USH. Although it is possible to develop a multi-stage model for uplift at steadily decreasing rates, this was considered to be an unnecessary refinement without first assessing the viability of a simpler model. In any case, the model can only be considered to be approximate due to fundamental uncertainties in the timing and duration of the overthrusting event.

Figure 5-5 illustrates the model PTt paths for the LSH and USH calculated from equation 5-1 for the parameter values presented above. Both of the PTt paths for the model units undergo isobaric heating for 20 Ma after thrusting (e.g. Oxburgh and England, 1980), after which time heating continues during the intial stages of decompression. Onset of cooling occurs at different times in the two model units, and their P-T paths cross one another at a depth of approximately 18 km; this crossover results from permitting the uplift rates for the entire package of rocks to change with time, and does not reflect differential uplift of the LSH relative to the USH.

Comparison between petrologic and model PTt paths.

The values of T_{max} and the time and depth at which T_{max} is attained for the two model units are compared with the actual values for the LSH and USH in Table 5-2. Calculated values of T_{max} of 538 and 462°C are in excellent agreement with the temperatures of final equilibration of 550±25°C and 475±25°C determined from geothermometry on the LSH and USH, respectively. The depths at which these temperatures were reached, as modeled, are also within the uncertainty limits of pressures obtained

Figure 5-6. Depth (Pressure) - Temperature diagram comparing model PTt paths for the "LSH" and "USH" (solid lines) with the LSH and USH paths determined petrologically (dashed and dot-dashed curves). Dotted line is hypothetical pre-thrusting geotherm for crust with thermal properties discussed in text. Lawsonite stability field from Chatterjee (1976) is shown for reference. "Glaucophane" curve marks experimentally determined glaucophane stability field of Carman and Gilbert (1983). Curve for Tremolite + Chlorite + Albite = Glaucophane + Clinozoisite + Quartz is from Maruyama et al. (1984) for endmember system; arrows indicate direction curve will shift due to solid solution effects in the reactants. Neither the basaltic USH rocks nor the more aluminous LSH metabasites show any evidence for early glaucophane; see text.

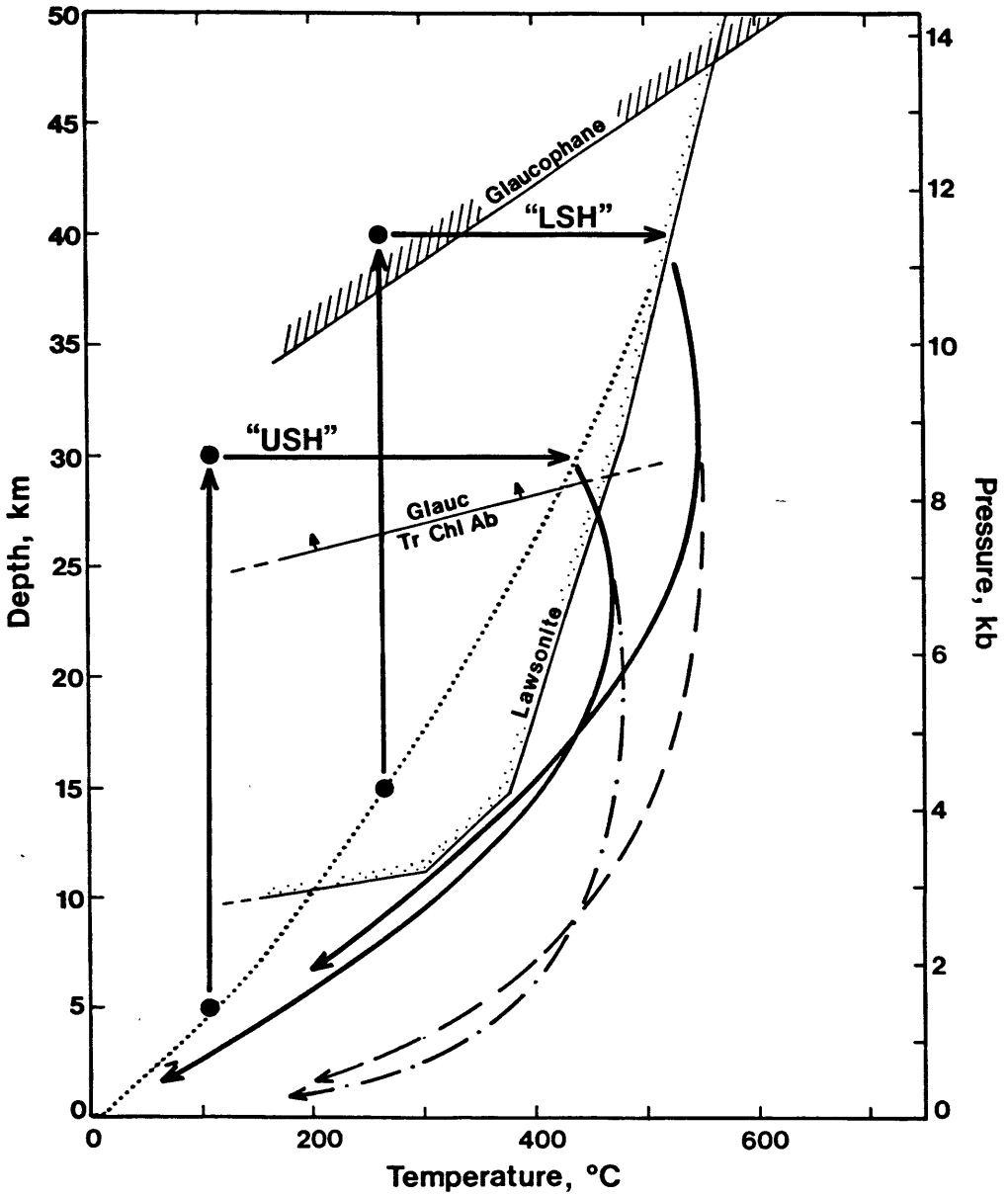
Glaucophane
"LSH"
"USH"
Glauc
Tr Chl Ab
Lawsonite
Depth, km
Pressure, kb
Temperature, °C
0
200
400
600
5
10
15
20
25
30
35
40
45
50
2
4
6
8
10
12
14

from geobarometry on the units. The model time at which T_{max} is attained in the LSH is in close agreement with the geochronological data for this unit, but the agreement is not as good for the USH. Despite the discrepancy in times for the USH, the physical conditions of peak metamorphism of both the LSH and USH can be adequately accounted for by overthrusting of a 25 km thick thrust sheet with the thermal parameters and initial uplift rates as specified above. Additional confirmation of this comes from the calculated present-day surface heat flow, which at 71 mW m^{-2} is remarkably close to the value of 75 mW m^{-2} measured by Clark (1966) in the Tauern tunnel approximately 40 km to the east.

The PTt paths determined for the LSH and USH in Chapters 3 and 4 are superimposed on the model PTt paths in Figure 5-6, along with an assumed prethrusting geotherm and experimentally determined stability fields for lawsonite and glaucophane. The lack of evidence for early glaucophane has been a puzzling feature of the blueschist metamorphism of both the LSH and USH, but it is clear from Figure 5-6 that the model PTt path for the LSH just barely passes through the glaucophane stability field determined by Carman and Gilbert (1983), and the USH path avoids it altogether. The experimental data of Maruyama et al. (1984) imply a lower pressure limit for the glaucophane field as bounded by the reaction Tremolite + Chlorite + Albite = Glaucophane + Clinozoisite + Quartz. As shown in the figure, the model paths for both the LSH and USH pass through the stability field for glaucophane as defined for this endmember reaction. The arrows on the reaction boundary, however, indicate that solid solution in the reactants will shift this curve to higher pressures. The net result is that glaucophane would be unlikely to form along the USH path, and would only be expected in truly basaltic

compositions along the LSH path. The calculated PTt paths thus provide a suitable model for early metamorphism of the LSH and USH along trajectories that pass through the lawsonite subfacies of the blueschist facies, but do not enter into the stability field of glaucophane.

Despite the good agreement between the early stages of the calculated PTt paths for the LSH and USH and those based on petrologic data, there is considerable discrepancy between the paths from T_{max} to the surface. This is evident from the superimposed curves of Figure 5-6: for both the LSH and USH, the calculated cooling paths are inconsistent with the fluid inclusion data indicating that significant cooling of the units did not occur until the rocks were at relatively shallow depths. In addition, the model crossover of the paths occurs at a greater depth than that estimated from the fluid inclusion data for the two units, even taking into account the uncertainty in location of this crossover indicated in Figure 5-1.

Discussion.

Two possibilities exist to account for the poor fit between the model PTt paths and the petrologically determined LSH and USH paths from T_{max} to the surface: (1) the fluid inclusion data cited in Chapters 3 and 4 are not representative of the P-T conditions that prevailed at the time of entrapment of the fluids, or (2) the parameters specified in the thermal model do not adequately reflect the burial and uplift history of the rocks. Each of these topics is briefly discussed below.

Use of fluid inclusions to constrain the uplift path of a rock requires accurate determination of the compositions and density of the entrapped fluid, and relies upon the assumption that these parameters

have not changed significantly since the time of entrapment. Freezing and homogenization temperatures (from which composition and density are determined) show little variation within any generation of inlusions in the LSH or USH. This implies that if there has been any post-entrapment modification, it must have affected all inclusions equally within a specific generation. Leakage of inclusions is unlikely to be such a uniform process (see Roedder, 1984); hydrogen diffusion or precipitation of silica from the inclusion fluid could cause uniform changes in the fluid characteristics, however. These latter two processes can have a significant effect on the density of aqueous inclusions (Pēcher and Boullier, 1984), but are of only minor importance in C-O-H fluid inclusions (Dubessy, 1984). The homogenization temperatures of inclusions in generations 1 through 3 in the LSH could be as much as 10% too high, based on the experimental results of Pēcher and Boullier (1984). If this is the case, the isochores shown in Fig. 3-12 may underestimate true trapping pressures by as much as 1 kb. The remaining inclusions in both the LSH and USH are predominantly composed of C-O-H fluids, and are less likely to have been uniformaly affected by post-entrapment modification processes (Dubessy, 1984). In both units, it is the positions of the isochores for these C-O-H inclusions that dominantly control the form of the uplift curves shown in Figure 5-6, and the uplift curves are thus not likely to be significantly in error. This is particularly true for the USH uplift path, which is principally defined by the occurrence of immiscible fluids in late-stage inclusions. The intersection of the isochores for these inclusions is in excellent agreement with experimental data on the CO_2-H_2O solvus, and requires that the rocks were at temperatures of ~350-380°C at a depth of less than 7 km.

This implies that much of the discrepancy between the paths results from the inability of the simplified model presented above to account for the differential uplift history experienced by the two units. Thermal models that use a constant uplift rate (e.g. England and Thompson, 1984) or an exponentially decreasing uplift rate (England and Richardson, 1977) predict that significant cooling generally begins at depths close to that at which T_{max} is achieved; regardless of the uplift rates or time constants used in these simple models, it does not seem possible to bring hot rocks close to the surface. Neither the model discussed in this thesis nor those cited above can account for the differential uplift history displayed by the LSH and USH, however. It is possible to model the LSH and USH separately, using step functions to deal with the variations in uplift rates for each unit, but the overall thermal evolution of the thickened package of rocks cannot be assessed. Development of a more sophistocated model for the LSH and USH is a goal of future research; a qualitative evaluation of the probable effects of differential uplift on the model PTt paths follows below.

Although the modeled uplift rates are in agreement with the maximum and minimum rates experienced by the LSH, in the period from 35 to 20 Ma the modeled rate is considerably slower than the observed uplift rate. (Fig. 5-4). Permitting a faster uplift rate throughout this interval would result in a model curve for the LSH that would be hotter near the surface than the curve shown in Figure 5-6; subsequent uplift at the slower rate would cause significant cooling at shallow crustal levels. The net PTt path would expose the LSH at the surface (in contrast to the model path of Figure 5-5) and should be in better agreement with the section of the observed LSH PTt path from T_{max} to the surface.

The modeled uplift rates for the USH provide a poor fit to the data throughout the interval from 45 to 10 Ma (Fig. 5-4): the maximum modeled rate occurs at the time of slowest uplift in the USH, and the minimum coincides with the fastest observed rates. Modeling of the USH with a slower initial uplift rate should result in attainment of T_{max} at a later time and somewhat shallower depth than calculated previously; subsequent uplift at faster rates would bring the rocks nearer the surface before the onset of significant cooling. Differential uplift that brings the hot LSH closer to the USH during exhumation would also prohibit cooling until the rocks were near the surface. Taking each of these factors into account should lead to a model PTt path that bears a greater resemblance to the observed USH trajectory in Figure 5-6.

It is not possible a priori to determine the influence that differential uplift would have on the calculated value of the present-day surface heat flow, nor is it clear that variations in uplift rate alone can account for the differences between the model and observed PTt paths. If the temperature-time histories of the LSH and USH cannot be reproduced by a thermal model involving the detailed depth-time curves for the units, it is necessary to examine other factors that could influence the thermal history of the rocks during uplift. Frisch (1978) has suggested that the closing of a second Penninic ocean basin to the north resulted in southward subduction of an additional plate beneath the Tauern Window. Such an event could result in a transient high value of Q_m beneath the Tauern Window if it caused melting or hydrothermal fluid circulation at depth (and could possibly account for the entrapment of fluid inclusions at high temperatures and shallow depths in the LSH and USH), and could influence the cooling histories of the overlying

LSH and USH. Underthrusting of granitic crust with a high concentration of radiogenic elements would also affect the thermal histories of the rocks in the Tauern Window. These possibilities are difficult to quantify in the model calculations, but need to be considered in evaluating the overall thermal and tectonic evolution of the Tauern Window.

Despite the discrepancies discussed above, the modeling results indicate that the general features of "peak" metamorphism in the SW Tauern Window are consistent with initial burial of the LSH and USH to different depths beneath a 25 km thick upper plate. There is no need to call upon an augmented heat flux from depth to produce the maximum temperatures of metamorphism, although as Oxburgh and England (1980) pointed out, it is difficult to eliminate the possibility of transient high heat flow at depth. Indeed, it may be necessary to consider a transient heat flux to account for the apparently high temperatures experienced by the LSH and USH at shallow depths during uplift.

Although the thermal parameters of the model presented here are essentially the same as those discussed by Bickle et al. (1975) and England (1978), the net results of the calculations are better able to account for the observed features of "peak" metamorphism in the SW Tauern area. This is due in part to modeling the burial of the LSH and USH to finite depths beneath a 25 km overthrust, rather than examining the effects of thrusting on the rocks directly at the interface. The more important difference between this model and those of prior studies comes from quantitative examination of the effects of time-dependent uplift rates, and from a qualitative evaluation of how differential uplift between the LSH and USH influences the results.

TECTONIC SYNTHESIS

General setting.

Synthesis of the pressure-temperature-time data presented in this thesis results in a picture that is broadly correlative with existing tectonic models for the Eastern Alps, but differs in several important details. The plate tectonic setting of the Eastern Alps has been discussed by many authors (e.g. Dewey et al., 1973; Ernst, 1973; Laubscher, 1975; Hawkesworth et al., 1975; Dietrich, 1976; Roeder and Bögel, 1978; Klemm et al., 1978; Frisch, 1978, 1979; Burchfiel, 1980; Smith and Woodcock, 1982), and there is general agreement that the principal features of the orogen can be accounted for by subduction of the European plate beneath various microplates or continental fragments located to the south. Closure of the intervening ocean basin began by 100 Ma and terminated with collision and northward overthrusting of the Austroalpine nappes between ~80 and 65 Ma. Prominent uplift and erosion, leading to exposure of the Tauern Window, commenced prior to 35 Ma and resulted in extensive sedimentation in the peri-Alpine basins. This section discusses the significance of the LSH and USH PTt trajectories in light of this generalized tectonic framework.

The hornblende garbenschist horizon of the LSH is a fragment of the Hercynian basement of the Eastern Alps that was remobilized and tectonically juxtaposed against the oceanic lithologies of the USH during the Alpine orogeny. The PTt paths determined from petrologic analysis of these two units suggest that initial imbrication of the LSH and the USH occurred prior to overthrusting of the Austroalpine nappes. This imbrication probably resulted from offscraping of oceanic deposits from the downgoing slab, and subsequent suturing of these lithologies with the

European basement during partial subduction of the continental crust.

Petrologic constraints on the maximum pressures attained by the LSH and USH, combined with the results of thermal modeling calculations, indicate burial of the LSH to a depth of 35-40 km and of the base of the USH to 25-30 km. These data imply a total thickness of ~25 km for the imbricate units of the Austroalpine sequence. The recent model of Lammerer (in press and personal commun.), which includes the rocks of the Ötztal massif in the overthrust sequence, could account for thicknesses of 25-30 km, and is consistent with the data presented in this thesis. Previous estimates suggest a thickness of only 15 km for the Austroalpine units in the vicinity of the Tauern Window (e.g. Oxburgh and Turcotte, 1974). An important conclusion of this thesis is that neither the geobarometric data nor the thermal modeling results can be explained by burial to depths of only 15 km.

The generalized tectonic histories of the LSH and USH are related to the PTt paths for the two units in the schematic cartoons of Figure 5-7. The first two diagrams, from ~80 to 60 Ma, show transport of the LSH and USH, separated by ~10 km of section, down a subduction zone beneath the Austroalpine (or Adriatic) continent. Model PTt paths for both units during this time interval are characterized by a nearly isothermal pressure increase, reflecting transport of relatively cool material to depth at rates too rapid to permit thermal equilibrium to be maintained. The prominent early foliation in the LSH garbenschists (Chapter 3) can be correlated with this stage in the P-T evolution of the rocks, and probably developed in response to shearing during subduction.

Emplacement of the Austroalpine nappes onto the European rocks of the Tauern Window occurred in response to continent-continent collision

Figure 5-7. Cartoons illustrating schematic tectonic and P-T evolution of the LSH (circles) and USH (squares). LSH is shown as upper part of Zentralgneis (ZG) complex, USH is unpatterned. AA = Austroalpine basement with unmetamorphosed cover (horizontal lines). During burial and heating, LSH and USH are separated by ~10 km. Initial stages of uplift of LSH are accomplished by ductile thinning of USH ± AA with little erosion of the thickened pile (50-35 Ma); separation between LSH and USH decreases to 2-5 km. Subsequent uplift and erosion of ~15 km of overburden affects the LSH and USH 'en masse' and exposes both units at the surface. Tectonic sketches are modified from Fig. 1 of Frisch (1978); TW = Tauern Window, PL = Periadriatic Lineament. P-T loops based on Figs. 5-2 and 5-6.

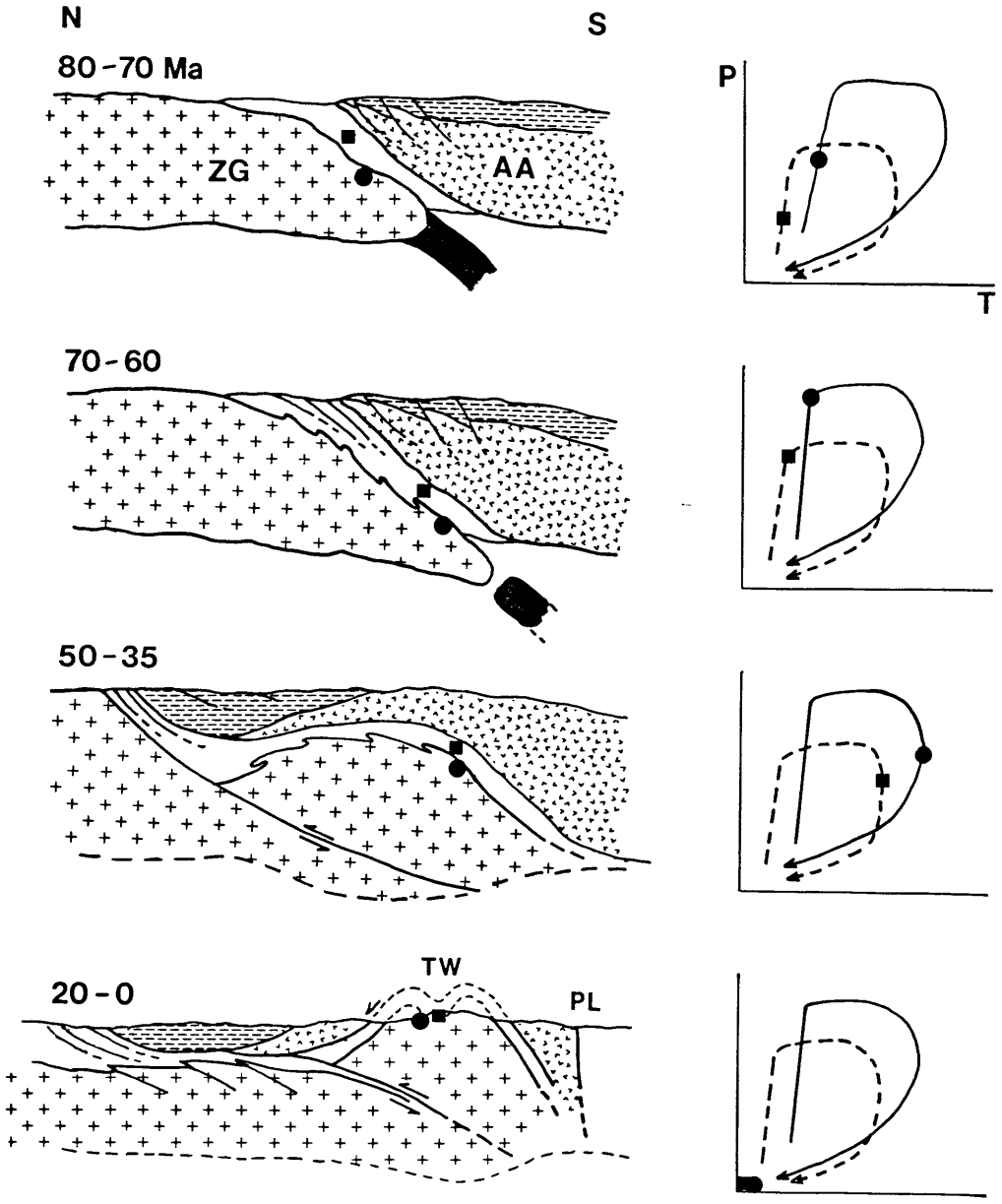
N
S
80-70 Ma
ZG
AA
P
T
70-60
50-35
20-0
TW
PL

and was probably complete by ~60 Ma (Hawkesworth, 1975), although considerable crustal shortening may have continued after this time. Following burial, heating of the thickened package of rocks began and may initially have occurred nearly isobarically (e.g. Richardson and England, 1977). The petrologic data indicate that the maximum temperatures experienced by the rocks were attained considerably after the onset of uplift (third diagram in Fig. 5-7). The final cartoon illustrates arching of the Tauern area and erosion of the overburden, accompanied by cooling of the rocks in the near-surface environment. Entrapment of most of the late-stage fluid inclusions occurred during this stage in the tectonic evolution of the rocks.

Uplift history.

The uplift rates presented in Figure 5-4 can be combined with the cartoons of Figure 5-7 to develop a model for the overall exhumation history for the SW Tauern Window. Calculated values of P_{max} in the LSH indicate uplift of the rocks from depths of 35-40 km since ~60 Ma; within the same time interval, the USH has been uplifted 25-30 km. The variations in uplift rates and in net amount of uplift between the two units suggest that not all of the vertical movement can be ascribed to surface erosion. This point is further supported by estimates of sediment volumes indicating average erosion of 15-20 km of overburden in the Eastern Alps, with local dissection to depths of ~25 km (England, 1982). Although there is considerable uncertainty in calculations of sediment volumes shed since the Alpine orogeny, stripping of 40 km of section off the top of the Tauern Window does not seem warranted by the data.

An alternative mechanism that is consistent with the petrologic and

structural evidence is one of tectonic uplift of the Paleozoic LSH associated with ductile deformation of the surrounding lithologies. The lack of evidence for internal deformation of the garbenschists during uplift suggests that much of the ZG and its Paleozoic cover behaved as an essentially rigid body throughout the exhumation process. In contrast, field and petrographic observations in the study area indicate that the Permo-Mesozoic part of the LSH and all of the USH behaved ductilely during the initial phases of uplift; total uplift of these units (based on P-T data) was ~10-12 km less than that of the Paleozoic LSH between 60 Ma and the present. These data imply that uplift of the Paleozoic LSH was accomplished by ductile thinning of the overburden (Permo-Mesozoic LSH, USH, ±AA) rather than by uplift 'en masse' of the entire imbricate crust. Lammerer (in press) claims that the USH and the overlying AA units are thinned from an original stratigraphic thickness of ~20 km to only 200 m in the vicinity of the Brenner Pass, which is consistent with the evidence in this thesis for >10 km of differential uplift between the LSH and the USH. The ultimate thickness of the overburden eroded off the top of the garbenschists would thus be on the order of 15 km, rather than the 40 km one would estimate from the calculated value of P_{max}.

This scenario of tectonic uplift without accompanying erosion is illustrated schematically in Figure 5-7, where the distance between the LSH and USH diminishes with time in response to shearing and ductile thinning of the USH. Final uplift and exposure of the rocks at the surface can be ascribed to erosional processes and is consistent with the data in Figure 5-4 indicating similar uplift histories for the two units from ~20 Ma to the present.

The reversals in the PTt paths determined from garnet zoning analysis in both the LSH and USH can be accounted for by increasing the thickness of the overburden, perhaps by further overriding of the rocks by the AA units. The difference in P-T path lengths of these reversals for the two units can be explained by the tectonic uplift model outlined above. Upward movement of the LSH relative to the USH during ongoing overthrusting would lead to greater apparent burial of the USH, and to correspondingly greater apparent uplift of the LSH following the event. The net result would be longer compression paths in the USH and longer decompression paths in the LSH, which is what is observed in Figure 5-1.

An important feature of the differential uplift history discussed above and sketched in Figure 5-7 is that it implies a normal sense of shear between the LSH and USH during the initial stages of uplift. This type of movement has not previously been considered in the Tauern Window, but could reflect development of a steep ramp anticline (Fig. 5-7) in the ZG and LSH, with ductile normal shearing of the USH along its southern flank. In this case, there would have been little lateral separation of the LSH and USH prior to uplift. In contrast, a purely compressional model for metamorphism, juxtaposition, and uplift of the LSH and USH requires considerable horizontal separation during the early phases of metamorphism; the observed thinning of the intervening section would result from ongoing thrusting during uplift. At present, it is not possible to distinguish unambiguosly between these alternatives, although the petrologic and field evidence suggesting early imbrication of the units is most consistent with some component of normal movement. In light of the tectonic ramifications such motion would have, a detailed structural study is necessary to document the sense of shear in the area of this study.

Burial and convergence rates.

The petrologic and time constraints discussed above can also be used to constrain time-averaged values of burial and convergence rates during the Alpine orogeny. Burial of the LSH to a depth of ~35-40 km beneath the USH and AA apparently occurred between ~80 Ma and ~65-60 Ma. Net burial rates for this interval are thus ~1.7 to 2.7 mm yr^{-1}. The total amount of closure that occurred during the Alpine orogeny is not well-documented, but was probably between 200 and 1000 km (e.g. Smith and Woodcock, 1982). If all of this closure occurred during a 15-20 Ma interval, average plate convergence rates would have been between 1.0 and 6.7 cm yr^{-1}. These values are only estimates averaged over time; actual rates, like the uplift rates in Figure 5-4, probably varied with time. Nonetheless, these values are of the same order as those estimated for continental subduction in the Zagros (Bird et al., 1975) and in the Himalaya (e.g. Molnar, 1984).

The most important feature of these estimated burial and convergence rates is that they do not require any excessively rapid processes to explain the observed metamorphic features in the SW Tauern Window: the entire orogenic cycle of burial (subduction), imbrication, metamorphism, and uplift can be accounted for by continental collision at rates similar to or slower than those observed in collisional zones that are active at the present time.

CONCLUSIONS

Correlation of the PTt paths for the LSH and USH with information on the timing of continental collision permits a detailed reconstruction of the interaction between tectonic and metamorphic processes in this area of the Eastern Alps. Calculated values of P_{max} indicate burial of the LSH to 35-40 km, which is considerably deeper than previous estimates based on petrologic data (e.g. Morteani, 1974; Hoschek, 1980; DeVecchi and Baggio, 1981), but is in good agreement with the predictions of England (1978). Thermal modeling calculations show that the metamorphic conditions of both the LSH and USH can be accounted for entirely by burial beneath a 25 km thrust sheet; there is no need to postulate an anomalously high deep-seated contribution to the thermal budget. The overthrusting event can be correlated with partial subduction of the European continent beneath the southern Austroalpine landmass.

Petrologic, geochronologic, and structural data all point to a history of differential uplift between the LSH and USH, probably accomplished in part by ductile thinning of the USH and possibly the overlying AA nappes. This phase of tectonic uplift is reflected by initially rapid uplift rates for the LSH and does not appear to have resulted in significant amounts of erosion; this is consistent with extreme thinning of the overlying units during this time (e.g. Lammerer, in press). Subsequent slower uplift of both the LSH and USH probably occurred 'en masse' in response to erosion of ~15-20 km of overburden.

A significant conclusion of this thesis is that all of the pressure-temperature-time data for both the LSH and USH can be explained as a result of the thermal evolution of crust thickened by a single collisional event around 65 Ma. There is no need to call upon discrete

thermal pulses or hiatuses to account for any of the petrologic or geochronologic data, although minor perturbations in the PTt paths may have resulted from subsequent stages of thrusting or folding. All of the PTt data are consistent with imbrication of the LSH and USH in the early stages of the Alpine orogeny. A consequence of this interpretation is that the Eclogite Zone, which contains 20 kb rocks and is sandwiched between the LSH and USH in the central part of the window, must have been metamorphosed at high pressure and emplaced prior to or during the imbrication and metamorphism of the LSH and USH. The rocks of the Eclogite Zone should thus be carefully evaluated with reference to possible polymetamorphism.

Overall, the material presented in this thesis indicate the extent to which petrologic data can be used to gain insight into the dynamics of continent-continent collisions. It is only by synthesizing petrologic data with structural, geophysical, and geochronologic information that the interactions between tectonic and metamorphic processes can be meaningfully assessed. This thesis represents a step in this direction; although the results are specific to the SW corner of the Tauern Window, the techniques and conclusions are relevant to the study of other orogens in other parts of the world. It is hoped that the results will prove useful to future modelers of collisional terranes, both in the Alps and elsewhere.

APPENDIX I

SAMPLE LOCALITY MAPS

Figure A1-1. Map showing hornblende garbenschist sample localities. Samples specifically discussed in the text are from Z3 and FH-1 localities, although preliminary analyses from PJ samples yield similar results. Altkristallin: pLSH = amphibolites, garbenschists, and serpentinites, Furt = Furtschaglschiefer; mLSH = conglomerates, quartzites, marbles, and schists of Permo-Mesozoic LSH; vUSH = greenstones of the USH; cUSH = calcmica schists, pelites, and marbles of the USH. Structure shown in Figs. 1-5 and 1-6; location of study area shown in Figure 1-2. PJ = Pfitscher Joch Haus (2277 m), R = Rotbachlspitze (2895 m), HF = Hochfeiler (3510 m), GG = Großer Greiner (3199 m). LSH = Lower Schieferhülle, USH = Upper Schieferhülle.

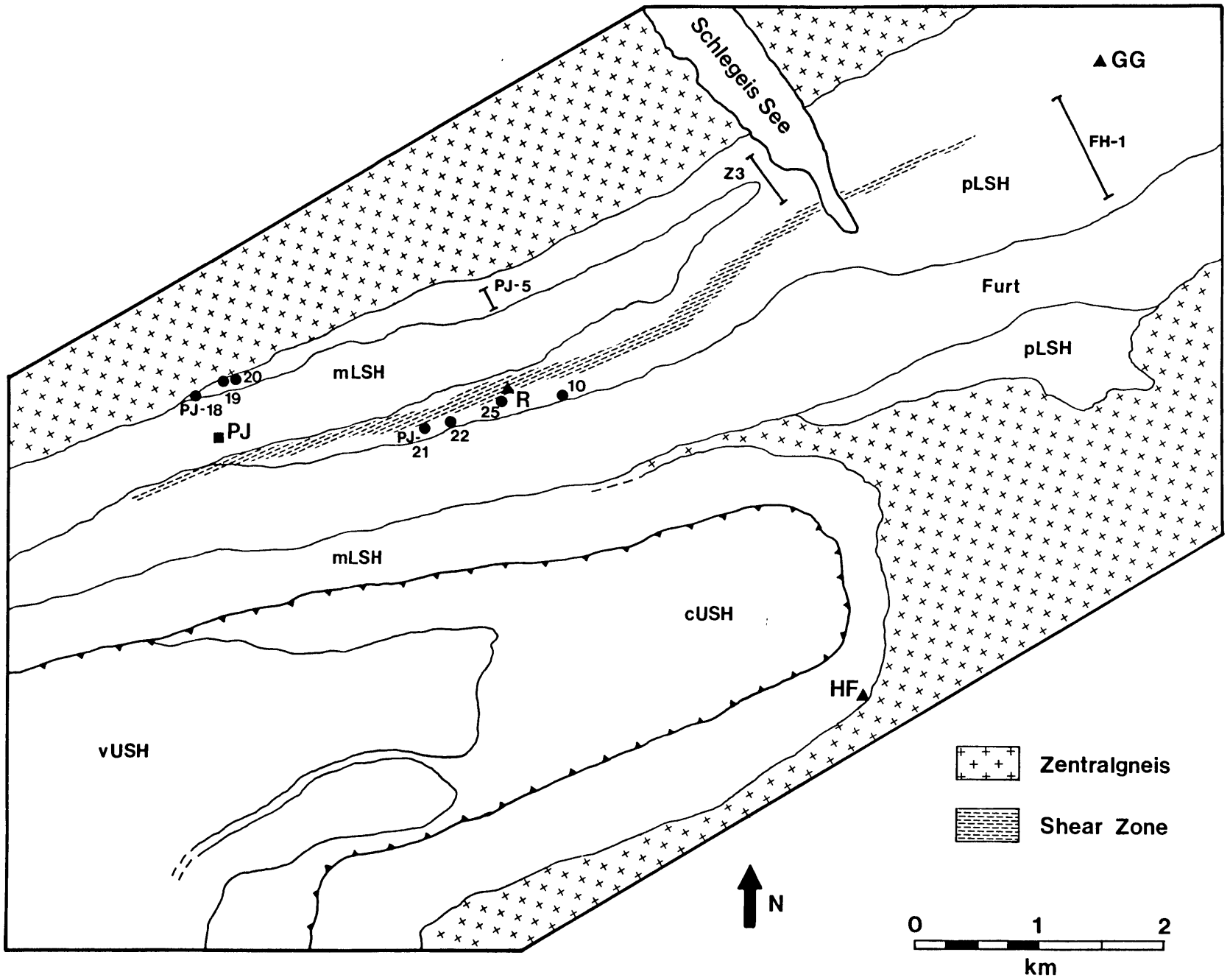
Schlegeis See
GG
FH-1
Z3
pLSH
PJ-5
Furt
pLSH
mLSH
20
19
PJ-18
PJ
25
R
10
PJ-
21
22
mLSH
cUSH
HF
vUSH
Zentralgneis
Shear Zone
N
0
1
2
km

Figure A1-2. Map showing Furtschaglschiefer sample localities. Work on these rocks is still in progress and is not discussed in this thesis. Results are in good agreement with those from garbenschist horizon, however. Abbreviations are the same as in Figure A1-1.

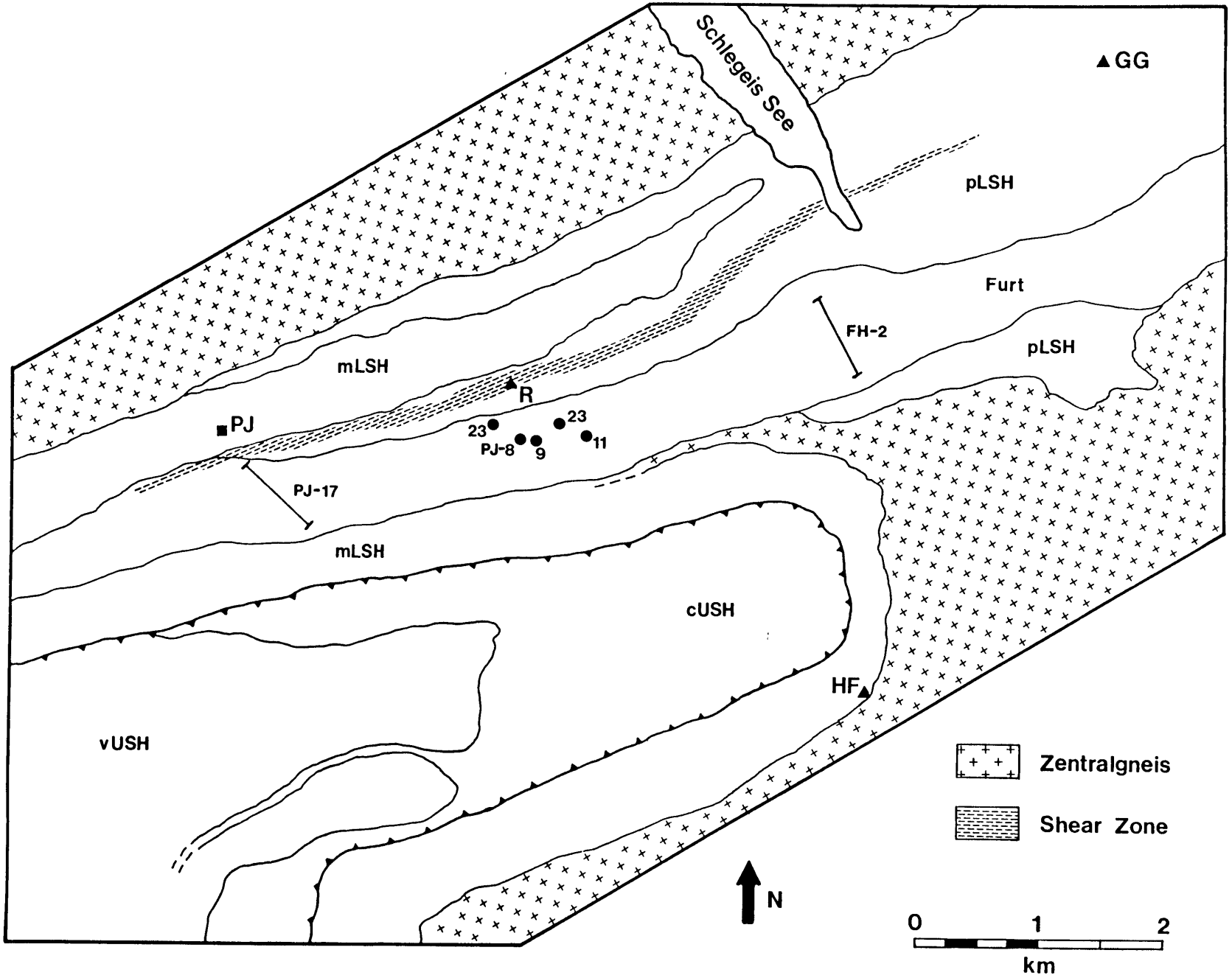
Schlegeis See
GG
pLSH
Furt
FH-2
pLSH
mLSH
R
PJ
23
PJ-8
9
23
11
PJ-17
mLSH
cUSH
HF
vUSH
Zentralgneis
Shear Zone
N
0
1
2
km

Figure A1-3. Map showing sample localities for conglomerates, impure quartzites, and garnetiferous schists of the Permo-Mesozoic LSH. Work on these samples is still in progress and is not discussed in this thesis. Abbreviations are the same as in Figure A1-1.

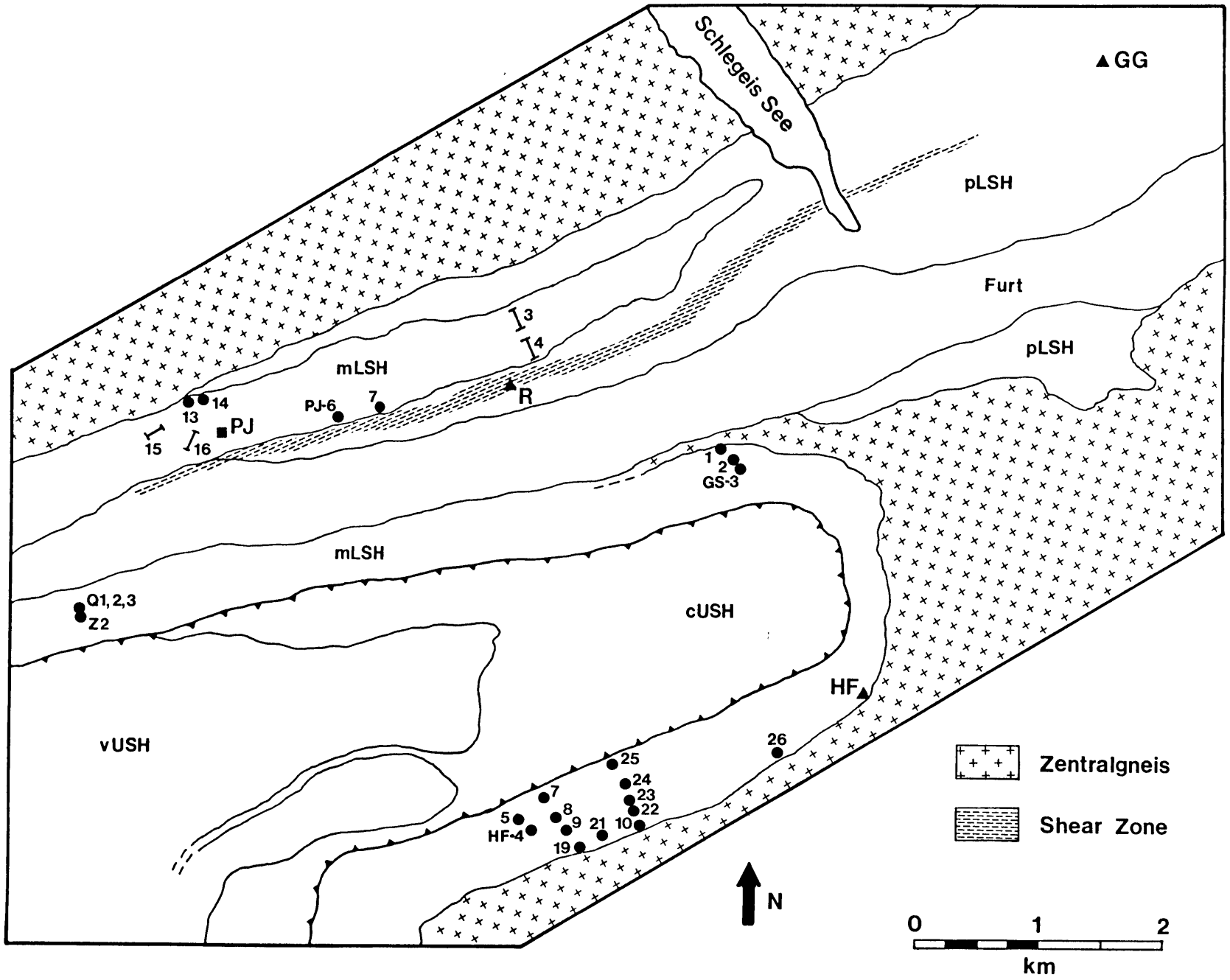
Schlegeis See
GG
pLSH
Furt
pLSH
mLSH
3
4
R
PJ-6
7
13
14
PJ
15
16
1
2
GS-3
mLSH
Q1,2,3
Z2
cUSH
HF
vUSH
26
25
24
23
22
7
8
5
9
21
10
HF-4
19
N
Zentralgneis
Shear Zone
0
1
2
km

Figure A1-4. Map showing sample localities for USH samples; all sample numbers have the prefix HF. Abbreviations are the same as in Figure A1-1.

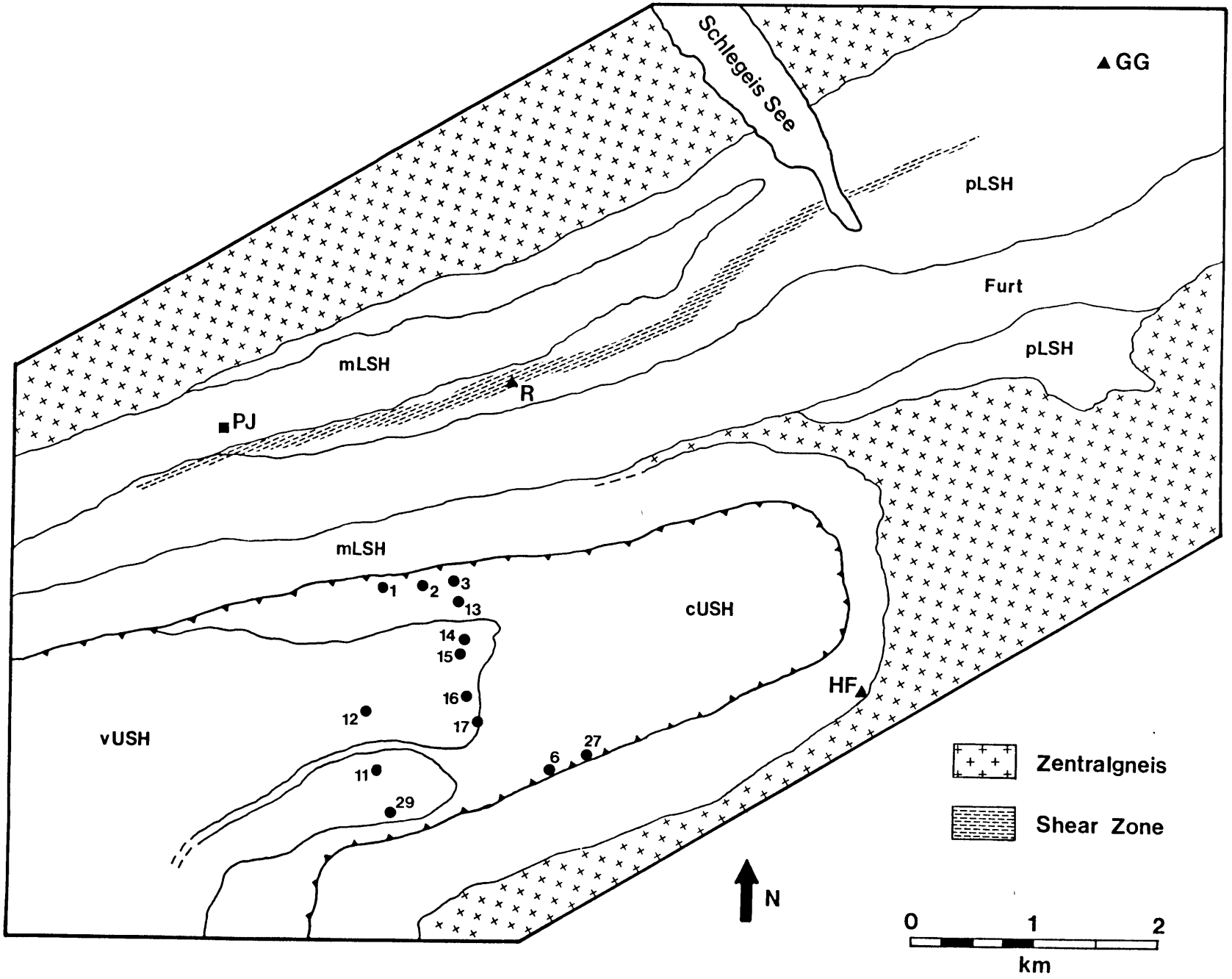
Schlegeis See
GG
pLSH
Furt
pLSH
mLSH
R
PJ
mLSH
cUSH
1
2
3
13
14
15
16
17
12
vUSH
11
29
6
27
HF
Zentralgneis
Shear Zone
N
0
1
2
km

APPENDIX 2

THE EFFECTS OF DIFFUSIONAL HOMOGENIZATION ON P-T PATHS CALCULATED FROM ZONED GARNETS

INTRODUCTION

Analytical formulation of the phase equilibria of metamorphic assemblages allows the calculation of quantitative P-T paths followed by the rocks during the growth of zoned minerals. A description of this technique, accompanied by several examples of the resultant metamorphic trajectories, has been presented by Spear and Selverstone (1983). The technique represents an extremely powerful tool in that it allows the determination of changes in P-T conditions in an assemblage of any variance, and also provides a quantitative basis for correlating tectonic and metamorphic processes. Because the method calculates changes in P and T rather than the absolute values of these parameters, it is relatively insensitive to small errors in the thermodynamic data required as input; the explicit dependence of ΔT and ΔP on the compositional variables ΔX_i determined from zoned minerals, however, suggests that errors in these values could have a significant effect on the calculated P-T path, and therefore also the tectonic interpretation of a metamorphic terrane. In particular, partial homogenization of zoned grains by volume diffusion processes could alter both the orientation and magnitude of calculated P-T vectors. This paper looks at the effects of partial homogenization of garnet on the P-T paths determined for two hypothetical cases and evaluates the significance of diffusional processes on these paths within the time frames of orogenic events.

P-T PATHS OF GARNET-BEARING SAMPLES

The assemblages (1) Garnet-Biotite-Sillimanite-Kspar-Plagioclase-Quartz-H_2O and (2) Garnet-Biotite-Sillimanite-Muscovite-Plagioclase-Quartz-H2O were selected for modeling of the effects of garnet diffusion on calculated metamorphic trajectories. These assemblages are trivariant in the CNKFMASH system (Mn has been ignored for the sake of simplicity), and ΔX_{alm}, ΔX_{gros}, and ΔX_{An} were selected as the monitor parameters to calculate ΔT and ΔP of garnet growth (see Spear and Selverstone, 1983, for explanation of technique). A fictitious garnet edge composition was chosen and the compositions of coexisting biotite and plagioclase were calculated from the formulations of Ferry and Spear (1978) and Ghent et al. (1979) to be consistent with final metamorphic conditions of 700°C, 4.5 kb for assemblage (1) and 650°C, 4.5 kb for assemblage (2); these compositions are given in Table A2-1. An original garnet zoning profile was assumed such that ΔX_{alm} = -0.20 (rim to core) in case (1) and -0.10 in case (2); ΔX_{gros} = +0.01 and ΔX_{An} = -0.10 were assumed for both assemblages. Biotite was taken to be homogeneous due to rapid diffusion rates.

Using these initial conditions, the P-T paths over which garnet grew and zoned were calculated according to the method of Spear and Selverstone (1983), and the results are shown in Figure A2-1. In both cases, garnet growth occurred in response to cooling and decompression, with values of ΔT and ΔP of -61°C, -2170 bars for assemblage (1) and -85°C, -3115 bars for assemblage (2). These paths imply that uplift and erosion were the dominant tectonic processes controlling the metamorphic equilibria in each of the hypothetical examples.

Table A2-1 - Compositions of phases and PTt parameters for different degrees of garnet homogenization

		Assemblage 1: T_o=700°C, P_o=4.5 kb					Assemblage 2: T_o=650°, P_o=4.5 kb			
		Initial		After homogenization			Initial		After homog.	
		Edge	Core	Core			Edge	Core	Core	
ΔX_{alm}		--	-.20	-.10	-.05	0	--	-.10	-.05	0
Garnet	X_{alm}	.85	.65	.75	.80	.85	.85	.75	.80	.85
	X_{pyr}	.10	.29	.19	.14	.09	.10	.19	.14	.09
	X_{gros}	.05	.06	.06	.06	.06	.05	.06	.06	.06
	Fe/Fe+Mg	.895	.691	.798	.851	.900	.895	.798	.851	.900
Biotite	Fe/Fe+Mg	.674	.36	.49	.58	.69	.643	.46	.55	.66
Plag	An	.44	.34	.34	.34	.34	.37	.27	.27	.27
ΔT (°C)		--	+61	+31	+13	-7	--	+85	-44	-191
ΔP (bars)		--	+2710	+2190	+1891	+1550	--	+3115	+917	-1574
Time, Ma	a=.05 cm	--	0	2.2	3.8	14.1	--	0	9.7	64.5
Time, Ma	a=.025 cm	--	0	0.5	0.95	3.5	--	0	2.4	16.1

ΔX_{alm}, ΔT, and ΔP refer to changes calculated from rim to core of the garnets.

Figure A2-1. P-T paths calculated from garnet zoning in Assemblages (1) and (2) for different degrees of garnet homogenization; calculations performed by combining the technique of Spear and Selverstone (1983) with the diffusion model discussed in the text. The curves marked "core" are the real P-T paths followed by the rocks and are determined from the original garnet zoning profiles; the other curves represent the erroneous paths that would be derived if the garnets underwent partial or complete post-crystallization homogenization. Numbers on the curves are values of ΔX_{alm} measured between the edge and core of each garnet.

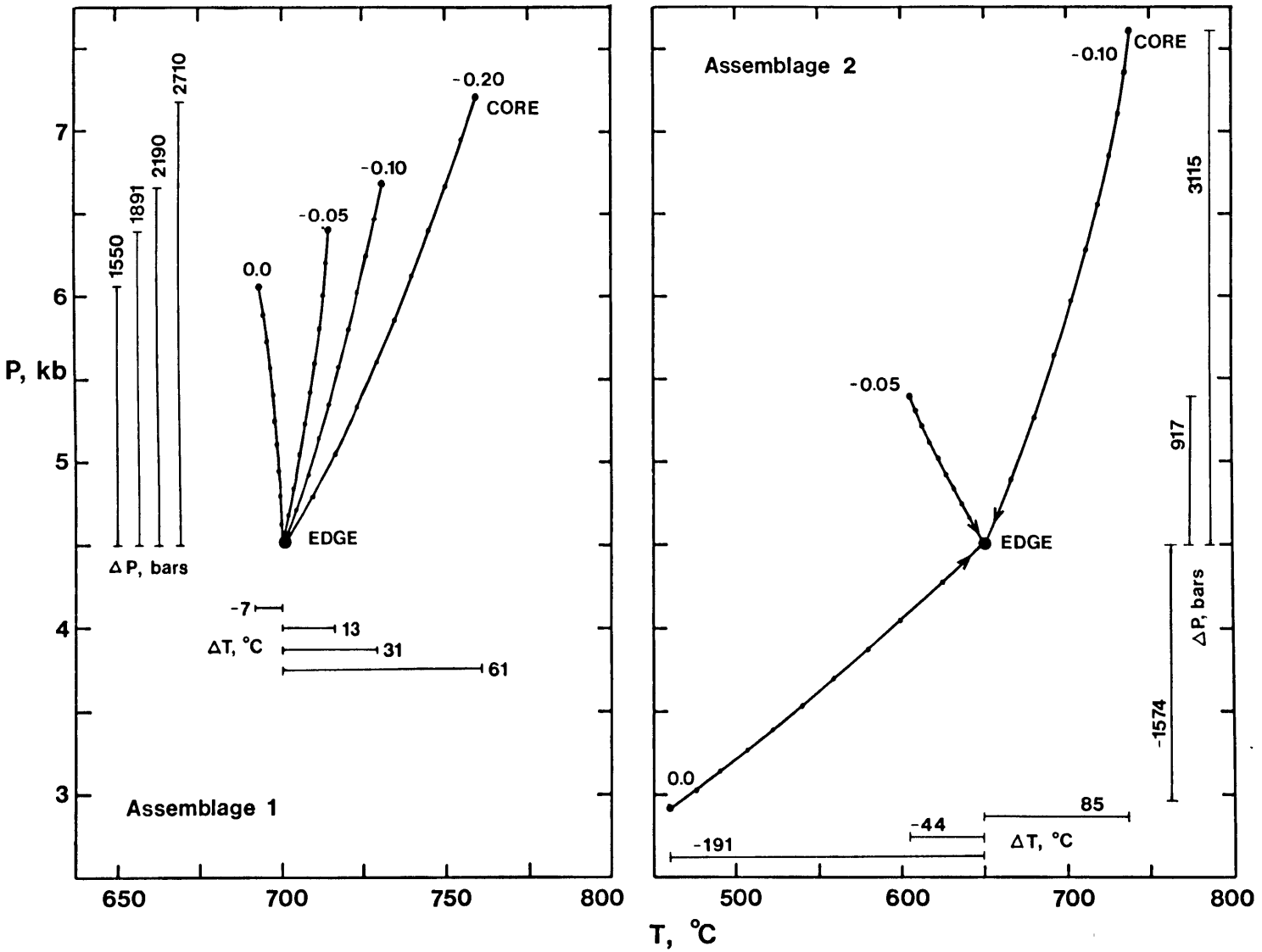
Assemblage 1
Assemblage 2
P, kb
T, °C
CORE
EDGE
-0.20
-0.10
-0.05
0.0
2710
2190
1891
1550
ΔP, bars
-7
13
31
61
ΔT, °C
3115
917
-1574
ΔP, bars
-191
-44
85
ΔT, °C

The question to consider at this point is, what would the effects of partial homogenization of the original zoned garnets be on these P-T paths? A simple but insightful first approximation to this problem results from considering only the effects of Fe-Mg interdiffusion in garnet, leaving ΔX_{gros} and ΔX_{An} unchanged. The details of the diffusional model will be discussed in the next section, but the calculated P-T paths are presented here.

Partial homogenization of the garnets would result in measured values of ΔX_{alm} that would be less than the original values generated during garnet growth. To determine the effects of such a process, the P-T paths of such an assemblage were recalculated for a range of smaller ΔX_{alm} values, and these results are also shown in Figure A2-1. For sample (1), the calculated P-T paths shorten and change slope with increasing degree of homogenization, but all still record considerable decompression accompanied by cooling (or only minor heating for the case of complete homogenization, $\Delta X_{alm}=0$). The results are more dramatic in the case of the muscovite-bearing assemblage. Partial homogenization from ΔX_{alm} = -0.10 to -0.05 results in a change in path from decompression and cooling to decompression accompanied by heating. Further homogenization to $\Delta X_{alm}=0.0$ produces a path that implies a significant heating event and increase in pressure during garnet growth. The magnitude of the changes in path length and direction reflect the wide spacing of composition contours in this assemblage due to the vapor-absent nature of all equilibria involving Fe and Mg components; in contrast, the K-feldspar assemblage is characterized by dehydration equilibria with more closely spaced contours. It is clear from this example

that partial homogenization of garnet can have a major effect on calculated P-T trajectories, and hence also on the tectonic interpretations of a region. For example, the original path for the muscovite rock implies mineral growth during uplift and erosion of a terrane, whereas the $\Delta X_{alm}=0$ path could be interpreted as reflecting mineral growth in response to overthrusting of a hot nappe. In light of these tectonic implications, it is necessary to evaluate the time scales of garnet diffusion in these assemblages to determine under what circumstances calculated paths should be viewed with suspicion in real rocks.

DIFFUSION CALCULATIONS

A computer program for calculation of finite-difference solutions to the diffusion equation (e.g. Crank, 1975) was modified from Sanford (1982) and was utilized to model homogenization of the original garnet zoning profiles. Simplifying assumptions made in this modeling are as follows: (1) the radius of curvature of the garnet grains is large relative to diffusion distances, and hence a planar geometry can be used. (2) The diffusion coefficient is independent of composition within the range of interest, e.g.,

$$\frac{\partial C}{\partial t} = D \frac{\partial^2 C}{\partial X^2}$$

where C is concentration, t is time, D is the diffusion coefficient, and X is distance. (3) Only interdiffusion of Fe and Mg in garnet is involved; Ca profiles remain unaffected. (4) No diffusion occurred during garnet growth so the diffusion length is constant. (5) Diffusion occurs at a constant temperature such that the edge composition of garnet

remains fixed by a K_D^{FeMg} term between garnet and biotite. (6) Diffusion in biotite is infinitely rapid with respect to garnet, so biotite acts as an Mg sink and Fe source for diffusion in garnet with no rate-limiting effects.

Clearly, the assumption that all homogenization of garnet occurs at a constant temperature after the cessation of garnet growth is a drastic oversimplification, as is the assumption of no Ca diffusion. Nonetheless, the results of these calculations provide some information on the time frame of garnet homogenization and can be compared with uplift rates to constrain the amount of homogenization to be expected under different geological conditions.

Values of $D_o=3.7\times10^{-4}$ cm^2 s^{-1} and E = 60 kcal mol^{-1} for the Fe-Mg interdiffusion coefficient in garnet were taken from Lasaga (1981) and Lasaga et al. (1977). These numbers are poorly constrained, but are nevertheless used without comment here as essentially the only numbers available for these parameters. The diffusion coefficient is therfore 1.236×10^{-17} cm^2 s^{-1} at 700°C (K-feldspar assemblage) and 2.301×10^{-18} cm^2 s^{-1} at 650°C (muscovite assemblage).

Using these values, the times necessary for relaxation of the original garnet profile towards $\Delta X_{alm}=0$ for grain sizes of 0.05 and 0.025 cm are given in Table A2-1. At 700°C for a grain of radius 0.025 cm, complete homogenization of the Fe-Mg profiles in garnet would require 3.5 Ma, but significant partial homogenization could occur in less than 1 Ma. In contrast, for the same grain size at 650°C, it would take 16.1 Ma for 100% and 2.4 Ma for 50% homogenization to occur. For the larger grain size, complete homogenization occurs in 14.1 Ma and 64.5 Ma at 700 and 650°C, respectively.

It is clear from these values that for grains in which the diffusion distances are on the order of 0.05 cm, significant homogenization of garnet is unlikely to be a concern unless the rocks have experienced a slow uplift and cooling history and/or diffusion was an active process during garnet growth. On the other hand, only 333 bars of post-crystallization, isothermal (700°C) decompression at 2 mm yr^{-1}, or 83 bars at 0.5 mm yr^{-1}, would suffice to homogenize the Fe-Mg profiles in garnets of radius 0.025 cm to 50% of their original magnitude, according to the parameters of this model. These numbers are well within the range of geological feasibility, and imply that for relatively small garnets in rocks that experienced temperatures of 700°C, P-T paths calculated from zoned garnets could be significantly in error. At lower temperatures and/or for larger grain sizes, however, post-crystallization modification of garnet zoning profiles should be relatively minor and tectonic interpretations based on calculated P-T paths should not be subject to large uncertainties.

DISCUSSION

Clearly, the treatment of diffusion in garnet considered here is oversimplified, but in light of empirical evidence indicating that Fe-Mg diffusion is more rapid than Ca diffusion in garnet (e.g. Yardley, 1977), it is not altogether unrealistic. Ultimately it should be possible to incorporate more sophisticated diffusion models into the method of Spear and Selverstone (1983) such that accurate P-T paths can be obtained from partially homogenized garnets. Specifically, models are needed that will take into account diffusion of all components in garnet

(including cross-coefficient terms) and diffusion during growth of the garnet (e.g. a moving interface). Above all, however, better diffusion data for garnet are needed.

At present, it is only possible to recognize those assemblages in simple systems in which partial homogenization of the garnet would result in erroneous tectonic interpretations by altering the orientation of calculated P-T vectors. For these cases, simple diffusion calculations such as those presented here can constrain the magnitude of homogenization to be expected within the duration of an orogenic cycle, and P-T corrections can be made accordingly.

REFERENCES

Ackermand, D. and Morteani, G., 1973. Occurrence and breakdown of paragonite and margarite in the Greiner Schiefer Series (Zillerthal Alps, Tyrol), Contrib. Mineral. Petrol., 40, 293-304.

Ackermand, D. and Morteani, G., 1976. Kontinuierlicher und diskontinuierlicher Zonarbau in der Granaten der penninischen Gesteine der Zillertaler Alpen, Tscher. Min. Petr. Mitt., 23, 117-136.

Ackermand, D., Morteani, G., and Raase, P., 1978. Metamorphism of the Penninic Series in the western Tauern Window (Austria/Italy) in: H. Closs, D. Roeder, and K. Schmidt, eds., Alps, Appenines, Hellenides. Inter-Union Comm. on Geodynamics Sci. Rept. 38, 121-124.

Bickle, M.J., Hawkesworth, C.J., England, P.C., and Athey, D.R., 1975. A preliminary thermal model for regional metamorphism in the eastern Alps. Earth Plan. Sci. Lett., 26, 13-28.

Bickle, M.J. and Powell, R., 1977. Calcite-dolomite geothermometry for iron-bearing carbonates: the Glockner area of the Tauern Window, Austria, Contrib. Mineral. Petrol., 59, 281-292.

Bird, P., Toksoz, M.N., and Sleep, N., 1975. Thermal and mechanical models of continent-continent convergence zones. J. Geophys. Res. 80, 4405-4416.

Black, P.M., 1977. Regional high-pressure metamorphism in New Caledonia: phase equilibria in the Ouegoa district, Tectonophys., 43, 89-107.

Bogel, H., 1976. Eine Geotraverse durch die mittleren Ost-und Sudalpen, Schweiz. Mineral. Petrogr. Mitt. 56, 567-579.

Bogel, H. and Roeder, D., 1978. The Eastern Alps - an Introduction, in, H. Closs, D. Roeder, and K. Schmidt, eds., Alps, Apennines, Hellenides, Inter-Union Comm. Geodynamics Sci. Rept. 38, 57-60.

Borsi, S., Del Moro, A., Sassi, F.P., Zanferrari, A., and Zirpolo, G., 1978. New geochronologic and radiometric data on the Alpine history of the Austridic continental margin south of the Tauern Window, Mem. Sci. Geol. Univ. Padova, 32, 1-17.

Bowers, T.S. and Helgeson, H.C., 1983. Calculation of the thermodynamic and geochemical consequences of nonideal mixing in the system H_2O-CO_2-NaCl on phase relations in geologic systems: equation of state for H_2O-CO_2-NaCl fluids at high pressures and temperatures, Geochim. Cosmochim. Acta, 47, 1247-1275.

Brewer, J., 1981. Thermal effects of thrust faulting, Earth Plan. Sci. Lett., 56, 233-244.

Bucher-Nurminen, K., Frank, E., and Frey, M., 1983. A model for the progressive regional metamorphism of margarite-bearing rocks in the Central Alps. Amer. J. Sci., 283-A, 370-395.

Burchfiel, B.C., 1980. Eastern European Alpine system and the Carpathian orocline as an example of collision tectonics, Tectonophys., 63, 31-61.

Burnham, C.W., Holloway, J.R., and Davis, N.F., 1969. Thermodynamic properties of water to 1000°C and 10,000 bars, Geol. Soc. Amer. Spec. Paper 132, 96 pp.

Burruss, R.C., 1984. Analysis of fluid inclusions: phase equilibria at contant volume. Amer. J. Sci. 281, 1104-1126.

Carman, J.H. and Gilbert, M.C., 1983. Experimental studies on glaucophane stability, Amer. J. Sci., 283-A, 414-437.

Carslaw, H.S. and Jaeger, J.C., 1959. Conduction of Heat in Solids. Oxford University Press, 510 pp.

Chamberlain, C.P. and England, P.C., 1985. The thermal history of the Merrimack Synclinorium in the northern Appalachians. J. Geol., in press.

Chatterjee, N.D., 1976. Margarite stability and compatibility relations in the system $CaO-Al_2O_3-SiO_2-H_2O$ as a pressure-temperature indicator, Amer. Mineral, 61, 699-709.

Chatterjee, N.D. and Froese, E., 1975. A thermodynamic study of the pseudobinary join muscovite-paragonite in the system $KAlSi_2O_8-Al_2O_3-SiO_2-H_2O$, Am. Mineral., 60, 985-993.

Chopin, C., 1983. High-pressure facies series in pelitic rocks: a review, Terra Cognita, 3, 183.

Chopin, C. and Schreyer, W., 1982. Progress concerning the low-temperature and high-pressure phase relations of the system $MgO-Al_2O_3-SiO_2-H_2O$: application to subducted metapelites, Geol. Soc. Amer. Prog. Abs., 14, 452.

Clark, S.P., 1961. Heat flow in the Austrian Alps, Geophys. Jour., 6, 54-63.

Clark, S.P. and Jager, E., 1969. Denudation rate in the Alps from geochronologic and heat flow data, Amer. J. Sci., 267, 1143-1160.

Cliff, R.A., 1981. Pre-Alpine history of the Pennine zone in the Tauern Window, Austria: U-Pb and Rb-Sr Geochronology, Contrib. Mineral. Petrol., 77, 262-266.

Cloos, M., 1982. Flow melanges: numerical modeling and geologic constraints on their origin in the Franciscan subduction complex, California, Geol. Soc. Amer. Bull., 93, 330-345.

Crank, J., 1975. The Mathematics of Diffusion. Oxford University Press.

Cuthbert, S.J., Harvey, M.A., and Carswell, D.A., 1983. A tectonic model for the metamorphic evolution of the Basal Gneiss Complex, western South Norway, J. Metamorphic Geol., 1, 63-90.

De Vecchi, G. and Baggio, P., 1982. The Pennine Zone of the Vizze region in the western Tauern Window (Italian Eastern Alps), Boll. Soc. Geol. It., 101, 89-116.

DeVore, G.W., 1983. Relations between subduction, slab heating, slab dehydration, and continental growth, Lithos, 16, 255-263.

Dewey, J.F., Pitman, W.C., Ryan, W., and Bonnin, J., 1973. Plate tectonics and the evolution of the Alpine system. Geol. Soc. Amer. Bull., 84, 3137-3180.

Dietrich, H., 1983. Zur Petrologie und Metamorphose des Brennermesozoikums (Stubaier Alpen, Tirol), Tscher. Min. Petr. Mitt., 31, 235-257.

Dietrich, V.J., 1976. Evolution of the Eastern Alps: a plate tectonics working hypothesis, Geology 4, 147-152.

Dodson, M.H.,, 1973. Closure temperature in cooling geochronological and petrological systems. Contrib. Mineral. Petrol. 40, 259-274.

Draper, G. and Bone, R., 1981. Denudation rates, thermal evolution, and preservation of blueschist terrains, J. Geol., 89, 601-613.

Droop, G.T.R., 1981. Alpine metamorphism of pelitic schists in the south-east Tauern Window, Austria, Schweiz. Mineral. Petrogr. Mitt., 61, 237-273.

Droop, G.T.R., 1982. A clinopyroxene paragenesis of albite-epidote-amphibolite facies in meta-syenites from the southeast Tauern Window, Austria, J. Petrol., 23, 163-185.

Droop, G.T.R., 1983. Pre-Alpine eclogites in the Pennine Basement Complex of the Eastern Alps, J. Metamorphic Geol., 1, 3-12.

Dubessy, J., 1984. Simulation des équilibres chimiques dans le system C-O-H. Conséquences méthodologiques pours les inclusions fluides. Bull. Minéral. 107, 155-168.

Enami, M. and Banno, S., 1980. Zoisite-clinozoisite relations in low- to medium-grade high-pressure metamorphic rocks and their implications, Mineral. Mag., 43, 1005-1013.

England, P.C., 1978. Some thermal considerations of the Alpine metamorphism - past, present, and future, Tectonophys., 46, 21-40.

England, P.C., 1981. Metamorphic pressure estimates and sediment volumes for the Alpine orogeny: an independent control on geobarometers?, Earth Plan. Sci. Lett., 56, 387-397.

England, P.C., and Holland, T.J.B., 1979. Archimedes and the Tauern eclogites: the role of buoyancy in the preservation of exotic eclogite blocks, Earth Planet. Sci. Lett., 44, 287-294.

England, P.C. and Richardson, S.W., 1977. The influence of erosion upon the mineral facies of rocks from different metamorphic environments, J. Geol. Soc. Lond., 134, 201-213.

England, P.C. and Richardson, S.W., 1980. Erosion and the age dependence of heat flow, Geophys. J.R. astr. Soc., 62, 421-437.

England, P. and Thompson, A.B., 1984. Pressure-temperature-time paths of regional metamorphism, Part I: Heat transfer during the evolution of regions of thickened continental crust, J. Petrol., 25, 894-928.

Ernst, W.G., 1973. Interpretive synthesis of metamorphism in the Alps. Geol. Soc. Amer. Bull., 84, 2053-2078.

Ernst, W.G., 1977. Tectonics and prograde versus retrograde P-T trajectories of high-pressure metamorphic belts. Rendiconti Societa Italiana di Mineralogia e Petrologia 33, 191-220.

Ferry, J.M. and Spear, F.S., 1978. Experimental calibration of the partitioning of Fe and Mg between garnet and biotite, Contrib. Mineral. Petrol., 66, 113-117.

Flowers, G.C., 1979. Correction of Holloway's (1977) adaptation of the modified Redlich-Kwong equation of state for calculation of the fugacities of molecular species in supercritical fluids of geologic interest, Contrib. Mineral. Petrol., 69, 315-318.

Fowler, C.M.R. and Nisbet, E.G., 1982. The thermal background to metamorphism II - Simple two-dimensional conductive models, Geoscience Can., 9, 208-213.

Frank, E., 1983. Alpine metamorphism of calcareous rocks along a cross-section in the Central Alps: occurrence and breakdown of muscovite, margarite, and paragonite, Schweiz. Mineral. Petrogr. Mitt., 63, 37-93.

Frank, E., and Stettler, A., 1979. K-Ar and ^{39}Ar-^{40}Ar systematics of white K-mica from an Alpine metamorphic profile in the Swiss Alps, Schweiz. Mineral. Petrogr. Mitt., 59, 375-394.

Franz, G. and Althaus, E., 1977. The stability relations of the paragenesis paragonite-zoisite-quartz, N. Jb. Mineral. Abh., 130, 159-167.

Franz, G. and Spear, F.S., 1983. High pressure metamorphism of siliceous dolomites from the central Tauern Window, Austria. Amer. J. Sci., 283-A, 396-413.

Frey, M., 1974. Alpine metamorphism of pelitic and marly rocks of the central Alps, Schweiz. Mineral. Petrogr. Mitt., 54, 489-506.

Frey, M., Bucher, K., Frank, E., and Mullis, J., 1980. Alpine metamorphism along the geotraverse Basel-Chiasso - a review, Eclogae Geol. Helv., 73, 527-546.

Frey, M., Hunziker, J.C., Frank, W., Bocquet, J., Dal Piaz, G.V., Jager, E., and Niggli, E., 1974. Alpine metamorphism of the Alps, Schweiz. Mineral. Petrogr., Mitt., 54, 247-291.

Frey, M. and Orville, P.M., 1974. Plagioclase in margarite-bearing rocks, Amer. J. Sci., 274, 31-47.

Frisch, W., 1977. Der alpidische Internbau der Venedigerdecke im westlichen Tauernfenster, N. Jb. Geol. Palaont. Mh. H. 11, 675-696.

Frisch, W., 1978. A plate tectonics model of the eastern Alps, in H. Closs, D. Roeder, K. Schmidt, eds., Alps, Apennines, Hellenides. Inter-Union Comm. on Geodynamics Sci. Rept. 38, 167-172.

Frisch, W., 1979. Tectonic progradation and plate tectonic evolution of the Alps, Tectonophys., 60, 121-139.

Frisch, W., 1980a. Plate motions in the Alpine region and their correlation to the opening of the Atlantic ocean. Mitt. osterr. geol. Ges. 71/72, 45-48.

Frisch, W., 1980b. Post-Hercynian formations of the western Tauern Window: sedimentological features, depositional environment, and age. Mitt. osterr. geol. Ges. 71/72, 49-63.

Frisch, W., 1984. Sedimentological response to late Mesozoic subduction in the Penninic windows of the Eastern Alps. Geol. Rund. 73, 33-45.

Frisch, W., 1984. Metamorphic history and geochemistry of a low-grade amphibolite in the Kaserer Formation (marginal Bundner Schiefer of the western Tauern Window, Eastern Alps). Schweiz. Mineral. Petrogr. Mitt. 64, 193-214.

Frisch, W., Neubauer, F., and Satir, M., 1984. Concepts of the evolution of the Austroalpine basement complex (Eastern Alps) during the Caledonian-Variscan cycle. Geol. Rund. 73, 47-68.

Fry, N., 1973. Lawsonite pseudomorphed in Tauern greenschist, Mineral. Mag., 39, 121-122.

Ganguly, J. and Kennedy, G.C., 1974. The energetics of natural garnet solid solution: I. Mixing of the aluminosilicate endmembers, Contrib. Mineral. Petrol., 48, 137-148.

Ghent, E.D., Robbins, D.B., and Stout, M.Z., 1979. Geothermometry, geobarometry, and fluid compositions of metamorphosed calcsilicates and pelites, Mica Creek, British Columbia, Amer. Mineral., 64, 874-885.

Ghent, E.D. and Stout, M.Z., 1981. Geobarometry and geothermometry of plagioclase-biotite-garnet-muscovite assemblages, Contrib. Mineral. Petrol., 76, 92-97.

Gibson, G.M., 1978. Staurolite in amphibolite and hornblendite sheets from the Upper Seaforth River, central Fiordland, New Zealand, Mineral. Mag., 42, 153-154.

Gibson, G.M., 1979. Margarite in kyanite-and corundum-bearing anorthosite, amphibolite, and hornblendite from central Fiordland, New Zealand, Contrib. Mineral. Petrol., 68, 171-179.

Green, T.H. and Hellman, P.L., 1982. Fe-Mg partitioning between coexisting garnet and phengite at high-pressure and comments on a garnet-phengite geothermometer, Lithos 15, 253-266.

Grundmann, G. and Morteani, G., 1982. Die Geologie des Smaragdvorkommens im Habachtal (Land Salzburg, Osterreich), Arch. F. Lagerst. Forsch. Geol. B-A.2, 71-107.

Grundmann, G. and Morteani, G., in press. The young uplift and thermal history of the central Eastern Alps (Austria/Italy) as deduced from apatite fission track studies, submitted, Geol. Rund.

Gutdeutsch, R., Steinhauser, P., Aric, K., Seiberl, W., Duma, G., and Drimmel, J., 1981. Geophysical contributions to the geodynamics of the Eastern Alps, Results of the Austrian Investigations in the International Geodynamics Project 1972-1979, p. 7-33.

Harrison, T.M. and McDougall, I., 1980. Investigations of an intrusive contact, northwest Nelson, New Zealand - I. Thermal, chronological, and isotopic constraints. Geochim. Cosmochim. Acta 44, 1985-2003.

Hawkesworth, C.J., 1974. Vertical distribution of heat production in the basement of the Eastern Alps, Nature 249, 435-436.

Hawkesworth, C.J., 1976. Rb/Sr geochronology in the Eastern Alps, 1976. Contrib. Mineral. Petrol., 54, 225-244.

Hawkesworth, C.J., Waters, D.J. and Bickle, M.J., 1975. Plate tectonics in the Eastern Alps, Earth Plan. Sci. Lett., 24, 405-413.

Hepburn, J.C., 1972. Geology of the metamorphosed Paleozoic rocks in the Brattleboro area, Vermont, PhD thesis, Harvard University, 342 pp.

Heinrich, W., 1981. Paragonite in Hochdruckgesteinen - experimentelle Untersuchungen zu Bildungs-und Abbaureaktionen, unpublished Ph.D. dissertation, Universitat Karlsruhe (Germany).

Helgeson, H.C., Delany, J.M., Nesbitt, H.W., and Bird, D.K., 1978. Summary and critique of the thermodynamic properties of rock-forming minerals. Amer. Jour. Sci., 278-A, 1-229.

Hietanen, A., 1974. Amphibole pairs, epidote minerals, chlorite, and plagioclase in metamorphic rocks, northern Sierra Nevada, California, Amer. Mineral., 59, 22-40.

Hock, V., 1974. Coexisting phengite, paragonite, and margarite in metasediments of the Mittlere Hohe Tauern, Austira, Contr. Mineral. Petrol., 43, 261-273.

Hodges, K.V., Tectonic evolution of the Aefjord-Sitas area, Norway-Sweden. PhD dissertation, M.I.T., Cambridge, Mass., 192 pp.

Hodges, K.V. and Crowley, P., 1985. Error estimation and empirical geothermobarometry for pelitic systems. Amer. Mineral., in press.

Hodges, K.V. and Spear, F.S., 1981. Geothermometry, geobarometry, garnet closure temperatures and the Al_2SiO_5 triple point, Mt. Moosilauke, N.H. Trans. Amer. Geophys. Union, 62, 1060.

Hodges, K.V. and Spear, F.S., 1982. Geothermometry, geobarometry, and the Al_2SiO_5 triple point at Mt. Moosilauke, New Hampshire, Amer. Mineral., 67, 1118-1134.

Hoefs, J. and Morteani, G., 1979. The carbon isotopic composition of fluid inclusions in Alpine fissure quartzes from the western Tauern Window (Tyrol, Austria), Neues Jb. Miner. Abh., 1979, 123-134.

Hoernes, S. and Friedrichsen, H., 1974. Oxygen isotope studies on metamorphic rocks of the western Hohe Tauern, Schweiz. Miner. Petr. Mitt., 54, 769-788.

Hoernes, S. and Friedrichsen, H., 1978. Oxygen isotope studies of the Austroalpine and Pennine units of the eastern Alps, in H. Closs, D. Roeder, and K. Schmidt, eds., Alps, Apennines, Hellenides, Inter-Union Comm. on Geodynamics Sci. Rept. 38, 127-131.

Holdaway, M.J., 1971. Stability of andalusite and the aluminum silicate phase diagram, Amer. J. Sci., 271, 97-131.

Holdaway, M.J., 1972. Thermal stability of Al-Fe epidote as a function of f_{O_2} and Fe content, Contrib. Mineral. Petrol., 37, 307-340.

Holland, T.J.B., 1979. High water activities in the generation of high pressure kyanite eclogites of the Tauern Window, Austria, J. Geol., 87, 1-27.

Holland, T.J.B. and Richardson, S.W., 1979. Amphibole zonation in metabasites as a guide to the evolution of metamorphic conditions. Contrib. Mineral Petrol., 70, 143-148.

Hollister, L.S., Burruss, R.C., Henry, D.L., and Hendel, E.M., 1979. Physical conditions during uplift of metamorphic terranes as recorded by fluid inclusions, Bulletin de Mineralogie, 102, 555-561.

Holloway, J.R., 1977. Fugacity and activity of molecular species in super-critical fluids, in: D.G. Fraser, ed., Thermodynamics in Geology, D. Reidel, Holland, p. 161-181.

Holloway, J.R., 1981. Volumes and compositions of supercitical fluids, in Hollister, L.S. and Crawford, M.L., eds., Fluid Inclusions: Petrologic Applications, Min. Assoc. Canada short course vol. 6, 13-38.

Holloway, J.R., 1984. Graphite-CH_4-H_2O-CO_2 equilibria at low-grade metamorphic conditions, Geology 12, 455-458.

Hoschek, G., 1969. The stability of staurolite and chloritoid and their significance in metamorphism of pelitic rocks, Contrib. Mineral. Petrol., 22, 208-232.

Hoschek, G., 1980. Phase relations of a simplified marly rock system with application to the western Hohe Tauern (Austria), Contr. Min. Pet., 73, 53-68.

Hoschek, G., 1981. Zur abschatzung von P-T-X Bedingungen der alpidischen metamorphose an hand karbonatfuhrender metasedimente der westlichen Hohen Tauern, Jber. 1980 Hochschulschwerpkt, S15, 59-66.

Hoschek, G., 1982. Alpidische Metamorphosebedingungen in Metasedimenten der westlichen Hohen Tauern, Jber. 1981 Hochschulschwerpkt, S15, 33-35.

Hoschek, G., 1984. Alpine metamorphism of calcareous metasediments in the western Hohe Tauern, Tyrol: mineral equilibria in COHS fluids, Contrib. Mineral Petrol., 87, 129-137.

Hsü, K., 1979. Thin-skinned plate tectonics during neo-Alpine orogenesis, Amer. J. Sci., 279, 353-366.

Janoschek, W.R. and Matura, A., 1980. Outline of the Geology of Austria, 26th I.G.C. Guidebook, 7-101.

Klemm, D.D., Lammerer, B., and Weber-Diefenbach, K., 1978. Geodynamics of the western Tauern Window, in H. Closs, D. Roeder, and K. Schmidt, eds., Alps, Apennines, Hellenides, Unter-Union Comm. on Geodynamics Sci. Rept. 38, 132-134.

Koller, F., 1976. Zur Petrologie der Hornblendegarbenschiefer, Tscherm. Min. Petr. Mitt., 23, 275-315.

Kreuzer, H., Morteani, G., and Roeder, D., 1980. Geodynamic evolution of the Eastern Alps along a geotraverse, in H. Closs et al., eds., Mobile Earth: Final report on International Geodynamics Project.

Laird, J., 1980. Phase equilibria in mafic schist from Vermont, 1980. J. Petrol., 21, 1-37.

Laird, J. and Albee, A.L., 1981. Pressure, temperature, and time indicators in mafic schist: their application to reconstructing the polymetamorphic history of Vermont, Amer. J. Sci., 281, 127-175.

Lammerer, B., in press. Ductile deformation versus nappe tectonics in the central Eastern Alps, (Austria and Italy), Proc. 5th Internat. Conf. on Basement Tectonics.

Lasaga, A.C., 1981. The atomistic basis of kinetics: defect n minerals. In: Lasaga and Kirkpatrick, eds., Kinetics of Geochemical Processes, Min. Soc. Amer. Rev. in Mineral. 8, 261-316.

Lasaga, A.c., Richardson, S.M., and Holland, H.D., 1977. The mathematics of cation diffusion and exchange between silicate minerals during retrograde metamorphism. In: Saxena and Battacharji, eds., Energetics of Geological Processes. Springer-Verlag.

Laubscher, H.P., 1975. Plate boundaries and microplates in Alpine history. Amer. J. Sci. 275, 865-876.

Leroy, J., 1979. Contribution a l'etalonnage de la pression interne des inclusions fluides lors de leur decrepitation, Bull. Mineral., 102, 584-593.

Liou, J.G., Kim, H.S., and Maruyama, S., 1984. Prehnite-epidote equilibria and their petrologic applications, J. Petrol. 24, 321-342.

Loomis, T.P. and Nimick, F.B., 1982. Equilibrium in Mn-Fe-Mg aluminous pelitic compositions and the equilibrium growth of garnet, Canad. Mineral., 20, 393-410.

Luckscheiter, B. and Morteani, G., 1980a. Microthermometrical and chemical studies of fluid inclusions in minerals from Alpine veins from the penninic rocks of the central and western Tauern Window (Austria/Italy), Lithos, 13, 61-77.

Luckscheiter, B. and Morteani, G., 1980b. The fluid phase in eclogites, glaucophane-bearing rocks and amphibolites from the central Tauern Window as deduced from fluid inclusion studies, Tscher. Min. Petr. Mitt., 27, 99-111.

Maresch, W.V., 1977. Experimental studies on glaucophane: an analysis of present knowledge, Tectonophysics, 43, 109-125.

Maruyama, S., Suzuki, K., and Liou, J.G., 1983. Greenschist-amphibolite transition equilibria at low pressures, J. Petrol., 24, 583-604.

Maruyama, S., Liou, J.G., and Cho, M., 1984. Experimental study on the blueschist-greenschist transition, Geol. Soc. Amer. Prog. abs., 16, 585.

Massone, H.-J., 1981. Phengite: eine experimentelle Untersuchung ihres Druck-Temperatur-Verhaltens im system K_2O-MgO-Al_2O_3-SiO_2-H_2O. Unpublished PhD thesis, Ruhr-Universitat Bochum, W. Germany.

Miller, C., 1974. On the metamorphism of the eclogites and high-grade blueschists from the Penninic terrane of the Tauern Window, Austria, Schweiz. Mineral. Petrogr. Mitt., 54, 371-384.

Miller, C., 1977. Chemismus und phasenpetrologische Untersuchungen der Gesteine aus der Eclogitzone des Tauernfensters, Osterreich, Tscher. Min. Petr. Mitt., 24, 221-278.

Miller, H., Mueller, S., and Perrier, G., 1982. Structure and dynamics of the Alps - a geophysical inventory, in H. Berckheimer and K. Hsu, eds., Alpine-Mediterranean Geodynamics, Amer. Geophys. Union, 175-203.

Molnar, P., 1984. Structure and tectonics of the Himalaya: constraints and implications of geophysical data. Ann. Rev. Earth Planet Sci. 12, 489-518.

Molnar, P. and Gray, D., 1979. Subduction of continental lithosphere: some constraints and uncertainties, Geology 7, 58-62.

Morteani, G., 1974. Petrology of the Tauern Window, Austrian Alps, Fortschr. Miner., 52, 195-220.

Newton, R.C. and Haselton, H.T., 1981. Thermodynamics of the garnet-plagioclase-Al_2SiO_5-quartz geobarometer, in R.C. Newton, A. Navrotsky, and B.J. Wood, eds., Thermodynamics of Minerals and Melts, Springer-Verlag, N.Y., p. 131-147.

Ohmoto, H. and D. Kerrick, 1977. Devolatization equilibria in graphitic systems, Amer. J. Sci. 277, p. 1013-1044.

Oxburgh, E.R., 1968. The geology of the eastern Alps. The Geologists' Assoc.: London.

Oxburgh, E.R. and England, P.C., 1980. Heat flow and the metamorphic evolution of the Eastern Alps. Eclogae Geol. Helv., 73, 379-398.

Oxburgh, E.R. and Turcotte, D.L., 1974. Thermal gradients and regional metamorphism in overthrust terrains with special reference to the Eastern Alps, Schweiz. Min. Pet. Mitt., 54, 641-662.

Parrish, R.R., 1983. Cenozoic thermal evolution and tectonics of the Coast Mountains of British Columbia 1. Fission track dating, apparent uplift rates, and patterns of uplift. Tectonics 2, 601-631.

Pavlis, T.L. and Bruhn, R.L., 1983. Deep-seated flow as a mechanism for the uplift of broad forearc ridges and its role in the exposure of high P/T metamorphic terranes, Tectonics, 2, 473-497.

Pécher, A. and Boullier, A.M., 1984. Evolution à pression et temperature élevées d'inclusions fluides dans un quartz synthetique. Bull. Mineral. 107, 139-153.

Pigage, L.C. and Greenwood, H.J., 1982. Internally consistent estimates of pressure and temperature: the staurolite problem, Amer. J. Sci., 282, 943-969.

Potter, R.W. and Brown, D.L., 1975. Volumetric properties of aqueous sodium chloride solutions from 0 to 500°C at pressures up to 2000 bars based on a regression of available literature data. U.S.G.S. open-file rept. 75-636.

Raith, M., 1976. The Al-Fe (III) Epidote miscibility gap in a metamorphic profile through the Penninic series of the Tauern Window, Austria, Contrib. Mineral. Petrol., 57, 99-117.

Raith, M., Hormann, P.K., and Abraham, K., 1977. Petrology and metamorphic evolution of the Penninic ophiolites in the western Tauern Window (Austria), Schweiz. Mineral. Petrogr. Mitt., 57, 187-232.

Raith, M., Raase, P., Kreuzer, H., and Muller, P., 1978. The age of the Alpidic metamorphism in the western Tauern Window, Austrian Alps, according to radiometric dating, in H. Closs, D. Roeder, K. Schmidt, eds., Alps, Apennines, Hellenides. Inter-Union Comm. on Geodynamics Sci. Rept. 38, 140-152.

Richardson, S.W. and England, P.C., 1979. Metamorphic consequences of crustal eclogite production in overthrust orogenic zones. Earth Plan. Sci. Lett., 42, 183-190.

Robie, R.A., Hemingway, B.S., and Fisher, J.R., 1978. Thermodynamic properties of minerals and related substances at 298.15K and 1 bar (10^5 pascals) pressure and at higher temperatures, U.S. Geol. Surv. Bull., 1452, 456 p.

Robinson, P., Spear, F., Schumacher, J., Laird, J., Klein, C., Evans, B., and Doolan, B., 1982. Phase relations of metamorphic amphiboles: natural occurrence and theory, in D.R. Veblen and P.H. Ribbe, eds., Min. Soc. Amer. Reviews in Mineralogy 9B, 1-228.

Roedder, E., 1984. Fluid Inclusions. Mineral. Soc. Amer. Rev. in Mineral. 12, 644 pp.

Roeder, D., 1978. Three central Mediterranean orogens - a geodynamic synthesis, in H. Closs, D. Roeder, K. Schmidt, eds., Alps, Apennines, Hellenides, Inter-Union Comm. on Geodynamics Sci. Rept. 38, 589-620.

Roeder, D. and Bogel, H., 1978. Geodynamic interpretation of the Alps, in, H. Closs, D. Roeder and K. Schmidt, eds., Alps, Apennines, Hellenides, Inter-Union Comm. Geodynamics Sci. Rept. 38, 191-212.

Royden, L. and Hodges, K.V., 1984. A technique for analyzing the thermal and uplift histories of eroding orogenic belts: a Norwegian example, J. Geophys. Res. 89, 7091-7106.

Rubie, D.C., 1983. Reaction-enhanced ductility: the role of solid-solid univariant reactions in deformation of the crust and mantle, Tectonophysics, 96, 331-352.

Rubie, D.C., 1984. A thermal-tectonic model for high-presure metamorphism and deformation in the Sesia Zone, western Alps, J. Geol., 92, 21-36.

Rumble, D., 1978. Mineralogy, petrology, and oxygen isotope geochemistry of the Clough Formation, Black Mountain, western New Hampshire. J. Petrol. 19, 317-340.

Ryzhenko, B.N. and Volkov, V.P., 1971. Fugacity coefficients of some gases in a broad range of temperatures and pressures, Geochem. Internat. 8, 468-481.

Sacks, I.S., 1983. The subduction of young lithosphere, J. Geophys. Res., 88, 3355-3366.

Sander, B., 1911. Geologische Studien am Westende Hohen Tauern (1. Bericht). Denkschr. Akad. Wiss. Wien, Math. Nat. Kl. 82, 257-319.

Sanford, R., 1982. Three FORTRAN programs for finite-difference solutions to binary diffusion in one and two phases with composition- and time-dependent diffusion coefficients. Computers and Geosciences 8, 235-263.

Sassi, F.P., Borsi, S., DelMoro, A., Zanferrari, A., and Zirpoli, G., 1978. Contribution to the geodynamic interpretation in the eastern Alps, in H. Closs, D. Roeder, K. Schmidt, eds., Inter-Union Comm. on Geodynamics Sci. Rept. 38, 154-160.

Satir, M. and Morteani, G., 1982. Petrological study and radiometric age determination of the migmatites in the Peninnic rocks of the Zillertaler Alpen (Tyrol/Austria), Tschermaks Min. Petr. Mitt. 30, 59-75.

Seidel, E., 1983. Fe-Mg carpholite -indicator of high P/low T metamorphism, Terra Cognita 3, 190.

Selverstone, J., 1982. Fluid inclusions as petrogenetic indicators in granulite xenoliths, Pali-Aike volcanic field, Chile, Contrib. Mineral. Petrol. 79, 28-36.

Selverstone, J., Spear, F., Franz, G., Morteani, G., High-pressure metamorphism in the SW Tauern Window, Austria: P-T paths from hornblende-kyanite-staurolite schists, J. Petrol., 25, 501-531.

Shmonov, V.M. and Shmulovich, K.I., 1974. Molar volumes and equation of state of CO_2 at temperatures from 100° to 1000°C and pressures from 2000 to 10,000 bars. Dokl. Acad. Sci. USSR 217, 206-209.

Smith, A.G. and Woodcock, N.H., 1982. Tectonic syntheses of the Alpine-Mediterranean region: a review. In H. Berckheimer and K. Hsu, eds., Alpine-Mediterranean Geodynamics, Amer. Geophys. Union Geodynamics Series 7, 15-38.

Spear, F.S., 1977. Phase equilibria of amphibolites from the Post Pond Volcanics, Vermont, Carnegie Institute of Washington Yearbook, 76, 613-619.

Spear, F.S., 1980. NaSi-CaAl exchange equilibrium between plagioclase and amphibole. Contrib. Mineral. Petrol., 72, 33-41.

Spear, F.S., 1981. Amphibole-plagioclase equilibria: an empirical model for the relation Albite + Tremolite = Edenite + 4 Quartz, Contrib. Mineral. Petrol., 77, 355-364.

Spear, F.S., 1982. Phase equilibria of amphibolites from the Post Pond Volcanics, Mt. Cube quadrangle, Vermont, Journal of Petrology, 23, 383-426.

Spear, F.S., Ferry, J.M., and Rumble, D., 1982. Analytical formulation of phase equilibria: the Gibbs method, in J.M. Ferry, ed., Mineral. Soc. Amer., Reviews in Mineralogy, 10, 105-152.

Spear, F.S. and Kimball, K.L., 1984. RECAMP: a FORTRAN IV program for recalculating Fe^{3+} in amphiboles, Computers in Geology, 10, 317-325.

Spear, F.S., Rumble, D. and Ferry, J.M., 1982b. Linear algebraic manipulation of N-dimensional composition space, in J.M. Ferry, ed., Characterization of Metamorphism through Mineral Equilibria, Min. Soc. Amer. Reviews in Mineralogy, 10, 53-104.

Spear, F.S. and Selverstone, J., 1983. Quantitative P-T paths from zoned minerals: theory and tectonic applications, Contributions to Mineralogy and Petrology, 83, 348-357.

Spear, F.S., Selverstone, J., Hickmott, D., Crowley, P., and Hodges, K.V., 1984. P-T paths from garnet zoning: a new technique for deciphering tectonic processes in crystalline terranes, Geology, 12, 87-90.

Storre, B. and Nitsch, K.H., 1974. Zur stabilitat von Margarit im System $CaO-Al_2O_3-SiO_2-H_2O$, Contrib. Mineral. Petrol., 43, 1-24.

Swanenberg, H.E.C., 1979. Phase equilibria in carbonic systems and their application to freezing studies of fluid inclusions. Contrib. Mineral. Petrol. 68, 303-306.

Thompson, A.B., 1981. The pressure-temperature (P,T) plane viewed by geophysicists and petrologists, Terra Cognita 1, 1-20.

Thompson, A.B. and England, P., 1984. Pressure-temperature-time paths of regional metamorphism of the continental crust, II: Some petrological constraints from mineral assemblages in metamorphic rocks, J. Petrol. 25, 929-955.

Thompson, J.B., 1957. The graphical analysis of mineral assemblages in pelitic schists. Am. Mineral. 42, 842-858.

Thompson, J.B., 1982. Composition space: an algebraic and geometric approach, in J.M. Ferry, ed., Characterization of metamorphism through mineral equilibria, Min. Soc. Amer. Rev. in Mineral., 10, 1-31.

Tollmann, A., 1977. Geologie von Osterreich, Band I, Franz Deuticke: Wien, 766 pp.

Tracy, R.J., 1982. Compositional zoning and inclusions in metamorphic minerals, in J.M. Ferry, ed., Mineral. Soc. Amer., Reviews in Mineralogy 10, 355-397.

Tracy, R.J. and Robinson, P., 1980. Evolution of metamorphic belts: information from detailed petrologic studies, in D.R. Wones, ed., Proceedings: The Caledonides in the U.S.A. Virginia Polytechnic Univ. Dept. of Geol. Mem. 2, 189-195.

Tröger, W.E., 1971. Optische Bestimmung der Gesteinsbildenden Minerale, Schweizerbartsche Verlags Buchhandlung, Stuttgart. 4th edition, 188 pp.

Trümpy, R., 1960. Paleotectonic evolution of the central and western Alps, Geol. Soc. Amer. Bull. 71, 843-908.

Vitorello, I. and Pollack, H.N., 1980. On the variation of heat flow with age and the thermal evolution of continents. J. Geophys. Res. 85, 983-995.

Wang, C.-Y., and Shi, Y.-L., 1984. On the thermal structure of subduction complexes: a preliminary study, J. Geophys. Res.

Yardley, B.W.D. 1977. An empirical study of diffusion in garnet. Amer. Min., 62, 793-800.